UNIVERSITY OF ALBERTA

THEORETICAL ANALYSIS AND EXPERIMENTAL INVESTIGATION OF THE PERFORMANCE OF OZONE BUBBLE COLUMNS

BY

MOHAMED GAMAL EL-DIN ©

A THESIS

SUBMITTED TO THE FACULTY OF GRADUATE STUDIES AND RESEARCH IN
PARTIAL FULFILLMENT OF THE REQUIREMENTS FOR THE DEGREE OF
DOCTOR OF PHILOSOPHY
IN
ENVIRONMENTAL ENGINEERING

DEPARTMENT OF CIVIL & ENVIRONMENTAL ENGINEERING

EDMONTON, ALBERTA
FALL, 2001

National Library of Canada
Acquisitions and Bibliographic Services
395 Wellington Street
Ottawa ON K1A 0N4
Canada

Bibliothèque nationale du Canada
Acquisitions et services bibliographiques
395, rue Wellington
Ottawa ON K1A 0N4
Canada

Your file Votre référence

Our file Notre référence

The author has granted a non-exclusive licence allowing the National Library of Canada to reproduce, loan, distribute or sell copies of this thesis in microform, paper or electronic formats.

L'auteur a accordé une licence non exclusive permettant à la Bibliothèque nationale du Canada de reproduire, prêter, distribuer ou vendre des copies de cette thèse sous la forme de microfiche/film, de reproduction sur papier ou sur format électronique.

The author retains ownership of the copyright in this thesis. Neither the thesis nor substantial extracts from it may be printed or otherwise reproduced without the author's permission.

L'auteur conserve la propriété du droit d'auteur qui protège cette thèse. Ni la thèse ni des extraits substantiels de celle-ci ne doivent être imprimés ou autrement reproduits sans son autorisation.

0-612-68934-4

Canadä

UNIVERSITY OF ALBERTA

RELEASE FORM

NAME OF AUTHOR: MOHAMED GAMAL EL-DIN

TITLE OF THESIS: THEORETICAL ANALYSIS AND EXPERIMENTAL INVESTIGATION OF THE PERFORMANCE OF OZONE BUBBLE COLUMNS

DEGREE FOR WHICH THIS THESIS HAS PRESENTED: DOCTOR OF PHILOSOPHY

YEAR THIS DEGREE GRANTED: FALL 2001

Permission is hereby granted to THE UNIVERSITY OF ALBERTA LIBRARY to reproduce single copies of this thesis and to lend or sell such copies for private, scholarly or scientific research purposes only.

The author reserves other publication rights, and neither the thesis nor extensive extracts from it may be printed or otherwise reproduced without the author's written permission.

(signed) Mohamed

PERMANENT ADDRESS:
611E Michener Park
Edmonton, Alberta
Canada
T6H 5A1

Date October 1, 2001

UNIVERSITY OF ALBERTA
FACULTY OF GRADUATE STUDIES AND RESEARCH

The undersigned certify that they have read, and recommended to the faculty of Graduate Studies and Research, for acceptance, a thesis entiltled: THEORETICAL ANALYSIS AND EXPERIMENTAL INVESTIGATION OF THE PERFORMANCE OF OZONE BUBBLE COLUMNS submitted by: Mohamed Gamal El-Din in partial fulfillment of the requirement for the degree of DOCTOR OF PHILOSOPHY IN ENVIRONMENTAL ENGINEERING.

Daniel W. Smith
Dr. Daniel W. Smith-Supervisor

Ian Buchanan
Dr. Ian D. Buchanan

Dr. Tong Yu

Dr. Nallamuthu Rajaratnam

Dr. Jerry Leonard

Dr. Nihar Biswas (External Examiner)

Date 1 Oct 2001

DEDICATION

This work is dedicated to my family who had a great influence on my life. My mother, Dr. Nadia El-Safory who has taught me that every thing is possible with hard work. My father, Mr. Galal Gamal El-Din, who has always encouraged me to seek more knowledge and has always been there for me when I needed him. My brother, Mr Ahmed Gamal El-Din, with whom I shared all the good and bad times throughout this journey.

ABSTRACT

The transient Back flow cell model (BFCM) has been presented as an alternative approach to describe the hydrodynamics of ozone bubble columns. Compared to the traditionally used models, transient BFCM provided a more flexible, reliable, and accurate tool to describe the backmixing in the liquid phase.

The two-phase steady-state axial dispersion model (2P-ADM) and BFCM have been developed for describing the performance of ozone bubble columns. Although, the 2P-ADM and BFCM have proven to be adequate for modeling the ozonation process, the BFCM was easier to formulate and solve.

A modified steady-state non-isobaric one-phase axial dispersion model (1P-ADM) has been developed. The 1P-ADM is composed of a single non-homogeneous linear second-order ordinary differential that was solved analytically. Compared to 2PADM, the 1P-ADM has provided reliable predictions of the dissolved and gaseous ozone concentrations.

An impinging-jet bubble column, that utilized two venturi injectors, has been tested for the ozone mass transfer applications. The venturi injectors created impinging gas-liquid jets in the ambient fluid and that caused an increase in the turbulence produced in the ambient fluid and therefore, the gas-liquid mass transfer rates increased. The 1P-ADM was applied to analyze the measured dissolved and gaseous ozone concentrations.

Excellent conformity between the measured and the predicted concentrations was observed. Therefore, the 1P-ADM model has proven to be an efficient, adequate, and easy-to-use tool for describing the ozonation in the impinging-jet bubble column.

Compared to conventional diffuser ozone bubble columns, the impinging-jet design has provided comparable reduction efficiencies of the impurities present in Kraft pulp mill effluents. However, the impinging-jet bubble column was more effective due to its smaller reactor volume and lower off-gas ozone concentrations.

A 2-D laser particle dynamics analyzer was used to measure the characteristics of the gas bubbles in the impinging-jet bubble column using clean deionized water and ozonated Kraft pulp mill effluent as the test liquid. The count mean bubble diameter (d_B) and Sauter mean bubble diameter (d_S) were smaller than those obtained in conventional bubble columns and that has led to a significant increase in the specific bubbles' interfacial area and gas hold-up.

ACKNOWLEDGEMENT

I would like to express my sincere and great appreciation to Dr. Daniel W. Smith for his guidance, support, encouragement, and patience throughout my research program. I also would like to thank him for encouraging me to attend many technical conferences and gave me the opportunity to submit and publish a number of papers.

I also want to express my great appreciation and thanks to my great brother and friend Mr. Ahmed Gamal El-Din who has been always there when I needed him and with whom I shared great discussions throughout my research program. He also has provided me with great suggestions and thoughts throughout the preparation of my thesis.

A special thank you to my great collogue and friend Mr. Kevin McCullum for his help during some of my experimental laboratory work. I also appreciate the suggestions and fruitful discussions he has shared with me throughout my research program.

I would to thank all the technical staff at the Environmental Engineering Laboratory at the University of Alberta for their great assistance during the laboratory program. Especially, Mr. Nick Chernuka, Mrs. Maria Demeter, and Mrs. Debra Long. I also appreciate the assistance by Mr. Garry Solonynko during the setting-up of the experimental apparatus.

The financial support throughout the research project was provided to Dr. Daniel W. Smith by the Sustainable Forest Management (SFM) network and the Natural Sciences and Engineering Research Council of Canada (NSERC) is greatly appreciated.

Finally a special thank you to my parents and my brother for their guidance, encouragement, understanding, and sacrifices during the course of the long journey of my graduate studies.

TABLE OF CONTENTS

CHAPTER 1. GENERAL INTRODUCTION 1
1.1 BACKGROUND 1
1.2 FUNDAMENTALS OF THE OZONATION PROCESS 6
1.2.1 Backmixing Process 6
1.2.2 Ozone Auto-Decomposition Process 6
1.2.3 Mass Transfer Process 8
1.2.3.1 Mass Transfer Without Chemical Reactions 8
1.2.3.2 Mass Transfer With Chemical Reactions 8
1.3 Practical ASPECTS OF OZONE CONTACTORS 10
1.3.1 Types of Ozone Contactors 10
1.3.2 Designing Ozone Contactors 12
1.4 OBJECTIVES AND SCOPES OF THE RESEARCH PROGRAM 13
1.5 REFERENCES 16
CHAPTER 2. DEVELOPMENT OF TRANSIENT BACK FLOW CELL MODEL (BFCM) FOR BUBBLE COLUMNS* 20
2.1 INTRODUCTION 20
2.2 TRACER TESTS 21
2.3 THEORY 23
2.3.1 Axial Dispersion Model 23
2.3.2 Transient Continuous-Flow-Stirred-Tank-Reactors In-Series Model 26
2.4 Transient Back Flow Cell Model (BFCM) 27
2.4.1 Development of the Transient BFCM 27
2.4.2 Numerical Simulations of the Transient BFCM 33
2.4.2.1 Numerical Solution Technique 33
2.4.2.2 Results 34
2.5 TESTING OF THE TRANSIENT BFCM 43
2.5.1 Experimental Study 43
2.5.2 Data Analysis Technique 43
2.5.3 Results 45

2.6 CONCLUSIONS 49
2.7 REFERENCES 50
CHAPTER 3. OZONE MASS TRANSFER IN WATER TREATMENT: MASS TRANSFER MODELING OF OZONE BUBBLE COLUMNS* 52
3.1 INTRODUCTION 52
3.2 THEORETICAL BACKGROUND 53
3.3 DEVELOPMENT OF THE BACK FLOW CELL MODEL (BFCM).. 56
3.3.1 Transient BFCM 56
3.3.2 Steady-State BFCM 59
3.4 RESULTS AND DISCUSSION 63
3.4.1 Transient BFCM 63
3.4.2 Steady-state BFCM 64
3.5 CONCLUSIONS 67
3.6 REFERENCES 68
CHAPTER 4. TWO-PHASE NON-ISOBARIC AXIAL DISPERSION MODELS FOR MODELING THE OZONATION PROCESS DYNAMICS–I. MODELS DEVELOPMENT 70
4.1 INTRODUCTION 70
4.1.1 Ozonation Process Dynamics 70
4.1.2 Bubble Column Parameters 70
4.1.3 Dispersion Models for Two-Phase Flows 71
4.2 PROCESSES FUNDAMENTALS 72
4.2.1 Slow-Chemical-Reaction-Kinetics-Regime Systems 72
4.2.2 Fast-Chemical-Reaction-Kinetics-Regime Systems 74
4.3 DEVELOPMENT OF THE TWO-PHASE AXIAL DISPERSION MODEL (2P-ADM) EQUATIONS 76
4.3.1 Considering the Gas-Phase Dispersion 77
4.3.1.1 Wastewater Treatment Conditions 77
4.3.1.2 Boundary Conditions 81
4.3.2 Special Conditions of the Two-Phase Axial Dispersion Model (2P-ADM) 83

4.3.2.1 Consideration of the Gas-Phase Dispersion (Water Treatment Conditions) ... 83
4.3.2.2 Neglecting the Gas-Phase Dispersion ... 83
4.4 NUMERICAL SOLUTION TECHNIQUE ... 85
4.4.1 2P-ADM With Gas-Phase Dispersion (Wastewater Treatment Conditions) ... 86
4.4.2 2P-ADM With Gas-Phase Dispersion (Water Treatment Conditions) ... 89
4.4.3 2P-ADM without gas phase dispersion ... 89
4.5 CONCLUSIONS ... 90
4.6 REFERENCES ... 91
CHAPTER 5. TWO-PHASE NON-ISOBARIC AXIAL DISPERSION MODELS FOR MODELING THE OZONATION PROCESS DYNAMICS–II. NUMERICAL ANALYSES AND EXPERIMENTAL VERIFICATION* ... 93
5.1 INTRODUCTION ... 93
5.2 NUMERICAL SIMULATIONS AND SENSITIVITY ANALYSES ... 94
5.2.1 Numerical Solution Techniques of the 2P-ADM Equations ... 94
5.2.2 Operating Conditions for Water Treatment Applications ... 95
5.2.3 Operating Conditions for Wastewater Treatment Applications ... 96
5.2.4 Operating Conditions for Model Testing (Water Treatment Applications) ... 97
5.3 RESULTS AND DISCUSSION ... 98
5.3.1 Counter-Current Flow Mode (Water Treatment Applications) ... 98
5.3.2 Co-Current Flow Mode (Water Treatment Applications) ... 108
5.3.3 Counter-Current and Co-Current Flow Modes (Wastewater Treatment Applications) ... 112
5.3.4 Model Testing for Water Treatment Applications ... 115
5.4 CONCLUSIONS ... 117
5.5 REFERENCES ... 118

CHAPTER 6. THEORETICAL ANALYSIS AND EXPERIMENTAL VERIFICATION OF OZONE MASS TRANSFER IN BUBBLE COLUMNS* 119
6.1 INTRODUCTION 119
6.2 THEORETICAL BACKGROUND 121
6.3 OUTLINE OF THE MATHEMATICAL MODELS AND THE NUMERICAL SOLUTIONS TECHNIQUES 124
6.3.1 Axial Dispersion Model (ADM) 124
6.3.2 Back Flow Cell Model (BFCM) 126
6.4 OPERATING CONDITIONS FOR MODELS TESTING AND NUMERICAL ANALYSES 129
6.4.1 Water Treatment 129
6.4.2 Wastewater Treatment 130
6.5 RESULTS AND DISCUSSION 131
6.5.1 Water Treatment: Initial Testing of the Models 131
6.5.2 Wastewater Treatment 133
6.6 CONCLUSIONS 139
6.7 REFERENCES 140
CHAPTER 7. DESIGNING OZONE BUBBLE COLUMNS: A SPREADSHEET APPROACH TO AXIAL DISPERSION MODEL* 142
7.1 INTRODUCTION 142
7.2 DISPERSION MODELS FOR TWO-PHASE FLOWS 145
7.2.1 Process Fundamentals 145
7.2.2 Mass Transfer Process with Chemical Reactions 147
7.2.3 Two-Phase Axial Dispersion Model (2P-ADM) 149
7.2.4 Development of the One-Phase Axial Dispersion Model (1P-ADM) 151
7.3 OPERATING CONDITIONS FOR THE MODEL SIMULATIONS AND TESTING 158
7.3.1 Water Treatment Conditions 158
7.3.2 Wastewater Treatment Conditions 158

7.4 RESULTS AND DISCUSSION 160
7.4.1 Theoretical Analyses of the 1P-ADM Predictions 160
7.4.1.1 Water Treatment Applications: Counter-Current Flow Mode 160
7.4.1.1 Water Treatment Applications: Co-Current Flow Mode 164
7.4.1.2 Wastewater Treatment Applications: Counter-Current and Co-Current Flow Modes 168
7.4.2 Initial Model Testing for Water Treatment Conditions 171
7.5 CONCLUSIONS 174
7.6 REFERENCES 175
CHAPTER 8. DEVELOPMENT OF DESIGN PARAMETERS OF AN IMPINGING-JET BUBBLE COLUMN* 178
8.1 INTRODUCTION 178
8.2 OUTLINE OF THE MODIFIED NON-ISOBARIC ONE-PHASE AXIAL DISPERSION MODEL (1P-ADM) 181
8.3 EXPERIMENTAL AND DATA ANALYSES METHODS 186
8.3.1 Bench Tests: Ozone Auto-Decomposition kinetics Study 186
8.3.2 Pilot-Scale Tests: Ozone Mass Transfer Study 188
8.3.3 Data Analysis Method for the Kinetics Study 193
8.3.4 Data Analysis Method for the Mass Transfer Study 193
8.4 EXPERIMENTAL RESULTS 194
8.4.1 Bench Tests: Ozone Auto-Decomposition Kinetics Study 194
8.4.2 Pilot-Scale Tests: Ozone Mass Transfer Study 196
8.5 DEVELOPMENT OF PROCESS-PARAMETER CORRELATIONS 200
8.5.1 Correlations of the Mass Transfer Coefficient 201
8.5.2 Correlations of the Backmixing Coefficient 209
8.5.3 Correlations of the Gas-phase-Concentration-Decrease Exponent 212
8.6 CONCLUSIONS 214
8.7 REFERENCES 215

CHAPTER 9. MAXIMIZING THE ENHANCED OZONE OXIDATION OF KRAFT PULP MILL EFFLUENTS IN AN IMPINGING-JET BUBBLE COLUMN* 219
- 9.1 INTRODUCTION 219
- 9.2 FUNDAMENTALS OF THE OZONATION PROCESS 222
- 9.3 THE MODIFIED NON-ISOBARIC ONE-PHASE AXIAL DISPERSION MODEL (1P-ADM) 222
- 9.4 EXPERIMENTAL METHODS 223
  - 9.4.1 Bench Tests: Ozone Auto-Decomposition Kinetics Study 223
  - 9.4.2 Pilot-Scale Tests: Continuous-Flow Mode/Ozonation of Water and Pulp Mill Effluent 224
  - 9.4.3 Pilot-Scale Tests: Semibatch-Flow Mode/Ozonation of Pulp mill Effluent 227
  - 9.4.4 Pulp Mill Effluent Characterization 227
- 9.5 RESULTS AND DISCUSSION 228
  - 9.5.1 Bench Tests: Ozone Auto-Decomposition Kinetics 228
  - 9.5.2 Pilot-Scale Tests: Ozone Mass Transfer in Water 230
  - 9.5.3 Ozone Mass Transfer in Pulp Mill Effluent: Gas Absorption Dynamics 232
  - 9.5.4 Ozone Oxidation Efficiencies 237
- 9.6 CONCLUSIONS 241
- 9.7 REFERENCES 243

CHAPTER 10. COMPARING DIFFERENT DESIGNS AND SCALES OF BUBBLE COLUMNS FOR THEIR EFFECTIVENESS IN TREATING KRAFT PULP MILL EFFLUENTS* 246
- 10.1 INTRODUCTION 246
- 10.2 EXPERIMENTAL METHODS 248
  - 10.2.1 Extra-Coarse-Bubble Diffuser Ozone Contactor 248
  - 10.2.2 Impinging-Jet Ozone Contactor 249
    - 10.2.2.1 Continuous-Flow Mode 249
    - 10.2.2.2 Semibatch-Flow Mode 252

10.2.3 Fine-Bubble Diffuser Ozone Contactor 252
10.2.4 Characterization of the Pulp Mill Wastewater 252
10.3 RESULTS AND DISCUSSION 253
10.3.1 Ozonation Treatment Efficiencies 253
10.3.1.1 Extra-Coarse-Bubble Diffuser Ozone Contactor 253
10.3.1.2 Impinging-Jet Ozone Contactor 255
10.3.2 Ozone Gas Absorption Dynamics 259
10.3.3 Modeling of the Ozonation Treatment Efficiencies 264
10.3.4 Scale-Up of the Ozonation Process 269
10.4 CONCLUSIONS 272
10.5 REFERENCES 273
CHAPTER 11. Measurements of the Size, Rise Velocity, and Specific Interfacial Area of Bubbles in an Impinging-Jet Bubble Column* 275
11.1 INTRODUCTION 275
11.2 MEASUREMENT METHODS 277
11.2.1 Particle Dynamics Analyzer 277
11.2.1.1 Operating Principle 277
11.2.1.2 Principle of the Bubble Rise Velocity Measurement 277
11.2.1.3 Principle of the Bubble Size and Concentration Measurements 278
11.2.1.4 PDA System Configuration and Operational Settings Adjustment 280
11.2.2 Digital Photographic Measurements of the Bubble Size and the Bubble Rise Velocity 280
11.2.3 Experimental Set-Up for the Photographic and the PDA Studies 282
11.2.4 Experimental Set-Up for the Ozonation of Kraft Pulp Mill Effluent 283
11.3 RESULTS AND DISCUSSION 285
11.3.1 Digital Photographic Measurements 285
11.3.2 Particle Dynamics Analyzer Measurements 287
11.3.2.1 Deionized Water 287
11.3.2.2 Kraft pulp mill effluent 297
11.4 Conclusions 305
11.5 REFERENCES 307

CHAPTER 12. GENERAL CONCLUSIONS AND RECOMMENDATIONS........... 309
12.1 GNERAL OVERVIEW 309
12.2 CONCLUSIONS.......... 311
12.3 RECOMMENDATIONS 317
APPENDIX A. CURRICULUM VITAE 319

LIST OF TABLES

Table 3.1 Operating conditions for the co-current flow mode. 64

Table 3.2 Operating conditions for the counter-current flow mode. 65

Table 5.1 Operating conditions for the counter-current flow mode (water treatment). 97

Table 5.2 Operating conditions for the co-current flow mode (water treatment). 98

Table 6.1 Mathematical representation of the ADM (Gamal El-Din and Smith, 2000). 125

Table 6.2 Mathematical representation of the BFCM (Gamal El-Din and Smith, 2000). 127

Table 6.3 Dimensionless parameters pertaining to the ADM and the BFCM. 129

Table 6.4 Operating conditions for the co-current and counter-current flow modes (water treatment). 130

Table 7.1 Dimensionless parameters that are used to describe the 1P-ADM and the 2P-ADM. 150

Table 7.2 Mathematical representation of the 2P-ADM for water and wastewater treatment applications. 151

Table 7.3 Coefficients of the exponential model used for the prediction of the gaseous ozone profiles. 153

Table 7.4 Operating conditions for the counter-current flow mode (water treatment). 159

Table 7.5 Operating conditions for the co-current flow mode (water treatment). 160

Table 8.1 Dimensionless parameters pertaining to the 1P-ADM. 184

Table 8.2 Mathematical representation of the 1P-ADM differential equation and boundary conditions. 184

Table 8.3 Main Average characteristics of the deionized water. 187

Table 8.4 Operating conditions of the pilot-scale ozone mass transfer experiments. 192

Table 9.1 Average characteristics of the deionized water. 224

Table 9.2 Average characteristics of the pulp mill effluent. 228
Table 10.1 Average characteristics of the raw pulp mill effluent. 251
Table 10.2 Regression parameters for the modeling of the induced reduction efficiencies of color, AOX, COD, and TOC. 268
Table 10.3 A comparison between three different scales and designs of ozone contactors in terms of the color, AOX, COD, and TOC reduction efficiencies. 270
Table 11.1 PDA system configuration and operational settings. 281
Table 11.2 Kraft pulp mill effluent average characteristics. 283

LIST OF FIGURES

Figure 2.1 Theoretical RTD curves for the transient ADM under closed-closed or closed-open boundary conditions. ... 25

Figure 2.2 Theoretical RTD curves for the transient CFSTR's in-series model. ... 26

Figure 2.3 Transient BFCM schematic for non-reactive tracer for a co-current flow conditions. ... 28

Figure 2.4 Theoretical RTD's for $N_{BFCM} = 10$ at the bottom sampling port. ... 35

Figure 2.5 Theoretical RTD's for $N_{BFCM} = 10$ at the top sampling port. ... 35

Figure 2.6 Effect of Pe_L and N_{BFCM} on the theoretical RTD's at the middle sampling port for $Pe_L = 1.0$. ... 36

Figure 2.7 Effect of Pe_L and N_{BFCM} on the theoretical RTD's at the top sampling port for $Pe_L = 1.0$. ... 37

Figure 2.8 Effect of Pe_L and N_{BFCM} on the theoretical RTD's at the middle sampling port for $Pe_L = 40.0$. ... 37

Figure 2.9 Effect of Pe_L and N_{BFCM} on the theoretical RTD's at the top sampling port for $Pe_L = 40.0$. ... 38

Figure 2.10 Comparison between the transient BFCM, ADM, and CFSTR's in-series model on the theoretical RTD's for $Pe_L = 1.0$ and $N_{BFCM} = N_{FCSTR} = 10$. ... 39

Figure 2.11 Comparison between the transient BFCM, ADM, and CFSTR's in-series model on the theoretical RTD's for $Pe_L = 20.0$ and $N_{BFCM} = N_{FCSTR} = 10$. ... 39

Figure 2.12 Comparison between the transient BFCM, ADM, and CFSTR's in-series model on the theoretical RTD's for $Pe_L = 1.0$ and $N_{BFCM} = N_{FCSTR} = 20$. ... 40

Figure 2.13 Comparison between the transient BFCM, ADM, and CFSTR's in-series model on the theoretical RTD's for $Pe_L = 20.0$ and $N_{BFCM} = N_{FCSTR} = 20$. ... 41

Figure 2.14 Theoretical RTD's for $N_{BFCM} = 20.0$ and variable Pe_L along the column height ($j = 1$ to 4). ... 42

Figure 2.15 Theoretical RTD's for $N_{BFCM} = 20.0$ and variable Pe_L along the column height (j = 5 to 20). 42
Figure 2.16 Experimental and predicted RTD's in a counter-current flow mode. 44
Figure 2.17 Experimental and predicted RTD's in a co-current flow mode. 45
Figure 2.18 Comparison between the transient BFCM and the regression model predictions of back flow ratios. 47
Figure 2.19 Comparison between the transient BFCM, ADM, and CFSTR's model in predicting the RTD's in a co-current bubble column. 47
Figure 3.1 BFCM schematic for co-current flow conditions in bubble columns. 56
Figure 3.2 Theoretical RTD at the bottom sampling port. 63
Figure 3.3 Theoretical RTD at the top sampling port. 64
Figure 3.4 Steady-state BFCM testing for co-current flow mode. 65
Figure 3.5 Steady-state BFCM testing for counter-current flow mode. 66
Figure 4.1 Schematic representation of the co-current axial dispersion model. 77
Figure 4.2 Computational upwind finite difference scheme. 85
Figure 5.1 Pe_L and Pe_G effects on the 2P-ADM predicted dissolved ozone concentration profiles in the counter-current flow mode and for water treatment applications (($Pe_L = 1.0, 2.5, 5.0, 10.0, 20.0$, and ∞) and ($Pe_G = 12.4/124.0, 30.9/309.0, 61.8/618.0, 123.7/1237.0, 247.3/2473.0$, and ∞)). 99
Figure 5.2 Pe_L and Pe_G effects on the 2P-ADM predicted gaseous ozone concentration and superficial gas velocity profiles in the counter-current flow mode and for water treatment applications (($Pe_L = 1.0, 2.5, 5.0, 10.0, 20.0$, and ∞) and ($Pe_G = 12.4/124.0, 30.9/309.0, 61.8/618.0, 123.7/1237.0, 247.3/2473.0$, and ∞)). 100
Figure 5.3 k_La effects on the 2P-ADM predicted dissolved ozone concentration profiles in the counter-current flow mode and for water treatment applications ($k_La = 1.0 \times 10^{-3}, 3.0 \times 10^{-3}, 5.0 \times 10^{-3}, 7.0 \times 10^{-3}, 1.0 \times 10^{-2}, 1.5 \times 10^{-2}$, and 2.0×10^{-2} s^{-1}). 101
Figure 5.4 k_La effects on the 2P-ADM predicted gaseous ozone concentration and superficial gas velocity profiles in the counter-current flow mode

and for water treatment applications ($k_La = 1.0 \times 10^{-3}$, 3.0×10^{-3}, 5.0×10^{-3}, 7.0×10^{-3}, 1.0×10^{-2}, 1.5×10^{-2}, and 2.0×10^{-2} s^{-1}). 102

Figure 5.5 D_a effects on the 2P-ADM predicted dissolved ozone concentration profiles in the counter-current flow mode and for water treatment applications (D_a = 0.0000, 0.0505, 0.0831, 0.1010, 0.5050, 1.0000, 3.0000, and 6.0000). 103

Figure 5.6 D_a effects on the 2P-ADM predicted gaseous ozone concentration and superficial gas velocity profiles in the counter-current flow mode and for water treatment applications (D_a = 0.0000, 0.0505, 0.0831, 0.1010, 0.5050, 1.0000, 3.0000, and 6.0000). 104

Figure 5.7 P_T or α effects on the 2P-ADM predicted dissolved ozone concentration profiles in the counter-current flow mode and for water treatment applications (P_T = 101.3, 303.9, 506.5, 709.1, 1013.0, and ∞ kPa). 105

Figure 5.8 P_T or α effects on the 2P-ADM predicted gaseous ozone concentration and superficial gas velocity profiles in the counter-current flow mode and for water treatment applications (P_T = 101.3, 303.9, 506.5, 709.1, 1013.0, and ∞ kPa). 107

Figure 5.9 k_La effects on the 2P-ADM predicted dissolved ozone concentration profiles in the co-current flow mode and for water treatment applications ($k_La = 1.0 \times 10^{-3}$, 3.0×10^{-3}, 5.0×10^{-3}, 7.0×10^{-3}, 1.0×10^{-2}, 1.5×10^{-2}, and 2.0×10^{-2} s^{-1}). 110

Figure 5.10 k_La effects on the 2P-ADM predicted gaseous ozone concentration and superficial gas velocity profiles in the co-current flow mode and for water treatment applications ($k_La = 1.0 \times 10^{-3}$, 3.0×10^{-3}, 5.0×10^{-3}, 7.0×10^{-3}, 1.0×10^{-2}, 1.5×10^{-2}, and 2.0×10^{-2} s^{-1}). 111

Figure 5.11 D_a and M effects on the 2P-ADM predicted dissolved ozone concentration profiles in the counter and co-current flow mode and for wastewater treatment applications (D_a = 89 and M = 0.037 to D_a = 8900000 and M = 11.659). 113

Figure 5.12 k_La effects on the 2P-ADM predicted gaseous ozone concentration and superficial gas velocity profiles in the counter and co-current flow modes and for wastewater treatment applications (k_La = 1.0×10^{-3}, 3.0×10^{-3}, 5.0×10^{-3}, 7.0×10^{-3}, 1.0×10^{-2}, 1.5×10^{-2}, and 2.0×10^{-2} s^{-1}). 114

Figure 5.13 Comparison between the predicted and the measured dissolved ozone concentration profiles in a counter-current fine-bubble diffuser ozone bubble column for water treatment applications. 115

Figure 5.14 Comparison between the predicted and the measured dissolved ozone concentration profiles in a co-current fine-bubble diffuser ozone bubble column for water treatment applications. 116

Figure 6.1 Reaction kinetics regimes for ozone absorption process (adapted from Zhou and Smith, 1997) 120

Figure 6.2 Schematic representation of the co-current ADM. 124

Figure 6.3 Schematic representation of the co-current BFCM. 126

Figure 6.4 Comparison between the predicted and the measured dissolved ozone concentrations in a co-current bubble column for water treatment applications. 132

Figure 6.5 Comparison between the predicted and the measured dissolved ozone concentrations in a counter-current bubble column for water treatment applications. 132

Figure 6.6 Effect of Pe_L on the dissolved ozone profiles in the co-current flow mode for wastewater treatment applications ((Pe_L = 1.0, 2.5, 5.0, 10.0, 20.0, and ∞), D_a = 89, k_La = 5.0×10^{-3} s^{-1}, M = 0.037, α = 0.48, and y_0 = 0.00675). 134

Figure 6.7 Effects of Pe_L on the gaseous ozone and the superficial gas velocity profiles in the co-current flow mode for wastewater treatment applications ((Pe_L = 1.0, 2.5, 5.0, 10.0, 20.0, and ∞), D_a = 89, k_La = 5.0×10^{-3} s^{-1}, M = 0.037, α = 0.48, and y_0 = 0.00675). . 135

Figure 6.8 Effect of k_La on the dissolved ozone profiles in the co-current flow mode for wastewater treatment applications ((k_La = 1.0×10^{-3},

3.0×10^{-3}, 5.0×10^{-3}, 7.0×10^{-3}, 1.0×10^{-2}, 1.5×10^{-2}, and 2.0×10^{-2} s^{-1}), $Pe_L = 5.0$, $D_a = 89$, $M = 0.037$, $\alpha = 0.48$, and $y_0 = 0.00675$). 136

Figure 6.9 Effects of k_La on the gaseous ozone and the superficial gas velocity profiles in the co-current flow mode for wastewater treatment applications (($k_La = 1.0 \times 10^{-3}$, 3.0×10^{-3}, 5.0×10^{-3}, 7.0×10^{-3}, 1.0×10^{-2}, 1.5×10^{-2}, and 2.0×10^{-2} s^{-1}), $Pe_L = 5.0$, $D_a = 89$, $M = 0.037$, $\alpha = 0.48$, and $y_0 = 0.00675$). 137

Figure 7.1 Reaction kinetics regimes for ozone absorption process (adapted from Zhou and Smith, 1997). 144

Figure 7.2 Schematic representation of the co-current ADM. 149

Figure 7.3 Typical gaseous ozone profiles in bubble columns for water and wastewater treatment conditions. 152

Figure 7.4 Pe_L effects on the concentration profiles in the counter-current flow mode and water treatment applications. 161

Figure 7.5 k_La effects on the concentration profiles in the counter-current flow mode and water treatment applications. 162

Figure 7.6 D_a effects on the concentration profiles in the counter-current flow mode and water treatment applications. 162

Figure 7.7 Pe_L effects on the concentration profiles in the co-current flow mode and water treatment applications. 164

Figure 7.8 k_La effects on the concentration profiles in the co-current flow mode and water treatment applications. 166

Figure 7.9 D_a effects on the concentration profiles in the co-current flow mode and water treatment applications. 167

Figure 7.10 Pe_L effects on the concentration profiles in the wastewater treatment applications. 169

Figure 7.11 k_La effects on the concentration profiles in the wastewater treatment applications. 169

Figure 7.12 D_a and M effects on the concentration profiles in the wastewater treatment applications. 170

Figure 7.13 Comparison between the predicted and the experimental dissolved ozone concentrations in an ozone bubble column under water treatment conditions for the counter-current flow mode. 172
Figure 7.14 Comparison between the predicted and the experimental dissolved ozone concentrations in an ozone bubble column under water treatment conditions for the co-current flow mode.......... 172
Figure 8.1 Schematic representation of the 1P-ADM. 182
Figure 8.2 Schematic of the headspace-free reactor.......... 186
Figure 8.3 Schematics of the pilot-scale impinging-jet bubble column and the configuration of the Mazzei® injector (model 384). 189
Figure 8.4 Typical ozone auto-decomposition kinetics in deionized water. 194
Figure 8.5 The effect of water temperature on the ozone auto-decomposition rate constant. 195
Figure 8.6 Typical dimensionless dissolved ozone concentration profiles in the impinging-jet bubble column operated in a gas-injection mode... 197
Figure 8.7 Typical dimensionless dissolved ozone concentration profiles in the impinging-jet bubble column operated in a gas-ejection mode. ... 197
Figure 8.8 Effects of the u_G and u_L on the gas bubble diameters and concentrations in the injection mode. 205
Figure 8.9 Comparison of the k_La correlations for gas sparging under positive pressure in various types of bubble columns. 207
Figure 8.10 Comparison of the k_La correlations for gas sparging under negative pressure in various types of bubble columns.......... 208
Figure 8.11 Comparison between the 1P-ADM and the non-linear regression correlations of k_La. 208
Figure 8.12 Comparison between the 1P-ADM and the non-linear regression correlations of D_L. 211
Figure 8.13 Comparison between the 1P-ADM and the linear regression correlations of a_I. 212
Figure 9.1 Schematic of the floating-lid headspace-free reactor.......... 223
Figure 9.2 Schematic of the experimental set-up of the pilot-scale

impinging-jet bubble column. 226
Figure 9.3 The effect of water temperature on the ozone auto-decomposition kinetics in deionized water. 230
Figure 9.4 A comparison between the k_La's predicted using the 1P-ADM and the non-linear regression analyses. 232
Figure 9.5 The effect of ozonation on Ek_La values. 234
Figure 9.6 The effect of ozonation on E values. 235
Figure 9.7 The effect of the ozone contact time on the amounts of the applied, utilized, and exhausted ozone. 236
Figure 9.8 A comparison between the measured and the predicted off-gas ozone concentrations. 237
Figure 9.9 The ozonation treatment reduction efficiencies of color, AOX, TOC, and COD. 238
Figure 9.10 The ozonation effects on the biodegradability of pulp mill effluents. 240
Figure 10.1 Schematic of the experimental set-up of the extra-coarse-bubble diffuser ozone contactor. 248
Figure 10.2 Schematic of the experimental set-up of the pilot-scale impinging-jet ozone contactor. 250
Figure 10.3 Reduction efficiencies of color, AOX, COD, and TOC in the extra-coarse-bubble diffuser ozone contactor. 254
Figure 10.4 The effect of ozonation on the BOD_5 of the pulp mill wastewater treated in the extra-coarse-bubble diffuser ozone contactor. 255
Figure 10.5 Reduction efficiencies of color, AOX, COD, and TOC in the impinging-jet ozone contactor operated in a semibatch-flow mode. 257
Figure 10.6 Reduction efficiencies of color, AOX, COD, and TOC in the impinging-jet ozone contactor operated in a continuous-flow mode...... 257
Figure 10.7 The effect of ozonation on the BOD_5 of the pulp mill wastewater treated in the impinging-jet ozone contactor. 258
Figure 10.8 The effect of ozonation on the off-gas ozone concentration profiles in three different ozone contactors operated in a semibatch-flow mode. 260

Figure 10.9 The effect of ozonation on the off-gas to the feed-gas ozone concentrations' ratio in the impinging-jet ozone contactor operated in a continuous-flow mode. 261
Figure 10.10 The effect of ozonation on the E values in three different ozone contactors operated in a semibatch-flow mode. 263
Figure 10.11 The effect of ozonation on the ESt_G values in three different ozone contactors operated in a semibatch-flow mode. 263
Figure 10.12 The effect of ozonation on the BOD_5/COD ratio of the treated Kraft pulp mill wastewater in the impinging-jet ozone contactor. 264
Figure 10.13 The effect of ozonation on the color/COD ratio of the treated Kraft pulp mill wastewater in the impinging-jet ozone contactor. 265
Figure 10.14 The effect of ozonation on the AOX/COD ratio of the treated Kraft pulp mill wastewater in the impinging-jet ozone contactor. 266
Figure 10.15 The effect of ozonation on the TOC/COD ratio of the treated Kraft pulp mill wastewater in the impinging-jet ozone contactor. 266
Figure 10.16 A comparison between the predicted and the measured reduction efficiencies of AOX. 269
Figure 11.1 Components of the particle dynamics analyzer set-up. 279
Figure 11.2 Schematic of the experimental set-up of the pilot-scale impinging-jet bubble column. 282
Figure 11.3 Schematic of the ozonation system set-up. 284
Figure 11.4 A digital image of the air bubbles at $u_L = 7.7 \times 10^{-3}$ ms^{-1} and $u_G = 1.0 \times 10^{-3}$ ms^{-1}. 286
Figure 11.5 A digital image of the air bubbles at $u_L = 7.7 \times 10^{-3}$ ms^{-1} and $u_G = 7.8 \times 10^{-3}$ ms^{-1}. 286
Figure 11.6 A digital image of the air bubbles at $u_L = 1.9 \times 10^{-2}$ ms^{-1} and $u_G = 8.7 \times 10^{-4}$ ms^{-1}. 287
Figure 11.7 Definition of angle ϕ. 287
Figure 11.8 Effects of u_G and u_L on d_B and d_S in deionized water. 288
Figure 11.9 A typical plot of the count-based bubble size distribution in deionized water at high u_G and low u_L. 289

Figure 11.10 A typical plot of the volume-based bubble size distribution in deionized water at high u_G and low u_L. 290

Figure 11.11 A typical plot of the surface area-based bubble size distribution in deionized water at high u_G and low u_L. 291

Figure 11.12 A typical plot of the count-based bubble size distribution in deionized water at low u_G and low u_L. 292

Figure 11.13 Effects of u_G and u_L on C_B in deionized water. 292

Figure 11.14 Effects of u_G and u_L on the gas-phase axial turbulence % in deionized water. 293

Figure 11.15 Typical probability density distributions of the gas-phase u and v in deionized water. 295

Figure 11.16 Effects of u_G and u_L on u in deionized water. 296

Figure 11.17 Effects of u_G and u_L on ε_G in deionized water. 297

Figure 11.18 Effects of u_G and u_L on a in deionized water. 297

Figure 11.19 Effects of u_G and u_L on d_B and d_S in raw Kraft pulp mill effluent. 299

Figure 11.20 Effects of ΔO_3 on d_B and d_S in Kraft pulp mill effluent. 300

Figure 11.21 Effects of u_G and u_L on C_B in raw Kraft pulp mill effluent. 301

Figure 11.22 Effects of u_G and u_L on ε_G in raw Kraft pulp mill effluent. 302

Figure 11.23 Effects of u_G and u_L on a in raw Kraft pulp mill effluent. 302

Figure 11.24 A typical plot of the count-based bubble size distribution in raw Kraft pulp mill effluent at low u_G and low u_L. 303

Figure 11.25 A typical plot of the count-based bubble size distribution in raw Kraft pulp mill effluent at high u_G and low u_L. 304

Figure 11.26 A typical plot of the count-based bubble size distribution in raw Kraft pulp mill effluent at low u_G and high u_L. 304

LIST OF SYMBOLS

A' to E'	dimensionless linear regression coefficients in Equation 8.20
a'	input parameter of the 1P-ADM defined in Equations 7.17 and 8.11, mgL^{-1}
A	gas bubbles' surface area, m^2
a	gas bubbles' specific interfacial area, m^{-1}
a_1	dimensionless empirical coefficient of the gas-phase mole fraction decrease along column height
A_j to N_j	dimensionless coefficients in the algebraic equations of the 2P-ADM
AOX	absorbable organic halides, mgL^{-1}
b'	input parameter of the 1P-ADM defined in Equations 7.18 and 8.12, mgL^{-1}
BOD_5	biochemical oxygen demand, mgL^{-1}
C_0^*	instantaneously-mixed tracer concentration in the first cell in the transient BFCM or transient CFSTR's in-series model, mgL^{-1}
C_B	gas bubbles concentration, #bubblesL^{-1}
C_G	gas-phase ozone concentration, mgL^{-1}
$C_{G,in}$	feed-gas ozone concentration, mgL^{-1}
$C_{G,off}$	off-gas (i.e., exhaust-gas) ozone concentration, mgL^{-1}
C_i	recorded tracer concentration at time step (Δt_i), mgL^{-1}
C_j	tracer concentration in cell number "j" in the transient BFCM, mgL^{-1}
C_L	instantaneous dissolved ozone concentration, mgL^{-1}
$C_{L,measured}$	measured tracer concentration, mgL^{-1}
$C_{L,predicted}$	predicted tracer concentration, mgL^{-1}
$C_{L,\ell}$	dissolved ozone concentration at depth (ℓ), mgL^{-1}
C_L^*	equilibrium dissolved ozone concentration, mgL^{-1}

$C^{*}_{L,\ell}$	equilibrium dissolved ozone concentration at depth (ℓ), mgL^{-1}
$C_\theta = C_t$	instantaneous tracer concentration, mgL^{-1}
C_0	tracer concentration in the influent to the reactor, mgL^{-1}
COD	chemical oxygen demand, mgL^{-1}
D	bubble column diameter, m
D_a	dimensionless Damköhler number
D_G	gas-phase axial dispersion coefficient, m^2s^{-1}
D_L	liquid-phase axial dispersion coefficient, m^2s^{-1}
D_{O_2}	oxygen gas diffusivity in the liquid phase, m^2s^{-1}
D_{O_3}	ozone gas diffusivity in the liquid phase, m^2s^{-1}
D_1	dimensionless input parameter of the 1P-ADM defined in Equations 7.29 and 8.8
d_B	count mean diameter of gas bubbles, μm
d_S	Sauter (i.e., volume-to-surface area) mean diameter of gas bubbles, μm
E	dimensionless enhancement factor
$E(\theta)$	dimensionless residence time density function, as a function of the dimensionless time (θ)
$E(t)$	residence time density function, as a function of the time (t), s^{-1}
E_1	dimensionless input parameter of the 1P-ADM defined in Equations 7.30 and 8.9
Ek_La	enhanced overall mass transfer coefficient, s^{-1}
Est_L	dimensionless enhanced liquid-phase Stanton number
f_j	dimensionless correction factor for the volume of cell number "j" in the transient BFCM
$f_{Z,j}$	dimensionless correction factor for the dimensionless distance (Z) for cell number "j" in the transient BFCM
g	gravitational acceleration, ms^{-2}
G/L	dimensionless gas-to-liquid flowrate ratio (= Q_G/Q_L)
$h_{c,j}$	height of cell number "j" in the transient BFCM, m

H	Henry's law constant, $kPaLmg^{-1}$
H_a	dimensionless Hatta number
I	diffusive flux of the dissolved mass, $molm^{-2}s^{-1}$
k_L	local mass transfer coefficient, ms^{-1}
k_La	overall mass transfer coefficient, s^{-1}
k_w	specific ozone utilization rate constant, s^{-1}
K_0	dimensionless input parameter of the 1P-ADM defined in Equations 7.27 and 8.6
K_1	dimensionless input parameter of the 1P-ADM defined in Equations 7.28 and 8.7
k_1	empirical ozone auto-decomposition rate constant, s^{-1}
k_2	empirical ozone auto-decomposition rate constant, s^{-1}
k_3	empirical ozone auto-decomposition rate constant, Lmg^{-1}
L	total height of the bubble column, m
ℓ	axial distance (i.e., axial coordinate) along the column height, m
M	dimensionless enhancement factor
M	mass of the injected tracer, kg
N	dimensionless input parameter of the 1P-ADM defined in Equations 7.31 and 8.10
N	total number of the time steps in the numerical simulation of the transient BFCM
N	total number of elements used in the finite difference scheme in the solution of the 2P-ADM
N_{BFCM}	number of cells in the transient BFCM
N_{CFSTR}	number of cells in the transient CFSTR's in-series model
P	liquid hydrostatic pressure, kPa
Pe	dimensionless Peclet number
$Q'_{B,j}$	back flowrate for cell number "j" in the transient BFCM, m^3s^{-1}
$Q_{B,j}$	exchange flowrate for cell number "j" in the transient BFCM, m^3s^{-1}

$Q_{G,0}$	feed-gas flowrate flowing into the first cell in the steady-state BFCM, m^3s^{-1}
$Q_{G,j}$	gas flowrate flowing out of cell number "j" in the steady-state BFCM, m^3s^{-1}
Q_L	liquid flowrate, m^3s^{-1}
r'_j	dimensionless back-flow ratio of cell number "j" in the transient BFCM
r_j	dimensionless exchange-flow ratio of cell number "j" in the transient BFCM
R	Universal gas constant, $atmLmole^{-1\,o}K^{-1}$
Re_j	dimensionless jet Reynolds number
St	dimensionless Stanton number
T	fluid temperature, ^oC or ^oK
t	ozone contact time, s
t_i	acquisition time of the tracer data, s
t_m	mean of the residence time distribution (RTD), s
TOC	total organic carbon, mgL^{-1}
u	instantaneous bubble rise velocity, ms^{-1}
u_G	superficial gas velocity = feed-gas flowrate/cross-sectional area of the bubble column (cross-sectional area of the straight section in case of the impinging-jet bubble column), ms^{-1}
u_L	superficial liquid velocity = liquid flowrate/cross-sectional area of the bubble column (cross-sectional area of the straight section in case of the impinging-jet bubble column), ms^{-1}
$V_{c,j}$	volume of cell number "j" in the transient BFCM, m^3
V	total volume of the bubble column, m^3
V_c	average cell volume in the transient BFCM, m^3
V_L	effective reactor volume, m^3

X	dimensionless dissolved ozone concentration in the liquid phase
Y	dimensionless ozone concentration in the gas phase
Y_j	normalized tracer concentration in cell number “j” in the transient BFCM
y	dimensionless ozone molar fraction in the gas phase
y_Z	ozone molar fraction in the gas phase at dimensionless axial co-ordinate (Z)
y_ℓ	ozone molar fraction in the gas phase at depth ℓ
Z	dimensionless distance (i.e., axial coordinate) along the column height
$Z_{j,act}$	actual dimensionless distance of cell number “j” in the transient BFCM
$Z_{j,avg}$	average dimensionless distance of cell number “j” in the transient BFCM

Greek Letters

ΔO_3	amount of the utilized ozone, mgL^{-1}
Δt_i	time step during the acquisition of the tracer data, s
ΔZ	dimensionless numerical spatial step in the numerical solution of the 2P ADM
$\Delta\theta$	dimensionless time step during the acquisition of the tracer data
α	non-linear regression parameter in Equations 8.15 and 8.17
α_1	input parameter of the 1P-ADM defined in Equations 7.20 and 8.11, mgL^{-1}
β	non-linear regression parameter in Equations 8.15 and 8.17
β_1	input parameter of the 1P-ADM defined in Equations 7.21 and 8.12, mgL^{-1}
ϵ	dimensionless fluid-phase hold-up

θ	dimensionless temperature correction factor in van't Hoff-Arrhenius relationship
λ_1	dimensionless input parameter of the IP-ADM defined in Equations 7.34 and 8.4
λ_2	dimensionless input parameter of the IP-ADM defined in Equations 7.34 and 8.5
θ	dimensionless time in the modeling of the hydrodynamics of the bubble column
ρ	liquid density, kgm^{-3}
σ_θ^2	variance of the RTD as a function of the dimensionless time (θ)
σ_t^2	variance of the RTD as a function of time (t), s^2
τ	mean theoretical hydraulic retention time of the bubble column, s
ψ	rate of gas absorption into the liquid phase, $mgL^{-1}s^{-1}$
γ	non-linear regression parameter in Equation 8.17

Subscripts

0	bottom of the bubble column, i.e., at Z = 0
act	actual
avg	average
B	back or exchange flow
BFCM	back flow cell model
c	cell
CFSTR	continuous-flow-stirred-tank reactors model
G	gas phase
i	number of the time step during the acquisition of the tracer data
in	feed-gas
inf	influent
j	cell number in the BFCM

j	identifier of the element number in the finite difference scheme used to solve the 2P-ADM ($N+1 \geq j \geq -1$)
L	liquid phase
m	mean
N	number of the top element in the finite difference scheme of the 2P-ADM
N+1	number of the imaginary element in the finite difference scheme of the 2P ADM
O_2	oxygen gas
O_3	ozone gas
out	off-gas
T	top of the bubble column
t	time
T	top of the column, i.e., at $Z = 1$
−1	number of the imaginary element beneath the bottom of the column

CHAPTER 1. GENERAL INTRODUCTION

1.1 BACKGROUND

Most of the models that dealt with ozone contactors were directed to the water treatment applications with very little done to model the ozonation process for wastewater treatment. Most of the models are two-phase flow (i.e., gas-liquid) models that are applied to predict the dissolved and the gaseous ozone profiles along bubble columns. In order to simplify the design process of ozone bubble columns, many of those models were based on one of the following two liquid-phase flow regimes: (1) complete mixing or; (2) plug flow (Alvarez-Cuenca *et al.*, 1980; Alvarez-Cuenca *et al.*, 1981; Chang and Chian, 1981; Laplanche *et al.*, 1991; Hull *et al.*, 1992; Lev and Regli, 1992). Although, the actual flow pattern in bubble columns is usually closer to being mixed flow rather than plug flow, but still not completely mixed flow (Zhou, 1995). Very few studies were conducted using the type of models that consider the backmixing process in the liquid-phase flow. One of those studies was the one conducted by Zhou *et al.* (1994), in which, they modeled the performance of ozone bubble columns by using the two-phase axial dispersion model, or referred to as the 2P-ADM, and an elaborate numerical technique was needed to solve the model equations. The 2P-ADM demonstrated excellent capability of predicting the dissolved ozone profiles in ozone contactors.

The design of ozone bubble columns usually encounter two major sources of uncertainties: (1) the complications and unreliable methods used in measuring and estimating the operating parameters of bubble columns; and (2) the application of the pertinent design model, particularly, when designing an ozonation treatment facility for a complex chemical systems such as the effluents produced from the pulping and bleaching processes. Although constructing ozone contactors is an easy task, optimizing their operations is not as simple. The operating parameters of ozone contactors are interrelated and thus, they cause difficulty in the design, operation, and scale-up. Therefore, reliable and accurate methods of measuring and estimating such parameters should be applied.

A number of processes occur simultaneously during the ozonation process. Those processes are: the convection and the backmixing processes of the liquid and gas phases flowing through the contacting chamber; the ozone gas mass transfer process; the ozone auto-decomposition process, and the competitive reactive processes of the constituents in water and wastewater with dissolved ozone (Zhou *et al.*, 1994). Besides those processes, the contactor configuration, the operating conditions, and the water or wastewater quality influence the overall performance of the ozonation process. For any ozonation system, it is crucial to quantify the dissolved ozone to achieve reliable rational design and optimum operation of ozone contactors. Meanwhile, quantifying the gaseous ozone, i.e., the ozone off-gas leaving the contactor, is essential for achieving optimum and reliable design of the off-gas destruction facilities.

Several studies have been conducted to study the fundamentals of the processes that control the performance of ozone contactors in water treatment over the past decades with a fewer number of studies aimed at investigating the ozone mass transfer mechanisms and the effect of chemical reactions on the rate of ozone absorption when treating industrial wastewater. Kraft pulp mill effluents are characterized by their high concentrations of color, AOX (absorbable organic halides), COD (chemical oxygen demand), and TOC (total organic carbon). Recently, the color and AOX-causing contaminants have become the center of attention as a result of their high resistance towards conventional biological treatment processes. In order to comply with the more stringent effluent discharge regulations, the focus of the pulp mill effluent treatment industry has shifted from the conventional biological treatment processes to other treatment alternatives (Haberl *et al.*, 1991; Zhou and Smith, 1997). Ozonation has emerged as a very promising technology for treating pulp mill effluents due to its high reduction efficiencies of color and AOX-causing compounds (Bauman and Lutz, 1974; Zhou and Smith, 1997). Ozone can selectively react with the chromophoric (color-causing) and halogenated (AOX-causing) functional groups through fast oxidation reactions as a result of these compounds' electrophilic nature (Bauman and Lutz, 1974). They observed that the color reduction efficiency was dependent mainly on the amount of the utilized ozone (ΔO_3), but to some extent it was also dependent on the wastewater initial characteristics in terms of color, COD, pH, and dissolved and suspended solids' concentrations.

Ozone contactors that utilize bubble diffusers are the most common practice used for treating water and wastewater. In water treatment applications, ozonation is limited by the mass transfer process as it is considered the controlling process that dictates the overall performance of ozone contactors (Zhou *et al.*, 1994; Gamal El-Din and Smith, 2000). In order to achieve higher treatment levels in ozone contactors, the configuration and the design of the contacting unit and the type of the gas absorber need to be modified in an attempt to achieve higher turbulent mixing in the liquid phase. According to the theory of surface renewal proposed by Danckwerts (1970), an increase in the mixing intensity will cause the liquid film at the gas-liquid interface to be renewed at a higher rate leading to a higher local mass transfer coefficient (k_L). The ozone gas-absorption in water treatment is assumed to follow the slow-reaction kinetics regime (Zhou *et al.*, 1994; Gamal El-Din and Smith, 2000). Since the ozone gas diffusivity in the liquid phase is much smaller than that in the gas phase, the gas diffusion through the liquid film becomes the rate-limiting step of the mass transfer process (Valentin, 1967). High turbulent shear stresses will also cause the liquid film to become thinner, and as a result, the ozone gas will diffuse through the liquid film at a higher rate causing k_L to increase. Higher turbulent shear stresses will also cause the gas bubbles to become smaller. As a result, the gas bubbles' specific interfacial area (gas bubbles' surface area/bubbly bed volume) will increase leading to higher overall mass transfer coefficient (k_La).

In the study of Witze (1974), when two axisymmetrical circular turbulent air jets (i.e., having the same nozzle diameter and momentum) intersected at an angle of 180°, the resultant jet behaved like a radial jet which grew at about three times the rate of a single radial jet. As a result of the impingement, higher turbulent shear stresses were developed in the ambient fluid and a region of backflow was observed. Guo and Sharp (1996) studied the characteristics of radial jets and mixing under buoyant conditions. They observed that the turbulence intensity increased with the width of the orifice. Unger and Muzzio (1999) investigated the effect of a jet impingement at an intersecting angle of

90° on the mixing characteristics. It was observed that efficient and homogeneous mixing occurred at jets' Reynolds numbers (Re_j's) greater than 300. Fitzgerald and Holley (1979) used two turbulent jets intersecting at an angle of 90° to investigate the resultant effects on the mixing behaviour. They observed more uniform and improved mixing across the annular tube.

Many researchers have attempted to improve the performance of bubble columns by maximizing the rate of physical gas absorption process. These attempts included: adding internal baffles (Catros, 1986), utilizing perforated plates (Chen *et al.*, 1986), inducing internal liquid circulation in air-lift reactors (Lewis and Davidson, 1985), and utilizing motionless mixers (Wang and Fan, 1978). Many researchers utilized gas injectors in order to improve the mass transfer process. Wachsmann *et al.* (1984) studied the mass transfer process using an injection-type nozzle. Gas was introduced under positive and negative pressures. They observed remarkable increase in the overall mass transfer coefficient (k_La) due to the generation of bubbles that had a large specific interfacial area. They also observed that the values of k_La in the gas-injection mode varied from those in the gas-ejection mode. Thalasso *et al.* (1995) used a venturi-type injector to increase the gas transfer rates and that led to an improvement in the performance of the bioreactor that they investigated. Under gas injection mode, they observed an increase in k_La as the liquid superficial velocity (u_L) and the gas superficial velocity (u_G) increased. In a gas-liquid spouted vessel, gas was absorbed under positive pressure into the liquid-phase flow (Nishikawa *et al.*, 1977). It was observed that as u_G and u_L increased, k_La increased and k_La was more dependent on u_G than on u_L. Wang and Fan (1978) studied the mass transfer process in bubble columns packed with motionless mixers. They observed that k_La was dependent on u_G and u_L and as u_G and u_L increased, k_La increased. Huynh *et al.* (1991) studied the mass transfer process in an upward venturi-bubble column combination. They correlated k_La with u_G and u_L for the bubble/venturi combination. As u_G and u_L increased, k_La increased. The increase in u_G could have caused an increase in the gas bubbles' specific interfacial area while the increase in u_L could have resulted in an increase in the liquid shear stresses (Huynh *et al.*, 1991).

Gas hold-up (ε_G) is one of the important variables that characterize the hydrodynamics of the gas-liquid, i.e., the two-phase flows, in bubble columns. It is defined as the fraction of the dispersed volume occupied by the gas bubbles. ε_G can affect the performance of bubble columns in two ways: (1) it provides the fractional volume of the gas phase and therefore, its residence time inside the reactor; and (2) in conjunction with the knowledge of the Sauter mean (i.e., volume-to-surface area mean) bubble diameter, it allows the determination of the and the gas bubbles' specific interfacial area (Jamialahmadi and Müller-Steinhagen, 1992). With the knowledge of gas hold-up and Sauter mean diameter, the gas bubbles' specific interfacial area can be determined. Zhou and Smith (2000) investigated the effects of gas flowrates on the gas bubbles' specific interfacial area using a 2D-Laser particle dynamics analyzer. They observed a proportional increase in the gas bubbles' specific interfacial area with the increase in u_G as a result of the linear increase in the gas hold-up. The same phenomenon was also reported by Roustan *et al.* (1996).

The use of computational fluid dynamics (CFD) has grown over the past decade since it can offer detailed predictions of the behaviour and the characteristics of multiphase flows such as gas-liquid flow in bubble columns. CFD can lead to significant improvements in the area of scale-up of bubble columns. In order to achieve successful application of CFD in the scale-up process, a better understanding of the fundamentals of the gas-liquid flow phenomena has to be provided. Gas-liquid flows are complex in their nature and their behaviour can vary substantially depending on the design, configuration, and operating conditions of the bubble columns. It is very hard to conduct experimental measurements inside gas-liquid flows because of their sensitive nature to any disturbances caused by intrusive measuring devices such as electric probes (Mudde *et al.*, 1998). As a result, the use of non-intrusive measurement techniques such as laser Doppler anemometry and Phase Doppler anemometry measurement systems can provide great tools for characterization and better understanding of the local rather than the global flow phenomena (Mudde *et al.*, 1998).

1.2 FUNDAMENTALS OF THE OZONATION PROCESS

A number of processes occur simultaneously during the ozonation process. Those processes are: the convection and the backmixing processes of the liquid and gas phases flowing through the contacting chamber; the ozone gas mass transfer process; the ozone auto-decomposition process, and the competitive reactive processes of the constituents in water and wastewater with dissolved ozone (Zhou *et al.*, 1994).

1.2.1 Backmixing Process

There are several models that account for backmixing in the liquid phase. Among those models that are available for predicting the performance of bubble columns, is the axial dispersion model (ADM). In the ADM, a diffusion-like process is assumed and superimposed on a plug flow (Levenspiel, 1972). An empirical Fick's law is applied by replacing the molecular diffusion coefficient by the axial dispersion coefficient (D_L) as the mixing parameter:

$$\text{Diffusive mass flux} = -D_L \frac{\partial C_L}{\partial \ell} \qquad [1.1]$$

where: C_L = dissolved ozone concentration (mgL^{-1}) and D_L = axial dispersion coefficient (m^2s^{-1}). In the D_L, the effects of the non-uniform velocity profile (shear dispersion), the molecular, and eddy diffusivities are lumped together. Equation 1.1 can be also applied to describe the backmixing process in the gas phase.

1.2.2 Ozone Auto-Decomposition Process

The overall ozone auto-decomposition rate is influenced by the concentration and the history of the ozonation process and this ozone auto-decomposition process could be represented by a modified pseudo-first-order rate expression (Yurteri and Gurol, 1988; Oke *et al.*, 1998). In the experimental study of Oke *et al.* (1998), it was shown that the commonly used first-order kinetics expression with a constant reaction rate constant was inadequate in describing the ozone auto-decomposition process especially in situations where the initial ozone demand was significant. It was demonstrated that the reaction rate constant was continuously decreasing along the course of ozonation as a result of the changes in the water characteristics. As a result, an exponentially decreasing function was proposed as a better alternative to describe the ozone auto-decomposition kinetics (Oke *et al.*, 1998). In that expression, the reaction rate constant was replaced by a variable referred to as the specific ozone utilization rate constant (k_w) that is a function of the utilized ozone dose (ΔO_3):

$$\frac{dC_L}{dt} = -k_w C_L = -\left(k_1 + k_2 e^{-k_3 \Delta O_3}\right) C_L \qquad [1.2]$$

where: C_L = instantaneous dissolved ozone concentration (mgL^{-1}), k_w = specific ozone utilization rate constant (s^{-1}), k_1 = empirical non-linear regression constant (s^{-1}), k_2 = empirical non-linear regression constant (s^{-1}), k_3 = empirical non-linear regression constant (Lmg^{-1}), t = reaction time (s), and ΔO_3 = amount of the utilized ozone (mgL^{-1}). k_1, k_2, and k_3 are empirical constants that can be obtained by applying non-linear regression analysis to the kinetics data and they are also characteristics of the water to be treated.

According to Equation 1.2, as the amount of the utilized ozone increases along the course of ozonation, k_w will decrease. At the beginning of the ozonation, i.e., when the amount of the utilized ozone is zero, k_w is equal to $k_1 + k_2$ as the ozone auto-decomposition process is only attributed to the initial ozone demand. In the study of Oke *et al.* (1998) and for clean deionized water, the initial ozone demand was practically equal to zero and therefore, k_w could be assumed constant during the course of the ozonation.

1.2.3 Mass Transfer Process

1.2.3.1 Mass Transfer Without Chemical Reactions

The two-film model is usually used to describe the absorption of ozone gas from the gas phase into the liquid phase. Assuming that no chemical reactions between the dissolved gas and any constituents, that can be resent in the liquid phase, occur during the mass transfer process, the gas-absorption rate (ψ) is defined as:

$$\psi = k_L a\left(C_L^* - C_L\right) \qquad [1.3]$$

where: ψ = gas-absorption rate ($mgL^{-1}s^{-1}$), k_L = local liquid mass transfer coefficient (ms^{-1}), a = gas bubbles' specific interfacial area (m^{-1}), C_L^* = concentration of the dissolved ozone in equilibrium with the bulk ozone gas (mgL^{-1}), and C_L = concentration of the dissolved ozone in the bulk liquid (mgL^{-1}). Due to the fact that ozone gas diffuses much faster in the gas phase than in the liquid phase, the mass transfer in the liquid phase is assumed to be the rate-controlling step. Consequently, the overall mass transfer coefficient ($k_L a$) is considered to entirely consist of the local mass transfer coefficient in the liquid phase.

1.2.3.2 Mass Transfer With Chemical Reactions

Chemical reactions occur during the ozonation of wastewater. In such applications, the dimensionless squared Hatta number ($H_a^2 = M$) is often applied to compare between the amount of dissolved gas that reacts at the gas-liquid interface or in the liquid film near the interface and the amount of dissolved gas that reaches the bulk liquid in an unreacted state:

$$H_a^2 = E^2 = M = \frac{D_{O_3} k_w}{k_L^2} \qquad [1.4]$$

where: $H_a = E = \sqrt{M}$ = dimensionless Hatta number, k_L = local mass transfer coefficient (ms^{-1}), D_{O_3} = molecular diffusivity of ozone gas in water (m^2s^{-1}), and k_w = specific ozone utilization rate constant (s^{-1}). For pseudo-first-order irreversible reactions, the location of those reactions that take place during the gas absorption process could be classified into two categories (Kramers and Westertrep, 1963; Kaštánek *et al.*, 1993). Reactions would take place in the bulk of the liquid or at the gas-liquid interface and/or in the liquid film near the interface at $H_a < 0.03$ and $H_a > 5.00$, respectively (Kramers and Westertrep, 1963; Kaštánek *et al.*, 1993). Although, generally for bubble columns it can also be assumed that at that at $H_a > 3.00$, reactions would still be fast enough to occur predominantly at the gas-liquid interface and/or in the liquid film near the interface (Kaštánek *et al.*, 1993). Therefore, reactions would simultaneously take place in both regions at at $0.03 < H_a < 3.00$. Equation 1.4 is only applicable in situations where two conditions have to be satisfied: (1) $\sqrt{M} >> 1$; and (2) fast or instantaneous irreversible first-order reactions with no bulk liquid concentration where the driving force for the mass transfer process will be maximized (Danckwerts, 1970). As a result, Equation 1.3 becomes:

$$\psi = Ek_L aC_L^* \qquad [1.5]$$

where: Ek_La = enhanced overall mass transfer coefficient (s^{-1}). Zhou and Smith (1999) proposed that for wastewater ozonation, both the ozone auto-decomposition and its reactions with the organic and inorganic constituents in wastewater could be lumped together in a first-order rate constant (k_w). Danckwerts (1970) proposed the following equation for the conditions when $M > 0$ and $C_L > 0$:

$$\psi = k_L a\sqrt{1+M}\left(C_L^* - \frac{C_L}{1+M}\right) \qquad [1.6]$$

When $M >> 1$ and C_L approaches zero (i.e., $C_L \cong 0$), Equation 1.6 reduces to Equation 1.5. The effects of chemical reactions on the local mass transfer coefficient for an irreversible first-order reaction could be neglected and the gas absorption could be dealt with as pure physical absorption when M approaches zero (Danckwerts, 1970). Therefore, this assumption is valid when:

$$H_a^2 = E^2 = M = \frac{D_{O_3} k_w}{k_L^2} << 1 \qquad [1.7]$$

k_w was reported to be 4.7×10^{-4} s^{-1} for the deionized water tested by Zhou (1995). Yurteri and Gurol (1988) reported that k_w was in the order of 2.8×10^{-3} s^{-1} for the tested raw surface water. The diffusivity of ozone in water was determined by the Wilke-Chang formula to be 1.74×10^{-9} m^2s^{-1} (at 20 °C) which is comparable to the value of 1.71×10^{-9} m^2s^{-1} obtained using the equation recommended by Johnson and Davis (1996). k_L was reported to be in the order of 3.1×10^{-4} ms^{-1} for clean water and in the order of 1.9×10^{-4} ms^{-1} for water containing organic substances (Beltrán *et al.*, 1997). Substituting for these typical values of D, k_w, and k_L into Equation 1.4 yields squared-Hatta numbers of 8.5×10^{-6} and 1.4×10^{-4} for the deionized and the surface water, respectively. Based on these small Hatta numbers, it can be concluded that the chemical reactions that occur during the course of clean or surface water ozonation has negligible effect on the local mass transfer coefficient and hence, Equation 1.3 will be applied for ozone absorption without any modification.

1.3 PRACTICAL ASPECTS OF OZONE CONTACTORS

1.3.1 Types of Ozone Contactors

Several designs of ozone contactors have been used in water and wastewater ozone treatment applications (Langlais *et al.* 1991). The type of ozone contactor, to be used in a specific ozone treatment application, would depend on the goal of the treatment process. Several designs of ozone contactors have been used in the ozone treatment industry. Those designs included:

(1) conventional diffuser contactors;
    (1.a) fine diffuser

    - (1.b) coarse diffuser
    - (1.c) extra-coarse diffuser
- (2) turbine mixer contactors;
    - (2.a) positive gas pressure
    - (2.b) negative gas pressure (aspirator)
- (3) side stream gas injector followed by gas-liquid separators;
    - (3.a) positive gas pressure
    - (3.b) negative gas pressure
- (4) packed bubble columns;
- (5) spray chambers;
- (6) deep U tube contactors
- (7) porous plate diffuser contactors; and
- (8) submerged static radial turbine contactors

Among those several designs, the conventional fine-diffuser contactor design is the most widely applied practice in both North America and Europe (Zhou, 1995). Based on the gas and liquid flow patterns, conventional diffuser contactors can be further generalized into three types (Zhou, 1995):

- (1) counter-current pattern, where the liquid phase flows downwards in an opposite direction to that of the rising gas bubbles;
- (2) co-current pattern, where both the liquid and gas phases flow upwards; and
- (3) reactive pattern, where no ozone gas is introduced while the liquid phase can still have a residual ozone concentration.

The first two flow patterns allow for dissolving the ozone gas from the gas phase into the liquid phase, while the reactive pattern provides the opportunity for further contact between the residual ozone and the different constituents present in the liquid phase.

Ozone contacting facilities are usually divided into several chambers, ranging from two to six chambers in series and there are usually practical limits to the number of chambers due to the cost of installing baffles and the buildup of the headloss (Zhou, 1995). Most of the conventional fine bubble contactors, in both North America and Europe, utilize two or three chambers for the ozone contacting and reaction purposes (Zhou, 1995).

1.3.2 Designing Ozone Contactors

In designing ozone contactors, some challenges can be experienced as a result of some distinct properties of ozone gas (Zhou, 1995). Most of the available commercial ozone generators can produce a ozone concentration in the gas phase (≥ 10 % w/w) and that will limit the driving force available for the mass transfer process. This is a result of the low dissolved ozone concentration that is in equilibrium with the bulk ozone gas due to the low solubility of ozone gas in water. Second, ozone is an unstable gas and can react with a variety of constituents present in the liquid phase (Zhou, 1995). Ozone reactions are complex in nature and therefore, it does not allow for a reliable prediction of the ozone consumption rate (Zhou, 1995). Also, the knowledge of scaling-up of an ozonation treatment system has not been well understood because of the complexity of ozone chemistry and the lack of reliable process design parameters (Zhou and Smith, 1997).

If the ozonation process involves mass-transfer-limited reactions such as the oxidation of the color or AOX-causing organic compounds, it is crucial to maximize the ozone mass transfer process. Alternatively, if the ozonation process involves chemical-reaction-rate-limited reactions, such as in during disinfection, it is recommended to maintain a desired residual ozone concentration for a specified time period. Therefore, a series of multiple chambers was suggested. A sufficient amount of ozone should be applied to achieve a high dissolved ozone concentration in the first chamber to satisfy the initial ozone demand. Then, additional ozone should be applied at a lower dose in the subsequent chambers to maintain the required residual concentration.

The hydrodynamic behaviour of ozone contactors has been recently identified as another key-design component (Lev and Regli, 1992). In typical full-scale diffuser contactors with two chambers in series, the liquid-phase backmixing was equivalent to that in reactor composed of two to five CFSTR's (continuous-flow-stirred-tank-reactors) in-series (Roustan *et al.*, 1993). They concluded that the liquid-phase backmixing depends on the water and gas flowrates as well as the geometry and the configuration of ozone contactors. Regarding the hydrodynamics of the gas phase and due to the large buoyancy of the gas bubbles, it usually assumed that the backmixing in the gas phase is negligible (Zhou *et al.*, 1994). As a result, the gas-phase is assumed to flow in perfect plug flow regime. However, this assumption is usually valid in ozone contactors and bubble columns with large aspect (L/D) ratios. Deckwer (1976) suggested that the performance of bubble columns could be affected by the gas phase dispersion in columns with diameters greater than 500 mm. As a result, the need for proper designs and configurations of ozone contactors has become the focus of the ozone treatment industry. Designing and configuring ozone contactors properly will lead to high and efficient ozone mass transfer rates and will ensure that the required retention times, for the intended ozone treatments, are satisfied. In order to design ozone contactors properly, accurate and reliable models are needed. Those models can be also useful for the on-line process control. Those models should be developed such that they take into consideration the various processes that occur simultaneously during the ozonation process.

1.4 OBJECTIVES AND SCOPES OF THE RESEARCH PROGRAM

As discussed earlier, the performance of ozone contactors is controlled by the combined effects of the hydrodynamics, ozone mass transfer, and ozone reactions with the constituents that can be present in the liquid phase. Although great advancements in the area of ozone treatment have been achieved, there is still a great demand for:

(1) more efficient and compact designs of ozone contactors that can provide higher treatment levels in more compact contactors and thus, the cost of the treatment process will be lowered;

(2) the development of reliable ozonation process parameters that can be used to predict the performance of the ozone treatment; and

(3) the development of a rational design approach that integrates the variables that affect the performance of the ozonation process and therefore, it can be used in the design and on-line process control of ozone contactors.

The main scope of this research project was to design a new compact ozone contactor that can provide higher treatment levels than those in the conventional ozone contactor designs.

This research program was designed to achieve several objectives. Those objectives included:

(1) development of a reliable, accurate, and simple-to-use model (transient back flow cell model (BFCM)) that can be used for modeling the hydrodynamics of ozone contactors (Chapter 2);

(2) development of models (steady-state two-phase axial dispersion model (2P-ADM) and steady-state BFCM)) that integrate the various processes that occur simultaneously during the ozonation process and therefore, those models can be used for the design and on-line process control of ozone contactors (Chapters 3,4, and 5);

(3) comparing the steady-state 2P-ADM with the steady-state BFCM in terms of their predictions of the performance of ozone contactors (Chapter 6);

(4) development of a simpler version of the axial dispersion model or referred to as the one-phase axial dispersion model (1P-ADM) and comparing its predictions of the performance of ozone contactors with those of the 2P-ADM (Chapter 7);

(5) modeling the ozone mass transfer process in the new design of ozone contactors or referred to as the impinging-jet bubble column for ozone treatment applications in water and wastewater (Chapters 8 and 9);

(6) comparing the performance of the impinging-jet bubble column with two other conventional ozone contactors for their performance during the ozonation of Kraft pulp mill effluents (Chapter 10); and

(7) conducting a phase Doppler anemometry (PDA) study to characterize the gas phase in terms of the bubble size, the bubble size distribution, the bubble rise velocity, the axial and radial mixing intensities in the impinging-jet bubble column during the treatment of water and Kraft pulp mill effluent (Chapter 11).

As a result, a number of models were developed first to describe the hydrodynamics and the overall ozonation process for water and wastewater treatment applications. Then, those models were initially tested using some existing experimental data that was obtained in a conventional fine-diffuser ozone bubble column.

The second step of this research work involved designing a new compact ozone contactor that can provide higher treatment levels than those in the conventional ozone contactor designs. For that purpose, an impinging-jet ozone bubble column was designed and constructed. This ozone bubble column was used for ozone applications in water and wastewater treatment. One of the previously developed models, was used for describing the performance of the impinging-jet ozone bubble column when used for water treatment applications.

The third step of this research work involved treating Kraft pulp mill effluents in the impinging-jet ozone bubble column for further exploration of the advantages of using this new ozone bubble column design over the common conventional designs of ozone bubble columns when used for treating highly reactive wastewaters such as Kraft pulp mill effluents.

The last step of this research work involved the use of a laser Doppler system for characterizing the gas bubbles produced in the impinging-jet bubble column in both water and Kraft pulp mill effluents. This study will lead to further understanding of the ozone mass transfer process during water and wastewater treatment applications.

1.5 REFERENCES

1. Alvarez-Cuenca, M. and M.A. Nerenberg, "Oxygen Mass Transfer in Bubble Columns Working at Large Gas and Liquid Flow Rates", AIChE J. 27(1): 66-73 (1981).
2. Alvarez-Cuenca, M., C.G.J. Baker, and M.A. Bergougnou, "Oxygen Mass Transfer in Bubble Columns", Chem. Eng. Sci. 35: 1121-1127 (1980).
3. Bauman, H.D. and L.R. Lutz, "Ozonation of a Kraft Mill Effluent", Tappi J. 57(5): 116-119 (1974).
4. Beltrán, F.J., J.F. García-Araya, and J.M. Encinar, "Henry and Mass Transfer Coefficients in the Ozonation of Wastewaters", Ozone Sci. & Eng. 19: 281-296 (1997).
5. Catros, A., "*Hydrodynamics and Mass Transfer in Three-Phase Fluidized Beds with Baffles: Ph.D. Thesis* (London, ON, Canada: University of Western Ontario, 1986).
6. Chang, B.-J. and E.S.K. Chian, "A Model Study of Ozone-Sparged Vessels for the Removal of Organics from Water", Wat. Res. 15: 929-936 (1981).
7. Chen, B.H., N.S. Yang, and A.F. McMillan, "Gas Hold-Up and Pressure Drop for Air-Water Flow Through Plate Bubble Columns", Can. J. Chem. Eng. 64: 387-399 (1986).
8. Danckwerts, P.V., *Gas-Liquid Reactions* (NY, USA: McGraw-Hill, Inc., 1970).
9. Deckwer, W.-D., "Non-Isobaric Bubble Columns With Variable Gas Velocity", Chem. Eng. Sci. 31: 309-317 (1976).
10. Fitzgerald, S.D. and E.R. Holley, *Research Report No. 144* (Urbana, IL, USA: Water Resources Centre, University of Illinois, 1979).
11. Gamal El-Din, M. and D.W. Smith, "Designing Ozone Bubble Columns: A Spreadsheet Approach to Axial Dispersion Model", *Proc. of IOA/PAG Conf.: Advances in Ozone Technology*, Orlando, FL, USA, 2000.
12. Guo, Z.-R. and J.J. Sharp, "Characteristics of Radial Jets and Mixing Under Buoyant Conditions", J. Hydr. Eng., ASCE 122: 495-502 (1996).

13. Haberl, R., R. Urban, R. Gehringer, and R. Szinovata, "Treatment of Pulp-Bleaching Wastewaters by Activated Sludge, Precipitation, Ozonation, and Irradiation", Wat. Sci. & Technol. 24: 229-239 (1991).

14. Hull, C.S., P.C. Singer, K. Saravanaan, and C.T. Miller, "Ozone Mass Transfer and Reaction: Completely Mixed Systems", *Proc. of the Annual AWWA Conf.: Water Quality*, Vancouver, BC, Canada, 1992.

15. Huynh, L.X., C.L. Briens, J.F. Large, A. Catros, J.R. Bernard, and M.A. Bergougnou, "Hydrodynamics and Mass Transfer in an Upward Venturi/Bubble Column Combination", Can. J. Chem. Eng. 69: 711-722 (1991).

16. Jamialahmadi, M. and H. Müller-Steinhagen, "Effect of Superficial Gas Velocity on Bubble Size, Terminal Bubble Rise Velocity and Gas Hold-Up in Bubble Columns", Develop. Chem. Eng. 1: 16-31 (1992).

17. Johnson, P.N. and R.A. Davis, "Diffusivity of Ozone in Water", J. Chem. Eng. Data 41: 1485-1487 (1996).

18. Kaštánek, J., J. Zahradník, J. Kratochvíl, and J. Čermák, *Chemical Reactors for Gas-Liquid Systems* (Chichester, England: Ellis Horwood, 1993).

19. Kramers, H. and K.R. Westerterp, *Elements of Chemical Reactor Design and Operation* (NY, USA: Academic Press, Inc., 1963).

20. Langlais, B., D.A. Reckhow, and D.R. Brink, *Ozone in Water Treatment: Application and Engineering* (MI, USA: Lewis Publishers, Inc., 1991).

21. Laplanche, A., N. Le Sauze, G. Martin, and B. Langlais, "Simulation of Ozone Transfer in Water: Comparison with a Pilot Unit", Ozone Sci. & Eng. 13(5): 13, 535-558 (1991).

22. Levenspiel, O., *Chemical Reaction Engineering, 2nd ed.* (NY, USA: John Wiley and Sons, Inc., 1972).

23. Lev, O. and S. Regli, "Evaluation of Ozone Disinfection Systems: Characteristic Contact Time T", J. Environ. Eng., ASCE 118(2): 268-285 (1992).

24. Lewis, D.A. and J.F. Davidson, "Mass Transfer in a Recirculation Bubble Column", Chem. Eng. Sci. 40: 2013-2017 (1985).

25. Mudde, R.F., J.S. Groen, and H.E.A. Van Den Akker, "Application of LDA to Bubbly Flows", Nuc. Eng. & Des. 184: 329-338 (1998).

26. Nishikawa, M., K. Kosaka, and K. Hashimoto, "Gas Absorption in Gas-Liquid or Solid-Gas-Liquid Spouted Vessel", *Proc. 2nd Pacific Chem. Eng. Congress*, Denver, CO, USA, 1977.

27. Oke, N.J., D.W. Smith, and H. Zhou, "An Empirical Analysis of Ozone Decay Kinetics in Natural Waters", Ozone Sci. & Eng. 20: 361-379 (1998).

28. Roustan, M., R.Y. Wang, and D. Wolbert, "Modeling Hydrodynamics and Mass Transfer Parameters in a Continuous Ozone Bubble Column", Ozone Sci. & Eng. 18: 99-115 (1996).

29. Roustan M., C. Beck, O. Wable, J. P. Duguet, and J. Mallevialle, "Modeling Hydraulics of Ozone Contactors", Ozone Sci. & Eng. 15: 213-226 (1993).

30. Thalasso, F., H. Naveau, and E.-J. Nyns, "Design and Performance of a Bioreactor Equipped with a Venturi Injector for High Gas Transfer Rates", Chem. Eng. J. 57: B1-B5 (1995).

31. Unger, D.R. and F. Muzzio, "Laser-Induced Fluorescence Technique for the Quantification of Mixing in Impinging Jets", AIChE J. 45: 2477-2486 (1999).

32. Valentin, F.H.H., *Absorption in Gas-Liquid Dispersions: Some Aspects of Bubble Technology*, Donald M.B. (Ed.). (London, England: E. & F.N. Spon Ltd., 1967).

33. Wachsmann, U., N. Räbiger, and A. Vogelpohl, "The Compact Reactor-A Newly Developed Loop Reactor with a High Mass Transfer Performance", Ger. Chem. Eng. 7: 39-44 (1984).

34. Wang, K.B. and L.T. Fan, "Mass Transfer in Bubble Columns Packed with Motionless Mixers", Chem. Eng. Sci. 33: 945-952 (1978).

35. Witze, P.O., *A Study of Impinging Axisymmetric Turbulent Flows: The Wall Jet, The Radial and Opposing Free Jets: Ph.D. Thesis* (Davis, CA, USA.: University of California, Davis, 1974).

36. Yurteri, C. and M.D. Gurol, "Ozone Consumption in Natural Waters: Effects of Background Organic Matter, pH and Carbonate Species", Ozone Sci. & Eng. 10: 277-290 (1988).

37. Zhou, H. and D.W. Smith, "Ozone Mass Transfer in Water and Wastewater Treatment: Experimental Observations Using a 2D-Laser Particle Dynamics Analyzer", Wat. Res. 34: 909-921 (2000).

38. Zhou, H. and D.W. Smith, "Applying Mass Transfer Theory to Study the Kinetics of Fast Ozone Reactions in Pulp Mill Effluents", *Proc. of the 14th Ozone World Congress*, Detroit, MI, USA, 1999.

39. Zhou, H. and D.W. Smith, "Process Parameter Development for Ozonation of Kraft Pulp Mill Effluents", Wat. Sci. & Technol. 35(2-3): 251-259 (1997).

40. Zhou, H., *Investigation of Ozone Disinfection Kinetics and Contactor Performance Modeling: Ph.D. Thesis* (Edmonton, AB, Canada: University of Alberta, 1995).

41. Zhou, H., D.W. Smith, and S.J. Stanley, "Modeling of Dissolved Ozone Concentration Profiles in Bubble Columns", J. Environ. Eng., ASCE 120(4): 821-840 (1994).

CHAPTER 2. DEVELOPMENT OF TRANSIENT BACK FLOW CELL MODEL (BFCM) FOR BUBBLE COLUMNS*

2.1 INTRODUCTION

Water and wastewater ozonation is usually conducted by dissolving the on-site generated ozone gas in the liquid phase. This is often achieved by using an ozone bubble column as the reacting chamber where ozone gas is bubbled through the liquid phase by utilizing conventional bubble diffusers, turbine mixers, negative pressure gas ejectors, positive pressure gas injectors, etc. In all these different bubble columns' designs there are number of processes that occur simultaneously. These processes are convection and backmixing of the liquid and gas phases flowing through the contacting chamber, ozone gas mass transfer from the gas phase to the liquid phase, ozone decay, and competitive reactions with the constituents in water and wastewater with the dissolved ozone (Zhou *et al.*, 1994).

The rates of the individual phase transport and transformation processes, contactor configuration, operating conditions, and water or wastewater quality influence the overall performance of any ozonation system. Backmixing of the gas phase is another important hydrodynamic property to be considered for the modeling, the design, and the optimization of the bubble columns' performance (Zahradník and Fialová, 1996).

Backmixing in the liquid phase flowing through bubble columns has been studied by several investigators to better understand the mixing behavior of bubble columns (Ohki and Inoune, 1970; Deckwer *et al.*, 1973; Hikita and Kikukawa, 1974; Chianese *et al.*, 1981; Ogawa *et al.*, 1982; Houzelot *et al.*, 1985; Le Sauze *et al.*, 1992). Therefore, the topic of gas and liquid phase backmixing in two-phase (i.e., gas-liquid) flows has received major attention in the chemical engineering field. Especially with regard to the gas phase backmixing, several investigators studied the effect of gas phase backmixing in bubble columns (Reith *et al.*, 1968; Deckwer, 1976; Van Vuuren, 1988; Kawagoe *et al.*, 1989; Wachi and Nojima, 1990; Shetty *et al.*, 1992; Zahradník and Fialová, 1996).

A version of this chapter has been published. Gamal El-Din, M. and D.W. Smith, Ozone Sci. & Eng. 23(4): 313-326 (2001).

In bubble columns with diameters larger than 140 mm, the gas phase dispersion is higher due to the occurrence of eddies at larger scales. In bubble columns with diameters less than 140 mm and large aspect ratios ($L/D \gg 1$), the gas-phase dispersion coefficient is less than the liquid-phase dispersion coefficient by an order of magnitude (Reith *et al.*, 1968). Based on the theoretical calculations of Deckwer (1976), the gas-phase backmixing could be neglected in bubble columns with diameters of less than 500 mm. Therefore, the gas phase could be considered in the plug flow regime. Thus, it is essential to adequately and accurately characterize these fundamental processes and determine the variables that control and dictate the overall performance of any ozonation system.

2.2 TRACER TESTS

Two types of tracer tests have been widely used to characterize the backmixing process in non-ideal flow conditions in a chemical reactor: pulse or stimulus-input tests and step-input tests. The results from these two types of tracer inputs are interrelated and can provide similar information on the residence time distribution of the fluid elements inside a chemical reactor (Levenspiel, 1972). In a pulse-input test, a pulse or stimulus of non-reactive tracer is introduced into the fluid influent line just upstream of the contactor inlet at time zero. As the injection time is minimized compared to the hydraulic theoretical retention time of the reactor (few seconds compared to few minutes), the pulse input can be assumed to be an ideal pulse, and therefore, it can be represented by the Dirac δ function. Simultaneously with the tracer injection, the concentrations of the tracer inside the reactor at different points along the reactor height and at the effluent exit point from the reactor are continuously recorded till the tracer is recovered. That can be confirmed by the residence time density (RTD) curve returning back to the background level of the tracer in the tested liquid. The measured concentrations (after being corrected for the background tracer level in the tested water, i.e., the background noise) are then normalized to produce a curve with an area of unity above the time axis. This curve represents the RTD function (E(t)) that is described mathematically as:

$$\int_0^\infty E(t) \cdot dt = 1 \qquad [2.1]$$

where: t_m = mean residence time of the RTD (s) and E(t) = residence time density function (s^{-1}). The RTD curve is often characterized by the mean residence time (t_m) and the variance (σ_t^2) (Levenspiel, 1972). Respectively, the mean and the variance represent the location and the spread of the RTD. Mathematically, they can be calculated from the discrete pulse-input tracer test data as follows:

$$t_m = \frac{\sum C_i t_i \Delta t_i}{\sum C_i \Delta t_i} \qquad [2.2]$$

and

$$\sigma_t^2 = \frac{\sum C_i t_i^2 \Delta t_i}{\sum C_i \Delta t_i} - t_m^2 \qquad [2.3]$$

where: t_i = data acquisition time (s), Δt_i = time step (s), C_i = recorded tracer concentration at time step (Δt_i) (mgL^{-1}), and σ_t^2 = variance of the RTD as a function of time (s^2). The results can then be used to estimate the traditional mixing parameters: the dimensionless Peclet number (Pe_L) and the equivalent number of the continuous-flow-stirred-tank-reactors (CFSTR) in-series (N_{CFSTR}). With respect to the sampling points inside the reactor, the boundary conditions can be considered as closed-open conditions and for the sampling point at the effluent exit point, the boundary conditions can be considered as closed-closed conditions (Levenspiel, 1972). For the closed-open boundary conditions:

$$\sigma_\theta^2 = \frac{\sigma_t^2}{\tau^2} = \frac{2}{Pe_L} + \frac{3}{Pe_L^2} = \frac{1}{N_{CFSTR}} \qquad [2.4]$$

where: τ = theoretical hydraulic retention time of the bubble column (s) and σ_θ^2 = variance of the RTD as a function of the dimensionless time (θ). And for the closed-closed boundary conditions:

$$\sigma_\theta^2 = \frac{\sigma_t^2}{\tau^2} = \frac{2}{Pe_L} - \frac{2}{Pe_L^2}\left(1 - e^{-Pe_L}\right) = \frac{1}{N_{CFSTR}} \qquad [2.5]$$

If potassium chloride or sodium chloride is used as the tracer material, the dissolved electrolytes can have an effect on the surface tension of the solution resulting in change in the bubble sizes and the bubbles' coalescence. At high dissolved electrolyte concentrations (> 5,000 mgL^{-1}), the bubble rise velocity and the bubbles' coalescence decrease resulting in higher gas hold-up and thus, causes the dispersion number $\left({}^{1}\!/_{Pe_L} \right)$ to decrease. This effect can be ignored if the dissolved electrolyte concentrations are low (< 1,000 to 2,000 mgL^{-1}) (Jamialahmadi and Müller-Steinhagen, 1990). Since tap water or deionized water could contain traces of these electrolytes, the recorded experimental RTD must be corrected for those traces by obtaining the base line RTD for the tested water. Therefore, the background noise can be eliminated. Comparing the theoretical RTD curves with the corrected-experimental RTD curves and using a minimization technique to reduce the summation of the squared residuals (SSR) between the two curves, the mixing parameters can be accurately determined.

2.3 THEORY

2.3.1 Axial Dispersion Model

Assuming that the liquid phase is in axial dispersion regime, i.e., a diffusion-like process is assumed and is superimposed on a plug flow regime (Levenspiel, 1972), the transient axial dispersion model (transient ADM) for a pulse-input can be mathematically described as:

$$\frac{\partial C_t}{\partial t} = D_a \frac{\partial^2 C_t}{\partial \ell^2} - u_L \frac{\partial C_t}{\partial \ell} \qquad [2.6]$$

where: ℓ = distance along the column height (m), t = measurement time (s), D_a = axial dispersion coefficient of the liquid phase (m^2s^{-1}), C_t = instantaneous tracer concentration (mgL^{-1}), and u_L = superficial liquid velocity (ms^{-1}). For a bubble column of a total height, L (m), Equation 2.6 can be written in a dimensionless form as follows:

$$\frac{\partial C_\theta}{\partial \theta} = \frac{1}{Pe_L}\frac{\partial^2 C}{\partial Z^2} - \frac{\partial C}{\partial Z} \qquad [2.7]$$

where:

$$Pe_L = \frac{u_L L}{D_a \varepsilon_L} \qquad [2.8]$$

$$\theta = \frac{t}{\tau} \qquad [2.9]$$

and

$$Z = \frac{\ell}{L} \qquad [2.10]$$

where: L = total column height (m), Z = dimensionless distance along the column height, $C_\theta = C_t$ = instantaneous tracer concentration (mgL^{-1}), θ = dimensionless time, and ε_L = dimensionless liquid-phase hold-up. For small Peclet numbers ($Pe_L < 100$) and for both the closed-closed and the closed-open boundary conditions, the analytical solution of Equation 2.7 is not available (Levenspiel, 1972). Therefore, Levenspiel (1972) suggested that the analytical solution of Equation 2.7 that can be obtained for small deviations from plug flow conditions ($Pe_L > 100$) at any given boundary conditions can still be applied to the closed-closed and the closed-open boundary conditions for situations where Pe_L is slightly less than 100. As a result, the theoretical RTD for a pulse-input tracer test under those operating and boundary conditions, can be represented by:

$$\text{theoretical } E_\theta = \frac{1}{2\sqrt{\dfrac{\pi}{Pe_L}}}\exp\left[-Pe_L\frac{(1-\theta)^2}{4}\right] \qquad [2.11]$$

and

$$\text{experimental } E_\theta = \frac{V}{M}C_\theta \qquad [2.12]$$

where: E_θ = dimensionless residence time density function as a function of the dimensionless time (θ), V = volume of the bubble column (m^3), and M = mass of the injected tracer (kg).

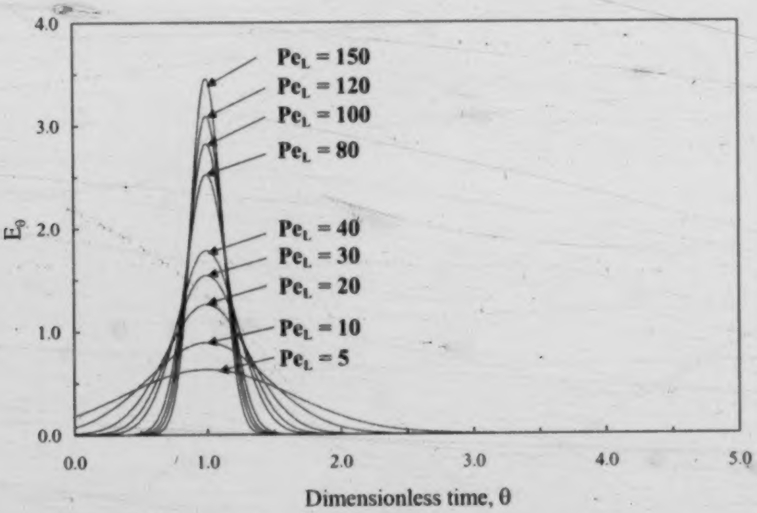

Figure 2.1 Theoretical RTD curves for the transient ADM under closed-closed or closed-open boundary conditions.

The theoretical RTD curves for such cases are shown in Figure 2.1. At low Pe_L (Pe_L << 100), the pulse response is broad and it passes the measurement point slowly enough that it changes and spreads causing the E_θ curve to be non-symmetrical. As shown in Figure 2.1, as the Pe_L approaches 100 or exceeds 100, the RTD narrows as the liquid flow approaches plug flow conditions.

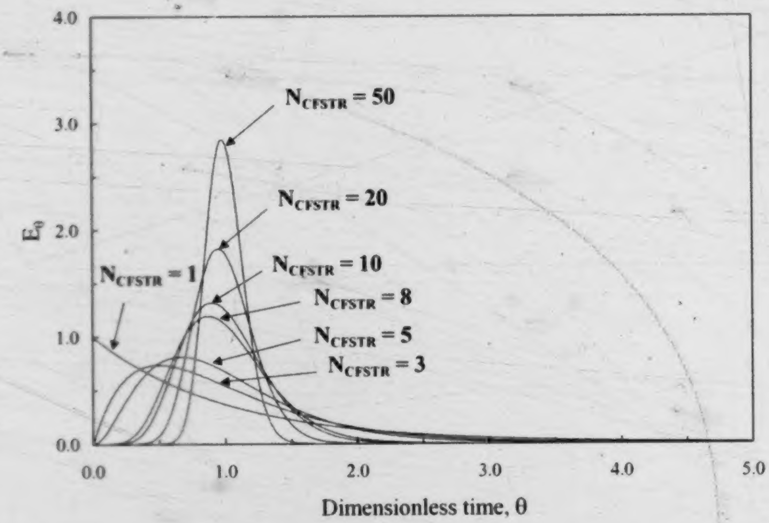

Figure 2.2 Theoretical RTD curves for the transient CFSTR's in-series model.

2.3.2 Transient Continuous-Flow-Stirred-Tank-Reactors In-Series Model

For a transient continuous-flow-stirred-tank-reactors (transient CFSTR's) in-series model, the theoretical RTD for a pulse-input tracer test can be represented by:

$$E_\theta = \frac{N_{CFSTR}\left(N_{CFSTR}\theta\right)^{N_{CFSTR}-1}}{\left(N_{CFSTR}-1\right)!} \qquad [2.13]$$

The CFSTR's in-series model is usually more reliable than the ADM for the flow conditions where the dispersion numbers are large (Levenspiel, 1972). The theoretical RTD curves, for CFSTR's in-series model, are shown in Figure 2.2. Despite being appropriate to describe the hydrodynamic behavior of tall bubble columns that have large aspect ratios, the ADM and the CFSTR's in-series model have limitations when they are used to describe the hydrodynamics of full-scale ozone contactors.

2.4 TRANSIENT BACK FLOW CELL MODEL (BFCM)

2.4.1 Development of the Transient BFCM

Transient BFCM hypothesizes both back flow and exchange flow to characterize the axial dispersion in the liquid phase (Zhou, 1995). Figure 2.3 represents a transient BFCM schematic for co-current flow conditions in bubble columns. It consists of two series of completely mixed cells, one series representing the liquid phase and the other representing the gas phase and each has a number of cells equals N_{BFCM}. As shown in Figure 2.3, it is assumed that the mixing parameter Pe_L varies along the reactor height. Three different distinct regions of mixing have been considered, which is usually the case in tall bubble columns with aspect ratio (L/D) >> 1. In tall bubble columns and as the liquid flow passes through the reactor, the Pe_L will increase as the backmixing decreases along the column height from that in the intense mixing zone near the column entrance. In full-scale industrial ozone multi-chamber reactors, the aspect ratio is usually not very large. Because of the complex nature of such systems, the shape of the overflow structure, the presence of intermediate baffles, and the shape and location of the gas diffusers should be considered along with the aspect ratio in characterizing the hydrodynamic behavior of those systems.

The assumptions that govern the transient BFCM are as follows: (1) back flow occurs only in the liquid phase; (2) backflow is negligible in the gas phase due to the large buoyancy of gas bubbles and large reactor aspect ratio, i.e., the gas phase is assumed to be in a plug flow regime; (3) the ozone bubble column is operated at constant liquid and gas flowrates; (4) no mass transfer and chemical decay should be considered for the inert tracer; and (5) gas hold-up and bubbles' interfacial area are constant along the column height. In order to ensure that the gas phase flow conditions are close to be in a plug flow regime, the number of mixed cells (N_{BFCM}) has to be equal to or greater than

10. Although, in some situations, the number of cells that are needed to model bubble columns of small aspect ratios are less than 10, the assumption that the gas phase is in plug flow regime could still be moderately valid due to the large buoyancy of gas bubbles.

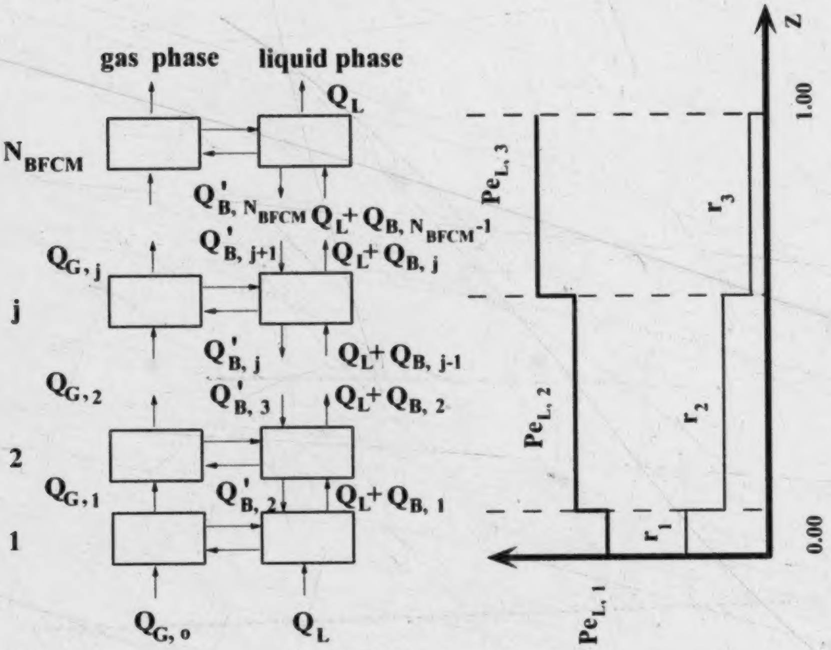
gas phase
liquid phase
Q_L
N_{BFCM}
$Q'_{B, N_{BFCM}}$
$Q_L + Q_{B, N_{BFCM}-1}$
$Q_{G,j}$
$Q'_{B, j+1}$
$Q_L + Q_{B, j}$
j
$Q'_{B, j}$
$Q_L + Q_{B, j-1}$
$Q_{G,2}$
$Q'_{B, 3}$
$Q_L + Q_{B, 2}$
2
$Q_{G,1}$
$Q'_{B, 2}$
$Q_L + Q_{B, 1}$
1
$Q_{G, o}$
Q_L
Z
1.00
0.00
$Pe_{L, 3}$
$Pe_{L, 2}$
$Pe_{L, 1}$
r_3
r_2
r_1

Figure 2.3 Transient BFCM schematic for non-reactive tracer for a co-current flow conditions.

Variable cell volume along the reactor length is considered in the model development to obtain a model that can be used to describe the hydrodynamics in ozone contactors of multiple chambers that have variable dimensions. By employing the mass balance with respect to the inert tracer around the cell number “1”, the mathematical relationship for the transient BFCM can be written as follows:

$$Q_L C_0 + Q'_{B,2} C_2 - \left(Q_L + Q_{B,1}\right) C_1 = \frac{dC_1}{dt} V_c f_1 \qquad [2.14]$$

where: C_0 = tracer concentration in the influent to the first cell in the reactor (mgL^{-1}), C_1 = tracer concentration in the first cell in the reactor (mgL^{-1}), C_2 = tracer concentration in the second cell in the reactor (mgL^{-1}), Q_L = liquid flowrate (m^3s^{-1}), $Q_{B,j}$ = exchange flowrate for cell number "1" (m^3s^{-1}), $Q'_{B,2}$ = back flowrate for cell number "2" (m^3s^{-1}), V_c = average cell volume (m^3) and it is equal to the total volume of the bubble column (V) divided by the number of cells (N_{BFCM}), and f_1 = dimensionless correction factor for the volume of cell number "1". Dividing Equation 2.14 by $V_c C_0^{*}$ where:

$$C_0^{*} = \frac{M}{V_c} = \frac{M}{V/N_{BFCM}} \qquad [2.15]$$

and

$$f_1 = \frac{V_{c,j}}{V/N_{BFCM}} \qquad [2.16]$$

where: C_0^{*} = instantaneously-mixed tracer concentration in the first cell (mgL^{-1}), M = mass of the injected tracer (kg), N_{BFCM} = number of cells in-series in the transient BFCM, and $V_{c,j}$ = volume of cell number "j" (m^3). Then, substituting in the resultant equation for:

$$r_1 = \frac{Q_{B,1}}{Q_L} \qquad [2.17]$$

and

$$r'_2 = \frac{Q'_{B,2}}{Q_L} \qquad [2.18]$$

where: r_1 = dimensionless exchange-flow ratio for cell number "1" and r'_2 = dimensionless back-flow ratio for cell number "2". As a result:

$$\frac{dY_1}{dt} = -\frac{1+r_1}{f_1\tau / N_{BFCM}} Y_1 + \frac{r'_2}{f_1\tau / N_{BFCM}} Y_2 \qquad [2.19]$$

where:

$$Y_j = \frac{C_j}{C_0^*} = \frac{E_{0,j}}{N_{BFCM}} \qquad [2.20]$$

and

$$Z_{j,act} = f_{Z,j} Z_{j,avg} = f_{Z,j} \frac{j-0.5}{N_{BFCM}} = \frac{\left(\left[\sum_{j=1}^{j=j-1} h_{c,j}\right] + h_{c,j}/2\right)}{L} \qquad [2.21]$$

where: Y_j = normalized tracer concentration in cell number "j" in the transient BFCM, $f_{Z,j}$ = dimensionless correction factor for the dimensionless distance (Z) for cell number "j", $h_{c,j}$ = height of cell number "j" (m), $Z_{j,act}$ = actual dimensionless distance of cell number "j", $Z_{j,avg}$ = average dimensionless distance of cell number "j", and j = cell number in the transient BFCM. Following the same procedure used to derive Equation 2.19, one can obtain the transient BFCM equations for the cells from j = 2 to j = N_{BFCM} as follows:

for $1 < j < N_{BFCM}$:

$$\frac{dY_j}{dt} = \frac{1+r_{j-1}}{f_j\tau / N_{BFCM}} Y_{j-1} - \frac{1+r'_j+r_j}{f_j\tau / N_{BFCM}} Y_j + \frac{r'_{j+1}}{f_j\tau / N_{BFCM}} Y_{j+1} \qquad [2.22]$$

and for j = N_{BFCM}:

$$\frac{dY_{N_{BFCM}}}{dt} = \frac{1 + r_{N_{BFCM}-1}}{f_{N_{BFCM}}\tau / N_{BFCM}} Y_{N_{BFCM}-1} - \frac{1 + r'_{N_{BFCM}}}{f_{N_{BFCM}}\tau / N_{BFCM}} Y_{N_{BFCM}} \quad [2.23]$$

where:

$$r_1 = \frac{1}{Pe_{L,1}} - 0.5 \quad [2.24]$$

$$r_2 = \frac{j-1}{Pe_{L,2}} - 0.5 \quad [2.25]$$

$$r_3 = \frac{N_{BFCM} - j}{Pe_{L,3}} - 0.5 \quad [2.26]$$

By employing a liquid-flow balance on each cell from j = 1 to j = N_{BFCM}, one can obtain:

$$Q_{B,1} = Q'_{B,2} = r_1 Q_L \qquad \text{for } j = 1 \quad [2.27]$$

$$Q_{B,2} = Q'_{B,3} = r_2 Q_L \qquad \text{for } j = 2 \quad [2.28]$$

$$Q_{B,j} = Q'_{B,j+1} = r_2 Q_L \qquad \text{for } 3 \le j \le j-1 \quad [2.29]$$

$$Q'_{B,j} = Q_{B,j-1} = r_2 Q_L \qquad \text{for } 3 \le j \le j \quad [2.30]$$

where: j = number of the cell at which the Pe_L changes from $Pe_{L,2}$ to $Pe_{L,3}$.

$$Q_{B,j} = Q'_{B,j+1} = r_3 Q_L \qquad \text{for } j \le j \le N_{BFCM}-1 \quad [2.31]$$

$$Q'_{B,j+2} = Q_{B,j+1} = r_3 Q_L \qquad \text{for } j+1 \le j \le N_{BFCM}-1 \qquad [2.32]$$

and

$$Q'_{B,N_{BFCM}} = Q_{B,N-1_{BFCM}} = r_3 Q_L \qquad \text{for } j = N_{BFCM} \qquad [2.33]$$

The transient BFCM and the transient ADM describe the backmixing of the liquid phase using different mixing parameters Pe_L, N_{BFCM}, and r'. These parameters are interrelated by the following equation:

$$r' = \frac{N_{BFCM}}{Pe_L} - 0.5 \qquad [2.34]$$

Equation 2.34 is an approximate relationship between the two models based on ignoring the $\left(\partial^3 C \big/ \partial Z^3\right)$ and higher-order terms in the Taylor series when the differential equation representing the transient ADM is transformed into a finite-difference equation (Mecklenburgh and Hartland, 1968). The term r' in Equation 2.34 refers to the backmixing between stages whilst the 0.5 refers to the perfect mixing within each stage. These two effects are added together to give the total backmixing effect $\left(N_{BFCM} \big/ Pe_L\right)$ (Mecklenburgh and Hartland, 1975). Stagewise systems may rather be said to consist of finite regions of perfect mixing connected by regions of zero volume but with finite backmixing (Hartland and Mecklenburgh, 1968). This means that a series of stages will always inherent backmixing although if there is no interstage backmixing (when $r' = 0$) (Mecklenburgh and Hartland, 1975). For this situation:

$$Pe_L = 2N_{BFCM} \qquad [2.35]$$

In the transient BFCM, ideal plug flow conditions exist if $r' = -0.5$, although, this ideal situation can not exist in nature (Mecklenburgh and Hartland, 1975).

2.4.2 Numerical Simulations of the Transient BFCM

2.4.2.1 Numerical Solution Technique

Equations 2.19, 2.22, and 2.23, are N_{BFCM} differential equations in N_{BFCM} unknowns (Y_j's). Those differential equations can be solved numerically by applying an explicit technique for the time discretization. This explicit technique allows the transformation of the equations from their differential form into an algebraic form. Solving the N_{BFCM} algebraic equations simultaneously at time step "n+1" allows for Y_j^{n+1} values to be determined as functions of Y_j^n values at time step "n" for j = 1 to j = N_{BFCM} as follows:

for j = 1:

$$\frac{dY_1^{n+1}}{dt} = \frac{Y_1^{n+1} - Y_1^n}{\Delta t} = \frac{Y_1^{n+1} - Y_1^n}{\tau\Delta\theta} = -\frac{1 + r_1}{f_1\tau \big/ N_{BFCM}} Y_1^n + \frac{r_2'}{f_1\tau \big/ N_{BFCM}} Y_2^n \qquad [2.36]$$

for 1 < j < N_{BFCM}:

$$\frac{dY_j^{n+1}}{dt} = \frac{Y_j^{n+1} - Y_j^n}{\Delta t} = \frac{Y_j^{n+1} - Y_j^n}{\tau\Delta\theta} = \frac{1 + r_{j-1}}{f_j\tau \big/ N_{BFCM}} Y_{j-1}^n - \frac{1 + r_j' + r_j}{f_j\tau \big/ N_{BFCM}} Y_j^n + \frac{r_{j+1}'}{f_j\tau \big/ N_{BFCM}} Y_{j+1}^n \qquad [2.37]$$

and for j = N_{BFCM}:

$$\begin{aligned} \frac{dY_{N_{BFCM}}}{dt} &= \frac{Y_{N_{BFCM}}^{n+1} - Y_{N_{BFCM}}^n}{\Delta t} = \frac{Y_{N_{BFCM}}^{n+1} - Y_{N_{BFCM}}^n}{\tau\Delta\theta} \\ &= \frac{1 + r_{N_{BFCM}-1}}{f_{N_{BFCM}}\tau \big/ N_{BFCM}} Y_{N_{BFCM}-1} - \frac{1 + r_{N_{BFCM}}'}{f_{N_{BFCM}}\tau \big/ N_{BFCM}} Y_{N_{BFCM}} \end{aligned} \qquad [2.38]$$

The initial condition for this system of equations is as follows:

$$\text{at } t = 0:$$
$$Y_1 = 1$$
$$Y_j = 0 \quad \text{for } 1 < j < N_{BFCM}$$

The Dirac δ function representing the ideal pulse tracer input is represented numerically by an assumption of $Y_1 = 1$ at $t = 0$ as an ideal instantaneous and complete mixing of the injected mass of the tracer is assumed to take place at $t = 0$ in cell number "1". The system of Equations 2.36 to 2.38 was solved for a wide range of simulated operating conditions. These conditions included: (1) a wide range of the completely mixed cells in-series (N_{BFCM} = 6 to 20); (2) a wide range of Peclet numbers (Pe_L = 1.0 to 40.0); (3) Peclet number was assumed to be constant along the column height unless otherwise it was mentioned that it varied along the column height; and (4) constant cell volume and cross-sectional area were assumed along the column height.

2.4.2.2 Results

The effect of Peclet number (Pe_L) on the theoretical RTD for N_{BFCM} equal to 10 are shown in Figures 2.4 and 2.5, in which the RTD is presented in terms of Y_j that is related to $E_{\theta,j}$ as shown in Equation 2.20. At the bottom sampling port and as Pe_L increases, the RTD narrows as observed before for the ADM theoretical RTD's as a result of the liquid-phase flow conditions being approaching a plug flow regime. At the top sampling port and as the Pe_L increases, the RTD narrows and becomes more symmetrical, and the peak of the RTD increases. Similar trends to those observed in Figures 2.4 and 2.5 were observed at the middle sampling port with higher peaks of the RTD,s than those predicted at the top sampling port. Generally, the peak of the RTD gets smaller and the RTD becomes more symmetrical as the sampling ports get closer to the effluent exit point from the reactor as a result of the liquid phase flow conditions are approaching more towards a plug flow regime.

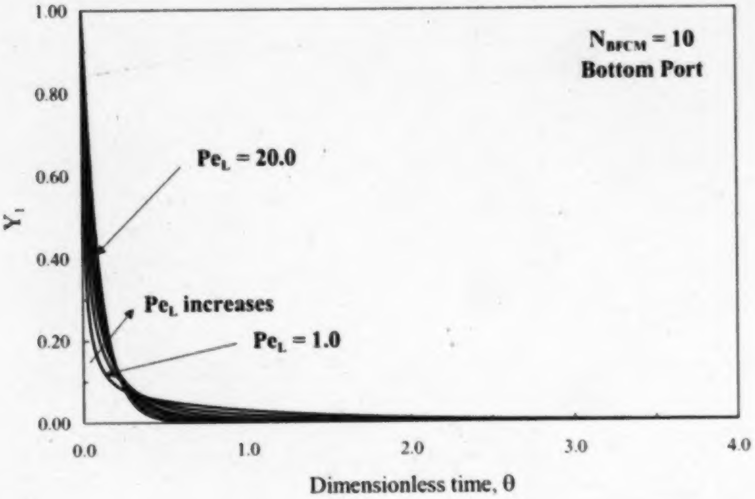

Figure 2.4 Theoretical RTD's for N_{BFCM} = 10 at the bottom sampling port.

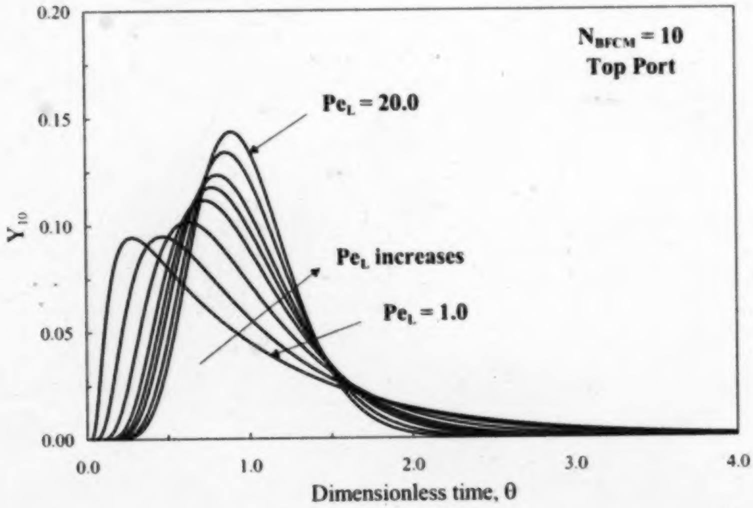

Figure 2.5 Theoretical RTD's for N_{BFCM} = 10 at the top sampling port.

Figures 2.6 to 2.9 depict the effects of the N_{BFCM} and the Pe_L on the theoretical RTD at the middle and the top sampling ports. For an N_{BFCM} equal to or less than 14, not all the Pe_L range was applicable for model simulations because at high Pe_L, r' approached –0.5 and therefore, that produced unstable solution of the transient BFCM equations, i.e., an oscillating solution. The –0.5 is the extreme limit of the model that corresponds to an ideal plug flow mode that does not exist in nature. The dimensionless time step used in those model simulations was set equal to 0.008. Attempts to reduce that dimensionless time step below 0.008 were done in order to obtain solutions for the cases of high Pe_L and low N_{BFCM}, but still no success was achieved. This could be explained by the fact that as Pe_L increases, larger N_{BFCM} (N_{BFCM} larger than 10) is needed to describe the hydrodynamics of bubble columns as the liquid flow approaches plug flow conditions.

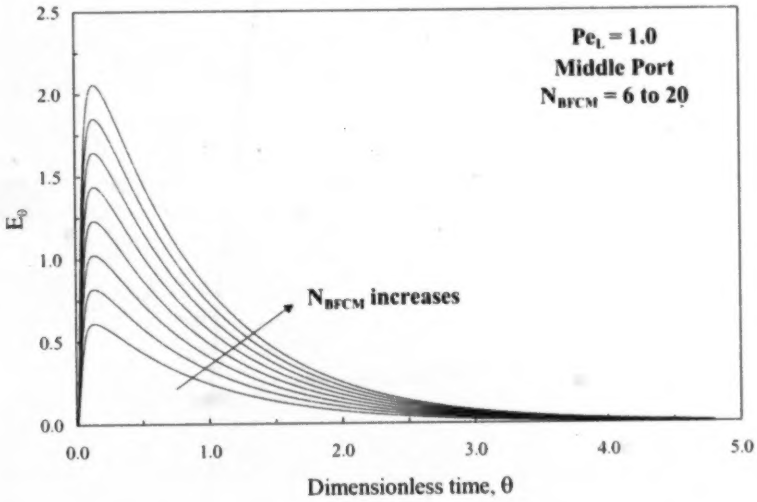

Figure 2.6 Effect of Pe_L and N_{BFCM} on the theoretical RTD's at the middle sampling port for Pe_L = 1.0.

Figures 2.6 and 2.7 show that varying the N_{BFCM} from 6 to 20 at Pe_L = 1.0 causes the peaks of the RTD's to increase which contradicts with what Zhou (1995) has reported. All the peaks almost occur at the same point of dimensionless time with a slight shift and all the RTD's are broad and non-symmetrical. This suggests that as the pulse-input slowly passes the sampling port it spreads. This is usually the case for bubble columns that have small aspect ratios. As the Pe_L increases to 40.0, i.e., the liquid phase is approaching plug flow conditions, we start to observe symmetrical RTD's at different N_{BFCM} ($14 \leq N_{BFCM} \leq 20$) as shown in Figures 2.8 and 2.9.

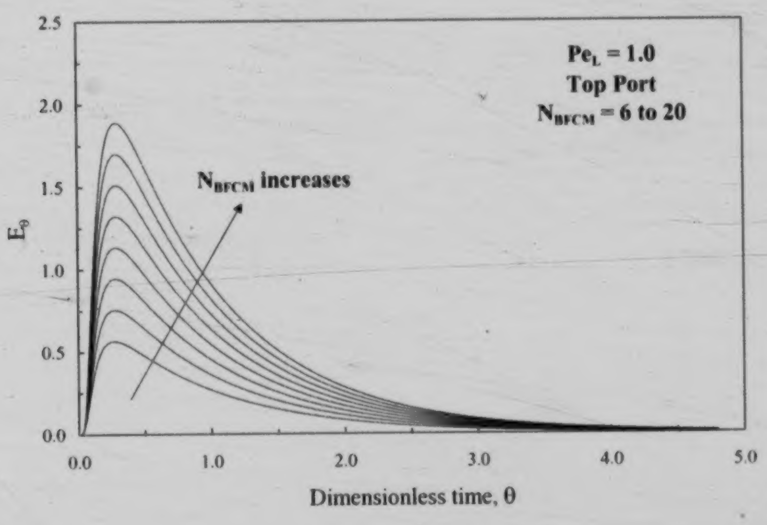

Figure 2.7 Effect of Pe_L and N_{BFCM} on the theoretical RTD's at the top sampling port for $Pe_L = 1.0$.

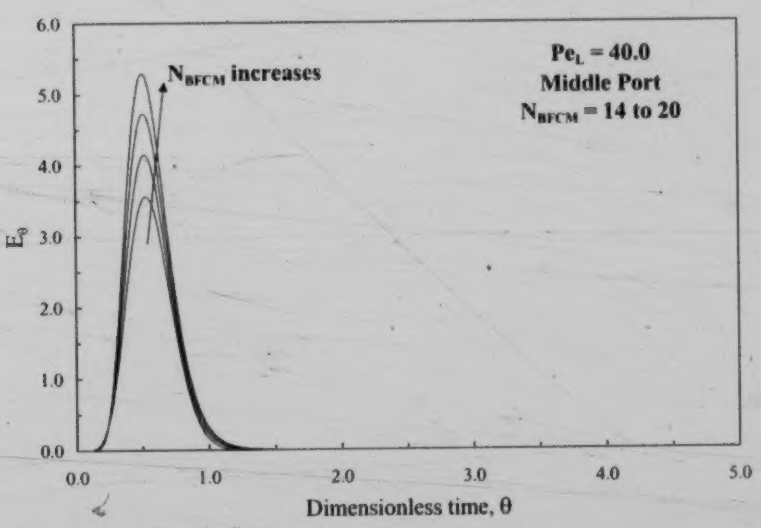

Figure 2.8 Effect of Pe_L and N_{BFCM} on the theoretical RTD's at the middle sampling port for $Pe_L = 40.0$.

Interestingly, at both the middle and the top sampling ports, the RTD's are spread with almost the same width, but the increase in the peak as N_{BFCM} increases from 14 to 20, is higher than that at $Pe_L = 1.0$. For $N_{BFCM} < 10$, the assumption of the gas phase being in a plug flow regime might not be very accurate, although it can still be moderately valid due to the large buoyancy of the gas bubbles. Therefore, those cases for $N_{BFCM} < 10$ were included in the model simulations for the sake of comparison.

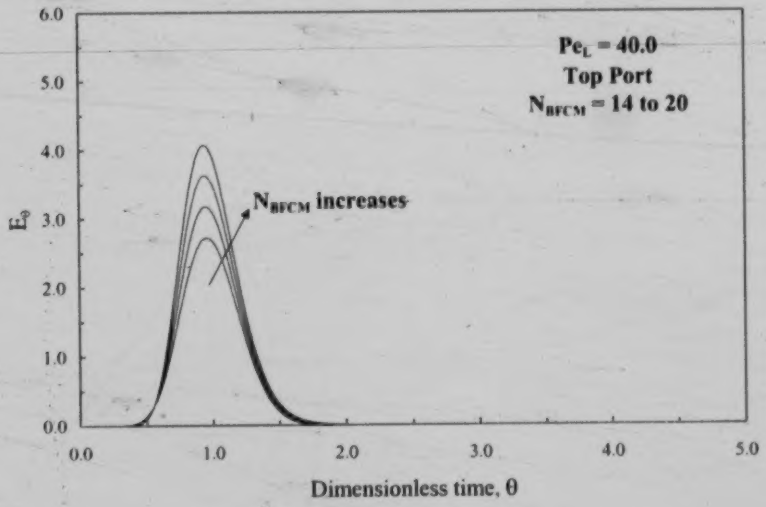

Figure 2.9 Effect of Pe_L and N_{BFCM} on the theoretical RTD's at the top sampling port for $Pe_L = 40.0$.

Comparisons between the transient BFCM, ADM, and CFSTR's in-series model for predicting the RTD's for $Pe_L = 1.0$ and 20.0 at the middle and the top sampling ports respectively, are shown in Figures 2.10 to 2.13. For 10 cells in-series and $Pe_L = 1.0$, the transient ADM predicts lower peak of the RTD compared to the one predicted by the transient BFCM. This can be explained by the Pe_L being very small and therefore, the assumption that the flow conditions are slightly deviated from the ideal plug flow conditions is not satisfied which makes the transient ADM not adequate for predicting the liquid phase backmixing under those flow conditions.

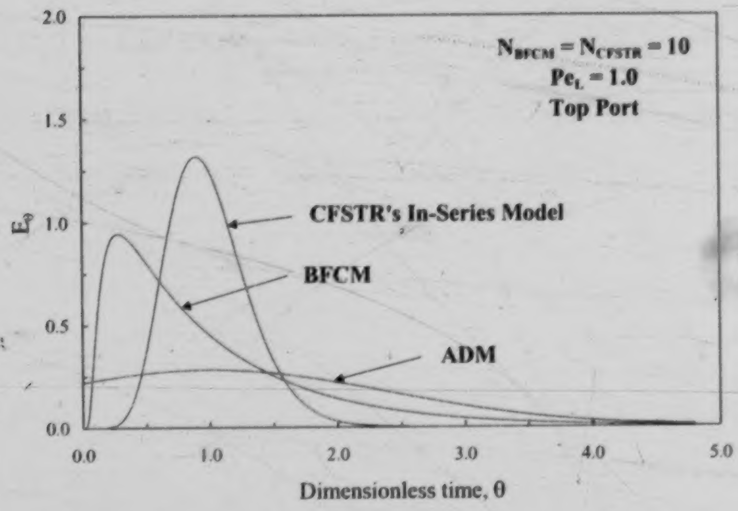

Figure 2.10 Comparison between the transient BFCM, ADM, and CFSTR's in-series model on the theoretical RTD's for $Pe_L = 1.0$ and $N_{BFCM} = N_{FCSTR} = 10$.

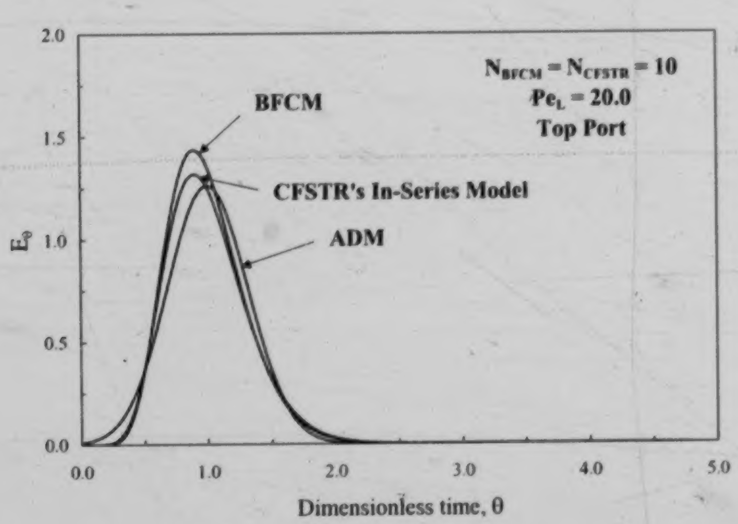

Figure 2.11 Comparison between the transient BFCM, ADM, and CFSTR's in-series model on the theoretical RTD's for $Pe_L = 20.0$ and $N_{BFCM} = N_{FCSTR} = 10$.

At the same Pe_L, the transient CFSTR's in-series model predicts higher peak of the RTD compared to the transient BFCM and the predicted RTD is symmetrical rather than being non-symmetrical which is usually the case when tracer tests are conducted in bubble column reactors. This can be explained by the fact that the transient CFSTR's in-series model does not account for the backmixing between the cells which is large at this low Pe_L. At $Pe_L = 20.0$, all three models predict symmetrical RTD's that have almost identical spreads and peaks as the backmixing ratio in the transient BFCM gets smaller at this high Pe_L.

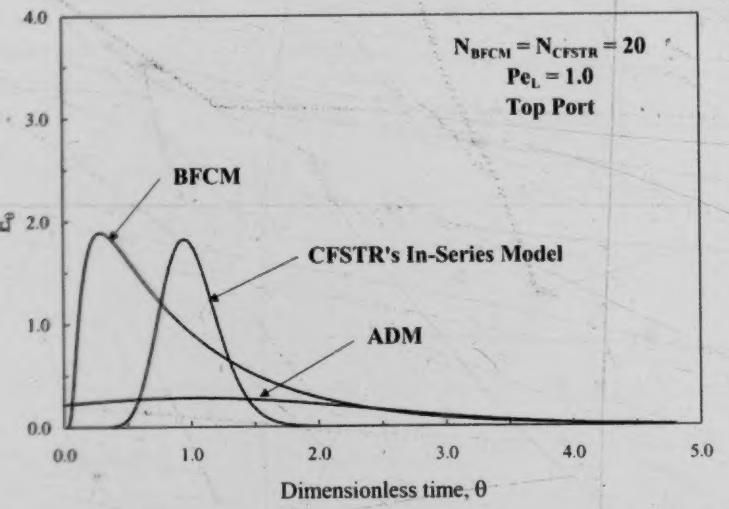

Figure 2.12 Comparison between the transient BFCM, ADM, and CFSTR's in-series model on the theoretical RTD's for $Pe_L = 1.0$ and $N_{BFCM} = N_{FCSTR} = 20$.

At $Pe_L = 1.0$, Figure 2.12 depicts a similar trend to the one observed in Figure 2.10 except that the RTD predicted by the transient CFSTR's in-series model has a slightly lower peak than the one predicted by the transient BFCM. The large number of cells in-series ($N_{BFCM} = 20$) at this very small Pe_L could have caused an increase in the RTD peak suggesting that the effect of the N_{BFCM} on the peak of the RTD is larger than the effect of the backmixing. As shown in Figure 2.13, as the Pe_L increases to 20.0 for the same number of cells ($N_{CFSTR} = 20$), the transient CFSTR's in-series model and the transient ADM predict lower peak of the RTD compared to the one predicted by the transient BFCM. This can be explained by the transient BFCM performance being closer to plug flow conditions than the performances of the transient ADM and the transient CFSTR's in-series model.

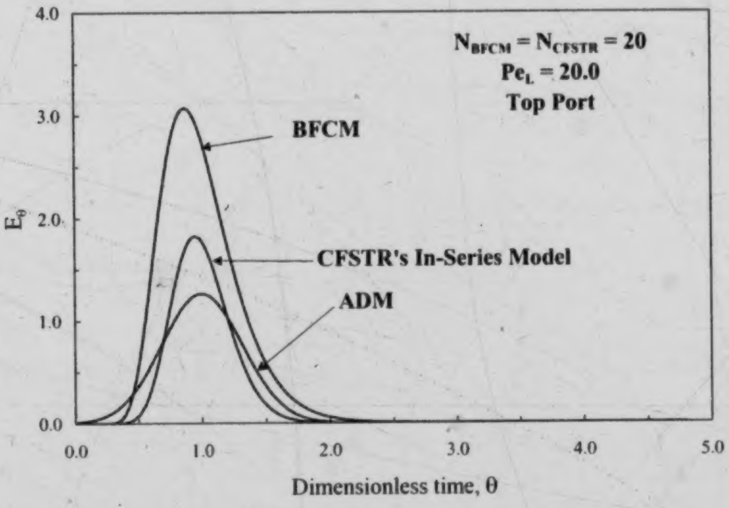

Figure 2.13 Comparison between the transient BFCM, ADM, and CFSTR's in-series model on the theoretical RTD's for $Pe_L = 20.0$ and $N_{BFCM} = N_{FCSTR} = 20$.

Figures 12.4 and 2.15 show the theoretical RTD's for a situation where the Pe_L varies along the column height as in tall bubble columns. Pe_L was assumed to equal 0.40 from Z = 0.00 to 0.05, 6.67 from Z = 0.05 to 0.53, and 9.00 from Z = 0.53 to 1.00. As shown and as the sampling port moves along the reactor height, i.e., as the cell number increases, the RTD's peak gets smaller and the RTD becomes more symmetrical, but still skewed to the left.

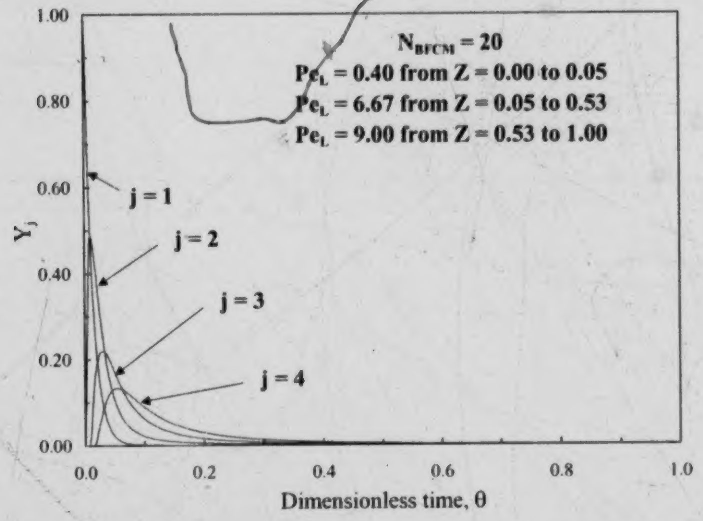

Figure 2.14 Theoretical RTD's for $N_{BFCM} = 20.0$ and variable Pe_L along the column height (j = 1 to 4).

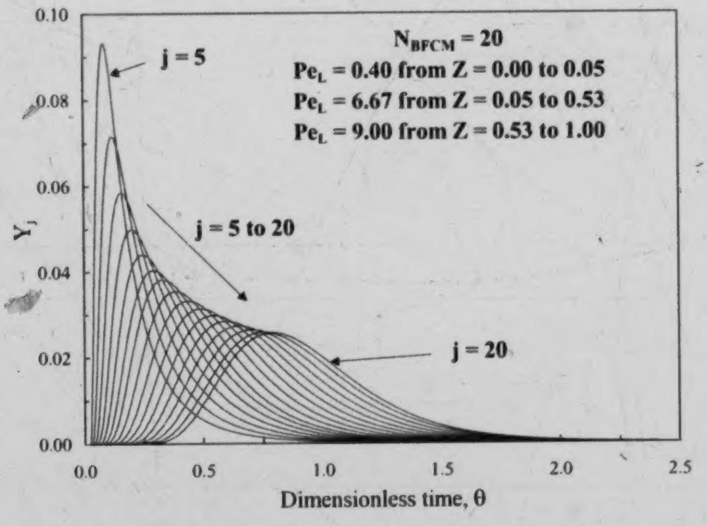

Figure 2.15 Theoretical RTD's for $N_{BFCM} = 20.0$ and variable Pe_L along the column height (j = 5 to 20).

2.5 TESTING OF THE TRANSIENT BFCM

2.5.1 Experimental Study

The experimental tracer data of Zhou (1995) was used for testing the applicability of the transient BFCM to describe the hydrodynamics in a fine-diffuser bubble column. The experimental set-up used in the study conducted by Zhou (1995) consisted of a glass bubble column with an inside diameter of 100 mm and a total column height of 2,000 mm. The water depth was maintained constant at 1,750 mm using an overflow weir. The tracer samples were collected from six sampling ports equally spaced along the column height as well as from the effluent exit line. The fine-bubble diffuser used in this bubble column was a 25 mm spherical fused crystalline aluminum stone that was elevated 5 mm from the bottom of the reactor to allow for good mixing between the gas bubbles and the liquid phase. The weir placed at the top of the column had 8 mm holes faced downward at the bottom of the headspace cap. This configuration helped minimizing the occurrence of swamp flows at the column exit (Zhou, 1995) and therefore, it could be concluded that the backmixing along the column height was uniform. The contactor was operated at two different flow modes: (1) the counter-current and (2) the co-current flow modes. The system was run for about eight turnovers to insure stable and steady-state operations before a Rhodamine WT tracer was injected upstream of the water inlet point into the column. The concentration of the Rhodamine in the collected samples ranged from 0 to 10^{-2} mgL^{-1} and was measured using the fluorescence method. In this experimental study, the theoretical hydraulic retention time ranged from 120 to 390 s and the gas-to-liquid flowrate (G/L) ratio ranged from 0.04 to 0.73.

2.5.2 Data Analysis Technique

Since the bubble column had a constant cross-sectional area, the cell volume was set constant along the column height and the cell volume correction factor, represented by Equation 2.16, was equal to 1. Also, since a uniform backmixing can be assumed along the column height due to the reactor configuration, Pe_L was assumed to be constant along the column height. As a result, the exchange-flow ratio (r) was equal to the back-flow ratio (r') and both were constant along the column height. The solutions of the transient BFCM equations were obtained using a spreadsheet program that was developed with a user-specified tolerance set equal to 10^{-4}. The target cell in this spreadsheet program was the summation of squared residuals (SSR) of the tracer concentrations. The minimization technique was used to minimize the SSR by changing the back-flow ratio (r') according to the following equation:

$$SSR(r') = \sum \left(C_{L,experimental} - C_{L,predicted}\right)^2 \qquad [2.39]$$

where: $C_{L,measured}$ = measured tracer concentration (mgL^{-1}) and $C_{L,predicted}$ = predicted tracer concentration (mgL^{-1}). During the transient BFCM testing, a minimum SSR was always achieved as a result of having no problems with respect to the divergence of the model equations to reach a final solution. The initial "guess value" of the Pe_L was calculated using Equation 2.24 where $r = r'$. Pe_L was calculated using the tracer data of Zhou (1995) and by applying Equations 2.4 and 2.5 for the closed-open and closed-closed boundary conditions, respectively. After examining a different number of cells (N_{BFCM}) for the transient BFCM analyses, it was found that 10 cells gave the lowest SSR's.

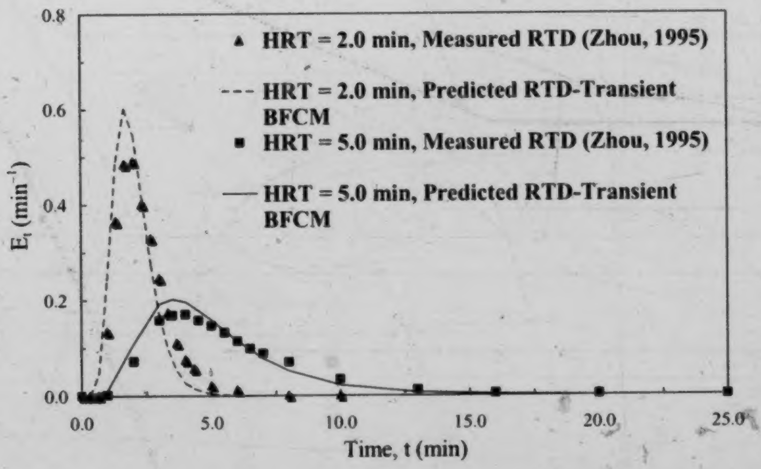

Figure 2.16 Experimental and predicted RTD's in a counter-current flow mode.

2.5.3 Results

The transient BFCM predictions of the RTD curves at the reactor exit point in the bubble column for the counter-current and the co-current flow modes are shown in Figures 2.16 and 2.17, respectively. Under a small hydraulic retention time of 120 s, the RTD curves were symmetrical. As the hydraulic retention time increased, tailing effects were observed and the RTD's were more asymmetrical rather than symmetrical. There were slight differences between the observed and the predicted RTD's in the two operating modes with the counter-current flow mode exhibiting higher backmixing. Examining the predicted back-flow ratios yielded findings that are in agreement with the literature. As the gas flowrate increased, the back-flow ratios increased in both the counter and the co-current flow modes. An explanation of this phenomenon is that as the gas flowrate increases, the bubbles' sizes increase and as a result, the circulation induced by the gas flow inside the bubble column will increase causing the backmixing to increase. By contrast, as the liquid flowrate increased, the back-flow ratios decreased as a result of the liquid flow being closer to plug flow conditions.

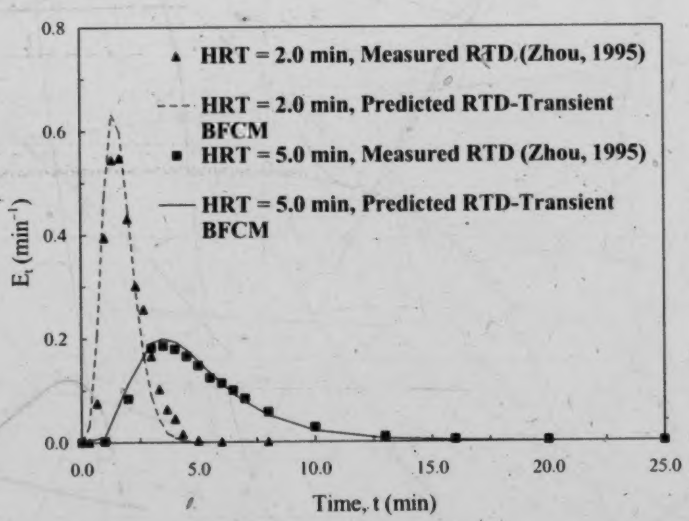

Figure 2.17 Experimental and predicted RTD's in a co-current flow mode.

Linear regression analyses of the predicted back-flow ratios obtained using the transient BFCM were conducted in order to obtain relationships that can be used to predict the back-flow (i.e., exchange-flow) ratios under different operating conditions in terms of the liquid flowrates, the gas flowrates, and the counter-current versus the co-current flow modes. Zhou (1995) proposed a generalized model for both the counter-current and the co-current flow modes in which log (r+0.5) was correlated to log(u_G) and log(u_L). The log of (r+0.5) was chosen for the proposed model for better comparison with the previous studies in the literature. This generalized model can be expressed as follows:

$$\log(r + 0.5) = a + b \cdot \log(u_G) + c \cdot \log(u_L) \qquad [2.40]$$

Zhou (1995) used the pooled data of the counter-current and the co-current flow modes to obtain the regression constants a, b, and c. They were determined to be 2.45, 0.40, and –1.03, respectively, with a correlation coefficient (r) equal to 0.96. In another attempt to model the back-flow ratio as a function of the gas and liquid flowrates, the data of the counter-current flow mode was analyzed separately from the data of the co-current flow mode. The proposed model predicted higher back-flow ratios under the counter-current flow mode at the same gas and liquid flowrates. The regression analyses produced regression constants (a, b, and c) of –1.06, 0.34, and –0.95, respectively, for the counter-current flow mode with a correlation coefficient equal to 1.00. For the co-current flow mode, the regression constants (a, b, and c) were –1.64, 0.36, and –1.21, respectively, with a correlation coefficient equal to 0.99. It can be concluded that the gas flowrate has similar effect on the back-flow ratio in the counter-current and the co-current flow modes while the liquid flowrate has higher effect on the back-flow ratio in the co-current flow mode. Figure 2.18 depicts the transient BFCM predictions of the back-flow ratios versus the predictions of the proposed regression model (Equation 2.40). An excellent correlation between the two sets of back-flow ratios is evident.

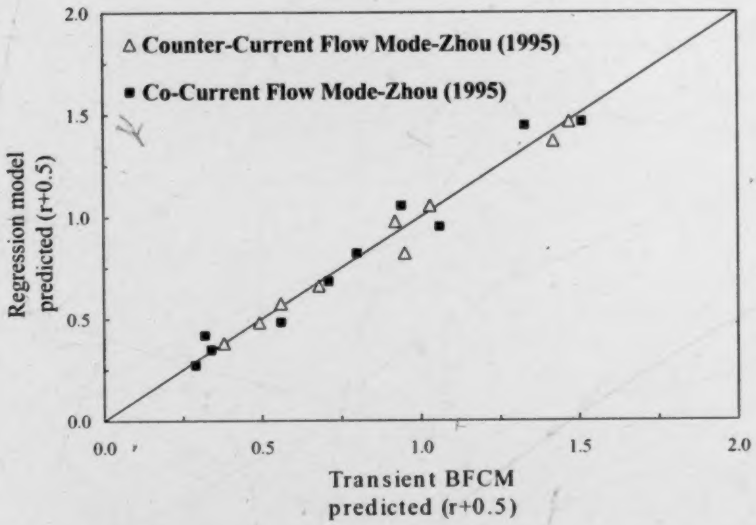

Figure 2.18 Comparison between the transient BFCM and the regression model predictions of back flow ratios.

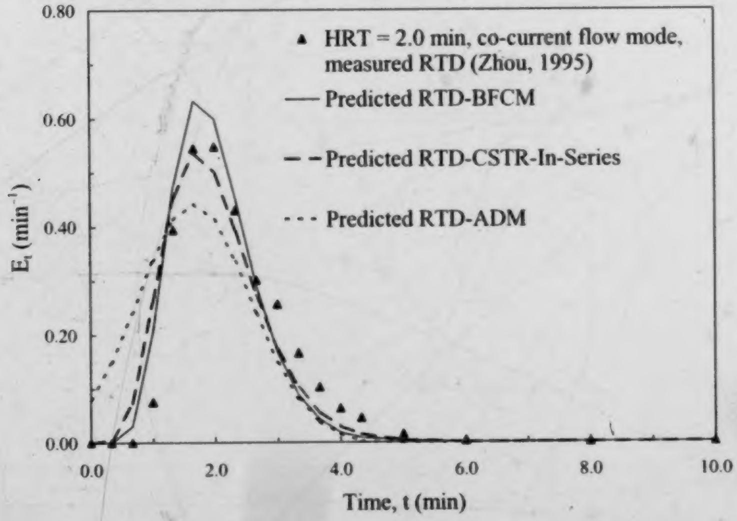

Figure 2.19 Comparison between the transient BFCM, ADM, and CFSTR's model in predicting the RTD's in a co-current bubble column.

In order to compare the predictions of the transient BFCM with the predictions of the traditionally used transient ADM and transient CFSTR's model, the RTD's obtained by the three models are shown in Figure 2.19. From the tracer data and by applying Equation 2.5, the Pe_L number and N_{CFSTR} were determined and used as initial guesses to determine the actual Pe_L and N_{CFSTR} using a similar minimization technique to the one previously used for the transient BFCM. The values of these parameters obtained using the experimental tracer data should only be used as initial guesses. This is due to the problems usually encountered while conducting tracer experiments. Those problems might be caused by some unrecorded data points as a result of using longer sampling intervals. It is shown that the transient BFCM was superior to the other models in describing the backmixing process in bubble columns. The transient ADM predicted similar RTD's using either the equation for small deviations from plug flow conditions or the equation for open-open boundary conditions presented in Levenspiel (1972). By applying the minimization technique, the two equations predicted a Pe_L of 19.2 while the tracer data yielded a Pe_L of 9.8. Both equations were not suitable for describing the hydrodynamics due to the inappropriate boundary conditions' assumptions associated with them. The inadequacy of the transient ADM in describing the hydrodynamics is also evident from Figure 2.19. The equation representing small deviations from plug flow conditions is not suitable due to the fact that actual conditions in the bubble column are closer to complete mixing conditions rather than plug flow conditions. On the other hand, the equation representing the open-open boundary conditions is not suitable for the actual boundary equations encountered in the bubble column due to the configuration at the column exit. The actual boundary conditions are usually closed-closed or closed-open conditions and unfortunately, no analytical solutions are available of the transient ADM for these conditions. The transient BFCM produced a Pe_L of 17.9 based on a number of cells equal to 10. The transient CFSTR's model produced an N_{CFSTR} of 5.5 and 7.0 using the experimental and the simulated RTD's, respectively. Applying a number of cells equal to 7 in the transient CFSTR's model produced a Pe_L of 12.9. As shown in Figure 2.19, the transient CFSTR's model predicted an RTD curve that was similar to the one predicted by the transient BFCM except for a lower peak. Using a number of cells equal to 7 in the transient CFSTR's model does not ensure plug flow conditions in the gas phase. Therefore, using the steady-state CFSTR's model to describe the overall ozonation process will not be appropriate.

2.6 CONCLUSIONS

As compared to the traditionally used transient ADM and transient CFSTR's in-series model, the transient BFCM can adequately describe the backmixing in the liquid phase in bubble columns over a wide range of operating conditions and under any given boundary conditions. Therefore, it has some advantages over the transient ADM and the transient CFSTR's in-series model. These advantages are as follows: (1) the transient BFCM can account for variable backmixing coefficient (i.e., variable Pe_L) along the column height or along the length of a contacting chamber while predicting simultaneously the RTD curves at various sampling ports; (2) the transient BFCM has the capability to account for variable cross-sectional area along the column height or along the length of a contacting chamber; (3) the analytical solution of the transient ADM for a tracer pulse-input is only available for small deviations from plug flow conditions (Equation 2.11) under any given boundary conditions and for large deviations from plug flow conditions under only open-open boundary conditions. The closed-closed and closed-open boundary conditions are usually the cases in ozone contacting chambers. Therefore, in order to use the solution of transient ADM for a tracer pulse-input under small deviations from plug flow conditions (Equation 2.11) to describe the backmixing in the liquid phase in such ozone reactors will lead to inadequate modeling of the hydrodynamics; and (4) the transient BFCM is easy to formulate and solve using a spreadsheet program even for the cases where the mixing parameters are variable along the column height.

The number of cells in-series, as one of the mixing parameters to be considered for the transient BFCM simulations, has to be chosen carefully so that the transient BFCM predictions, of the hydrodynamic behavior in ozone contactors performance under different operating conditions, are closer to the actual backmixing conditions. The transient BFCM should be expanded to account for the backmixing in the gas phase to allow studying the effect of the gas-phase backmixing on the hydrodynamic performance of ozone bubble columns of small aspect ratios and full-scale ozone contactors where the gas phase can no longer be considered in the plug flow regime.

2.7 REFERENCES

1. Chianese, A., M.C. Annesini, R. De Santis, and L. Marrelli, "A Model of a Pilot Bubble Column Reactor for Benzene Alkylation by Ethylene", Chem. Eng. J. 22: 151-158 (1981).
2. Deckwer, W.-D., "Non-Isobaric Bubble Columns with Variable Gas Velocity", Chem. Eng. Sci. 31: 309-317 (1976).
3. Deckwer, W.-D., U. Graeser, H. Langemann, and Y. Serpemen, "Zones of Different Mixing in the Liquid Phase of Bubble Columns", Chem. Eng. Sci. 28: 1223-1225 (1973).
4. Hartland, S. and J.C. Mecklenburgh, "The Concept of Backmixing", Chem. Eng. J. 23: 186-187 (1968).
5. Hikita, H. and H. Kikukawa, "Liquid-Phase Mixing in Bubble Columns: Effect of Liquid Properties", Chem. Eng. J. 8: 191-197 (1974).
6. Houzelot, J.-L., M.-F. Thiebaut, J.-C. Charpentier, and J. Schiber, "Contribution to the Hydrodynamic Study of Bubble Columns", Int. Chem. Eng. 25: 645-650 (1985).
7. Jamialahmadi, M. and H. Müller-Steinhagen, "Effect of Electrolyte Concentration on Bubble Size and Gas Hold-Up in Bubble Columns", Chem. Eng. Res. Des. 68: 202-204 (1990).
8. Kawagoe, M., T. Otake, and C.W. Robinson, "Gas-Phase Mixing in Bubble Columns", J. Chem. Eng. Japan 22: 136-142 (1989).
9. Le Sauze, N., A. Laplanche, M.T. Orta De Velasquez, G. Martin, B. Langlais, and N. Martin, "The Residence Time Distribution of the Liquid Phase in a Bubble Column and its Effect on Ozone Transfer", Ozone Sci. & Eng. 14: 245-262 (1992).
10. Levenspiel, O., *Chemical Reaction Engineering, 2nd Edition* (New York, NY, USA: John Wiley and Sons, Inc., 1972), pp. 253-293.
11. Mecklenburgh, J.C. and S. Hartland, *The Theory of Backmixing*, (New York, NY, USA: John Wiley and Sons, Inc., 1975), pp. 1-32.
12. Mecklenburgh, J.C. and S. Hartland, "Design of Reactors with Backmixing-III. Numerical Difference Between Differential and Stagewise Models", Chem. Eng. Sci. 23: 81-85 (1968).

13. Ogawa, S., M. Kobayashi, S. Tone, and T. Otake, "Liquid Phase Mixing in the Gas-Liquid Jet Reactor with Liquid Jet Ejector", J. Chem. Eng. Japan 15: 469-474 (1982).

14. Ohki, Y. and H. Inoue, "Longitudinal Mixing of the Liquid Phase in Bubble Columns", Chem. Eng. Sci. 25: 1-16 (1970).

15. Reith, T., S. Renken, and B.A. Israel, "Gas Hold-Up and Axial Mixing in the Liquid Phase of Bubble Columns", Chem. Eng. Sci. 32: 619-629 (1968).

16. Shetty, S.A., M.V. Kantak, and B.G. Kelkar, "Gas-Phase Backmixing in Bubble-Column Reactors", AIChE J. 38: 1013-1026 (1992).

17. Van Vuuren, D. "The Transient Response of Bubble Columns", Chem. Eng. Sci. 43: 213-220 (1988).

18. Wachi, S. and Y. Nojima, "Gas-Phase Dispersion in Bubble Columns", Chem. Eng. Sci. 45: 901-905 (1990).

19. Zahradník, J. and M. Fialová, "The Effect of Bubbling Regime on Gas and Liquid Phase Mixing in Bubble Column Reactors", Chem. Eng. Sci. 51: 2491-2500 (1996).

20. Zhou, H., *Investigation of Ozone Disinfection Kinetics and Contactor Performance Modeling, Ph.D. Thesis* (Edmonton, AB, CANADA: University of Alberta, 1995), pp. 129-135.

21. Zhou, H., D.W. Smith, and S.J. Stanley "Modeling of Dissolved Ozone Concentration Profiles in Bubble Columns", J. Environ. Eng., ASCE 120: 821-840 (1994).

CHAPTER 3. OZONE MASS TRANSFER IN WATER TREATMENT: MASS TRANSFER MODELING OF OZONE BUBBLE COLUMNS*

3.1 INTRODUCTION

Ozonation of water is usually conducted in ozone bubble columns as the reacting chambers where ozone gas is bubbled through the liquid phase by utilizing conventional bubble diffusers, turbine mixers, negative pressure gas ejectors, positive pressure gas injectors, etc. During ozonation, a number of processes occur simultaneously. Those processes are convection and backmixing of the liquid flowing through the contacting chamber, convection of the gas flowing through the contacting chamber, ozone gas mass transfer from the gas phase to the liquid phase, ozone auto-decomposition, and competitive reactivity of constituents in water with dissolved ozone (Zhou *et al.*, 1994). The rates of individual phase transport and chemical transformation processes, contactor configuration, operating conditions, and water quality influence the overall performance of any ozonation system (Zhou, 1995). Ozonation process relies in its effectiveness on the concentration of dissolved ozone. Quantifying the dissolved ozone is crucial to obtain optimized designs and operations of ozone contactors.

Mathematical models that are often applied to predict the dissolved ozone profiles along bubble columns are based on one of the following liquid-phase flow regime assumptions: (1) complete mixing or (2) plug flow (Alvarez-Cuenca *et al.*, 1980; Alvarez-Cuenca *et al.*, 1981; Chang and Chian, 1981; Laplanche *et al.*, 1991; Hull *et al.*, 1992; Lev *et al.*, 1992). Applying such simplified models to describe the performance of ozone bubble columns will lead to unoptimized and unreliable designs and consequently poor performance of ozone contactors. The actual flow pattern in bubble columns is usually closer to being mixed flow rather than being plug flow, but still not completely mixed flow. Thus, it is essential to accurately characterize those fundamental processes and determine the variables that control and dictate the overall performance of any ozonation system.

A version of this chapter has been published. Gamal El-Din, M. and D.W. Smith, Wat. Sci. & Technol.: Wat. Suppl. 1: 123-130 (2001).

This chapter presents: (1) formulation of the steady-state BFCM for modeling the ozone mass transfer process in bubble columns; and (2) initial testing of the steady-state BFCM using the pilot-scale experimental data of Zhou (1995).

3.2 THEORETICAL BACKGROUND

In bubble columns, non-ideal flow conditions affect the rate of absorption and concentration profiles of dissolved ozone in tubular bubble columns. The backmixing process of the liquid phase involves the redistribution of liquid elements either by slippage due to shear forces or by turbulent eddies. Since, the redistribution process is repeated a considerable number of times during the flow of the fluid through the contacting chamber, it was assumed that these disturbances are statistical in nature as in molecular diffusion. Therefore, the empirical Fick's law is applied with replacing the molecular diffusion coefficient by a mixing parameter, the axial dispersion coefficient (D_L), which combines the effects of a non-uniform velocity profile (shear dispersion), molecular and eddy diffusivities:

$$\text{Diffusive mass flux} = -D_L \frac{\partial C_L}{\partial \ell} \qquad [3.1]$$

The mass transfer of ozone gas from the gas phase into the liquid phase can be described and quantified by the two-film model:

$$\psi = k_L a\left(C_L^* - C_L\right) \qquad [3.2]$$

where: ψ = gas-absorption rate ($mgL^{-1}s^{-1}$), k_L = local liquid mass transfer coefficient (ms^{-1}), a = gas bubbles' specific interfacial area (m^{-1}), C_L^* = concentration of the dissolved ozone in equilibrium with the bulk ozone gas (mgL^{-1}), and C_L = concentration of the dissolved ozone in the bulk liquid (mgL^{-1}). Since ozone gas diffuses much faster in the gas phase than in the liquid phase, the mass transfer in the liquid phase becomes a rate-controlling step and the overall mass transfer coefficient is considered to consist entirely of the local mass transfer coefficient in the liquid phase (Zhou, 1995).

As ozone gas dissolves in water, it starts decaying through two pathways, auto-decomposition and oxidation of impurities in the liquid phase due to its extremely high oxidative properties (Hoigné, 1982). The overall ozone auto-decomposition rate is influenced by the concentration and the history of the ozonation process and this ozone auto-decomposition process could be represented by a modified pseudo-first-order rate expression (Yurteri and Gurol, 1988; Oke *et al.*, 1998). In the experimental study of Oke *et al.* (1998), it was shown that the commonly used first-order kinetics expression with a constant reaction rate constant was inadequate in describing the ozone auto-decomposition process especially in situations where the initial ozone demand was significant. It was demonstrated that the reaction rate constant was continuously decreasing along the course of ozonation as a result of the changes in the water characteristics. As a result, an exponentially decreasing function was proposed as a better alternative to describe the ozone auto-decomposition kinetics (Oke *et al.*, 1998). In that expression, the reaction rate constant was replaced by a variable referred to as the specific ozone utilization rate constant (k_w) that is a function of the utilized ozone dose (ΔO_3):

$$\frac{dC_L}{dt} = -k_w C_L = -\left(k_1 + k_2 e^{-k_3 \Delta O_3}\right) C_L \qquad [3.3]$$

where: C_L = instantaneous dissolved ozone concentration (mgL^{-1}), k_w = specific ozone utilization rate constant (s^{-1}), k_1 = empirical non-linear regression constant (s^{-1}), k_2 = empirical non-linear regression constant (s^{-1}), k_3 = empirical non-linear regression constant (Lmg^{-1}), t = reaction time (s), and ΔO_3 = amount of the utilized ozone (mgL^{-1}). k_1, k_2, and k_3 are empirical constants that can be obtained by applying non-linear regression analysis to the kinetics data and they are also characteristics of the water to be treated. According to Equation 1.2, as the amount of the utilized ozone increases along the course of ozonation, k_w will decrease. At the beginning of the ozonation, i.e., when the amount of the utilized ozone is zero, k_w is equal to $k_1 + k_2$ as the ozone auto-decomposition process is only attributed to the initial ozone demand. In the study of Oke *et al.* (1998) and for clean deionized water, the initial ozone demand was practically equal to zero and therefore, k_w could be assumed constant during the course of the ozonation.

For an irreversible first-order reaction, Danckwerts (1970) proposed a criterion for neglecting the effect of chemical reactions on the local mass transfer coefficient and hence, the gas absorption can be dealt with as pure physical absorption in which the dissolved gas diffuses from the surface to the bulk liquid without reacting on the way:

$$H_a^2 = E^2 = M = \frac{D_{O_3} k_w}{k_L^2} << 1 \text{ (i.e., it reaches zero)} \qquad [3.4]$$

where: $H_a = E = \sqrt{M}$ = dimensionless Hatta number, k_L = local mass transfer coefficient (ms^{-1}), D_{O_3} = molecular diffusivity of ozone gas in water (m^2s^{-1}), and k_w = specific ozone utilization rate constant (s^{-1}). k_w was reported to be 4.7×10^{-4} s^{-1} for the deionized water tested by Zhou (1995). Yurteri and Gurol (1988) reported that k_w was in the order of 2.8×10^{-3} s^{-1} for the tested raw surface water. The diffusivity of ozone in water was determined by the Wilke-Chang formula to be 1.74×10^{-9} m^2s^{-1} (at 20 °C) which is comparable to the value of 1.71×10^{-9} m^2s^{-1} obtained using the equation recommended by Johnson and Davis (1996). k_L was reported to be in the order of 3.1×10^{-4} ms^{-1} for clean water and in the order of 1.9×10^{-4} ms^{-1} for water containing organic substances (Beltrán *et al.*, 1997). Substituting for these typical values of D, k_w, and k_L into Equation 3.4 yields squared-Hatta numbers of 8.5×10^{-6} and 1.4×10^{-4} for the deionized and the surface water, respectively. Based on these small Hatta numbers, it can be concluded that the chemical reactions that occur during the course of clean or surface water ozonation has negligible effect on the local mass transfer coefficient and hence, Equation 3.2 will be applied for ozone absorption without any modification.

3.3 DEVELOPMENT OF THE BACK FLOW CELL MODEL (BFCM)

3.3.1 Transient BFCM

BFCM hypothesizes both back flow and exchange flow to characterize the axial dispersion in the liquid phase (Zhou, 1995). Figure 3.1 represents a BFCM schematic for co-current flow conditions in bubble columns, where the back flow ratio is equal to the exchange flow ratio, and both are constant along the column height. BFCM consists of two series of completely mixed cells, one series representing the liquid phase and the other representing the gas phase and each has a number of cells equals N_{BFCM}. The assumptions that govern the transient BFCM are: (1) back flow occurs only in the liquid phase; (2) back flow is negligible in the gas phase due to the large buoyancy of gas bubbles; (3) ozone bubble column is operated at constant liquid and gas flow rates; (4) gas hold-up and gas bubbles' interfacial surface area are constant along the column height; and (5) the inert tracer material does not exhibit any mass transfer or chemical decay.

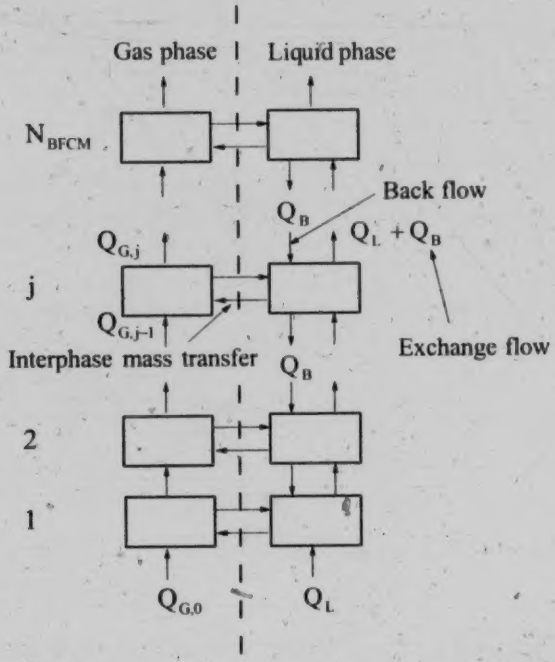

Figure 3.1 BFCM schematic for co-current flow conditions in bubble columns.

For the gas phase to flow in a regime close to the plug flow conditions, the number of the completely mixed cells (N_{BFCM}) has to be equal to or greater than 10. By employing the mass balance with respect to the inert tracer around cell number 1, the mathematical relationship for the TBFCM is as follows:

$$Q_L C_0 + Q_B C_2 - (Q_L + Q_B) C_1 = \frac{dC_1}{dt} V_c \qquad [3.5]$$

where: V_c is the cell volume and is equal to the total volume of the bubble column (V) divided by the number of cells (N_{BFCM}). Dividing Equation 3.5 by $V_c C_0^*$ where:

$$C_0^* = \frac{M}{V_c} = \frac{M}{V / N_{BFCM}} \qquad [3.6]$$

and M = volume of inert tracer, substituting in the resultant equation for:

$$r = \frac{Q_B}{Q_L} \qquad [3.7]$$

where r is the back flow ratio, and rearranging, one can obtain:

$$\frac{dY_1}{dt} = -\frac{1+r}{\tau / N_{BFCM}} Y_1 + \frac{r}{\tau / N_{BFCM}} Y_2 \qquad [3.8]$$

where:

$$Y_j = \frac{C_j}{C_0^*} = \frac{VC_j}{MN_{BFCM}} = \frac{E_{\theta,j}}{N_{BFCM}} \qquad [3.9]$$

Following the same procedure used to derive Equation 3.8, one can obtain the transient BFCM equations for the cells from j = 2 to j = N_{BFCM} as follows. For $2 \le j \le N_{BFCM}-1$:

$$\frac{dY_j}{dt} = \frac{1+r}{\tau / N_{BFCM}} Y_{j-1} - \frac{1+2r}{\tau / N_{BFCM}} Y_j + \frac{r}{\tau / N_{BFCM}} Y_{j+1} \qquad [3.10]$$

and for j = N_{BFCM}:

$$\frac{dY_{N_{BFCM}}}{dt} = \frac{1+r}{\tau / N_{BFCM}} Y_{N_{BFCM}-1} - \frac{1+r}{\tau / N_{BFCM}} Y_{N_{BFCM}} \qquad [3.11]$$

BFCM and ADM describe the backmixing of the liquid phase using different mixing parameters (Pe_L, N_{BFCM}, and r). Those parameters are interrelated by the following relationship (Mecklenburgh and Hartland, 1975):

$$r = \frac{N_{BFCM}}{Pe_L} - 0.5 = \frac{D_L N_{BFCM}}{u_L L} - 0.5 \qquad [3.12]$$

Equations 3.8, 3.10, and 3.11 are N_{BFCM} first-order ordinary differential equations in N_{BFCM} unknowns (Y_j's). Those differential equations were solved numerically by applying an explicit technique for time discretisation to transform them into a system of linear algebraic equations which were then solved using a simple spreadsheet program. The initial conditions for that system of equations (for pulse-input tracer tests) are as follows:

at $t = 0$:
$Y_1 = 1$
$Y_j = 0$ for $2 \le j \le N_{BFCM}$

3.3.2 Steady-State BFCM

The assumptions that govern the application of the BFCM for modeling two-phase flows in ozone bubble columns are the same as the assumptions, 1 through 4, used to derive the TBFCM equations. In addition to those assumptions, further assumptions are needed. Those assumptions include: (1) ozone mass transfer process is limited by the mass rate in the liquid phase; (2) enhancement factor of the mass transfer due to the occurrence of chemical reactions was assumed to be 1.0 as the absorption of ozone in water could be considered to occur in the slow-reaction kinetics regime; (3) steady-state isothermal operation; (4) Henry's law applies; (5) gas-phase constituents, other than ozone, are assumed to be inerts; (6) local mass transfer coefficient (k_L) is constant along the column height; (7) owing to the hydrostatic head, total pressure varies linearly with the column depth; (8) superficial gas velocity is variable due to ozone absorption, ozone gas depletion, and hydrostatic pressure decrease along the column height; and (9) ozone auto-decomposition in the liquid phase, is described by a pseudo-first-order rate expression and is negligible in the gas phase.

For a co-current flow mode and by referring to Figure 1, the basic mass balance with respect to the dissolved ozone within each cell leads to the following equations.

For $j = 1$:

$$\begin{aligned} & Q_L C_{L,0} + Q_B C_{L,2} + k_L a\left(C^*_{L,1} - C_{L,1}\right)\frac{V}{N_{BFCM}} \\ & - k_w C_{L,1}\varepsilon_L \frac{V}{N_{BFCM}} - \left(Q_L + Q_B\right)C_{L,1} = 0 \end{aligned} \qquad [3.13]$$

For $2 \leq j \leq N_{BFCM} - 1$:

$$\begin{aligned} & \left(Q_L + Q_B\right)C_{L,j-1} + Q_B C_{L,j+1} + k_L a\left(C^*_{L,j} - C_{L,j}\right)\frac{V}{N_{BFCM}} \\ & - k_w C_{L,j}\varepsilon_L \frac{V}{N_{BFCM}} - \left(Q_L + 2Q_B\right)C_{L,j} = 0 \end{aligned} \qquad [3.14]$$

For j = N_{BFCM}:

$$(Q_L + Q_B)C_{L,N_{BFCM}-1} + k_L a\left(C^{*}_{L,N_{BFCM}} - C_{L,N_{BFCM}}\right)\frac{V}{N_{BFCM}} - k_w C_{L,N_{BFCM}} \varepsilon_L \frac{V}{N_{BFCM}} - (Q_L + Q_B)C_{L,N_{BFCM}} = 0 \qquad [3.15]$$

For cell number j, and for the gaseous ozone and total gas respectively, the basic mass balance leads to the following equations:

$$Q_{G,j-1}C_{G,j-1} - Q_{G,j}C_{G,j} - k_L a\left(C^{*}_{L,j} - C_{L,j}\right)\frac{V}{N_{BFCM}} = 0 \qquad [3.16]$$

$$Q_{G,j-1}C_{T,j-1} - Q_{G,j}C_{T,j} - k_L a\left(C^{*}_{L,j} - C_{L,j}\right)\frac{V}{N_{BFCM}} = 0 \qquad [3.17]$$

The hydrostatic head P_j in the column decreases linearly with the depth l assuming that the change in the liquid hold-up is negligible, therefore:

$$P_j = P_T + \rho g \varepsilon_L \left(1 - \frac{j - 0.5}{N_{BFCM}}\right) L = P_0\left[1 + \alpha(j - 0.5)\right] \qquad [3.18]$$

where α is defined by Equation 3.22. The equilibrium concentration ($C^{*}_{L,j}$) is given by:

$$C^{*}_{L,j} = \frac{P_j}{H} y_j \qquad [3.19]$$

The gaseous ozone concentration ($C_{G,j}$) and the total gas concentration ($C_{T,j}$) respectively, are given by:

$$C_{G,j} = \frac{P_j y_j}{RT} \qquad [3.20]$$

$$C_{T,j} = \frac{P_j}{RT} \qquad [3.21]$$

Introducing the following dimensionless terms into Equations 3.13 to 3.17:

$$\alpha = \frac{-\rho g \varepsilon_L L}{N_{BFCM} P_0} \qquad [3.22]$$

$$r = \frac{Q_B}{Q_L} \qquad [3.23]$$

$$St_L = \frac{k_L a L}{N_{BFCM} u_L} \qquad [3.24]$$

$$St_G = \frac{k_L a L}{N_{BFCM} u_{G,0}} \frac{RT}{H} \qquad [3.25]$$

$$D_a = \frac{k_w \varepsilon_L L}{N_{BFCM} u_L} \qquad [3.26]$$

$$X_j = \frac{C_{L,j}}{C^*_{L,0}} \qquad [3.27]$$

$$Y_j = \frac{y_j}{y_0} \qquad [3.28]$$

$$q_{G,j} = \frac{Q_{G,j}}{Q_{G,0}} \qquad [3.29]$$

and rearranging the resultant equations, yields the steady-state BFCM equations. For dissolved ozone and j = 1:

$$X_0 - (1 + r + D_a + St_L)X_1 + rX_2 + St_L\left(1 + \frac{\alpha}{2}\right)Y_1 = 0 \qquad [3.30]$$

For $2 \le j \le N_{BFCM} - 1$:

$$(1 + r)X_{j-1} - (1 + 2r + D_a + St_L)X_j + rX_{j+1} + St_L[1 + \alpha(j - 0.5)]Y_j = 0 \qquad [3.31]$$

For $j = N_{BFCM}$:

$$(1 + r)X_{N_{BFCM}-1} - (1 + r + D_a + St_L)X_{N_{BFCM}} + St_L[1 + \alpha(N_{BFCM} - 0.5)]Y_{N_{BFCM}} = 0 \qquad [3.32]$$

For gaseous ozone and cell number j:

$$(1 + \alpha(j - 1.5))q_{G,j-1}Y_{j-1} - (1 + \alpha(j - 0.5))q_{G,j}Y_j - St_G[(1 + \alpha(j - 0.5))Y_j - X_j] = 0 \qquad [3.33]$$

For total gas and cell number j:

$$(1 + \alpha(j - 1.5))q_{G,j-1} - (1 + \alpha(j - 0.5))q_{G,j} - St_G y_0[(1 + \alpha(j - 0.5))Y_j - X_j] = 0 \qquad [3.34]$$

Based on the definitions of variables (Equations 27 to 29), the zero-index variables are:

$$X_0 = \frac{C_{L,0}}{C^*_{L,0}} \qquad [3.35]$$

$$Y_0 = 1 \qquad [3.36]$$

$$q_{G,0} = 1 \qquad [3.37]$$

A similar approach could be used to derive the equations for the counter-current flow mode. Equations 3.30 to 3.34 represent the steady-state BFCM for two-phase ozone absorption in surface waters systems and can be used to predict the performance of bubble columns as long as the operating parameters (Pe_L, St_L, St_G, D_a, α, and y_0) are specified.

3.4 RESULTS AND DISCUSSION

3.4.1 Transient BFCM

The system of Equations 3.8, 3.10, and 3.11 was solved, for $N_{BFCM} = 10$ and Pe_L ranging from 1 to 20, to examine the effect of Pe_L or r on the theoretical RTD. As shown in Figure 3.2, as Pe_L increases, the RTD at the bottom port narrows as the liquid phase flow conditions are approaching plug flow. The effect of Pe_L on RTD at the top sampling port is shown in Figure 3.3. As Pe_L increases, the RTD narrows and becomes more symmetrical and the peak increases as well, suggesting that the liquid flow conditions are approaching plug flow.

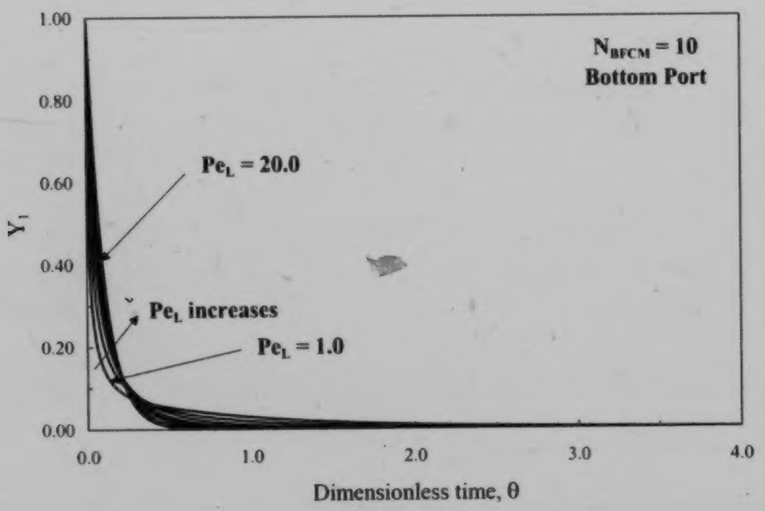

Figure 3.2 Theoretical RTD's for $N_{BFCM} = 10$ at the bottom sampling port.

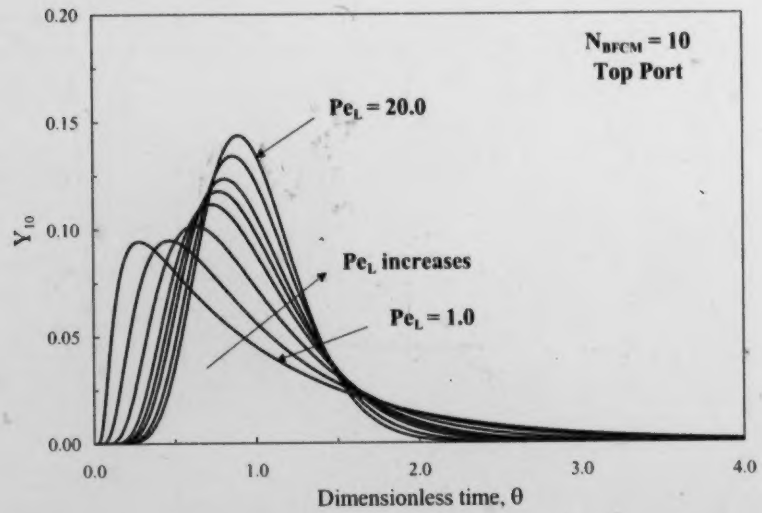

Figure 3.3 Theoretical RTD's for $N_{BFCM} = 10$ at the top sampling port.

3.4.2 Steady-state BFCM

The predictions of the steady-state BFCM were tested using the pilot-scale experimental data of Zhou (1995). The bubble column used in the experiments was a cylindrical glass column with an inside diameter of 100 mm and a height of 2,000 mm. The water depth was kept constant at 1,750 mm. The gas sparger used was a 25 mm spherical fused crystalline aluminum stone. The water samples were withdrawn from six bell-shaped sampling taps that were installed at equal intervals along the column height. The operating conditions for the co-current and counter-current flow modes are shown in Tables 3.1 and 3.2 respectively.

Table 3.1 Operating conditions for the co-current flow mode.

Case #	N_{BFCM}	Pe_L	r	α	St_L	St_G	D_a	y_0	$C_{L,0}^*$ (mgL^{-1})
DW4	10	34.48	-0.21	-0.014	0.024	0.125	0.006	0.013	7.20
DW5	10	17.86	0.06	-0.014	0.176	0.126	0.006	0.002	0.92
DW9	10	4.63	1.66	-0.014	0.024	0.008	0.014	0.002	0.88

Table 3.2 Operating conditions for the counter-current flow mode.

Case #	N_{BFCM}	Pe_L	r	α	St_L	St_G	D_a	y_0	$C_{L,0}^*$ (mgL^{-1})
DW17	10	10.53	0.45	-0.014	0.056	0.112	0.014	0.010	5.56
DW18	10	5.35	1.37	-0.014	0.379	0.130	0.014	0.002	0.92

The number of completely mixed cells (N_{BFCM}) was set equal to 10. A pseudo-first-order specific ozone utilization rate constant was assumed to equal 4.7 x 10^{-4} s^{-1} for deionized water based on the measurements of Zhou (1995). Steady-state BFCM equations (Equations 3.30 to 3.34) were solved numerically using Newton Raphson technique by utilizing the TKSOLVER™ software. The program executed until a user-specified comparison tolerance of 10^{-6} was satisfied. The program execution time was less than 1 s using a 366 MHz processor.

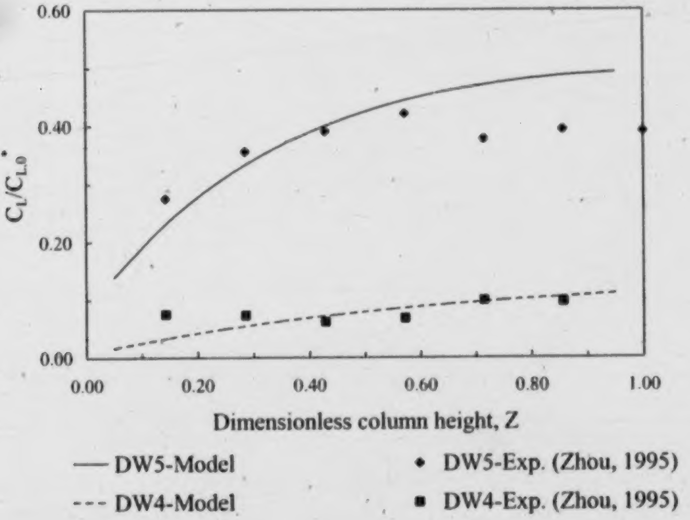

Figure 3.4 Steady-state BFCM testing for co-current flow mode.

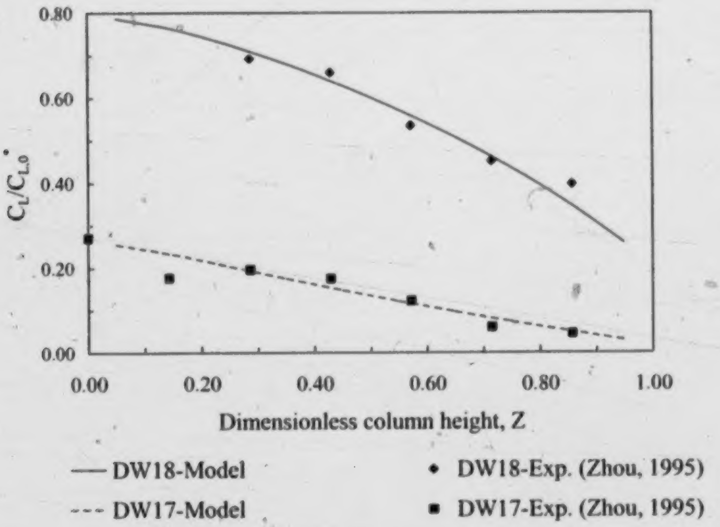

Figure 3.5 Steady-state BFCM testing for counter-current flow mode.

Figures 3.4 and 3.5 illustrate the applicability of the steady-state BFCM to describe the performance of an ozone bubble column that utilizes diffusers as the gas spargers in the co and counter-current flow modes, respectively. As shown, there was good agreement between the experimental dissolved ozone profiles and the predicted ozone profiles, except for few data points, where there was small deviation between the measured and the predicted dissolved ozone concentrations.

3.5 CONCLUSIONS

The steady-state BFCM has proven to provide good predictions of the performance of a pilot-scale fine-diffuser ozone bubble column. The model predictions should be further tested for different designs and scales of ozone bubble columns and under different operating conditions. Also, the model should be further expanded to account for variable mass transfer coefficient along the height bubble column for special bubble column designs where the mass transfer process is enhanced near the entrance of the contactor rather than along the entire column height.

3.6 REFERENCES

1. Alvarez-Cuenca, M. and M.A. Nerenberg, "Oxygen Mass Transfer in Bubble Columns Working at Large Gas and Liquid Flow Rates", AIChE J. 27(1): 66-73 (1981).
2. Alvarez-Cuenca, M., C.G.J. Baker, and M.A. Bergougnou, "Oxygen Mass Transfer in Bubble Columns", Chem. Eng. Sci. 35: 1121-1127 (1980).
3. Beltrán, F.J., J.F. García-Araya, and J.M. Encinar, "Henry and Mass Transfer Coefficients in the Ozonation of Wastewaters", Ozone Sci. & Eng. 19: 281-296 (1997).
4. Chang, B.-J. and E.S.K. Chian, "A Model Study of Ozone-Sparged Vessels for the Removal of Organics from Water", Wat. Res. 15: 929-936 (1981).
5. Danckwerts, P.V., *Gas-Liquid Reactions* (NY, USA: McGraw-Hill, Inc., 1970).
6. Hoigné, J., "Mechanisms, Rates and Selectivities of Oxidants of Organic Compounds Initiated by Ozonation in Water", *Handbook of Ozone Technology and Applications* (MI, USA: Ann Arbor Science Publishers, 1982).
7. Hull, C.S., P.C. Singer, K. Saravanaan, and C.T. Miller, "Ozone Mass Transfer and Reaction: Completely Mixed Systems", *Proc. of the Annual AWWA Conf.: Water Quality*, Vancouver, BC, Canada, 1992.
8. Johnson, P.N. and R.A. Davis, "Diffusivity of Ozone in Water", J. Chem. Eng. Data 41: 1485-1487 (1996).
9. Laplanche, A., N. Le Sauze, G. Martin, and B. Langlais, "Simulation of Ozone Transfer in Water: Comparison with a Pilot Unit", Ozone Sci. & Eng. 13(5): 13, 535-558 (1991).
10. Levenspiel, O., *Chemical Reaction Engineering, 2nd ed.* (NY, USA: John Wiley and Sons, Inc., 1972).
11. Lev, O. and S. Regli, "Evaluation of Ozone Disinfection Systems: Characteristic Contact Time T", J. Environ. Eng., ASCE 118(2): 268-285 (1992).
12. Mecklenburgh, J.C. and S. Hartland, *The Theory of Backmixing*, (New York, NY, USA: John Wiley and Sons, Inc., 1975), pp. 1-32.

13. Oke, N.J., D.W. Smith, and H. Zhou, "An Empirical Analysis of Ozone Decay Kinetics in Natural Waters", Ozone Sci. & Eng. 20: 361-379 (1998).
14. TKSOLVER^{TM}, Release 3.32, Universal Technical Systems, Inc., IL, USA (1997).
15. Yurteri, C. and M.D. Gurol, "Ozone Consumption in Natural Waters: Effects of Background Organic Matter, pH and Carbonate Species", Ozone Sci. & Eng. 10: 277-290 (1988).
16. Zhou, H., *Investigation of Ozone Disinfection Kinetics and Contactor Performance Modeling: Ph.D. Thesis* (Edmonton, AB, Canada: University of Alberta, 1995).
17. Zhou, H., D.W. Smith, and S.J. Stanley, "Modeling of Dissolved Ozone Concentration Profiles in Bubble Columns", J. Environ. Eng., ASCE 120(4): 821-840 (1994).

CHAPTER 4. TWO-PHASE NON-ISOBARIC AXIAL DISPERSION MODELS FOR MODELING THE OZONATION PROCESS DYNAMICS–I. MODELS DEVELOPMENT

4.1 INTRODUCTION

4.1.1 Ozonation Process Dynamics

Ozonation of water and wastewater has been focused on, over the past two decades, as an advanced oxidation process (AOP) alternative for water and wastewater treatment. During ozonation of water and wastewater, it is important to quantify the dissolved and gaseous ozone concentrations in order to evaluate the effectiveness of the ozonation process. Regarding wastewater ozone treatment applications, the experimental data of Zhou and Smith (2000, 1997) showed that the ozonation of Kraft pulp mill effluents is a dynamic process. As a result, the enhanced overall mass transfer coefficient (Ek_La), the induced enhancement factor (E) of the fast or instantaneous chemical reactions, the reaction rate constant (k_w) between ozone and the liquid-phase impurities, mainly organic compounds, were dependent on the amount of the utilized ozone. Also, the reduction efficiencies of color, AOX (absorbable organic halides), TOC (total organic carbon), and COD (chemical oxygen demand) varied over the course of ozonation. As the amount of the utilized ozone increases, Ek_La and k_w will decrease gradually after most of the highly reactive organic compounds are depleted. As the ozonation treatment proceeds, the color and AOX reduction efficiencies will decline gradually (Zhou and Smith, (2000, 1997).

4.1.2 Bubble Column Parameters

It is becoming more important to develop more efficient, accurate, and reliable models that can be used for describing the performance of ozone contactors to reduce the operating costs and to insure that the treatment objectives are met. By applying the appropriate design models, optimized designs and operating conditions of both the ozone contactors and the ozone off-gas destruction facilities can be achieved. The number of process variables, that affect the performance of ozone contactors, is large and obtaining accurate estimates of those variables becomes a difficult task, especially, in situations where ozonation is carried out in complex chemical systems such as Kraft pulp mill effluents. Those process variables, that are dependent on the ozonation process operating conditions, can be estimated by applying simple mathematical models. Some of the process variables are influenced by the ozone contactor configuration, the type of the gas sparging technique, and the chemical composition of the treated liquid phase (Deckwer, 1976). Those variables include: the gas and liquid hold-ups; the enhanced overall mass transfer coefficient; the enhancement factor; the gas bubbles' specific interfacial area; and the backmixing coefficient.

4.1.3 Dispersion Models for Two-Phase Flows

It is well known that in non-ideal flow conditions that exist in bubble columns, applying inappropriate design models can lead to significant lowering of the treatment efficiency of the bubble column. A large number of those models were based on one of the following two liquid-phase flow regimes' assumptions: (1) complete mixing flow regime; or (2) ideal plug flow regime. Although, the actual flow pattern in bubble columns is usually closer to the completely mixed flow regime rather than the plug flow regime (Zhou, 1995).

The objective of this chapter was to present more accurate two-phase axial dispersion models (2P-ADM's) for describing the performance of ozone bubble columns. Those dispersion models take into consideration the opposite effects of shrinkage of the gas phase caused by ozone gas absorption and ozone auto-decomposition. Those models also consider the gas-phase expansion caused by the reduced hydrostatic head. As a result, the superficial gas velocity will be considered to vary along the column height and ozone bubble columns will be dealt with as non-isobaric two-phase systems.

In bubble columns with small aspect (L/D) ratios, the order of magnitude of the gas phase dispersion coefficient (D_G) can be comparable to that of the liquid phase dispersion coefficient (D_L) (Deckwer, 1976). Therefore, during the development of the two-phase axial dispersion models (2P-ADM's), two conditions were considered: $D_G = D_L/10$, and $D_G = D_L$. The low-end of the gas-phase dispersion coefficient represents situations where gas bubbles are relatively large and due to their high buoyancy, they can rise inside the columns with high velocities but still those bubbles will be partially backmixed. Meanwhile, the high gas-phase dispersion coefficient represents situations where gas bubbles are relatively small and their buoyancy is relatively small. As a result, the gas phase can be assumed to be backmixed to a large extent and since the small bubbles are recirculated along with the liquid phase recirculation, it is assumed that their backmixing coefficient can be equal to that of the liquid phase (Shetty *et al.*, 1992). In the other type of the dispersion models, the gas phase is assumed to follow an ideal plug flow regime, and hence, the gas phase dispersion will be neglected in the development the model equations, i.e., $D_G = 0$. This condition can be reasonably valid in bubble columns with large aspect ratios.

The most computationally efficient mechanistic models are those, for which, closed-form analytical solutions can be obtained. Unfortunately, for adequate and accurate description of the performance of bubble columns, dispersion models are needed and the analytical solutions of the equations representing those models are not available due to their complex construction. Those models are represented by non-linear differential equations that have to be solved simultaneously via numerical techniques.

4.2 PROCESSES FUNDAMENTALS

4.2.1 Slow-Chemical-Reaction-Kinetics-Regime Systems

During the ozonation of surface waters, the chemical reactions between the dissolved ozone and the organic and inorganic constituents in the liquid phase are considered to be in the slow-reaction-kinetics regime (Zhou *et al.*, 1994; Gamal El-Din and Smith, 2000). In order to describe the backmixing in the liquid phase, a diffusion-like process is assumed and superimposed on plug flow (Levenspiel, 1972). An empirical Fick's law is applied by replacing the molecular diffusion coefficient by the axial dispersion coefficient (D_L) as the mixing parameter in which the effects of the shear dispersion, molecular and eddy diffusivities are lumped together:

$$\text{Diffusive liquid-phase mass flux} = -D_L \frac{\partial C_L}{\partial \ell} \qquad [4.1]$$

where: C_L = dissolved ozone concentration (mgL^{-1}) and D_L = liquid-phase axial dispersion coefficient (m^2s^{-1}). After a comprehensive review of the literature, it was found that the dispersion models that are applied to describe the performance of ozone bubble columns are based on the assumption that the gas phase follows an ideal plug flow regime and therefore, the gas phase backmixing was neglected. Development of new theoretically-based models such as the axial dispersion models that account for the backmixing in the liquid and gas phases simultaneously can lead to a great progress in the area of the design of ozone bubble columns. Deckwer (1976) suggested that the performance of bubble columns could be affected by the gas phase dispersion in columns with diameters greater than 500 mm. Although in columns with small diameters the assumption of the gas phase being in an ideal plug flow regime can be valid (Wachi and Morikawa, 1987), gas phase dispersion can be a significant factor in the ozonation process scale-up. In homogeneous bubble flow regimes, the bubble sizes are relatively small and their buoyancy is low and therefore, they are assumed to be backmixed (Shetty *et al.*, 1992). Gas phase backmixing can be measured experimentally using several techniques such as gas disengaging technique (GDT) or thermal conductivity detectors (TCD), etc. In those techniques, gases of low solubility such as helium are used as the tracer gases. There are several models, available in the literature, that can be used to estimate the gas phase backmixing (Towell and Ackermann 1972; Mangartz and Pilhofer, 1981; Wachi and Nojima, 1990). In most of those models, the gas phase backmixing is mainly dependent on the superficial gas velocity and the column diameter. In order to describe the backmixing in the gas phase, a diffusion-like process is assumed and superimposed on plug flow and Fick's law is applied by replacing the molecular diffusion coefficient by the axial dispersion coefficient (D_G) as the mixing parameter:

$$\text{Diffusive gas-phase mass flux} = -D_G \frac{\partial C_G}{\partial \ell} \qquad [4.2]$$

where: C_G = gaseous ozone concentration (mgL^{-1}) and D_G = gas-phase axial dispersion coefficient (m^2s^{-1}).

The overall ozone auto-decomposition process was represented by the modified pseudo-first-order rate expression as recommended by Oke. *et al.* (1998). The two-film model was applied to describe the ozone gas absorption in water. Assuming that no chemical reactions, between the dissolved gas and any constituents present in the liquid phase, occur during the mass transfer process, the gas-absorption rate (ψ) is defined as:

$$\psi = k_L a\left(C_L^* - C_L\right) \qquad [4.3]$$

where: ψ = gas-absorption rate ($mgL^{-1}s^{-1}$), k_L = local liquid mass transfer coefficient (ms^{-1}), a = gas bubbles' specific interfacial area (m^{-1}), C_L^* = concentration of the dissolved ozone in equilibrium with the bulk ozone gas (mgL^{-1}), and C_L = concentration of the dissolved ozone in the bulk liquid (mgL^{-1}).

4.2.2 Fast-Chemical-Reaction-Kinetics-Regime Systems

The backmixing in the liquid and gas phases are also represented by Equations 4.1 and 4.2, respectively. Chemical reactions occur during the ozonation of wastewater. In such applications, the dimensionless squared Hatta number ($H_a^2 = M$) is often applied to compare between the amount of dissolved gas that reacts at the gas-liquid interface or in the liquid film near the interface and the amount of dissolved gas that reaches the bulk liquid in an unreacted state:

$$H_a^2 = E^2 = M = \frac{D_{O_3} k_w}{k_L^2} \qquad [4.4]$$

where: $H_a = E = \sqrt{M}$ = dimensionless Hatta number, k_L = local mass transfer coefficient (ms^{-1}), D_{O_3} = molecular diffusivity of ozone gas in water (m^2s^{-1}), and k_w = specific ozone utilization rate constant (s^{-1}). For pseudo-first-order irreversible reactions, the location of those reactions that take place during the gas absorption process could be classified into two categories (Kramers and Westertrep, 1963; Kaštánek *et al.*, 1993). Reactions would take place in the bulk of the liquid or at the gas-liquid interface and/or in the liquid film near the interface at $H_a < 0.03$ and $H_a > 5.00$, respectively (Kramers and Westertrep, 1963; Kaštánek *et al.*, 1993). Although, generally for bubble columns it can also be assumed that at that at $H_a > 3.00$, reactions would still be fast enough to occur predominantly at the gas-liquid interface and/or in the liquid film near the interface (Kaštánek *et al.*, 1993). Therefore, reactions would simultaneously take place in both regions at at $0.03 < H_a < 3.00$. Equation 4.4 is only applicable in situations where two conditions have to be satisfied: (1) $\sqrt{M} >> 1$; and (2) fast or instantaneous irreversible first-order reactions with no bulk liquid concentration where the driving force for the mass transfer process will be maximized (Danckwerts, 1970). As a result, Equation 4.3 becomes:

$$\psi = Ek_L aC_L^* \qquad [4.5]$$

where: Ek_La = enhanced overall mass transfer coefficient (s^{-1}). Zhou and Smith (1999) proposed that for wastewater ozonation, both the ozone auto-decomposition and its reactions with the organic and inorganic constituents in wastewater could be lumped together in a first-order rate constant (k_w). Danckwerts (1970) proposed the following equation for the conditions when $M > 0$ and $C_L > 0$:

$$\psi = k_L a\sqrt{1+M}\left(C_L^* - \frac{C_L}{1+M}\right) \qquad [4.6]$$

When $M >> 1$ and C_L approaches zero (i.e., $C_L \cong 0$), Equation 4.6 reduces to Equation 4.5. The effects of chemical reactions on the local mass transfer coefficient for an irreversible first-order reaction could be neglected and the gas absorption could be dealt with as pure physical absorption when M approaches zero (Danckwerts, 1970). Therefore, this assumption is valid when:

$$H_a^2 = E^2 = M = \frac{D_{O_3} k_w}{k_L^2} << 1 \qquad [4.7]$$

k_w was reported to be 4.7 x 10^{-4} s^{-1} for the deionized water tested by Zhou (1995). Yurteri and Gurol (1988) reported that k_w was in the order of 2.8 x 10^{-3} s^{-1} for the tested raw surface water. The diffusivity of ozone in water was determined by the Wilke-Chang formula to be 1.74 x 10^{-9} m^2s^{-1} (at 20 °C) which is comparable to the value of 1.71 x 10^{-9} m^2s^{-1} obtained using the equation recommended by Johnson and Davis (1996). k_L was reported to be in the order of 3.1 x 10^{-4} ms^{-1} for clean water and in the order of 1.9 x 10^{-4} ms^{-1} for water containing organic substances (Beltrán *et al.*, 1997). Substituting for these typical values of D, k_w, and k_L into Equation 4.4 yields squared-Hatta numbers of 8.5 x 10^{-6} and 1.4 x 10^{-4} for the deionized and the surface water, respectively. Based on these small Hatta numbers, it can be concluded that the chemical reactions that occur during the course of clean or surface water ozonation has negligible effect on the local mass transfer coefficient and hence, Equation 4.3 will be applied for ozone absorption without any modification.

4.3 DEVELOPMENT OF THE TWO-PHASE AXIAL DISPERSION MODEL (2P-ADM) EQUATIONS

When modeling a two-phase flow, the assumptions that govern the two-phase axial dispersion model (2P-ADM) are: (1) backmixing (i.e., dispersion) occurs in the liquid and gas phases; (2) ozone bubble column is operated at constant liquid and gas flowrates; (3) gas hold-up and gas bubbles' specific interfacial area are constant along the column height; (4) ozone mass transfer resistance for the ozone absorption is confined to the liquid side alone; (5) the enhancement factor (E) of the mass transfer due to the occurrence of chemical reactions was assumed to be 1 (i.e., M = 0) as the absorption of ozone in water treatment could be considered in the slow-reaction-kinetics regime and for wastewater the fast-reaction regime was assumed to prevail and the enhancement factor was assumed to be higher than 1(i.e., M > 0); (6) steady-state isothermal operation for the liquid and gas phases; (7) Henry's law applies; (8) other air constituents are assumed to be inert gases; (9) local mass transfer coefficient (k_L) is constant along the column height; (10) owing to the hydrostatic head, the total pressure (P) varies linearly with the column height; (11) superficial gas velocity is variable due to ozone gas absorption and depletion, and hydrostatic pressure decrease along the column height; and (12) overall ozone auto-decomposition rate is assumed to follow a pseudo-first-order expression in the liquid phase, whereas negligible in the gas phase.

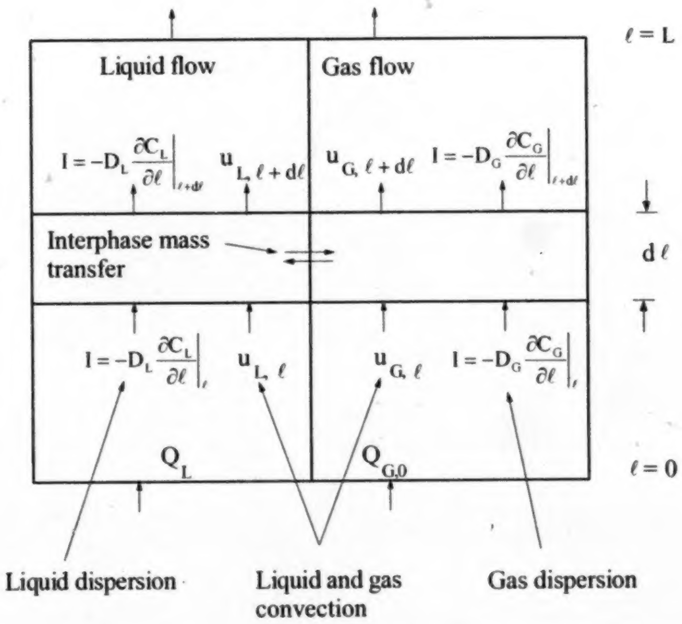
$\ell = L$
Liquid flow
Gas flow
$I = -D_L \frac{\partial C_L}{\partial \ell}\Big|_{\ell+d\ell}$
$u_{L,\ell+d\ell}$
$u_{G,\ell+d\ell}$
$I = -D_G \frac{\partial C_G}{\partial \ell}\Big|_{\ell+d\ell}$
Interphase mass transfer
$d\ell$
$I = -D_L \frac{\partial C_L}{\partial \ell}\Big|_{\ell}$
$u_{L,\ell}$
$u_{G,\ell}$
$I = -D_G \frac{\partial C_G}{\partial \ell}\Big|_{\ell}$
Q_L
$Q_{G,0}$
$\ell = 0$
Liquid dispersion
Liquid and gas convection
Gas dispersion

Figure 4.1 Schematic representation of the co-current axial dispersion model.

4.3.1 Considering the Gas-Phase Dispersion

4.3.1.1 Wastewater Treatment Conditions

Considering the control volume shown in Figure 4.1 and conducting mass balance of the liquid and gas phases for wastewater treatment and steady-state conditions, yields:

$$\frac{d^2C_{L,\ell}}{d\ell^2}D_L\varepsilon_L + a'u_L\frac{dC_{L,\ell}}{d\ell} + k_La\sqrt{1+M}(C^*_{L,\ell} - \frac{C^*_{L,\ell}}{1+M}) - k_wC_{L,\ell}\varepsilon_L = 0 \qquad [4.8]$$

$$\frac{d^2C_{G,\ell}}{d\ell^2}D_G\varepsilon_G - \frac{d(u_{G,\ell}C_{G,\ell})}{d\ell} - k_La\sqrt{1+M}(C^*_{L,\ell} - \frac{C_{L,\ell}}{1+M}) = 0 \qquad [4.9]$$

where: a' is an identifier of the liquid phase flow direction. $a' = +1$ for counter-current flow conditions and $a' = -1$ for co-current flow conditions. Equations 4.8 and 4.9 are the steady-state mass balance equations for the liquid and gas phases, respectively. The relationships of $P_\ell, P_0, C^*_{L,\ell}$, and $C^*_{L,0}$ are as follows:

$$P_\ell = P_T + \rho g\varepsilon_L(L-\ell) \qquad [4.10]$$

$$P_0 = P_T + \rho g\varepsilon_L L \qquad [4.11]$$

$$C^*_{L,\ell} = \frac{P_T + \rho g\varepsilon_L(L-\ell)}{H}y_\ell \qquad [4.12]$$

$$C^*_{L,0} = \frac{P_T + \rho\varepsilon_L L}{H}y_0 \qquad [4.13]$$

From Equations 4.10 and 4.11, it can be seen that the hydrostatic head pressure (P) is assumed to decreases linearly with the column depth (ℓ). In order to account for the dependency of the superficial gas velocity ($u_{G,\ell}$) on the column depth, a mass balance of the inert gas phase constituents is considered. Since the concentration of ozone in the gas phase is usually small, the total amount of the gas will not be decreased significantly along the column height. Thus, the mass balance of the inert gas phase constituents yields:

$$\frac{d^2C_{n,\ell}}{d\ell^2}D_G\varepsilon_G - \frac{d(u_{G,\ell}C_{n,\ell})}{d\ell} = 0 \qquad [4.14]$$

where: $C_{n,\ell}$ = concentration of the inert constituents in the gas phase and it can be described as follows by:

$$C_{n,\ell} = \frac{n_{n,\ell}}{V} = \frac{p_{n,\ell}}{RT} = \frac{P_\ell(1-y_\ell)}{RT} \qquad [4.15]$$

Therefore, substituting for Equation 4.15 into Equation 4.14 yields:

$$\frac{d^2}{d\ell^2}\left[\frac{P_\ell(1-y_\ell)}{RT}\right]D_G\varepsilon_G - \frac{d}{d\ell}\left[\frac{u_{G,\ell}P_\ell(1-y_\ell)}{RT}\right] = 0 \qquad [4.16]$$

The ozone gas concentration ($C_{G,\ell}$) is represented by:

$$C_{G,\ell} = \frac{n_{O_3,\ell}}{V} = \frac{P_T + \rho g \varepsilon_L (L-\ell)}{RT} y_\ell \qquad [4.17]$$

The partial pressure of the liquid vapour in the gas phase was assumed to be negligible with respect to the total pressure. Introducing the following dimensionless quantities:

$$Z = \frac{\ell}{L} \qquad [4.18]$$

$$\alpha = \frac{\rho g \varepsilon_L L}{P_T} \qquad [4.19]$$

$$\beta = 1 + \alpha \qquad [4.20]$$

$$Pe_L = \frac{u_L L}{D_L \varepsilon_L} \qquad [4.21]$$

$$Pe_G = \frac{u_{G,o} L}{D_G \varepsilon_G} \qquad [4.22]$$

$$St_L = \frac{k_L a L}{u_L} \qquad [4.23]$$

$$St_G = \frac{k_L a L}{u_{G,o}} \frac{RT}{H} \qquad [4.24]$$

$$D_a = \frac{k_w \varepsilon_L L}{u_L} \qquad [4.25]$$

$$X = \frac{C_{L,\ell}}{C^*_{L,0}} = \frac{C_{L,\ell}}{(P_T + \rho g \varepsilon_L L)} \frac{H}{y_o} = \frac{C_{L,\ell} H}{P_T (1+\alpha) y_o} \qquad [4.26]$$

$$Y = \frac{y_\ell}{y_o} \qquad [4.27]$$

and

$$U = \frac{u_{G,\ell}}{u_{G,o}} \qquad [4.28]$$

where: y_0 = inlet ozone molar fraction in the gas phase and $u_{G,0}$ = inlet superficial gas velocity at $\ell = 0$. Equations 4.18, 4.19, and 4.20 are substituted into Equations 4.10, 4.12, and 4.17. Then, the resultant equations and the dimensionless quantities are substituted into Equations 4.8, 4.9, and 4.16. Simplifying and rearranging the resultant equations gives:

$$\frac{1}{Pe_L} \frac{d^2X}{dZ^2} + a' \frac{dX}{dZ} + \frac{St_L \sqrt{1+M}}{\beta} (\beta - \alpha Z) Y - \left(\frac{St_L}{\sqrt{1+M}} + D_a \right) X = 0 \qquad [4.29]$$

$$\frac{1}{Pe_G}\frac{d^2Y}{dZ^2}-\left(\frac{2\alpha}{(\beta-\alpha Z)Pe_G}+U\right)\frac{dY}{dZ}=\sqrt{1+M}\,St_G Y(1-y_0Y) - \frac{St_G\beta}{\sqrt{1+M}(\beta-\alpha Z)}X(1-y_0Y) \qquad [4.30]$$

$$\frac{dU}{dZ}=\frac{\alpha}{(\beta-\alpha Z)}U-y_0\sqrt{1+M}\,St_G Y+\frac{y_0 St_G\beta}{\sqrt{1+M}(\beta-\alpha Z)}X \qquad [4.31]$$

Equations 4.29 and 4.30 represent the model equations of the ozone concentration in the liquid and gas phases, respectively. Equation 4.31 is a result of the mass balance of the gas-phase inert constituents and it represents the change in the superficial gas velocity with the column height. Equations 4.29, 4.30, and 4.31 are non-linear differential equations.

4.3.1.2 Boundary Conditions

No special measurements are required for the boundary conditions except for the boundary condition at the column inlet where the inlet liquid and gas phases ozone concentrations ($C_{L,inf}$ and y_0, respectively) have to be measured. The implementation of the boundary conditions follows logically from the physical basis of the model development approach. Assuming closed-closed boundary conditions and by referring to Figure 4.1, the mass balance of the ozone concentrations in the liquid and gas phases leads to the following boundary conditions. For the counter-current flow conditions ($a' = +1$):

$$\left.\frac{dX}{dZ}\right|_{Z=0}=0 \qquad [4.32]$$

$$Y\big|_{Z=0}=Y_0=1+\frac{1}{Pe_G}\left.\frac{dY}{dZ}\right|_{Z=0} \qquad [4.33]$$

$$X\big|_{Z=1} = X_1 = X_{inf} - \frac{1}{Pe_L}\frac{dX}{dZ}\bigg|_{Z=1} \qquad [4.34]$$

$$\frac{dY}{dZ}\bigg|_{Z=1} = 0 \qquad [4.35]$$

For the co-current flow conditions ($a' = -1$), the equations for the gas-phase boundary conditions are the same as those for the counter-current flow conditions. For the liquid phase, the equations, representing the boundary conditions, are:

$$X\big|_{Z=0} = X_0 = X_{inf} + \frac{1}{Pe_L}\frac{dX}{dZ}\bigg|_{Z=0} \qquad [4.36]$$

$$\frac{dX}{dZ}\bigg|_{Z=1} = 0 \qquad [4.37]$$

where:

$$X_{inf} = \frac{C_{L,inf}}{C^{*}_{L,0}} \qquad [4.38]$$

The gas phase superficial velocity is assumed to increase continuously from the bottom to the top of the column with no occurrence of velocity jump at any point along the column height. Therefore the boundary condition with respect to the superficial gas velocity at the bottom of the column for the counter and co-current flow conditions is:

$$U\big|_{Z=0} = U_0 = 1 \qquad [4.39]$$

4.3.2 Special Conditions of the Two-Phase Axial Dispersion Model (2P-ADM)

4.3.2.1 Consideration of the Gas-Phase Dispersion (Water Treatment Conditions)

During the ozonation of surface water, the enhancement factor (E) is assumed to equal 1 (i.e., M = 0). As a result, the model equations (Equations 4.29, 4.30, and 4.31) reduce to:

$$\frac{1}{Pe_L}\frac{d^2X}{dZ^2}+a'\frac{dX}{dZ}+\frac{St_L}{\beta}(\beta-\alpha Z)Y-\left(St_L+D_a\right)X=0 \qquad [4.40]$$

$$\frac{1}{Pe_G}\frac{d^2Y}{dZ^2}-\left(\frac{2\alpha}{(\beta-\alpha Z)Pe_G}+U\right)\frac{dY}{dZ}=St_G Y(1-y_0Y) - \frac{St_G\beta}{(\beta-\alpha Z)}X(1-y_0Y) \qquad [4.41]$$

$$\frac{dU}{dZ}=\frac{\alpha}{(\beta-\alpha Z)}U-y_0St_G\left(Y-\frac{\beta}{(\beta-\alpha Z)}X\right) \qquad [4.42]$$

Equations 4.40, 4.41, and 4.42 are non-linear differential equations and their boundary equations are also represented by Equations 4.32 to 4.39.

4.3.2.2 Neglecting the Gas-Phase Dispersion

Neglecting the gas-phase backmixing, i.e., assuming that the gas phase follows in an ideal plug flow regime, the model equations reduce to a system of two non-linear differential equations. Those equations can be developed logically from the physical basis of the model development approach as done previously for the model that accounts for the gas phase backmixing. As a result, we can obtain the following model equations for wastewater treatment conditions:

$$\frac{1}{Pe_L}\frac{d^2X}{dZ^2}+a'\frac{dX}{dZ}+\frac{St_L\sqrt{1+M}}{\beta}(\beta-\alpha Z)Y-\left(\frac{St_L}{\sqrt{1+M}}+D_a\right)X=0 \qquad [4.43]$$

$$\frac{dY}{dZ}+\frac{St_G}{\beta(1-y_0)}(1-y_0Y)^2\left(\sqrt{1+M}(\beta-\alpha Z)Y-\frac{\beta}{\sqrt{1+M}}X\right)=0 \qquad [4.44]$$

The liquid-phase boundary equations for this system of equations are the same as for the model equations that consider the gas-phase backmixing. For the gas phase and since no backmixing is considered in the gas phase, the ozone concentration in the gas phase is assumed to decrease continuously from the bottom to the top of the column with no occurrence of concentration jump at any point along the column height. Therefore, the boundary condition with respect to the gas phase ozone concentration at the bottom of the column for the counter and co-current flow conditions is:

$$Y\big|_{Z=0}=Y_0=1 \qquad [4.45]$$

In order to account for the dependency of the superficial gas velocity ($u_{G,\ell}$) on the column depth (ℓ), a mass balance of the inert gas phase constituents is considered. Thus, the mass balance of the inert gas phase constituents yields:

$$\frac{d\left(u_{G,\ell}C_{n,\ell}\right)}{d\ell}=0 \qquad [4.46]$$

Equation 4.46 is equivalent to:

$$u_{G,\ell}P_\ell\left(1-y_\ell\right)=u_{G,0}P_0\left(1-y_0\right) \qquad [4.47]$$

For the water treatment conditions, M is set equal to zero in Equations 4.43 and 4.44. With respect to the liquid and gas-phase boundary conditions, they are represented by the same equations used for the wastewater treatment conditions.

4.4 NUMERICAL SOLUTION TECHNIQUE

The proposed models are 1-D-type models that are represented by systems of 2 or 3 non-linear differential equations. Those equations are interrelated and have to be solved simultaneously. Closed-form analytical solutions are not available for such systems of equations. Therefore, the finite difference technique was applied for the spatial discretization of the model differential equations. The backward (or upwind) difference scheme was applied to transform a system of non-linear differential equations into a system of non-linear algebraic equations that can be solved numerically using any of the available numerical solving algorithms such as Newton Raphson technique. The upwind difference scheme is shown in Figure 4.2.

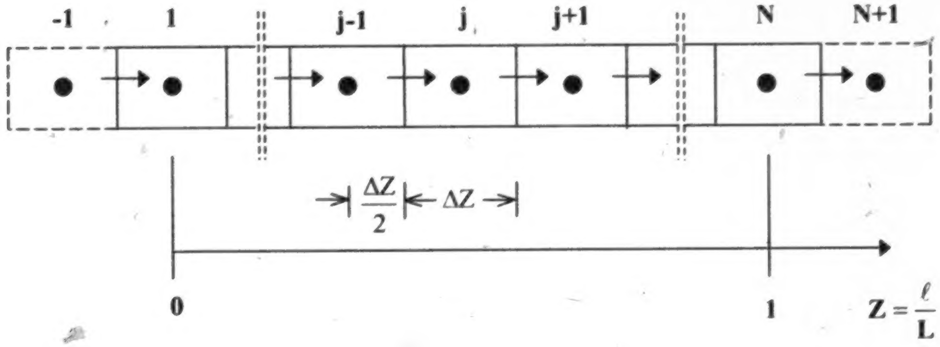

Figure 4.2 Computational upwind finite difference scheme.

In this scheme, the first and second-order derivatives, respectively, are defined as follows:

$$\left.\frac{dX}{dZ}\right|_j \cong \frac{X_j - X_{j-1}}{\Delta Z} \qquad [4.48]$$

$$\left.\frac{d^2X}{dZ^2}\right|_j \cong \frac{X_{j+1} - 2X_j + X_{j-1}}{\Delta Z^2} \qquad [4.49]$$

where: ΔZ = the numerical dimensionless spatial step. It should be noted that the first-order derivatives representing the boundary conditions at Z = 0 and 1 are defined using the centered-difference scheme since those boundary conditions are based on the dispersion term in the original mass balance equation. These first-order derivatives are defined as follows:

$$\left.\frac{dX}{dZ}\right|_{Z=0} \cong \frac{X_1 - X_{-1}}{2\Delta Z} \qquad [4.50]$$

$$\left.\frac{dX}{dZ}\right|_{Z=1} \cong \frac{X_{N+1} - X_{N-1}}{2\Delta Z} \qquad [4.51]$$

4.4.1 2P-ADM With Gas-Phase Dispersion (Wastewater Treatment Conditions)

In the finite difference technique, a number of elements (N) was assumed to represent the total column height (L) and each element has a dimensionless length of ($\Delta Z = 1/N$). As shown in Figure 4.2, two imaginary elements at j = –1 and j = N+1 were assumed for the numerical transformation of the differential boundary equations at the column boundaries. Referring to Figure 4.2 and applying the finite difference technique with the backward difference scheme, Equations 4.29, 4.30, and 4.31 were transformed into a system of three non-linear algebraic equations as follows:

$$X_{j+1} = A_j X_j - B_j X_{j-1} - C_j Y_j \qquad [4.52]$$

$$Y_{j+1} = D_j Y_j - E_j Y_{j-1} - F_j Y_j^2 - G_j X_j + H_j X_j Y_j - I_j U_j Y_{j-1} + I_j U_j Y_j \qquad [4.53]$$

$$U_j = J_j U_{j-1} - K_j Y_j + L_j X_j \qquad [4.53]$$

where:

$$A_j = \left[2 - a' \, Pe_L \Delta Z + Pe_L \, \Delta Z^2 \left(\frac{St_L}{\sqrt{1+M}} + D_a\right)\right] \qquad [4.54]$$

$$B_j = \left(1 - a' \, Pe_L \, \Delta Z\right) \qquad [4.55]$$

$$C_j = \left[\frac{\sqrt{1+M} St_L Pe_L \, \Delta Z^2}{\beta}(\beta - \alpha Z_j)\right] \qquad [4.56]$$

$$D_j = \left[2 + \frac{2\alpha \Delta Z}{(\beta - \alpha Z_j)} + Pe_G \, \Delta Z^2 St_G \sqrt{1+M}\right] \qquad [4.57]$$

$$E_j = \left[1 + \frac{2\alpha \Delta Z}{(\beta - \alpha Z_j)}\right] \qquad [4.58]$$

$$F_j = \left(Pe_G \, \Delta Z^2 y_0 St_G \sqrt{1+M}\right) \qquad [4.59]$$

$$G_j = \left[\frac{Pe_G \, \Delta Z^2 \beta St_G}{(\beta - \alpha Z_j)\sqrt{1+M}}\right] \qquad [4.60]$$

$$H_j = \left[\frac{Pe_G \, \Delta Z^2 y_0 \beta St_G}{(\beta - \alpha Z_j)\sqrt{1+M}}\right] \qquad [4.61]$$

$$I_j = Pe_G \, \Delta Z \qquad [4.62]$$

$$J_j = \left[\frac{(\beta - \alpha Z_j)}{(\beta - \alpha Z_j) - \alpha \Delta Z}\right] \qquad [4.63]$$

$$K_j = \left[\frac{\sqrt{1+M}St_G y_0(\beta - \alpha Z_j)\Delta Z}{(\beta - \alpha Z_j) - \alpha \Delta Z} \right] \quad [4.64]$$

$$L_j = \left[\frac{St_G y_0 \beta \Delta Z}{\sqrt{1+M}\left((\beta - \alpha Z_j) - \alpha \Delta Z\right)} \right] \quad [4.65]$$

By applying the same numerical spatial discretization technique on the differential boundary equations obtained before, the following algebraic equations are obtained for the following boundary conditions:

$X_{N-1} - X_{N+1} + M_j X_{inf} - M_j X_N = 0$ (counter-current flow conditions) [4.66]

$X_{-1} - X_1 + M_j X_0 + M_j X_{inf} = 0$ (co-current flow conditions) [4.67]

$X_{-1} - X_1 = 0$ (counter-current flow conditions) [4.68]

$X_{N+1} - X_{N-1} = 0$ (co-current flow conditions) [4.69]

$Y_{-1} - Y_1 + N_j Y_0 - N_j = 0$ (counter and co-current flow conditions) [4.70]

$Y_{N+1} - Y_{N-1} = 0$ (counter and co-current flow conditions) [4.71]

$U_0 = 1$ (counter and co-current flow conditions) [4.72]

where:

$$M_j = 2Pe_L \, \Delta Z \quad [4.73]$$

$$N_j = 2Pe_G \, \Delta Z \quad [4.74]$$

4.4.2 2P-ADM With Gas-Phase Dispersion (Water Treatment Conditions)

The non-linear differential equations are transformed into non-linear algebraic equations similar to those equations developed before for the wastewater treatment conditions with the exception of setting the factor (M) equal to zero.

4.4.3 2P-ADM without gas phase dispersion

For the special case of 2P-ADM with no dispersion in the gas phase, the same procedure is used for the numerical transformation of the model non-linear differential equations into non-linear algebraic equations.

4.5 CONCLUSIONS

In this chapter, the two-phase axial dispersion model (2P-ADM) has been developed for describing the performance of ozone bubble columns. Two cases of the model have been developed: (1) the axial dispersion was considered for the liquid and gas phases; and (2) the axial dispersion was considered only in the liquid phase. The 2P-ADM non-linear differential equations were numerically transformed into non-linear algebraic equations that can be easily solved using any of the available numerical solving algorithms.

The main advantage of applying those comprehensive models is to be able to compare between their predictions when used to model the performance of ozone bubble columns. Those models' predictions may vary depending on the bubble column configuration and design as well as the operating conditions. As an example, regarding the effect of bubble column configuration, columns with small aspect ratios might exhibit large gas-phase backmixing that must be accounted for in the model equations. Therefore, most of the models that are currently applied to describe the performance of such ozone contactors are outdated because they are based on inaccurate assumptions with respect to the prevailing liquid and gas-phase flow regimes.

4.6 REFERENCES

1. Beltrán, F.J., J.F. García-Araya, and J.M. Encinar, "Henry and Mass Transfer Coefficients in the Ozonation of Wastewaters", Ozone Sci. & Eng. 19: 281-296 (1997).
2. Danckwerts, P.V., *Gas-Liquid Reactions* (NY, USA: McGraw-Hill, Inc., 1970).
3. Deckwer, W.-D., "Non-Isobaric Bubble Columns With Variable Gas Velocity", Chem. Eng. Sci. 31: 309-317 (1976).
4. Gamal El-Din, M. and D.W. Smith, "Designing Ozone Bubble Columns: A Spreadsheet Approach to Axial Dispersion Model", *Proc. of IOA/PAG Conf.: Advances in Ozone Technology*, Orlando, FL, USA, 2000.
5. Hoigné, J., "Mechanisms, Rates and Selectivities of Oxidants of Organic Compounds Initiated by Ozonation in Water", *Handbook of Ozone Technology and Applications* (MI, USA: Ann Arbor Science Publishers, 1982).
6. Johnson, P.N. and R.A. Davis, "Diffusivity of Ozone in Water", J. Chem. Eng. Data 41: 1485-1487 (1996).
7. Kaštánek, J., J. Zahradník, J. Kratochvíl, and J. Čermák, *Chemical Reactors for Gas-Liquid Systems* (Chichester, England: Ellis Horwood, 1993).
8. Kramers, H. and K.R. Westerterp, *Elements of Chemical Reactor Design and Operation* (NY, USA: Academic Press, Inc., 1963).
9. Levenspiel, O., *Chemical Reaction Engineering, 2nd ed.* (NY, USA: John Wiley and Sons, Inc., 1972).
10. Mangartz, K.H. and Th. Pilhofer, "Interpretation of Mass Transfer Measurements in Bubble Columns Considering Dispersion of Both Phases", Chem. Eng. Sci. 31: 1069-1077 (1981).
11. Oke, N.J., D.W. Smith, and H. Zhou, "An Empirical Analysis of Ozone Decay Kinetics in Natural Waters", Ozone Sci. & Eng. 20: 361-379 (1998).
12. Shetty, S.A., M.V. Kantak, and B.G. Kelkar, "Gas-Phase Backmixing in Bubble Column Reactors", AIChE J. 38(7): 1013-1026(1992).

13. Towell, G.D. and G.H. Ackermann, "Axial Mixing of Liquid and Gas in Larger Bubble Reactors", *Proc. 5th European and 2nd Int. Sympos. Chem. Reaction Eng.* B3-1, Elsevier, Amsterdam, Netherlands (1972).

14. Wachi, S. and Y. Nojima., "Gas-Phase Dispersion in Bubble Columns", Chem. Eng. Sci. 45(4): 901-905 (1990).

15. Wachi, S. and H. Morikawa., "Chlorination of Ethylene in a Boiling Bubble Column Reactor", J. Chem. Eng. Japan 20: 238-245 (1987).

16. Yurteri, C. and M.D. Gurol, "Ozone Consumption in Natural Waters: Effects of Background Organic Matter, pH and Carbonate Species", Ozone Sci. & Eng. 10: 277-290 (1988).

17. Zhou, H. and D.W. Smith, " Ozonation Dynamics and its Implication for Off-Gas Ozone Control in Treating Pulp Mill Wastewaters", Ozone Sci & Eng. 22: 31-51 (2000).

18. Zhou, H. and D.W. Smith, "Applying Mass Transfer Theory to Study the Kinetics of Fast Ozone Reactions in Pulp Mill Effluents", *Proc. of the 14th Ozone World Congress*, Detroit, MI, USA, (1999).

19. Zhou, H. and D.W. Smith, "Process Parameter Development for Ozonation of Kraft Pulp Mill Effluents", Wat. Sci. & Technol. 35(2-3): 251-259 (1997).

20. Zhou, H., *Investigation of Ozone Disinfection Kinetics and Contactor Performance Modeling: Ph.D. Thesis* (Edmonton, AB, Canada: University of Alberta, 1995).

CHAPTER 5. TWO-PHASE NON-ISOBARIC AXIAL DISPERSION MODELS FOR MODELING THE OZONATION PROCESS DYNAMICS–II. NUMERICAL ANALYSES AND EXPERIMENTAL VERIFICATION*

5.1 INTRODUCTION

In chapter 4, a two-phase-non-isobaric axial dispersion model (2P-ADM) was developed for describing the dynamics of ozonation process in bubble columns for water and wastewater treatment applications. The 2P-ADM consists of a system of three non-linear differential equations representing the liquid-phase ozone concentration, the gas-phase ozone concentration, and the gas-phase inerts' concentrations. One of the special conditions of the 2P-ADM, that represents the situations where the gas phase is assumed to flow in an ideal plug flow regime, has been previously developed and applied for describing the performance of ozone contactors (Zhou *et al.*, 1994). Therefore, the backmixing in the gas phase can be neglected and the 2P-ADM reduces to a system of two non-linear differential equations. By applying the 2P-ADM, to describe the dynamics of the ozonation process in bubble columns, instead of the traditionally applied models such as plug flow model (PFM) or continuous flow stirred tank reactors (CFSTR's) in-series model, accurate and reliable designs of ozone contactors can be achieved. Consequently, the operating and capital costs can be minimized and the desired treatment objectives can be met. Accurate and reliable predictions of the ozone concentration in the exhaust gas leaving the ozone contactors will allow for more accurate and optimized designs of the ozone off-gas destruction facilities.

The objectives of this chapter are (1) to demonstrate the two-phase axial dispersion model capability to predict the performance of ozone bubble columns under different operating conditions for water and wastewater treatment applications; and (2) to test the model predictions against some existing experimental data from the literature.

A version of this chapter has been submitted for publication. Gamal El-Din, M. and D.W. Smith, J. Environ. Eng. & Sci. (July 2001).

First, the two-phase axial dispersion model was simulated under two different conditions of the gas-phase backmixing: (1) high gas-phase dispersion; and (2) low gas-phase dispersion. In situations where the gas-phase backmixing can be ignored and the gas-phase flow is considered to be in the ideal plug flow regime, were also considered in the model simulations. Under those conditions, the model was simulated for a wide range of typical operating conditions that are usually encountered in water and wastewater treatment applications. Sensitivity analyses of the model predictions were also performed to obtain the model sensitivities and responses towards changes in the model input parameters.

Second, the model predictions were tested against the experimental data of Zhou (1995) to demonstrate the model capability to describe the performance of a fine-bubble diffuser ozone contactor in the counter and co-current flow modes.

5.2 NUMERICAL SIMULATIONS AND SENSITIVITY ANALYSES

5.2.1 Numerical Solution Techniques of the 2P-ADM Equations

The system of three non-linear differential equations representing the general 2P-ADM was transformed numerically into a system of non-linear algebraic equations by applying the finite-difference technique, in which, a backward difference scheme was applied for spatial discretization. In the finite difference technique, the number of elements (N) was set equal to 50. As a result, 51 nodes were used and that led to 153 non-linear algebraic equations in addition to the boundary equations. When the gas-phase was assumed to flow in an ideal plug flow regime, the number of algebraic equations was reduced from 153 to 102. Those non-linear algebraic equations were solved using the Newton Raphson technique by utilizing the TKSOLVER^{TM} software. The program executed until a user-specified comparison tolerance of 10^{-6} was satisfied. The program execution time varied between runs depending on the values of the model input parameters.

5.2.2 Operating Conditions for Water Treatment Applications

The effects of the model input parameters (Pe_L, Pe_G, k_La, D_a, α, and y_0) on the dissolved ozone concentration, gaseous ozone concentration, and superficial gas velocity profiles were examined. The following typical conditions for the operation of ozone bubble columns were assigned as the base values for the model simulations: column height (L) = 5,000 mm, ozone concentration in the feed gas ($C_{G,0}$) = 1 % (w/w), applied ozone dose = 1.35 mgL^{-1}, mean theoretical hydraulic detention time = τ = 180 s, Pe_L = 5.0, $k_w = 4.7 \times 10^{-4}\ s^{-1}$, $k_La = 5.0 \times 10^{-3}\ s^{-1}$, bubble column aspect ratio = L/D = 12.5, G/L ratio = 0.1, and gas hold-up (ε_G) = 0.008. The ozone decay process was assumed to follow pseudo-first-order reaction kinetics with the specific ozone utilization rate constant (k_w) being constant throughout the course of ozonation. This is typical for situations where the concentrations of impurities in the liquid phase are too small, as in clean deionized water, to cause k_w to decrease during the course of ozonation as a result of the increasing amount of the utilized ozone as the ozonation process proceeds. Henry's law constant (H) of 0.22 $kPaLmg^{-1}$ was obtained from Sotelo *et al.* (1989). Water temperature was assumed to be 20°C and the pressure at the top of the column (P_T) was set equal to 101.3 kPa. Therefore, α and β were calculated to be 0.48 and 1.48, respectively.

The basic model input parameters were then calculated and they were as follows: Pe_L = 5.0 (corresponding to $D_L = 0.028\ m^2s^{-1}$), Pe_G = 618.3 ($D_G = D_L/10$), 61.83 ($D_G = D_L$), and 0.0 ($D_G = 0$), St_L = 0.90, St_G = 2.07, D_a = 0.0831, and y_0 = 0.00675. The 2P-ADM predictions of the dissolved ozone concentration, gaseous ozone concentration, and superficial gas velocity profiles along the bubble column were obtained for wide ranges of the model input parameters. The effects of each of the parameters (Pe_L, Pe_G, k_La, D_a, α, and y_0) on the model predictions, were studied by varying the parameter of interest while maintaining the others constant except for Pe_L and Pe_G, as they were varied together as the gas-phase backmixing is somewhat dependent on the liquid-phase backmixing.

5.2.3 Operating Conditions for Wastewater Treatment Applications

It was reported by Zhou and Smith (1999) that during the ozonation of Kraft pulp mill wastewaters, k_w ranged from 1,000 to 5,000 s^{-1} and the enhancement factor pretreatment level the pulp mill wastewater had received before it was ozonated. E was smaller for the final pulp mill effluent than for the untreated pulp mill wastewater as the untreated pulp mill wastewater contained more organic content causing its reactivity towards ozone to be higher (Zhou and Smith, 2000). In their calculations of the amount of the utilized ozone, the bulk liquid ozone concentration was assumed to equal zero since it was practically below the detection limit and it was less significant compared to the total amount of applied ozone. They suggested that a typical value of k_L ranged from 6.6×10^{-4} to 9.3×10^{-4} ms^{-1} and k_La ranged from 8.3×10^{-3} to 2.5×10^{-2} s^{-1}. The effects of Pe_L, Pe_L, k_La, D_a, M, α, and y_0 on the dissolved ozone concentration, gaseous ozone concentration, and superficial gas velocity profiles in bubble columns were examined by assigning the same typical operating conditions, used for the water treatment applications. Except for the specific ozone utilization rate constant (k_w), the enhancement factor (M), and the local mass transfer coefficient (k_L). Lower values of k_w, M, and k_L were chosen to study the model predictions for wastewater treatment applications in lower reactive environments compared to the highly reactive environments such as pulp mill wastewaters. k_w and k_L were set equal to 500 s^{-1} and 8.0×10^{-4} ms^{-1}, respectively. The effects of the type of wastewater on k_w, and consequently, on the ozone reactivity with the liquid-phase impurities were investigated by varying k_w over a wide range (5.0×10^{-1} to 5.0×10^{4} s^{-1}). The change in the amount of the utilized ozone dose along the column height in the main direction of the liquid flow passing through the reactor was assumed to be negligible as a result of the relatively short mean theoretical hydraulic detention time in the reactor.

The basic model input parameters were then calculated and they were as follows: $Pe_L = 5.0$ (corresponding to $D_L = 0.028$ m^2s^{-1}), $Pe_G = 618.3$ ($D_G = D_L/10$), 61.83 ($D_G = D_L$), and 0.0 ($D_G = 0$), $St_L = 0.90$, $St_G = 2.07$, $D_a = 89000$, $M = 1.166$, and $y_0 = 0.00675$. The lower value of M was chosen to investigate the effect of chemical reactions in the intermediate reaction-kinetics regime where they occur simultaneously near and/or at the gas-liquid interface and in the bulk liquid as usually experienced in lower reactive environments. The effects of each of the parameters (Pe_L, Pe_G, k_La, D_a, M, α, and y_0) on the model predictions, were studied by varying the parameter of interest while maintaining the others constant except for: (1) Pe_L and Pe_G; and (2) D_a and M. D_a and M are interrelated through the pseudo-first-order specific ozone utilization rate constant (k_w).

5.2.4 Operating Conditions for Model Testing (Water Treatment Applications)

The 2P-ADM was tested, for ozone application in water treatment, using the pilot-scale experimental data of Zhou (1995). The pilot-scale bubble column utilized in the experiments was a cylindrical glass column with an inside diameter of 100 mm and a height of 2,000 mm. The water depth was maintained constant at 1,750 mm by using an overflow weir. A 25 mm spherical fused crystalline aluminum stone was used as the gas sparger. For the deionized water used in the experiments, a pseudo-first-order specific ozone utilization rate constant (k_w) was assumed to equal 4.7 x 10^{-4} s^{-1} based on the measurements of Zhou (1995). The operating conditions for the counter-current and co-current flow modes are presented in Tables 5.1 and 5.2, respectively.

Table 5.1 Operating conditions for the counter-current flow mode (water treatment).

Case #	**Pe_L**	**P_T (atm)**	**St_L**	**St_G**	**D_a**	**y_0**	**$C^*_{L,0}$ (mgL^{-1})**
DW17	10.53	1.0	0.560	1.119	0.139	0.010	5.56
DW18	5.35	1.0	3.788	1.299	0.139	0.002	0.92

Table 5.2 Operating conditions for the co-current flow mode (water treatment).

Case #	**Pe_L**	**P_T (atm)**	**St_L**	**St_G**	**D_a**	**y_0**	**$C_{L,0}^*$ (mgL^{-1})**
DW4	34.48	1.0	0.235	1.247	0.056	0.013	7.20
DW5	9.84	1.0	1.755	1.258	0.056	0.002	0.92
DW9	4.63	1.0	0.235	0.081	0.139	0.002	0.88

5.3 RESULTS AND DISCUSSION

5.3.1 Counter-Current Flow Mode (Water Treatment Applications)

The main feature of the counter-current flow mode is that the liquid flow passes from the top to the bottom of the column in the opposite direction to that of the gas flow. Figures 5.1 to 5.10 represent the predicted dissolved ozone concentration, gaseous ozone concentration, and superficial gas velocity profiles, along the column height, as functions of the dimensionless axial co-ordinate (Z). The profiles representing the conditions of $D_G = D_L/10$ and $D_G = 0$ were virtually identical. Therefore, only the profiles representing the condition of $D_G = D_L/10$ were presented. The effects of the inflow superficial liquid and gas velocities on the process overall mass transfer coefficient (k_La) are represented by St_L and St_G, respectively. Since St_L and St_G are interrelated through k_La, therefore, the effects of St_L and St_G were studied simultaneously by varying k_La. In all the cases, the gaseous ozone concentration decreased monotonically along the column height. The maximum dissolved ozone concentration occurred at the bottom of the column where the liquid exits the column.

Figure 5.1 represents the effects of Pe_L and Pe_G on the dissolved ozone concentration profiles. The Pe_L and Pe_G effects decreased as Pe_L and Pe_G increased from 1.0 to infinity and 12.4 (for $D_G = D_L$) or 124.0 (for $D_G = D_L/10$) to infinity with the rate of increase of the effluent dissolved ozone concentration per increase of Pe_L being virtually identical for both $D_G = D_L$ and $D_G = D_L/10$. Meanwhile, the rate of increase in the effluent dissolved ozone concentration per increase in Pe_G was higher by almost one fold for $D_G = D_L/10$. As Pe_L increased from 1.0 to 20.0, the rate of increase in the effluent dissolved ozone concentration per increase in Pe_L decreased from almost 1.5 x 10^{-2} to 7.0 x 10^{-4} and was virtually identical for both $D_G = D_L$ and $D_G = D_L/10$. As Pe_G increased from 12.4 to 247.3 (for $D_G = D_L$) and 124.0 to 2473.0 (for $D_G = D_L/10$), respectively, the rate of increase in the effluent dissolved ozone concentration per increase in Pe_G decreased from almost 1.1 x 10^{-2} to 6.0 x 10^{-5} for $D_G = D_L$ and was almost lower by one fold for $D_G = D_L/10$.

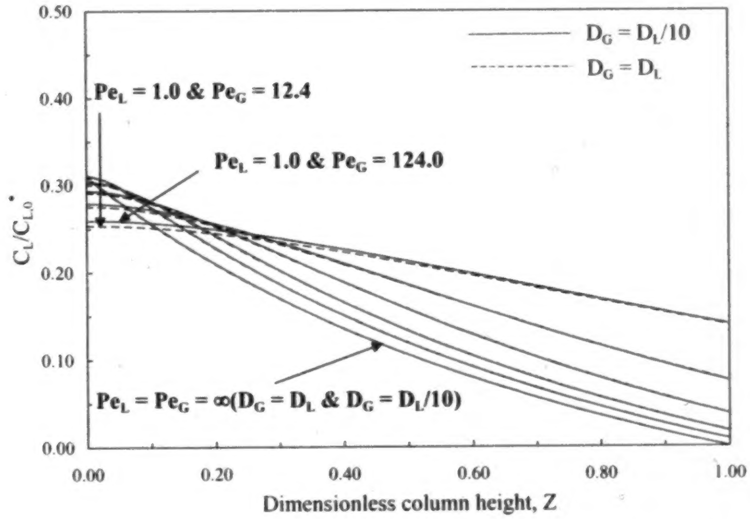

Figure 5.1 Pe_L and Pe_G effects on the 2P-ADM predicted dissolved ozone concentration profiles in the counter-current flow mode and for water treatment applications ((Pe_L = 1.0, 2.5, 5.0, 10.0, 20.0, and ∞) and (Pe_G = 12.4/124.0, 30.9/309.0, 61.8/618.0, 123.7/1237.0, 247.3/2473.0, and ∞)).

As shown in Figure 5.1, as Pe_L and Pe_G increased, the dissolved ozone concentration in the effluent increased and the profiles became steeper as the flow conditions in both phases approached the plug flow regime. The profiles exhibited an increasing axial gradient up to a turning point after which they started decreasing. As Pe_L and Pe_G increased from 1.0 to 20.0 and from 12.4 to 247.3 (for $D_G = D_L$) or 124.0 to 2473.0 (for $D_G = D_L/10$), respectively, the position of the turning point shifted from Z = 0.70 and 0.74 to 0.12 and 0.12 at $D_G = D_L/10$ and $D_G = D_L$, respectively. That could be explained by the boundary conditions applied at the bottom (zero-axial gradient of the profile) and at the top of the column (a concentration jump). As the liquid and gas phases reached the plug flow regime at Pe_L and Pe_G = infinity, the backmixing and the concentration jump diminished and as a result the dissolved ozone concentration profiles exhibited a decreasing trend along the entire column height.

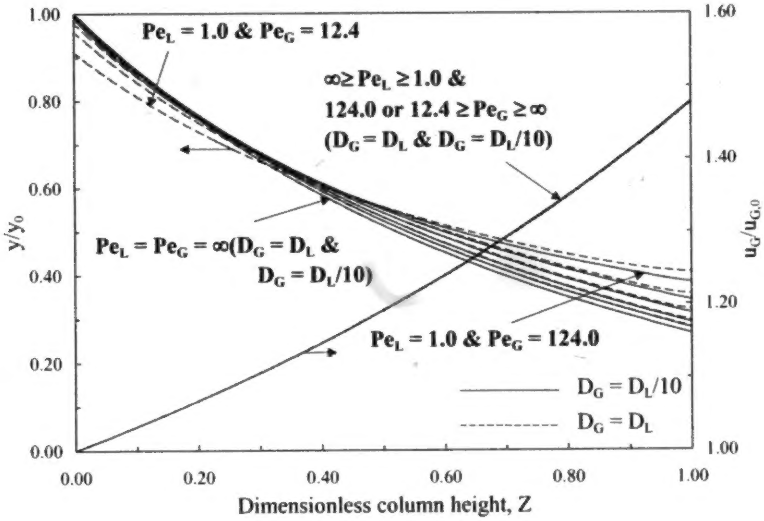

Figure 5.2 Pe_L and Pe_G effects on the 2P-ADM predicted gaseous ozone concentration and superficial gas velocity profiles in the counter-current flow mode and for water treatment applications ((Pe_L = 1.0, 2.5, 5.0, 10.0, 20.0, and ∞) and (Pe_G = 12.4/124.0, 30.9/309.0, 61.8/618.0, 123.7/1237.0, 247.3/2473.0, and ∞)).

As shown in Figure 5.2, the effects of Pe_L and Pe_G on the gaseous ozone concentration profiles decreased and the profiles became steeper as Pe_L and Pe_G increased. As Pe_L increased from 1.0 to 20.0, the rate of decrease in the ozone off-gas concentration per increase in Pe_L decreased from almost 2.5×10^{-2} to 1.0×10^{-3} and was virtually identical for both $D_G = D_L$ and $D_G = D_L/10$. As Pe_G increased from 12.4 to 247.3 (for $D_G = D_L$) and 124.0 to 2473.0 (for $D_G = D_L/10$), respectively, the rate of decrease in ozone off-gas concentration per increase in Pe_G decreased from almost 2.7×10^{-3} to 1.0 x

10^{-4} for $D_G = D_L$ and was almost lower by one fold for $D_G = D_L/10$. The highest effects of Pe_L and Pe_G on the gaseous ozone concentration profiles were in the upper one half of the column height where higher Pe_L and Pe_G improved the absorption efficiency due to the lower dissolved ozone concentrations in that region of the column resulting in higher mass transfer driving force (Zhou *et al.*, 1994). The superficial gas velocity profiles were virtually identical for the entire studied range of Pe_L and Pe_G.

The superficial gas velocity at the column exit was about 1.5 times higher than the inflow superficial gas velocity and the superficial gas velocity increase was almost a linear function of the axial co-ordinate (Z) as a result of the gas expansion due to the linear decrease in the hydrostatic head along the column height. The slight deviation from the linearity is contributed to the effects of the ozone gas absorption and auto-decomposition processes.

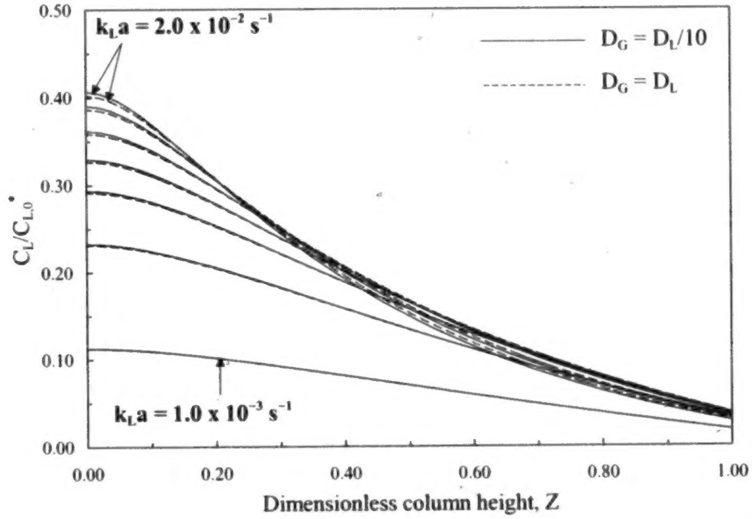

Figure 5.3 k_La effects on the 2P-ADM predicted dissolved ozone concentration profiles in the counter-current flow mode and for water treatment applications ($k_La = 1.0 \times 10^{-3}$, 3.0×10^{-3}, 5.0×10^{-3}, 7.0×10^{-3}, 1.0×10^{-2}, 1.5×10^{-2}, and $2.0 \times 10^{-2}\ s^{-1}$).

As shown in Figure 5.3, the effects of k_La on the dissolved ozone concentration profiles decreased and the profiles became steeper as k_La increased from 1.0×10^{-3} to 2.0×10^{-2} s^{-1} and the rate of increase in the effluent dissolved ozone concentration per increase in k_La decreased from 1.00 to 0.05 and was virtually identical for both $D_G = D_L$ and $D_G = D_L/10$. The profiles exhibited an increasing axial gradient up to a turning point after which they started decreasing. As k_La increased, the position of the turning point shifted from Z = 0.46 to 0.18 for $D_G = D_L/10$ and $D_G = D_L$. As shown in Figure 5.3, as k_La increased from 1.0×10^{-2} to 2.0×10^{-2} s^{-1} (i.e., the higher range of k_La), the dissolved ozone concentrations increased only up to a "Z" equal to about 0.20 and at "Z" higher than 0.20, the concentrations decreased. That could be explained by the fact that the mass transfer process was increased only near the bottom of the column. Therefore, the model predictions support the idea of the mass transfer enhancement near the bottom of the column being sufficient for better ozone bubble column performance (Zhou *et al.*, 1994; Gamal El-Din and Smith, 2000).

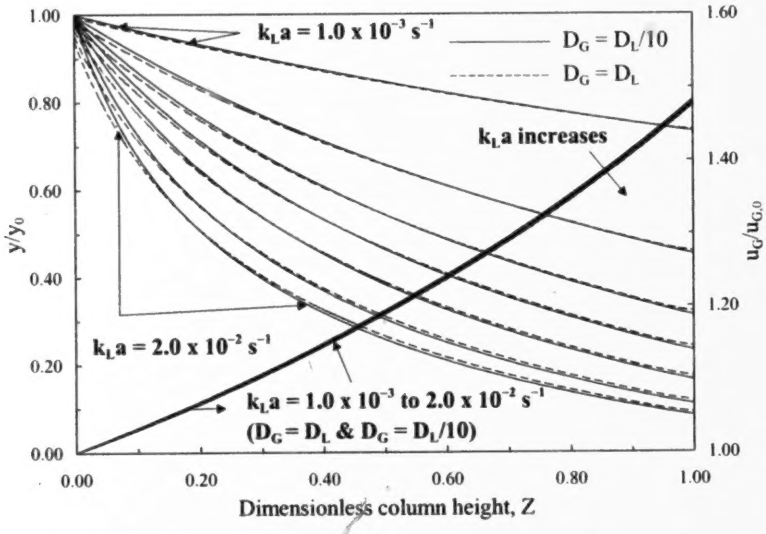

Figure 5.4 k_La effects on the 2P-ADM predicted gaseous ozone concentration and superficial gas velocity profiles in the counter-current flow mode and for water treatment applications ($k_La = 1.0 \times 10^{-3}$, 3.0×10^{-3}, 5.0×10^{-3}, 7.0×10^{-3}, 1.0×10^{-2}, 1.5×10^{-2}, and 2.0×10^{-2} s^{-1}).

As shown in Figure 5.4, the effects of k_La on the gaseous ozone concentration profiles decreased and the profiles became steeper as k_La increased and the rate of decrease in the ozone off-gas concentration per increase in k_La decreased from 2.3 to 0.1 and was virtually identical for both $D_G = D_L$ and $D_G = D_L/10$. The superficial gas velocity profiles were almost identical for the entire studied range of k_La with the superficial gas velocity being higher at lower k_La. The superficial gas velocity at the column exit was about 1.5 times higher than the inflow superficial gas velocity and the superficial gas velocity increase was almost a linear function of the axial co-ordinate (Z).

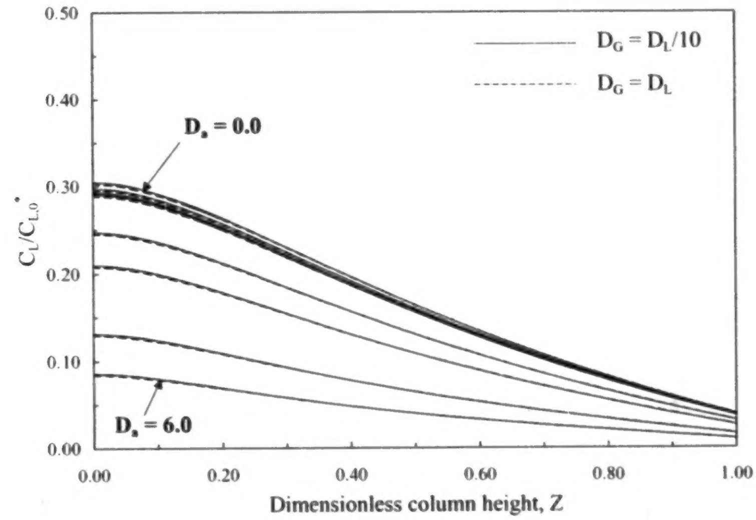

Figure 5.5 D_a effects on the 2P-ADM predicted dissolved ozone concentration profiles in the counter-current flow mode and for water treatment applications (D_a = 0.0000, 0.0505, 0.0831, 0.1010, 0.5050, 1.0000, 3.0000, and 6.0000).

Figure 5.5 depicts the effects of the overall pseudo-first-order specific ozone utilization rate constant (k_w) on the dissolved ozone concentration profiles. k_w is one of the parameters that describe the quality of the water being treated. A case where there is no decay of the dissolved gas, as in oxygen bubble columns, has been included in the analysis for the sack of comparison. As k_w increased from 0.0 to 5.0×10^{-2} s^{-1} (i.e., D_a

increased from 0.0 to 6.0) the dissolved ozone concentration profiles became flatter and the effluent dissolved ozone concentration decreased as observed before by (Gamal El-Din and Smith, 2000). This is in agreement with the fact that the higher the pollution level in waters, i.e., the higher the pH, the higher the overall ozone decay rate resulting in higher ozone doses to be applied to meet the required residual ozone concentration in the effluents from ozone contactors (Zhou *et al.*, 1994). The effect of D_a on the dissolved ozone concentration profiles decreased as D_a increased from 0.0 to 6.0 and the rate of decrease in the effluent dissolved ozone concentration per increase in D_a decreased from 0.14 to 0.02 and was virtually identical for both $D_G = D_L$ and $D_G = D_L/10$. The dissolved ozone concentration profiles exhibited an increasing axial gradient up to a turning point after which they started decreasing. As D_a increased from 0.0 to 6.0, respectively, the position of the turning point shifted from "Z" = 0.32 to 0.20 for $D_G = D_L/10$ and $D_G = D_L$.

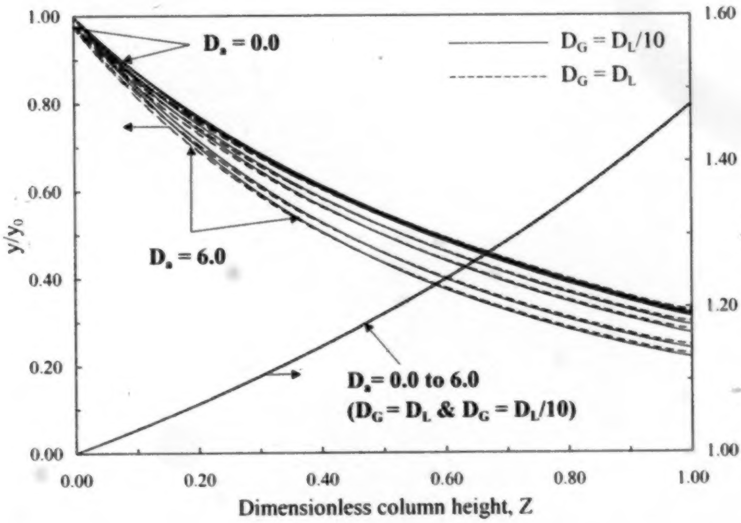

Figure 5.6 D_a effects on the 2P-ADM predicted gaseous ozone concentration and superficial gas velocity profiles in the counter-current flow mode and for water treatment applications (D_a = 0.0000, 0.0505, 0.0831, 0.1010, 0.5050, 1.0000, 3.0000, and 6.0000).

As shown in Figure 5.6, the effects of D_a on the gaseous ozone concentration profiles decreased and the profiles became steeper as D_a increased and the rate of decrease in the ozone off-gas concentration per increase in D_a decreased from 0.06 to 0.01 and was virtually identical for both $D_G = D_L$ and $D_G = D_L/10$. The effects of D_a on the gaseous ozone concentration profiles were less significant than the effects of k_La. As noted before in chapter 4, the occurrence of chemical reactions during water treatment does not affect the pure physical mass transfer rate through the liquid film beneath the gas-liquid interface. As a result, any improvement in the absorption efficiency with increasing D_a is due to the auto-decomposition of the dissolved ozone concentration in the bulk liquid. The superficial gas velocity profiles were identical for the entire studied range of D_a. The superficial gas velocity at the column exit was about 1.5 times higher than the inflow superficial gas velocity and the superficial gas velocity increase was almost a linear function of the axial co-ordinate (Z).

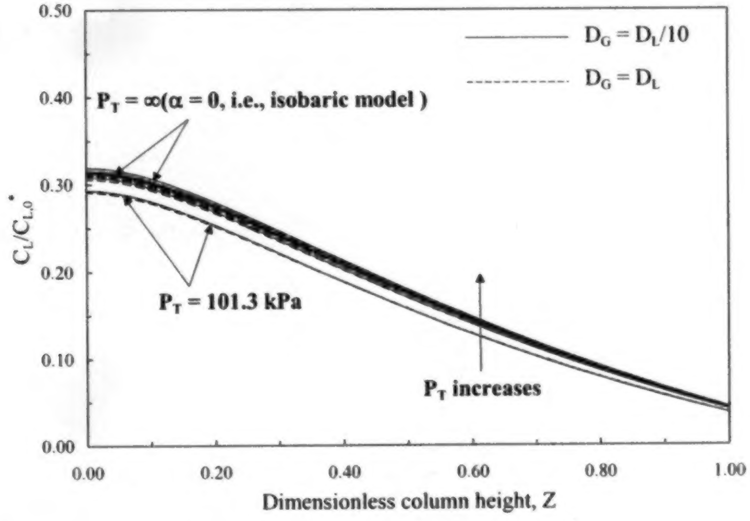

Figure 5.7 P_T or α effects on the 2P-ADM predicted dissolved ozone concentration profiles in the counter-current flow mode and for water treatment applications (P_T = 101.3, 303.9, 506.5, 709.1, 1013.0, and ∞ kPa).

Figure 5.7 shows the effects of α (i.e., the pressure at the top of the column (P_T)). For $\alpha = 0$, this means that the model is isobaric. As a result, the opposite effects of shrinkage and expansion of the gas phase caused by absorption, decay, and reduced hydrostatic head, respectively are neglected. Increasing P_T from 101.3 kPa to infinity (i.e., decreasing α from 0.48 to 0.00), caused the dissolved ozone concentration profiles to become steeper and the effluent dissolved ozone concentration increased. The increase in the total hydrostatic head due to the increase of P_T can cause the gas bubbles to become smaller and therefore the gas bubbles' specific interfacial area (a) will increase causing the overall mass transfer coefficient (k_La) to increase. Compared to the k_La effects on the dissolved ozone concentration profiles, the P_T effects were less significant. The rate of increase in the effluent dissolved ozone concentration per increase in P_T (i.e., decrease in α) increased from 0.04 to 0.07 and was virtually identical for both $D_G = D_L$ and $D_G = D_L/10$. The effects of P_T on the dissolved ozone concentration profiles were more significant in the bottom half than in the upper half of the column. As shown in Figure 5.7, the dissolved ozone concentration profiles exhibited an increasing axial gradient up to a turning point after which they started decreasing. As α decreased from 0.48 to 0.00, respectively, the effect of α on the dissolved ozone concentration profiles increased and the position of the turning point shifted from "Z" = 0.32 and 0.32 to 0.34 and 0.36 for $D_G = D_L/10$ and $D_G = D_L$.

As shown in Figure 5.8, the effects of α on the gaseous ozone concentration profiles decreased and the profiles became steeper as α decreased and the rate of decrease in the ozone off-gas concentration per decrease in α increased from 0.12 to 0.17 and was virtually identical for both $D_G = D_L$ and $D_G = D_L/10$. The superficial gas velocity profiles became flatter as α decreased. The superficial gas velocity at the column exit was about 1.5 times higher than the inflow superficial gas velocity and the superficial gas velocity increase was almost a linear function of the axial co-ordinate (Z) at $\alpha = 0.48$ (i.e., P_T = 101.3 kPa). The increase in the off-gas superficial velocity compared to the inflow superficial gas velocity decreased as α decreased. Eventually, at $\alpha = 0$ (isobaric conditions), the superficial gas velocity was constant along the entire column height. This phenomenon supports the importance of applying the appropriate model to describe the performance of ozone bubble columns. Applying non-isobaric models would result in under-prediction of the total mass of the ozone off-gas and consequently the ozone destruction units will be under-designed and health hazardous conditions might occur.

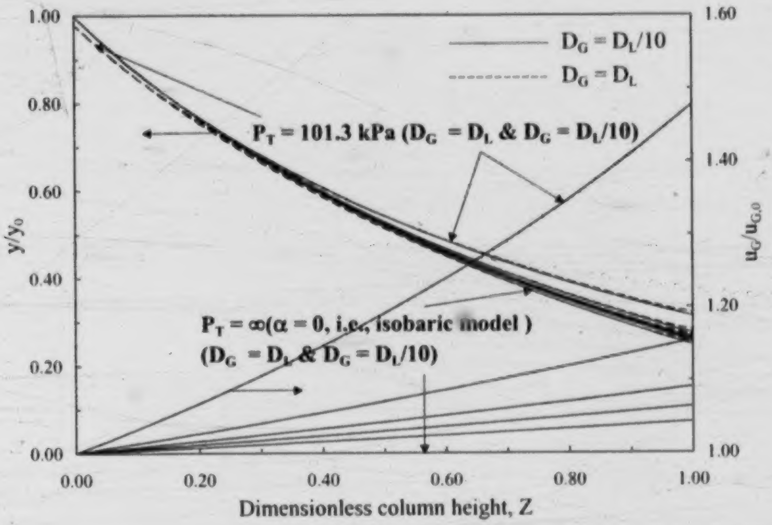

Figure 5.8 P_T or α effects on the 2P-ADM predicted gaseous ozone concentration and superficial gas velocity profiles in the counter-current flow mode and for water treatment applications (P_T = 101.3, 303.9, 506.5, 709.1, 1013.0, and ∞ kPa).

The effects of the inflow ozone gas concentration ($C_{G,0}$) on the dissolved ozone concentration, gaseous ozone concentration, and superficial gas velocity profiles in were also studied. The effluent dissolved ozone and ozone off-gas concentrations increased linearly with increasing $C_{G,0}$ and their rates of increases per increase in $C_{G,0}$ were virtually constant at 0.10 and 0.32, respectively. Those rates were identical for both $D_G = D_L$ and $D_G = D_L/10$. The superficial gas velocity profiles became flatter as $C_{G,0}$ increased. The maximum and minimum increases in the superficial gas velocity at the column exit, compared to the inflow superficial velocity, ranged from almost 1.5 to 1.4 times at $C_{G,0}$ of 1 % w/w and 12 % w/w, respectively.

5.3.2 Co-Current Flow Mode (Water Treatment Applications)

In contrast to the counter-current flow mode, the liquid and gas phases flow through the bubble column from the bottom to the top. As the liquid and gas phases flow through the reactor, the ozone in the gas phase approaches equilibrium with the bulk liquid dissolved ozone concentration. Therefore, the mass transfer driving force ($C_L^* - C_L$) becomes smaller and the bulk liquid concentration increases along the column height up to a certain point depending on the operating conditions. Thus, the model input parameters would exhibit effects on the dissolved ozone concentration, gaseous ozone concentration, and superficial gas velocity profiles. Those effects were different from those observed in the counter-current flow mode. Based on the flow arrangements in the co-current flow mode, the boundary conditions that are applied at the column entrance and exit are different from those applied in the counter-current flow mode. Therefore, the model predicted a concentration jump at the column inlet and the dissolved ozone concentration profiles reached their peaks at different locations along the column height. Those locations depended on the operating conditions. Also, the effluent from the column did not have the highest dissolved ozone concentration.

The predicted dissolved ozone concentration profiles were flatter than those predicted in the counter-current flow mode and under some operating conditions, the profiles were almost uniformly distributed along the column height. Generally the dissolved ozone concentration profiles exhibited a decreasing axial gradient along the entire column height except for the studied ranges of k_La and D_a where the profiles exhibited a decreasing axial gradient up to a turning point after which it started increasing. The gaseous ozone concentration and superficial gas velocity profiles varied in a similar way as they did in the counter-current flow mode. As reported before by Gamal El-Din and Smith (2000), under the same operating conditions, the counter-current flow mode was superior compared to the co-current flow mode in terms of the predicted effluent dissolved ozone concentration. Since the maximum dissolved ozone concentration in the co-current flow conditions occurred somewhere along the column height rather than in the column effluent, therefore, it was relevant to compare the effluent dissolved ozone concentration in the counter-current flow mode with the maximum dissolved ozone concentration in the co-current flow mode. This comparison revealed that the counter-current flow mode was superior compared to the co-current flow mode. The relative difference ranged from about 8 to 20 %, 5 to 29 %, 16 to 23 %, 18 to 16 %, and was constant at 17 % for the studied ranges of Pe_L, Pe_G, k_La, D_a, P_T, and y_0, going from the low to the high end of those ranges, respectively, for both $D_G = D_L$ and $D_G = D_L/10$.

Regarding the ozone off-gas concentration, the co-current flow mode predicted higher concentrations compared to the counter-current flow mode as a result of the relatively higher ozone gas absorption efficiency in the counter-current flow mode. The relative difference ranged from about 10 to 34 %, 1 to 77 %, 24 to 1 %, 23 to 27 %, and was constant at 23 % for the studied ranges of Pe_L, Pe_G, k_La, D_a, P_T, and y_0, going from the low to the high end of those ranges, respectively, for both $D_G = D_L$ and $D_G = D_L/10$.

For both the counter and co-current flow modes, k_La had the most significant effects on the dissolved and gaseous ozone concentration profiles. This phenomenon is in agreement with the fact that the gas-liquid mass transfer process is the main process that dictates the overall performance of ozone contactors operating in the slow-reaction kinetics regime. Compared to the rest of the parameters, α (i.e., P_T) had the most significant effects on the superficial gas velocity profiles.

In both the counter and co-current flow conditions, the dissolved ozone concentration profiles representing the condition of $D_G = D_L$ were lower, near the bottom of the column, than the ones representing the condition of $D_G = D_L/10$. As k_La, P_T, and y_0 increased and Pe_L, Pe_G, and D_a decreased, respectively, the difference in the profiles between the tow conditions of the gas-phase backmixing increased. The gaseous ozone concentration profiles were higher for the case of $D_G = D_L/10$ near the bottom of the column and as Z increased, the gaseous ozone concentration profiles for the case of $D_G = D_L$ became higher leading to higher ozone off-gas concentration. This phenomenon could be explained by the gas-phase boundary conditions applied at the bottom of the column (a concentration jump) and at the top of the column (zero-axial gradient of the profile).

As shown in Figure 5.9, the effects of k_La on the dissolved ozone concentration profiles decreased and the profiles became steeper as k_La increased from 1.0 x 10^{-3} to 2.0 x 10^{-2} s^{-1}. The rate of increase in the effluent dissolved ozone concentration per increase in k_La decreased from about 8.2 x 10^{-1} to 5.0 x 10^{-3} and was virtually identical for both $D_G = D_L$ and $D_G = D_L/10$. The profiles exhibited a decreasing axial gradient up to a turning point after which they started increasing up a second turning point after which they started decreasing again.

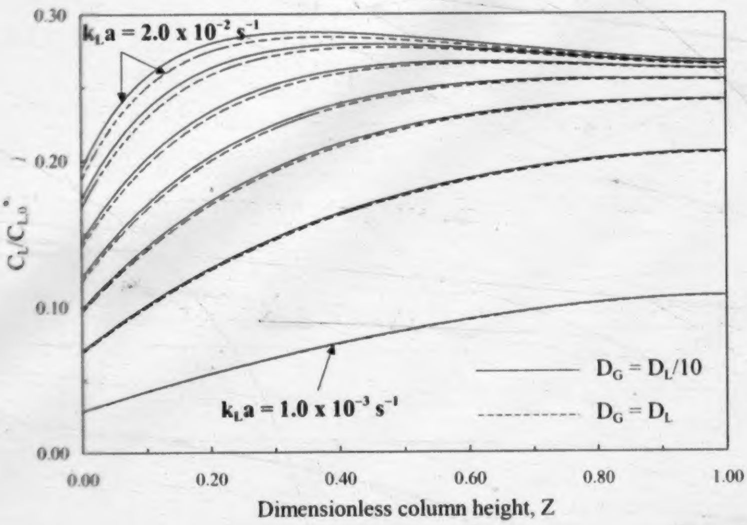

Figure 5.9 k_La effects on the 2P-ADM predicted dissolved ozone concentration profiles in the co-current flow mode and for water treatment applications (k_La = 1.0 x 10^{-3}, 3.0 x 10^{-3}, 5.0 x 10^{-3}, 7.0 x 10^{-3}, 1.0 x 10^{-2}, 1.5 x 10^{-2}, and 2.0 x 10^{-2} s^{-1}).

As shown in Figure 5.9, when k_La was increased from 7.0 x 10^{-3} to 2.0 x 10^{-2} s^{-1}, the dissolved ozone concentrations increased only up to a point after which the concentrations started decreasing. The position of that point was at "Z" = 0.82, 0.60, 0.44, and 0.36 for k_La = 7.0 x 10^{-3}, 1.0 x 10^{-2}, 1.5 x 10^{-2}, and 2.0 x 10^{-2} s^{-1}, respectively. Once again, that could be explained by the fact that the mass transfer process was increased only near the bottom of the column. Therefore, the model predictions support the idea of the mass transfer enhancement near the bottom of the column being sufficient for better ozone bubble column performance (Zhou *et al.*, 1994; Gamal El-Din and Smith, 2000).

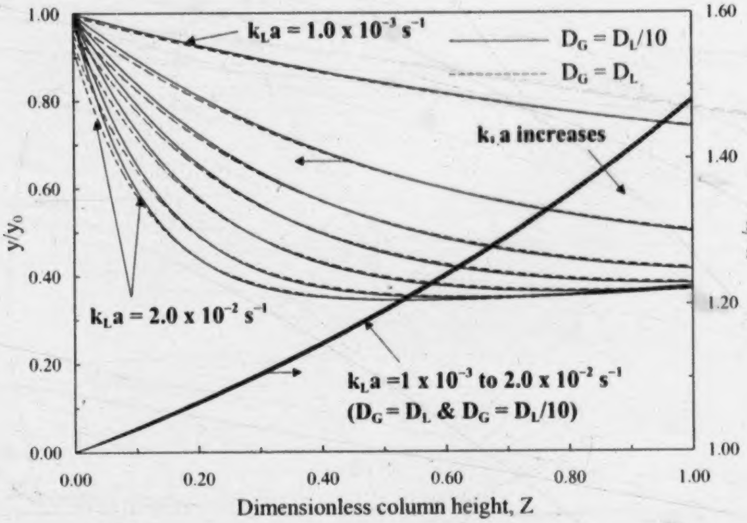

Figure 5.10 k_La effects on the 2P-ADM predicted gaseous ozone concentration and superficial gas velocity profiles in the co-current flow mode and for water treatment applications (k_La = 1.0 x 10^{-3}, 3.0 x 10^{-3}, 5.0 x 10^{-3}, 7.0 x 10^{-3}, 1.0 x 10^{-2}, 1.5 x 10^{-2}, and 2.0 x 10^{-2} s^{-1}).

As shown in Figure 5.10, the effects of k_La on the gaseous ozone concentration profiles decreased and the profiles became steeper as k_La increased and the rate of decrease in the ozone off-gas concentration per increase in k_La decreased from about 2.00 to 0.02 and was virtually identical for both $D_G = D_L$ and $D_G = D_L/10$. As k_La increased from 1.0 x $10^{-3}$to 7.0 x 10^{-3} s^{-1}, the gaseous ozone concentration profiles exhibited a decreasing axial gradient along the entire column height. In contrast, as k_La increased from 7.0 x 10^{-3} to and 2.0 x 10^{-2} s^{-1}, the gaseous ozone concentration profiles exhibited a decreasing axial gradient up to a turning point after which it started increasing. The position of that turning point shifted from about Z = 0.82 to 0.53 for both $D_G = D_L$ and $D_G = D_L/10$. The superficial gas velocity profiles were almost identical for the entire studied range of k_La with the superficial gas velocity being higher at lower k_La. The superficial gas velocity at the column exit was about 1.5 times higher than the inflow superficial gas velocity and the superficial gas velocity increase was almost a linear function of the axial co-ordinate (Z).

5.3.3 Counter-Current and Co-Current Flow Modes (Wastewater Treatment Applications)

Interestingly, for both flow modes, the dissolved ozone concentration, gaseous ozone concentration, and superficial gas velocity profiles were virtually identical. Although, in the lower range of D_a and M from $D_a = 89$ and M = 0.037 to $D_a = 534$ and M = 0.090, the model predicted a concentration jump in the dissolved ozone concentration profile near the bottom of the column in the co-current flow mode. Generally, the dissolved ozone concentration profiles exhibited a decreasing axial gradient along the entire column height except for the lower range of D_a and M. The predicted dissolved ozone concentration, gaseous ozone concentration, and superficial gas velocity profiles were virtually identical for the counter and co-current flow conditions as Pe_L, Pe_G, α or P_T, and y_0 increased over their studied ranges.

The effects of k_La on the gaseous ozone concentration profiles were more significant than the effects of any other parameter since the D_a-M range, used for the model simulations, represent situations where the intermediate-reaction kinetics regime prevails. As expected for the wastewater treatment conditions and in contrast to the water treatment conditions, the effects of D_a and M on the dissolved ozone concentration profiles were more significant than the effects of any other parameter. As observed before in the water treatment conditions, compared to the rest of the parameters, α (i.e., P_T) had the most significant effects on the superficial gas velocity profiles.

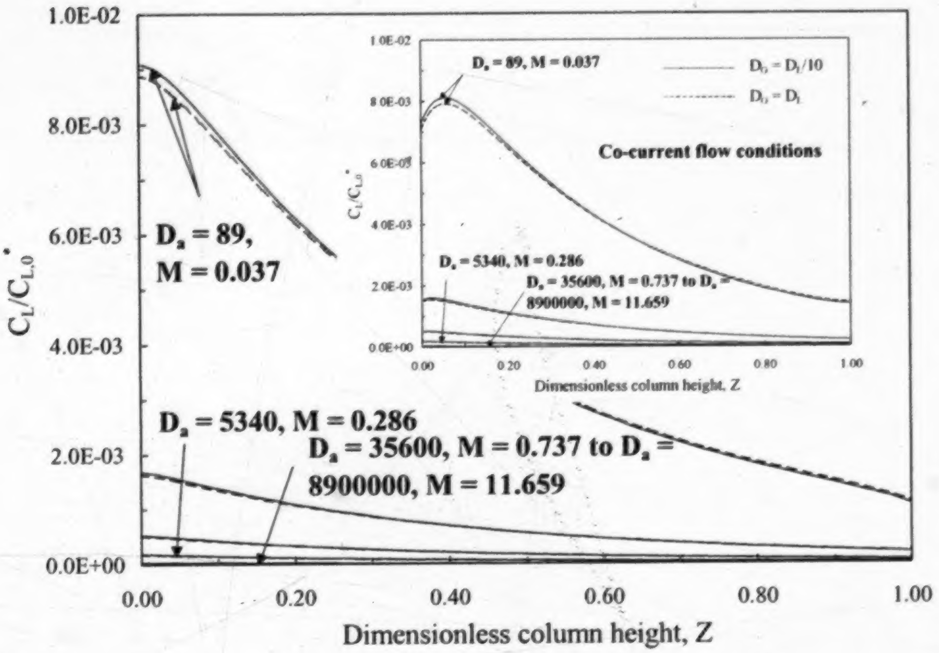

Figure 5.11 D_a and M effects on the 2P-ADM predicted dissolved ozone concentration profiles in the counter and co-current flow mode and for wastewater treatment applications (D_a = 89 and M = 0.037 to D_a = 8900000 and M = 11.659).

Figure 5.11 depicts the effects of D_a and M on the dissolved ozone concentration profiles. The profiles, representing the co-current flow mode, are shown in a small-inserted picture. As D_a and M increased, the profiles became flatter till the concentrations virtually approached zero at $35600 \le D_a \le 8900000$ and $0.737 \le M \le 11.659$. As shown in Figure 5.11, as D_a and M increased from 89 and 0.037 to 8900000 and 11.659, respectively, indicating the shift of the reaction kinetics from the slow to the fast regime. Also, the effluent dissolved ozone concentration decreased from about 5.0 x 10^{-3} to almost 0.0 mgL^{-1} and the rate of decrease in the effluent dissolved ozone concentration per increase in M decreased from 1.4 x 10^{-1} to 6.6 x 10^{-8}. The low values of the predicted dissolved ozone concentrations are in agreement with the observations of Zhou and Smith (1997). They reported that the dissolved ozone concentrations, in their continuous-flow operations of the fine-diffuser ozone bubble column, were smaller than the detection limits and they were less insignificant compared to the amount of the applied ozone. Regarding the effect of D_G, the dissolved ozone concentrations for $D_G = D_L$ were lower than those for $D_G = D_L/10$.

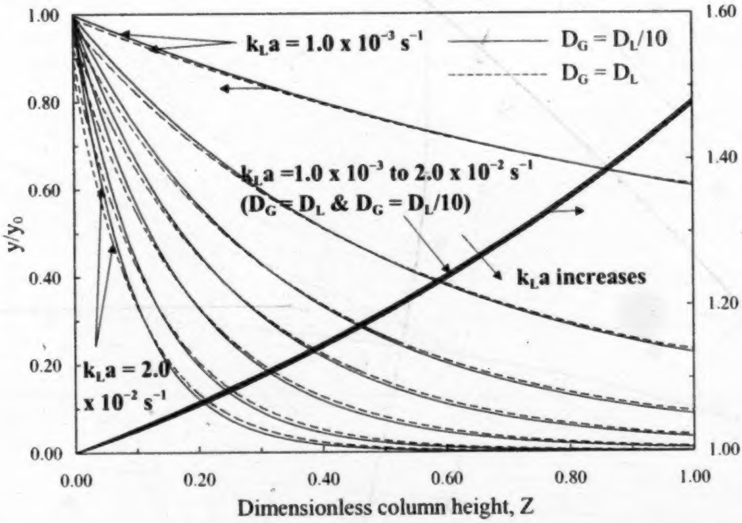

Figure 5.12 k_La effects on the 2P-ADM predicted gaseous ozone concentration and superficial gas velocity profiles in the counter and co-current flow modes and for wastewater treatment applications (k_La = 1.0 x 10^{-3}, 3.0 x 10^{-3}, 5.0 x 10^{-3}, 7.0 x 10^{-3}, 1.0 x 10^{-2}, 1.5 x 10^{-2}, and 2.0 x 10^{-2} s^{-1}).

Figure 5.12 depicts the effects of k_La on the gaseous ozone concentration and superficial gas velocity profiles. As k_La increased from = 1.0 x 10^{-3} to = 2.0 x 10^{-2} s^{-1}, the gaseous ozone concentration profiles became steeper and the effect of k_La on the profiles decreased. The rate of decrease in the ozone off-gas concentration per increases in k_La decreased from about 3.2 to 3.0 x 10^{-3} and was virtually identical for both $D_G = D_L$ and $D_G = D_L/10$. As k_La increased, the ozone off-gas concentration decreased from about 8.2 to 1.0 x 10^{-3} mgL^{-1}. The predicted ozone off-gas concentration, of 1.0 x 10^{-3} mgL^{-1}, represents situations where the reactions between ozone and the liquid-phase impurities fall within the fast-reaction kinetics regime. This is in agreement with the observations of

Zhou and Smith (2000). They observed that the ozone off-gas concentrations were below the detection limit of the iodometric titration method (KI method) which is about 7.0 x 10^{-2} mgL^{-1}. The same phenomena that was observed before in the water treatment conditions regarding the superficial gas velocity profiles were also observed in the model simulations for the wastewater treatment applications.

5.3.4 Model Testing for Water Treatment Applications

Figures 5.13 and 5.14 demonstrate the applicability of the 2P-ADM to predict the performance of the fine-diffuser ozone bubble column operating in a counter-current flow. There was excellent agreement between the predicted and the experimental dissolved ozone profiles. At 5 % significance level, t-tests have shown that there was no significant difference between the predictions of the different versions of the 2P-ADM.

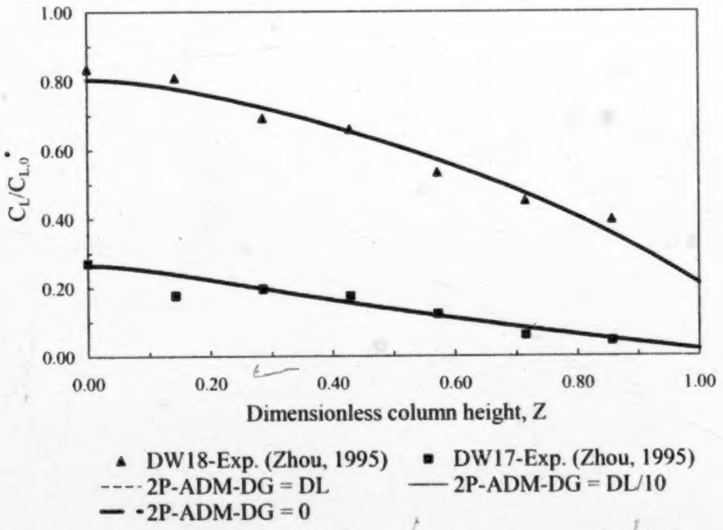

Figure 5.13 Comparison between the predicted and the measured dissolved ozone concentration profiles in a counter-current fine-bubble diffuser ozone bubble column for water treatment applications.

The same phenomenon was observed for the co-current flow mode. These observations are in agreement with the theoretical observations of Deckwer (1976) who suggested that the gas-phase dispersion could be ignored in bubble columns with diameters less than 500 mm. Although, it should be pointed out that in columns with small diameters, the assumption of the gas phase being in an ideal plug flow regime can be valid (Wachi and Morikawa, 1987), the gas-phase dispersion can be a significant factor in the ozonation process scale-up.

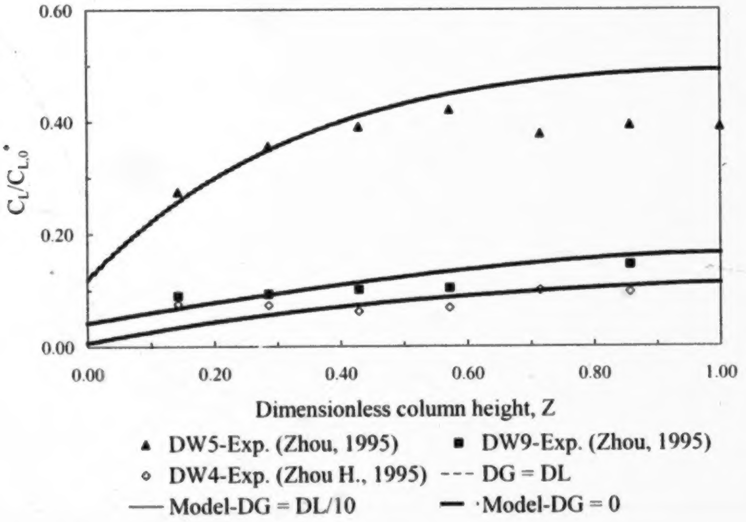

Figure 5.14 Comparison between the predicted and the measured dissolved ozone concentration profiles in a co-current fine-bubble diffuser ozone bubble column for water treatment applications.

5.4 CONCLUSIONS

The two-phase axial dispersion model (2P-ADM) has proven to be a powerful, accurate and reliable tool for predicting the performance of ozone contactors for both water and wastewater treatment applications. By applying the 2P-ADM instead of the traditionally applied models such as the plug flow model (PFM) or the continuous-flow stirred-tank-reactors (CFSTR's) in-series model, accurate and reliable designs of ozone contactors can be achieved. As a result, the operating and capital costs will be minimized and the desired treatment objectives can be met.

It should be noted that the current model testing is just an initial testing step. Therefore, further studies need to be conducted for both water and wastewater treatment applications and in different ozone contactors of different configurations, designs, and scales. This will help obtain a large and high-quality data set that can allow for further model testing in order to eliminate any uncertainties in the model predictions.

The simple version of the 2P-ADM that neglects the backmixing in the gas phase can be applied without affecting the accuracy of the model predictions in situations such as: (1) bubble columns that have large aspect ratios; and (2) when large bubbles are dominant in the gas-liquid flow as a result of using a gas sparging technique that creates large bubbles.

5.5 REFERENCES

1. Deckwer, W.-D., "Non-Isobaric Bubble Columns With Variable Gas Velocity", Chem. Eng. Sci. 31: 309-317 (1976).
2. Gamal El-Din, M. and D.W. Smith, "Designing Ozone Bubble Columns: A Spreadsheet Approach to Axial Dispersion Model", *Proc. of IOA/PAG Conf.: Advances in Ozone Technology*, Orlando, FL, USA, 2000.
3. Sotelo, J.L., F.J. Beltrán, F.J. Benitez, and J. Beltrán-Heredia, "Henry's Law Constant for the Ozone-Water System", Wat. Res. 23(10): 1239-1246 (1989).
4. TKSOLVER™, Release 3.32, Universal Technical Systems, Inc., IL, USA (1997).
5. Wachi, S. and H. Morikawa., "Chlorination of Ethylene in a Boiling Bubble Column Reactor", J. Chem. Eng. Japan 20: 238-245 (1987).
6. Zhou, H. and D.W. Smith, " Ozonation Dynamics and its Implication for Off-Gas Ozone Control in Treating Pulp Mill Wastewaters", Ozone Sci & Eng. 22: 31-51 (2000).
7. Zhou, H. and D.W. Smith, "Applying Mass Transfer Theory to Study the Kinetics of Fast Ozone Reactions in Pulp Mill Effluents", *Proc. of the 14th Ozone World Congress*, Detroit, MI, USA, 1999.
8. Zhou, H. and D.W. Smith, "Process Parameter Development for Ozonation of Kraft Pulp Mill Effluents", Wat. Sci. & Technol. 35(2-3): 251-259 (1997).
9. Zhou, H., *Investigation of Ozone Disinfection Kinetics and Contactor Performance Modeling: Ph.D. Thesis* (Edmonton, AB, Canada: University of Alberta, 1995).
10. Zhou, H., D.W. Smith, and S.J. Stanley, "Modeling of Dissolved Ozone Concentration Profiles in Bubble Columns", J. Environ. Eng., ASCE 120(4): 821-840 (1994).

CHAPTER 6. THEORETICAL ANALYSIS AND EXPERIMENTAL VERIFICATION OF OZONE MASS TRANSFER IN BUBBLE COLUMNS*

6.1 INTRODUCTION

During the course of ozonation, convection and backmixing processes of the liquid and gas phases flowing through the contacting chamber, ozone gas mass transfer process, ozone decay process, and competitive reactive processes of constituents in water and wastewater with dissolved ozone occur simultaneously (Zhou *et al.*, 1994). In addition to those processes, contactor configuration, operating conditions, and water or wastewater quality influence the overall performance of the ozonation treatment (Zhou, 1995). The ozonation process depends on the mass transfer of ozone gas into the liquid phase. Quantifying the dissolved ozone is essential for achieving reliable rational-design and optimum operation of ozone contactors while quantifying the off-gas ozone concentration leaving the contactor is important for achieving proper design of the ozone off-gas destruction facilities.

Several researchers have extensively studied the fundamentals of the processes dictating the performance of ozonation systems in water treatment over the last two decades (Langlais *et al.*, 1991). However, fewer studies have been conducted to examine the ozone mass transfer mechanisms and the effect of chemical oxidation on the rate of ozone absorption when treating industrial wastewater. Zhou and Smith (1997) showed that during the ozonation of Kraft pulp mill effluents, the chemical reactions were fast enough for the dissolved ozone to be completely depleted at the gas-liquid interface and/or within the liquid film. As a result, the dissolved ozone gradient became steeper than the one of the maximum physical absorption process. As shown in Figure 6.1, two distinct reaction kinetics regimes for the ozone gas absorption process were proposed by Zhou and Smith (1997): the fast or instantaneous-reaction kinetics regime and the slow-reaction kinetics regime. The relative rate of the gas absorption process with the occurrence of chemical reactions compared to the maximum physical gas absorption rate will determine the prevailing mass transfer regime (Zhou and Smith, 1997).

A version of this chapter has been accepted for publication. Smith, D.W. and M. Gamal El-Din, Environ. Technol. (May 2001).

Due to the low dissolved ozone concentrations during the mass transfer process occurring in the fast-reaction kinetics regime, the driving force of the mass transfer process is increased and also the local mass transfer coefficient will be enhanced by an enhancement factor (E). During the ozonation of Kraft pulp mill effluents and regarding the gas absorption process, it was assumed that the fast or instantaneous-reaction kinetics regime prevailed at the beginning of the ozonation process as the amount of the utilized ozone was still relatively small (Zhou and Smith, 1997). That assumption was based on the experimental observations of Zhou and Smith (1997) that no dissolved ozone concentrations were detected during the course of ozonation. As the ozonation treatment proceeded, the gas absorption process shifted from the fast or instantaneous-reaction kinetics regime to the slow-reaction kinetics regime and the enhancement factor decreased (Zhou and Smith, 1997).

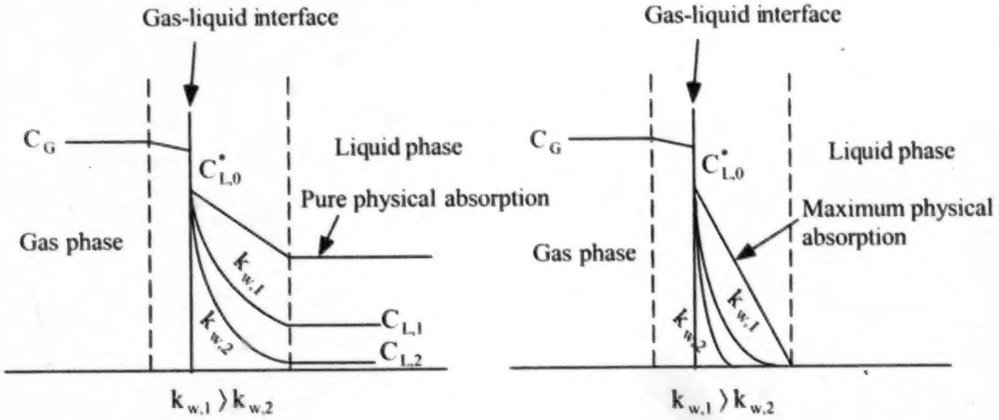
Gas-liquid interface
C_G
$C^{*}_{L,0}$
Liquid phase
Pure physical absorption
Gas phase
$k_{w,1}$
$k_{w,2}$
$C_{L,1}$
$C_{L,2}$
$k_{w,1} \rangle k_{w,2}$
Gas-liquid interface
C_G
$C^{*}_{L,0}$
Liquid phase
Maximum physical absorption
Gas phase
$k_{w,2}$
$k_{w,1}$
$k_{w,1} \rangle k_{w,2}$

a- slow-reaction regime

b- fast or instantaneous-reaction regime

Figure 6.1 Reaction kinetics regimes for ozone absorption process (adapted from Zhou and Smith, 1997).

The mathematical models that were usually applied to predict the dissolved ozone and gaseous ozone profiles along ozone bubble columns were based on one of the following liquid-phase flow regimes: (1) complete mixing or; (2) plug flow (Alvarez-Cuenca *et al.*, 1980; Alvarez-Cuenca *et al.*, 1981; Chang and Chian, 1981; Laplanche *et al.*, 1991; Hull *et al.*, 1992, Lev and Regli, 1992). Neither one of those two liquid-phase flow regimes can adequately describe the actual liquid-phase flow conditions in bubble columns as a result of the actual liquid-flow pattern in bubble columns usually being closer to mixed flow rather than plug flow, but still not completely mixed flow. Because of the low solubility and high reactivity of ozone gas, effective improvement and accurate quantification of the ozone absorption process is essential for achieving proper design and optimum operation of ozonation systems (Zhou, 1995). This goal can be met by applying more reliable and accurate models that can adequately describe the ozone gas absorption process in water and wastewater treatment applications.

This chapter presents: (1) the applicability of the back flow cell model (BFCM) and the axial dispersion model (ADM) for describing the ozonation process in bubble columns, and (2) initial testing of the models' predictions of the dissolved ozone concentration profiles, for water treatment applications, using the pilot-scale experimental data of Zhou (1995).

6.2 THEORETICAL BACKGROUND

In order to model the performance of ozone bubble columns, it is crucial to describe and quantify the rates of various physical and chemical processes that occur during the ozonation treatment. In tubular bubble columns, the non-ideal flow conditions affect the rate of absorption and the concentration profiles of dissolved and gaseous ozone. Although, a number of researchers proposed the BFCM for describing the performance of ozone bubble columns (Zhou *et al.*, 1994; Gamal El-Din and Smith, 2000b), the axial dispersion model has received the largest attention among researchers. In the ADM, it is assumed that the liquid phase is in axial dispersion regime, i.e., a diffusion-like process is assumed and superimposed on a plug flow regime (Levenspiel, 1972). During surface water ozonation, it was observed that the overall ozone auto-decomposition rate was influenced by the instantaneous dissolved ozone concentration and the changes in the properties of the water during the course of ozonation (Watt *et al.*, 1989; Zhou, 1995). Accordingly, a modified pseudo-first-order rate expression was proposed. In that expression, the reaction rate constant was replaced by a variable referred to as the specific ozone utilization rate constant (k_w):

$$\frac{dC_L}{dt} = -k_w C_L \qquad [6.1]$$

where: C_L = instantaneous concentration of the dissolved ozone in the bulk liquid (mgL^{-1}) and k_w = specific ozone utilization rate constant (s^{-1}).

The mass transfer of ozone gas from the gas phase into the liquid phase can be described and quantified by the two-film model in which the rate of gas absorption (ψ) is defined as:

$$\psi = k_L a\left(C_L^* - C_L\right) \qquad [6.2]$$

where: ψ = gas absorption rate ($mgL^{-1}s^{-1}$), k_L = local mass transfer coefficient (ms^{-1}), a = gas bubbles' specific interfacial area (m^{-1}), C_L^* = concentration of dissolved ozone in equilibrium with the ozone in the gas-phase (mgL^{-1}), and C_L = concentration of the dissolved ozone in the bulk liquid (mgL^{-1}). Ozone gas diffuses much faster in the gas phase than in the liquid phase, therefore, the mass transfer in the liquid phase becomes a rate-controlling step and the overall mass transfer coefficient is considered to entirely consist of the local mass transfer coefficient in the liquid phase. Ozonation of wastewater involves chemical reactions and the dimensionless squared Hatta number (referred to as H_a^2 or E^2 or M) is used as a measure of the amount of dissolved ozone that reacts at the gas-liquid interface or in the liquid film near the interface compared to the amount of dissolved ozone that reaches the bulk liquid in an unreacted state. The dimensionless-squared Hatta number is defined as:

$$H_a^2 = E^2 = M = \frac{D_{O_3} k_w}{k_L^2} \qquad [6.3]$$

where: D_{O_3} = molecular diffusivity of ozone in water (m^2s^{-1}), k_L = local mass transfer coefficient (ms^{-1}), and k_w = specific ozone utilization rate constant (s^{-1}). Two distinctive regions of the location of reactions that occur during the ozone mass transfer process could be defined (Danckwerts; 1970; Kaštánek *et al.*, 1993). For $H_a \langle 0.03$, reactions would occur in the bulk of the liquid, while for $H_a \rangle 3.00$, reactions would occur at the gas-liquid interface or in the liquid film near the interface. Therefore, for $0.03 \langle H_a \langle 3.00$, reactions would occur simultaneously in both regions. For a first-order irreversible reaction, Equation 6.3 is only applicable when M >> 1 (Danckwerts, 1970). This is usually the case for fast or instantaneous irreversible first-order reactions with no bulk liquid concentration where the driving force for the mass transfer will be maximized. For such a case, Equation 6.2 would become:

$$\psi = Ek_L aC_L^* \qquad [6.4]$$

where: Ek_La = enhanced overall mass transfer coefficient (s^{-1}). For wastewater ozonation, we could assume that both ozone auto-decomposition and its reactions with the organic and inorganic constituents in wastewater could be lumped together in one rate constant (k_w) (Zhou and Smith, 1999). During the ozonation of surface water, little enhancement of the mass transfer rate will occur leading to a lower value of M compared to those values encountered in wastewater ozonation. As a result, Equation 6.2 becomes:

$$\psi = k_L a\sqrt{1+M}\left(C_L^* - \frac{C_L}{1+M}\right) \qquad [6.5]$$

For surface water ozonation and assuming that ozone reactions with the various impurities that are present in water follow an irreversible first-order kinetics, the effect of chemical reactions on the mass transfer coefficient can be neglected when M << 1 (Danckwerts, 1970; Gamal El-Din and Smith, 2000b). As a result, the ozone gas absorption process can be dealt with as a pure physical absorption process as described by Equation 6.2.

6.3 OUTLINE OF THE MATHEMATICAL MODELS AND THE NUMERICAL SOLUTIONS TECHNIQUES

6.3.1 Axial Dispersion Model (ADM)

The ADM visualizes the flow of fluids in tubular bubble columns as a plug flow on top of which a diffusion-like process is superimposed (Levenspiel, 1972). When modeling two-phase flows in bubble columns, several assumptions should be considered for the development and the formulation of the ADM. Detailed presentation of those assumptions can be found elsewhere (Zhou *et al.*, 1994; Gamal El-Din and Smith, 2000a). Considering the control volume shown in Figure 6.2, and conducting mass balance analyses in the liquid and the gas phases and applying mathematical manipulations, one can obtain the non-linear differential equations representing the ADM as reported before by Zhou *et al.* (1994) and Gamal El-Din and Smith (2000a). The ADM equations are presented in Table 6.1 and the dimensionless parameters pertaining to those equations are presented in Table 6.3.

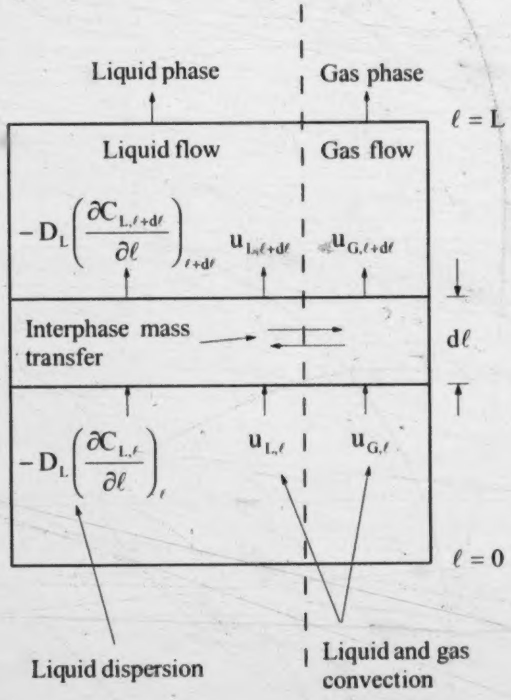
Liquid phase
Gas phase
$\ell = L$
Liquid flow
Gas flow
$-D_L\left(\frac{\partial C_{L,\ell+d\ell}}{\partial \ell}\right)_{\ell+d\ell}$
$u_{L,\ell+d\ell}$
$u_{G,\ell+d\ell}$
Interphase mass transfer
$d\ell$
$-D_L\left(\frac{\partial C_{L,\ell}}{\partial \ell}\right)_{\ell}$
$u_{L,\ell}$
$u_{G,\ell}$
$\ell = 0$
Liquid dispersion
Liquid and gas convection

Figure 6.2 Schematic representation of the co-current ADM.

Table 6.1 Mathematical representation of the ADM (Zhou *et al.*, 1994; Gamal El-Din and Smith, 2000a).

Fluid phase		**Equations**
Aqueous ozone		$\frac{1}{Pe_L}\frac{\partial^2 X}{\partial Z^2} + a'\frac{\partial X}{\partial Z} + \frac{\sqrt{1+M}St_L}{\beta}(\beta - \alpha Z)Y - \left(\frac{St_L}{\sqrt{1+M}} + D_a\right)X = 0$
Gaseous ozone		$\frac{\partial Y}{\partial Z} + \frac{St_G}{\beta(1-y_0)}(1-y_0 Y)^2\left[\sqrt{1+M}(\beta - \alpha Z)Y - \frac{\beta}{\sqrt{1+M}}X\right] = 0$
Closed-closed boundary conditions	Co-current flow mode	at $Z = 0$: $X_{inf} = X\big\vert_{Z=0} - \frac{1}{Pe_L}\frac{\partial X}{\partial Z}\Big\vert_{Z=0}$ $Y = 1$ at $Z = 1$: $\frac{\partial X}{\partial Z}\Big\vert_{Z=1} = 0$
	Counter-current flow mode	at $Z = 0$: $\frac{\partial X}{\partial Z}\Big\vert_{Z=0} = 0$ $Y = 1$ at $Z = 1$: $X\big\vert_{Z=1} = X_{inf} - \frac{1}{Pe_L}\frac{\partial X}{\partial Z}\Big\vert_{Z=1}$

Note:

$a' = -1$ for co-current flow mode

$a' = +1$ for counter-current flow mode

$M = 0$ for surface water treatment

$M > 0$ for wastewater treatment

As shown in Table 6.1, the ADM is described mathematically by a set of two non-linear partial differential equations that were solved numerically by applying a backward (upwind) finite difference scheme to transform those equations into non-linear algebraic equations. In the finite difference scheme, the total height of the column along the direction of the main liquid flow was divided into 50 elements. As a result, 51 nodes were used and that led to 102 equations in addition to the boundary conditions' equations. Those equations were solved numerically using the Newton Raphson technique by utilizing the TKSOLVER™ software. The program executed until a user-specified comparison tolerance of 10^{-6} was satisfied. The program execution time was under a minute using a 366 MHz processor.

6.3.2 Back Flow Cell Model (BFCM)

The BFCM is another mathematical model that is used to describe the performance of ozone bubble columns. The BFCM hypothesizes a back flow (Q_B) in the opposite direction to the main liquid flow (Q_L) and an exchange flow (Q_B) in the main direction of the liquid flow (Zhou and Smith, 1994; Gamal El-Din and Smith, 2000b). Those two flows are used to characterize the axial dispersion in the liquid phase.

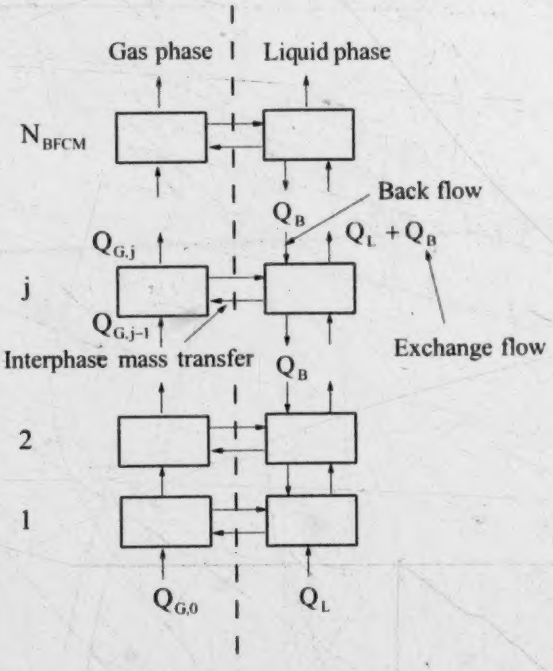
Gas phase
Liquid phase
N_{BFCM}
Back flow
Q_B
$Q_L + Q_B$
$Q_{G,j}$
j
$Q_{G,j-1}$
Interphase mass transfer
Q_B
Exchange flow
2
1
$Q_{G,0}$
Q_L

Figure 6.3 Schematic representation of the co-current BFCM.

Table 6.2 Mathematical representation of the BFCM (Gamal El-Din and Smith, 2000b).

Fluid phase	**Equations**
Aqueous ozone	**j = 1:** $a_2X_0 - \left(1 + r + D_a + \frac{St_L}{1+M}\right)X_1 + (a_1 + r)X_2$ $+ \sqrt{1+M}St_L\left(1 + \frac{\alpha}{2}\right)Y_1 = 0$ **$2 \le j \le N_{BFCM}-1$:** $(a_2 + r)X_{j-1} - \left(1 + 2r + D_a + \frac{St_L}{1+M}\right)X_j + (a_1 + r)X_{j+1}$ $+ \sqrt{1+M}St_L[1 + \alpha(j - 0.5)]Y_j = 0$ **$j = N_{BFCM}$:** $a_1X_0 + (a_2 + r)X_{N_{BFCM}-1} - \left(1 + r + D_a + \frac{St_L}{1+M}\right)X_{N_{BFCM}}$ $+ \sqrt{1+M}St_L[1 + \alpha(N_{BFCM} - 0.5)]Y_{N_{BFCM}} = 0$
Gaseous ozone	**j = j:** $(1 + \alpha(j-1.5))q_{G,j-1}Y_{j-1} - (1 + \alpha(j-0.5))q_{G,j}Y_j$ $- \sqrt{1+M}St_G\left[(1 + \alpha(j-0.5))Y_j - \frac{X_j}{1+M}\right] = 0$
Total gas	**j = j:** $(1 + \alpha(j-1.5))q_{G,j-1} - (1 + \alpha(j-0.5))q_{G,j}$ $- \sqrt{1+M}St_G y_0\left[(1 + \alpha(j-0.5))Y_j - \frac{X_j}{1+M}\right] = 0$
Closed-closed boundary conditions	$X_0 = \frac{C_{L,inf}}{C^*_{L,0}}, Y_0 = 1, q_{G,0} = 1$

Note:

$a_1 = 0$ and $a_2 = +1$ for co-current flow mode

$a_1 = +1$ and $a_2 = 0$ for counter-current flow mode

$M = 0$ for surface water treatment

$M > 0$ for wastewater treatment

Figure 6.3 represents a BFCM schematic for co-current flow conditions in bubble columns where the back flow ratio (Q_B/Q_L) is equal to the exchange flow ratio and both are assumed to remain constant along the column height. The BFCM consists of two series of completely mixed cells in which one series represents the liquid phase and the other represents the gas phase and each has a number of cells equal to N_{BFCM} (Mecklenburgh and Hartland, 1975; Deckwer and Hallensleben, 1980). The same assumptions that were used to develop the ADM equations were used to develop the BFCM equations. Considering the BFCM schematic shown in Figure 6.3 and conducting mass balance analyses for the liquid and gas phases and applying mathematical manipulations, one can obtain the non-linear algebraic equations representing the BFCM as reported before by Gamal El-Din and Smith (2000b). The BFCM equations are presented in Table 6.2 and the dimensionless parameters pertaining to those equations are presented in Table 6.3. As shown in Table 6.2, the BFCM is described mathematically by a set of 3 x N_{BFCM} non-linear algebraic equations. Those equations were numerically solved using the Newton Raphson technique by utilizing the TKSOLVER™ software. Compared to the ADM, the BFCM was easier to formulate and solve as a result of the BFCM equations being in a non-linear algebraic form while the ADM non-linear differential equations had to be transformed first into non-linear algebraic form before applying the Newton Raphson technique to obtain their solutions.

It should be noted that the BFCM and the ADM describe the backmixing of the liquid phase using different mixing parameters (Pe_L, and r). Those parameters are interrelated by the following relationship (Mecklenburgh and Hartland, 1975):

$$r = \frac{N_{BFCM}}{Pe_L} - 0.5 = \frac{D_L \varepsilon_L N_{BFCM}}{u_L L} - 0.5 \qquad [6.6]$$

where: N_{BFCM} = number of cells in series, $r = \frac{Q_B}{Q_L}$ = back flow ratio = exchange flow ratio (dimensionless), Pe_L = Peclet number (dimensionless), D_L = liquid-phase axial dispersion coefficient (m^2s^{-1}), ε_L = liquid-phase hold-up (dimensionless), and u_L = superficial liquid-phase velocity (ms^{-1}).

Table 6.3 Dimensionless parameters pertaining to the ADM and the BFCM.

Dimensionless parameter	**ADM**	**BFCM**
Z	ℓ/L	$(j-0.5)/N_{BFCM}$
α	$\rho g\varepsilon_L L/P_T$	$-\rho g\varepsilon_L L/N_{BFCM}P_0$
β	$1+\alpha$	
r		Q_B/Q_L
Pe_L	$u_L L/D_L\varepsilon_L$	
St_L	$k_L aL/u_L$	$k_L aL/N_{BFCM}u_L$
St_G	$(k_L aL/u_{G,0})(RT/H)$	$(k_L aL/N_{BFCM}u_{G,0})(RT/H)$
D_a	$k_w\varepsilon_L L/u_L$	$k_w\varepsilon_L L/N_{BFCM}u_L$
M	Dk_w/k_L^2	Dk_w/k_L^2
X, X_j	$C_{L,\ell}/C^*_{L,0}$	$C_{L,j}/C^*_{L,0}$
Y, Y_j	y_ℓ/y_0	y_j/y_0
$q_{G,j}$		$Q_{G,j}/Q_{G,0}$

6.4 OPERATING CONDITIONS FOR MODELS TESTING AND NUMERICAL ANALYSES

6.4.1 Water Treatment

The ADM and the BFCM were tested, for the ozone applications in water treatment, using the pilot-scale experimental data of Zhou (1995). The pilot-scale bubble column used in those experiments was a cylindrical glass column with an inside diameter of 100 mm and a height of 2000 mm. The water depth was kept constant at 1750 mm using an overflow weir. A 25 mm spherical fused crystalline aluminum stone was utilized as the gas sparger. Detailed information on those experiments and their operating conditions can be found in Zhou (1995). The operating conditions for the co-current and the counter-current flow modes are shown in Table 6.4. Based on the kinetics experiments conducted by Zhou (1995) to characterize the ozone decay process in deionized water, the pseudo-first-order specific ozone utilization rate constant (k_w) was found to be equal to 4.7 x 10^{-4} s^{-1}.

Table 6.4 Operating conditions for the co-current and counter-current flow modes (water treatment).

Run #	**Flow mode**	**Q_L (m^3s^{-1})**	**Q_G (m^3s^{-1})**	**Inlet O_3 gas conc. (% w/w)**	**Water temperature (°C)**	**N_{BFCM}**	**Pe_L**	**r**	**$C_{L,0}^*$ (mgL^{-1})**
DW4	↑↑	1.1E–04	5.0E–06	1.98	21	10	34.5	–0.21	7.2
DW5		1.1E–04	3.7E–05	0.26	21	10	17.9	0.06	0.9
DW9		4.6E–05	3.1E–05	0.25	21	10	4.6	1.66	0.9
DW17	↑↓	4.6E–05	5.3E–06	1.54	21	10	10.5	0.45	5.6
DW18		4.6E–05	3.1E–05	0.25	21	10	5.4	1.37	0.9

6.4.2 Wastewater Treatment

During the ozonation of Kraft pulp mill effluents, the overall pseudo-first-order ozone specific utilization rate constant (k_w) ranged from 1,000 to 5,000 s^{-1} and the enhancement factor (E) ranged from 2 to 10 (Zhou and Smith, 1999). Also, the local mass transfer coefficient (k_L) ranged from 0.066 to 0.093 ms^{-1} and the overall mass transfer coefficient (k_La) ranged from 8.3 x 10^{-3} to 2.5 x 10^{-2} s^{-1}.

In order to examine the effects of Pe_L and k_La on the dissolved ozone, gaseous ozone, and superficial gas velocity profiles in bubble columns for wastewater treatment applications, the following typical conditions for the operation of ozonation systems were assigned as the base values for the numerical analyses: column height (L) = 5,000 mm, ozone concentration in the feed gas (C_0) = 1 % (w/w %), applied ozone dosage = 1.35 mg/L, mean hydraulic detention time = τ = 180 s, Pe_L = 5.0, k_w = 0.5 s^{-1}, k_La = 5 x 10^{-3} s^{-1}, k_L = 8 x 10^{-4} ms^{-1}, bubble column aspect ratio = L/D = 12.5, and gas-to-liquid flow ratio (G/L) = 0.1. The Henry's law constant (H) was set equal to 0.22 $kPaLmg^{-1}$ (Sotelo *et al.*, 1989). The liquid-phase temperature was assumed to be 20 °C. The basic model input parameters were then calculated and for the ADM as an example they were as follows: Peclet number (Pe_L) = 5.0, liquid-phase Stanton number (St_L) = 0.9, gas-phase Stanton number (St_G) = 2.07, Damköhler number (D_a) = 89, M = 0.037, α (see Table 6.3) = 0.48, and the dimensionless mole fraction of ozone in the feed gas (y_0) = 0.00675. The relatively low values of k_w and M were chosen for the models' simulations to investigate the effect of chemical reactions when they occur simultaneously near and/or at the gas-liquid interface and in the bulk liquid as it is usually the case when treating wastewaters that have relatively low reactivity towards ozone. The basic value assigned for Pe_L represents the typical mixing conditions that are normally encountered in ozone contactors of similar aspect ratios to the one assumed for the models' simulations. With respect to k_La, the chosen value of 5.0 x 10^{-3} s^{-1} represents the ozone mass transfer conditions that are usually encountered in wastewaters of relatively low reactivity towards ozone. The sensitivity analyses of the models' predictions to changes in Pe_L and k_La, respectively, were performed by varying each one of the two parameters while maintaining the other one constant.

6.5 RESULTS AND DISCUSSION

6.5.1 Water Treatment: Initial Testing of the Models

Figures 6.4 and 6.5 for the co-current and the counter-current flow modes, respectively, illustrate the applicability of the steady-state ADM and BFCM to describe the performance of ozone bubble columns in which conventional fine bubble diffusers were used as the gas spargers.

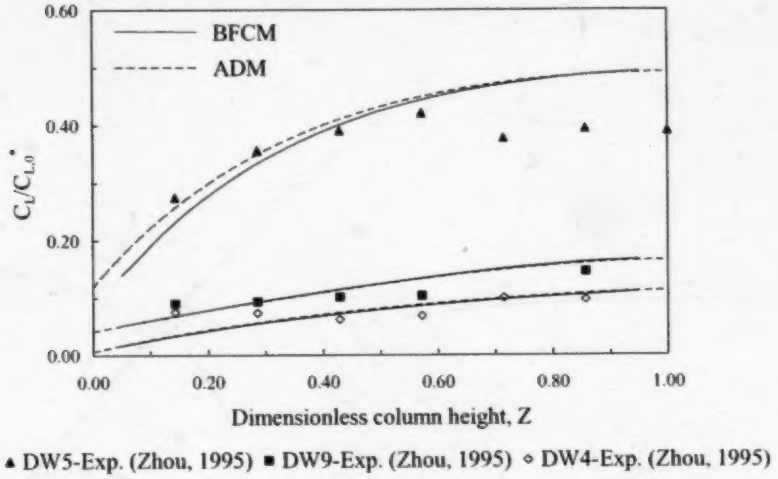

Figure 6.4 Comparison between the predicted and the measured dissolved ozone concentrations in a co-current bubble column for water treatment applications.

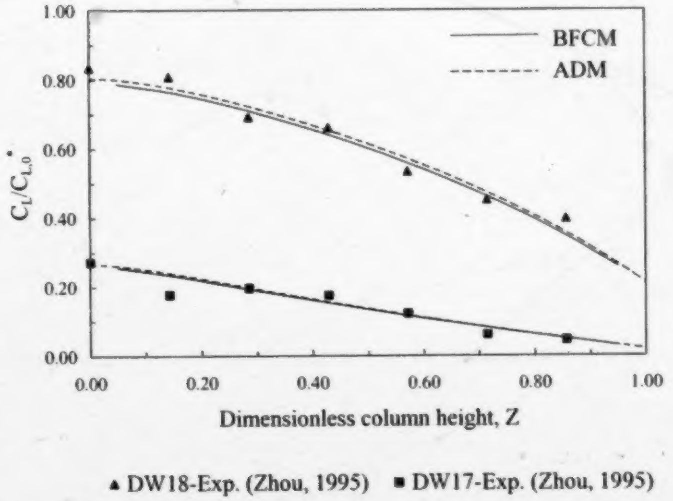

Figure 6.5 Comparison between the predicted and the measured dissolved ozone concentrations in a counter-current bubble column for water treatment applications.

The two models predicted virtually identical dissolved ozone concentration profiles except for run DW5 (co-current flow mode), where the two models were slightly different in their predictions in the vicinity of the column entrance (first quarter of the total column height). That could be explained by the concentration jump (due to the backmixing) predicted by the ADM at the column entrance being somewhat higher than it should be as a result of assigning a lower value to the Pe_L as one of the operating parameters in the ADM simulations. Generally, the two models were capable of providing good predictions of the dissolved ozone concentration profiles with the exception of few data points where the predicted concentrations were slightly deviated from the measured concentrations.

6.5.2 Wastewater Treatment

The dissolved ozone, gaseous ozone, and superficial gas velocity profiles were virtually identical for the co-current and the counter-current flow modes with the exception that the dissolved ozone concentration profiles did not exhibit a concentration jump near the bottom of the column for the case of ADM predictions in the counter-current flow mode. As shown in Figures 6.6 to 6.9, the profiles of the dissolved ozone, the gaseous ozone, and the superficial gas velocity are presented as functions of the dimensionless axial co-ordinate (Z) in the co-current flow mode. The effects of the superficial liquid velocity (u_L) and the superficial gas velocity (u_G) were investigated together by studying the effects of the overall mass transfer coefficient (k_La). This is because the liquid-phase dimensionless Stanton number (St_L) and the gas-phase dimensionless Stanton number (St_G) take into account the effects of u_L and u_G, respectively, and both St_L and St_G are directly proportional to k_La.

As shown in Figure 6.6 and Figure 6.8, the ADM predicted a peak of the dissolved ozone profiles near the bottom of the column $(Z\langle 0.1)$. This concentration jump is due to the boundary condition applied at the column inlet under the co-current flow conditions. The same phenomenon was reported before by several researchers (Levenspiel, 1972; Zhou *et al.*, 1994; Zhou and Smith, 1994; Zhou, 1995; Gamal El-Din and Smith, 2000a).

The BFCM did not predict the same concentration jump due to the fact that only 10 cells were used for the model simulations and complete mixing was assumed to take place in each cell. The dissolved ozone concentration profiles started from their highest points near the bottom of the column then monotonically decreased along the column height. In both models' predictions, the gradient of the dissolved ozone profiles exhibited a decreasing trend near the bottom of the column, followed by an increasing trend. The two models were more sensitive to changes in k_La than changes in Pe_L in their predictions of the dissolved ozone profiles.

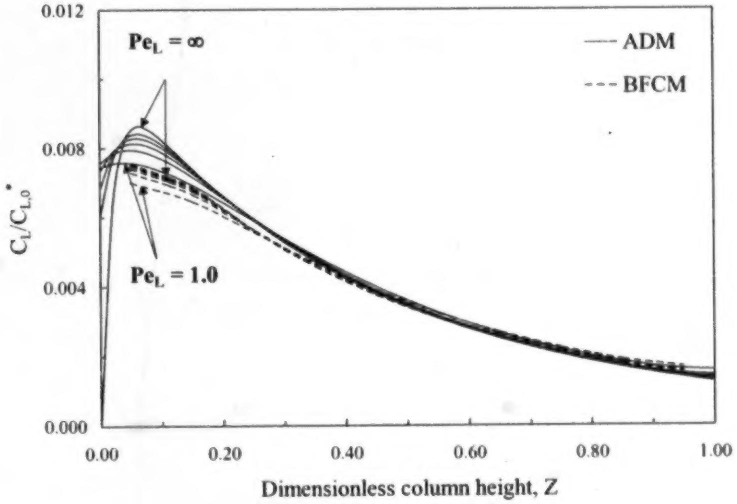

Figure 6.6 Effect of Pe_L on the dissolved ozone profiles in the co-current flow mode for wastewater treatment applications ((Pe_L = 1.0, 2.5, 5.0, 10.0, 20.0, and ∞), $D_a = 89$, $k_La = 5.0 \times 10^{-3}\ s^{-1}$, $M = 0.037$, $\alpha = 0.48$, and $y_0 = 0.00675$).

The effect of backmixing, characterized by Pe_L, on the dissolved ozone profiles are shown in Figure 6.6. As Pe_L increased, the extent of backmixing decreased as the liquid flow was approaching plug flow conditions. Therefore, the dissolved ozone profile became steeper and the peak of the profile increased. Also as Pe_L increased and at a dimensionless co-ordinate beyond $Z \cong 0.25$, the dissolved ozone concentration profiles became steeper leading to lower effluent-residual ozone concentrations.

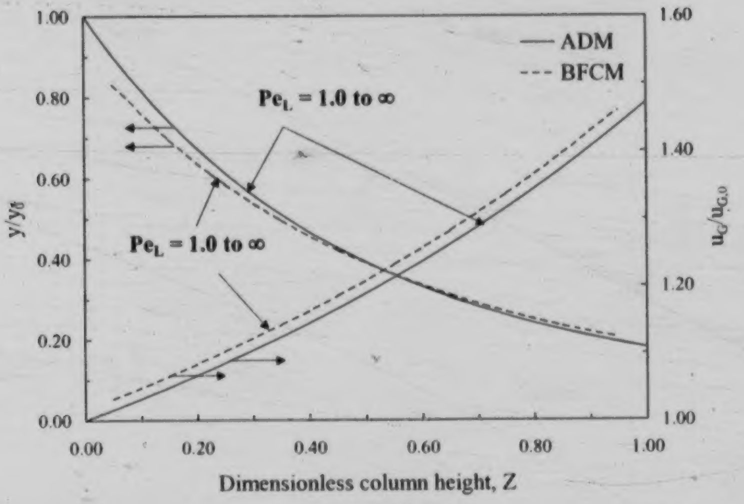

Figure 6.7 Effects of Pe_L on the gaseous ozone and the superficial gas velocity profiles in the co-current flow mode for wastewater treatment applications ((Pe_L = 1.0, 2.5, 5.0, 10.0, 20.0, and ∞), D_a = 89, $k_La = 5.0 \times 10^{-3}$ s^{-1}, M = 0.037, $\alpha = 0.48$, and $y_0 = 0.00675$).

This phenomenon could be explained by the fact that most of the gaseous ozone would be consumed before reaching the end of the column height, and thus, resulting in a lower driving force for the mass transfer process and causing lower ozone residuals in the effluent. Regarding the predictions of the ADM and the BFCM, the effect of Pe_L was higher in the range of Pe_L from 1.0 to 2.5 than in the range of Pe_L from 2.5 to infinity. With respect to the effect of Pe_L and compared to the BFCM, the ADM predicted higher dissolved ozone concentrations with the exception in the top quarter of the column where it predicted lower concentrations.

As shown in Figure 6.8 and as k_La increased from 1×10^{-3} to 5×10^{-3} s^{-1}, an increase in the dissolved ozone concentrations occurred along the entire height of the column. Then as k_La increased from 5×10^{-3} to 1×10^{-2} s^{-1}, an increase in the dissolved ozone concentrations occurred in the bottom half of the column. Finally, as k_La increased from 1×10^{-2} to 2×10^{-2} s^{-1}, an increase in the dissolved ozone concentrations occurred in the bottom quarter of the column. Based on these observations, more efforts should be directed towards enhancing the mass transfer process in the vicinity of the column entrance that could lead to higher treatment levels in ozone bubble columns. Therefore, the use of new gas sparging techniques such as venturi injectors could improve the mass transfer process, and consequently, lead to higher ozonation treatment levels. The venturi injectors can be used to create two-phase impinging turbulent jets in the ambient fluid that can lead to an increase in the mass transfer rates by maximizing the turbulence produced in the liquid phase.

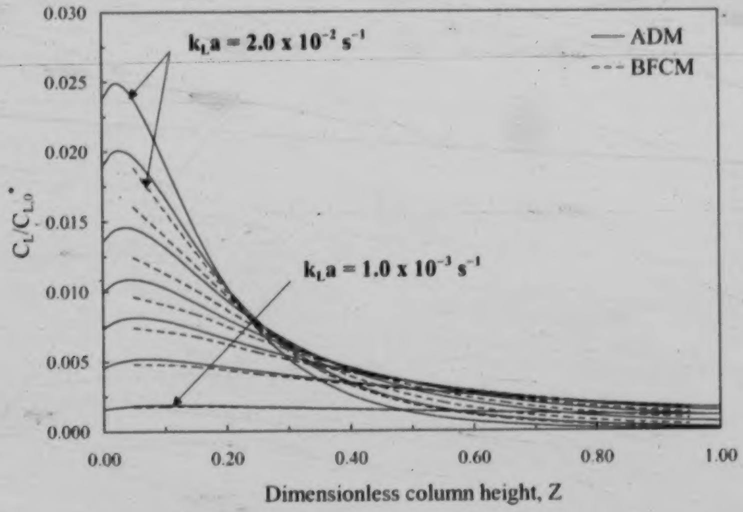

Figure 6.8 Effect of k_La on the dissolved ozone profiles in the co-current flow mode for wastewater treatment applications (($k_La = 1.0 \times 10^{-3}$, 3.0×10^{-3}, 5.0×10^{-3}, 7.0×10^{-3}, 1.0×10^{-2}, 1.5×10^{-2}, and $2.0 \times 10^{-2}\ s^{-1}$), $Pe_L = 5.0$, $D_a = 89$, $M = 0.037$, $\alpha = 0.48$, and $y_0 = 0.00675$).

As shown in Figure 6.8 and regarding the effect of k_La, the ADM predicted higher dissolved ozone concentrations than those predicted by the BFCM with the exception in the top half of the column where it predicted lower concentrations.

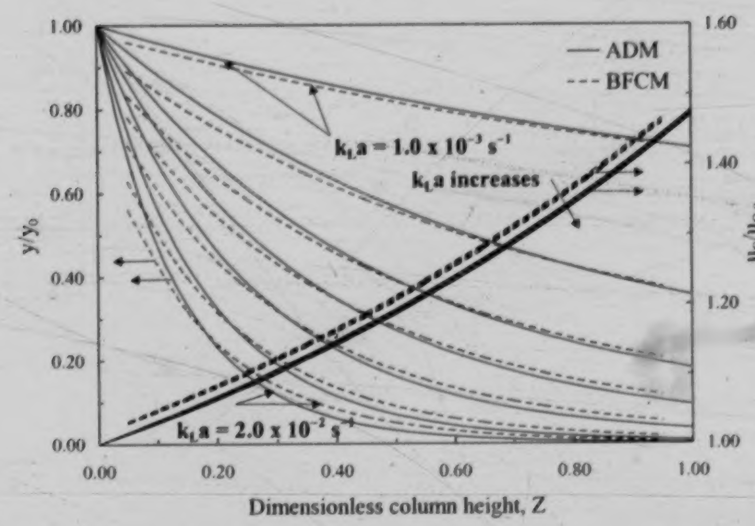

Figure 6.9 Effects of k_La on the gaseous ozone and the superficial gas velocity profiles in the co-current flow mode for wastewater treatment applications (($k_La = 1.0 \times 10^{-3}$, 3.0×10^{-3}, 5.0×10^{-3}, 7.0×10^{-3}, 1.0×10^{-2}, 1.5×10^{-2}, and $2.0 \times 10^{-2}\ s^{-1}$), $Pe_L = 5.0$, $D_a = 89$, $M = 0.037$, $\alpha = 0.48$, and $y_0 = 0.00675$).

As shown in Figure 6.7 and Figure 6.9, the two models predicted that the gaseous ozone concentration profiles would decrease monotonically along the column height as the ozone in the gas phase would be continuously depleted along the column height during the gas absorption process. The axial gradient of the gaseous ozone profiles exhibited an increasing trend along the column height. As shown in Figure 6.9 and at higher k_La values, the decreasing trend of the gaseous ozone profile was faster. This could be explained by the mass transfer rates being high enough to cause faster depletion of the gaseous ozone.

As shown in Figure 6.7 and Figure 6.9, both models were sensitive in their predictions of the gaseous ozone profiles to changes in k_La while the predicted gaseous ozone profiles were virtually insensitive to changes in Pe_L. As shown in Figure 6.7 and Figure 6.9, the two models predicted that the superficial gas velocity would increase monotonically along the column height with both models being slightly sensitive to changes in k_La and virtually insensitive to changes in Pe_L. The BFCM predicted slightly higher superficial gas velocities than those predicted by the ADM. As Z increases, the mass transfer rate would decrease and further ozone gas depletion would occur leading to gas-phase shrinkage. Also, a gas-phase expansion would occur due to the decreasing hydrostatic pressure along the column height. The effect of the gas-phase expansion would be higher than that of the gas-phase shrinkage, and as a result, the superficial gas velocity would increase along the column height. Generally, the gradient of the superficial gas velocity profiles exhibited an increasing trend along the column height.

In the co-current and the counter-current flow modes, the maximum predicted dissolved ozone concentration was observed at the highest k_La. Under the same operating conditions and in the counter-current and the co-current flow modes, the two models predicted virtually identical dissolved ozone concentrations (0.13 and 0.11 mgL^{-1}, respectively) at the highest k_La (2×10^{-2} s^{-1}). These predicted low dissolved ozone concentrations are in agreement with the experimental observations of Zhou and Smith (1997 and 2000).

The predicted off-gas ozone concentration ranged from 9.50 to 0.02 mgL^{-1} at k_La ranging from 1×10^{-3} to 2×10^{-2} s^{-1} which suggests that most of the amount of the applied ozone would be absorbed near the bottom of the ozone contactor. During the ozonation experiments conducted by Zhou and Smith (2000) on Kraft pulp mill effluents, the enhancement factor (E) was > 2 (i.e., M > 4) and the typical k_La value was 1.7×10^{-2} s^{-1}. Under such high M and k_La conditions, they reported that the off-gas ozone concentration was always below the detection limit (0.03 mgL^{-1}) of the modified KI method. Those observations by Zhou and Smith (2000) are in agreement with the current models' predictions of the off-gas ozone concentrations under high k_La conditions.

6.6 CONCLUSIONS

The axial dispersion model (ADM) and the back flow cell model (BFCM) have proven to be sufficient and reliable in their predictions of the performance of ozone bubble columns, however, the BFCM was easier to formulate and solve.

For wastewater treatment applications and with all the operating conditions being the same, the ADM and the BFCM predicted that the counter-current and the co-current flow modes would exhibit similar characteristics with respect to the dissolved ozone, gaseous ozone, and superficial gas velocity profiles. Changes in the backmixing coefficient, represented by changes in Pe_L, had relatively small effect on the dissolved ozone concentration profiles and virtually no effect on the gaseous ozone concentration and superficial gas velocity profiles. On the other hand, changes in the overall mass transfer coefficient (k_La) had large effects on the dissolved ozone and gaseous ozone profiles and a very small effect on the superficial gas velocity profiles.

Reliable and accurate quantification of the dissolved ozone concentrations is essential for achieving optimized designs and operations of ozone contactors. Additional information on the performance of the models can be developed through the examination of their sensitivity to changes in the other operating parameters including k_w, and M. The sensitivity analyses should be conducted using typical operating conditions that are often used in the operations of ozone bubble columns.

6.7 REFERENCES

1. Alvarez-Cuenca, M. and M.A. Nerenberg, "Oxygen Mass Transfer in Bubble Columns Working at Large Gas and Liquid Flow Rates", AIChE J. 27(1): 66-73 (1981).
2. Alvarez-Cuenca, M., C.G.J. Baker, and M.A. Bergougnou, "Oxygen Mass Transfer in Bubble Columns", Chem. Eng. Sci. 35: 1121-1127 (1980).
3. Chang, B.-J. and E.S.K. Chian, "A Model Study of Ozone-Sparged Vessels for the Removal of Organics from Water", Wat. Res. 15: 929-936 (1981).
4. Danckwerts, P.V., *Gas-Liquid Reactions* (NY, USA: McGraw-Hill, Inc., 1970).
5. Deckwer, W.-D. and J. Hallensleben, "Exclusion of Gas Sparger Influence on Mass Transfer in Bubble Columns", Canadian J. Chem. Eng. 58: 190-196 (1980).
6. Gamal El-Din, M. and D.W. Smith, "Designing Ozone Bubble Columns: A Spreadsheet Approach to Axial Dispersion Model", *Proc. of IOA/PAG Conf.: Advances in Ozone Technology*, Orlando, FL, USA, 2000a.
7. Gamal El-Din, M. and D.W. Smith, "Ozone Mass Transfer in Water Treatment: Hydrodynamics and Mass Transfer Modeling of Ozone Bubble Columns", *Proc. of the Water Supply and Water Quality Conf.*, Kraków, Poland, 2000b.
8. Hull, C.S., P.C. Singer, K. Saravanaan, and C.T. Miller, "Ozone Mass Transfer and Reaction: Completely Mixed Systems", *Proc. of the Annual AWWA Conf.: Water Quality*, Vancouver, BC, Canada, 1992.
9. Kaštánek, J., J. Zahradník, J. Kratochvíl, and J. Čermák, *Chemical Reactors for Gas-Liquid Systems* (Chichester, England: Ellis Horwood, 1993).
10. Langlais, B., D.A. Reckhow, and D.R. Brink, *Ozone in Water Treatment: Application and Engineering* (MI, USA: Lewis Publishers, Inc., 1991).
11. Laplanche, A., N. Le Sauze, G. Martin, and B. Langlais, "Simulation of Ozone Transfer in Water: Comparison with a Pilot Unit", Ozone Sci. & Eng. 13(5): 13, 535-558 (1991).
12. Levenspiel, O., *Chemical Reaction Engineering, 2nd ed.* (NY, USA: John Wiley and Sons, Inc., 1972).

13. Lev, O. and S. Regli, "Evaluation of Ozone Disinfection Systems: Characteristic Contact Time T", J. Environ. Eng., ASCE 118(2): 268-285 (1992).

14. Mecklenburgh, J.C. and S. Hartland, *The Theory of Backmixing*, (New York, NY, USA: John Wiley and Sons, Inc., 1975), pp. 1-32.

15. Sotelo, J.L., F.J. Beltrán, F.J. Benitez, and J. Beltrán-Heredia, "Henry's Law Constant for the Ozone-Water System", Wat. Res. 23: 1239-1246 (1989).

16. TKSOLVER^{TM}, Release 3.32, Universal Technical Systems, Inc., IL, USA (1997).

17. Watt, R.D., E.J. Kirsch, and C.P.Jr. Leslie Grady, "Ozone Consumption Kinetics in Filtered Activated Sludge Effluents: A Modified Approach", Wat. Res. 23: 471-480 (1989).

18. Zhou, H. and D.W. Smith, "Applying Mass Transfer Theory to Study the Kinetics of Fast Ozone Reactions in Pulp Mill Effluents", *Proc. of the 14th Ozone World Congress*, Detroit, MI, USA, 1999.

19. Zhou H. and D.W. Smith, "Ozonation Dynamics and its Implications for Off-Gas Ozone Control in Treating Pulp Mill Wastewaters", Ozone Sci. Eng. 22: 31-51 (2000).

20. Zhou, H. and D.W. Smith, "Process Parameter Development for Ozonation of Kraft Pulp Mill Effluents", Wat. Sci. & Technol. 35(2-3): 251-259 (1997).

21. Zhou H. and D.W. Smith, "Theoretical Analysis of Ozone Disinfection Performance in a Bubble Column", Ozone Sci. Eng. 16: 429-441 (1994).

22. Zhou, H., *Investigation of Ozone Disinfection Kinetics and Contactor Performance Modeling: Ph.D. Thesis* (Edmonton, AB, Canada: University of Alberta, 1995).

23. Zhou, H., D.W. Smith, and S.J. Stanley, "Modeling of Dissolved Ozone Concentration Profiles in Bubble Columns", J. Environ. Eng., ASCE 120(4): 821-840 (1994).

CHAPTER 7. DESIGNING OZONE BUBBLE COLUMNS: A SPREADSHEET APPROACH TO AXIAL DISPERSION MODEL*

7.1 INTRODUCTION

Based on a literature review, it was found that most of the models that dealt with ozone contactors were directed to the water treatment applications with very little done to model the ozonation process for wastewater treatment. Most of the models are two-phase flow (i.e., gas-liquid) models that are applied to predict the dissolved and the gaseous ozone profiles along bubble columns. In order to simplify the design process of ozone bubble columns, a large number of the models were based on one of the following two liquid-phase flow regimes: (1) complete mixing or; (2) plug flow (Alvarez-Cuenca *et al.*, 1980; Alvarez-Cuenca *et al.*, 1981; Chang and Chian, 1981; Laplanche *et al.*, 1991; Hull *et al.*, 1992; Lev and Regli, 1992). Although, the actual flow pattern in bubble columns is usually closer to being mixed flow rather than plug flow, but still not completely mixed flow. Zhou *et al.* (1994) modeled the performance of ozone bubble columns by using the 2P-ADM and an elaborate numerical technique was needed to solve the model equations. The 2P-ADM demonstrated excellent capability of predicting the dissolved ozone profiles in bubble columns.

The design of ozone bubble columns usually encounter two major sources of uncertainties: (1) the complications and unreliable methods utilized for measuring and estimating operating parameters of bubble columns; and (2) the application of the pertinent design model, particularly, when designing an ozonation treatment facility for a complicated chemical system such as the effluents from the pulping and bleaching processes. Although constructing ozone contactors is an easy task, optimizing their operations is not as simple. The operating parameters of ozone contactors are interrelated and thus, they cause difficulty in the design, operation, and scale-up. Therefore, reliable and accurate methods of measuring and estimating such parameters should be applied.

A version of this chapter has been accepted for publication. Gamal El-Din, M. and D.W. Smith, Ozone Sci. & Eng. (June 2001).

A number of processes occur simultaneously during the ozonation process. Those processes are: the convection and the backmixing processes of the liquid and gas phases flowing through the contacting chamber; the ozone gas mass transfer process; the ozone auto-decomposition process, and the competitive reactive processes of the constituents in water and wastewater with dissolved ozone (Zhou *et al.*, 1994). Besides those processes, the contactor configuration, the operating conditions, and the water or wastewater quality influence the overall performance of the ozonation process (Zhou, 1995). For any ozonation system, it is crucial to quantify the dissolved ozone to achieve reliable rational design and optimum operation of ozone contactors. Meanwhile, quantifying the gaseous ozone, i.e., the ozone off-gas leaving the contactor, is essential for achieving optimum and reliable design of the off-gas destruction facilities.

Several studies have been conducted to study the fundamentals of the processes that control the performance of ozone contactors in water treatment over the past decades with a fewer number of studies aimed at investigating the ozone mass transfer mechanisms and the effect of chemical reactions on the rate of ozone absorption when treating industrial wastewater. Heinzel *et al.* (1992) could not detect any dissolved nor gaseous ozone when they studied the ozonation of the wastewater generated from the chlorine bleaching and the proceeding alkaline extraction processes after being passed through a biological treatment. As the ozone dose increased to 250 mgL^{-1} or higher, ozone off-gas began to exit the system and it was detected at levels that increased gradually as the ozone dose increased. Meanwhile, as the ozone dose reached 500 mgL^{-1} or higher, they started detecting dissolved ozone. Similar observations were reported by Beltrán *et al.* (1995) as they investigated the ozonation of distillery and tomato industrial wastewater in a laboratory-scale bubble column. During the ozonation of pulp mill effluents, Zhou and Smith (2000) simulated the pilot-scale bubble column operations in the counter-current and the co-current flow conditions using a number of CFSTR's in series ranging from 8 to 39. The ozone off-gas concentrations were predicted to be lower than 0.01 mgL^{-1} while the measured concentrations were lower than 0.03 mgL^{-1}. The low off-gas concentrations could be a result of the initial chemical reactions being fast enough for the dissolved ozone to be completely depleted at the gas-liquid interface and/or within the liquid film during the course of ozonation of Kraft pulp mill effluents as reported before by Zhou and Smith (1997). Consequently, the dissolved ozone gradient became steeper than the gradient of the maximum physical ozone absorption process. Based on that, they assumed that the fast or instantaneous-reaction regime prevailed for the gas absorption process when ozonating pulp mill effluents. Two distinct reaction kinetics regimes were defined as shown in Figure 7.1: (1) the slow-reaction kinetics regime; and (2) the fast or instantaneous-reaction kinetics regime. In the fast-reaction kinetics regime and because of the low dissolved ozone concentrations, the driving force of the mass transfer process is increased and also the local mass transfer coefficient is enhanced by an enhancement factor (E). This factor is defined as the actual rate of mass transfer with the occurrence of chemical reactions divided by the maximum rate of physical absorption with no occurrence of chemical reactions.

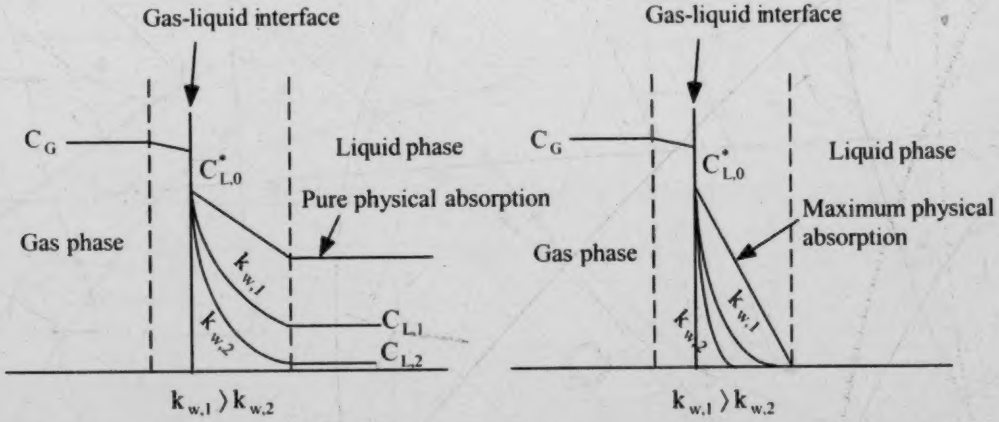
Gas-liquid interface
C_G
$C^*_{L,0}$
Liquid phase
Pure physical absorption
Gas phase
$k_{w,1}$
$k_{w,2}$
C_{L1}
C_{L2}
$k_{w,1} \rangle k_{w,2}$
Gas-liquid interface
C_G
$C^*_{L,0}$
Liquid phase
Maximum physical absorption
Gas phase
$k_{w,2}$
$k_{w,1}$
$k_{w,1} \rangle k_{w,2}$

a- slow-reaction regime

b- fast or instantaneous-reaction regime

Figure 7.1 Reaction kinetics regimes for ozone absorption process (adapted from Zhou and Smith, 1997).

This chapter presents: (1) a detailed formulation of the one-phase axial dispersion model (1P-ADM) to provide a simple and accurate method to predict the performance of the counter-current and the co-current ozone contactors for ozone applications in water and wastewater treatment; and (2) initial model testing for ozone applications in water treatment using the pilot-scale experimental data of Zhou (1995).

7.2 DISPERSION MODELS FOR TWO-PHASE FLOWS

7.2.1 Process Fundamentals

There are several models that account for backmixing in the liquid phase. Among those models that are available for predicting the performance of bubble columns, is the axial dispersion model (ADM). In the ADM, a diffusion-like process is assumed and superimposed on a plug flow (Levenspiel, 1972). An empirical Fick's law is applied by replacing the molecular diffusion coefficient by the axial dispersion coefficient (D_L) as the mixing parameter:

$$\text{Diffusive mass flux} = -D_L \frac{\partial C_L}{\partial \ell} \qquad [7.1]$$

where: C_L = dissolved ozone concentration (mgL^{-1}) and D_L = axial dispersion coefficient (m^2s^{-1}). In the D_L, the effects of the non-uniform velocity profile (shear dispersion), the molecular, and eddy diffusivities are lumped together.

The overall ozone auto-decomposition rate is influenced by the concentration and the history of the ozonation process and this ozone auto-decomposition process could be represented by a modified pseudo-first-order rate expression (Yurteri and Gurol, 1988; Oke *et al.*, 1998). In the experimental study of Oke *et al.* (1998), it was shown that the commonly used first-order kinetics expression with a constant reaction rate constant was inadequate in describing the ozone auto-decomposition process especially in situations where the initial ozone demand was significant. It was demonstrated that the reaction rate constant was continuously decreasing along the course of ozonation as a result of the changes in the water characteristics. As a result, an exponentially decreasing function was proposed as a better alternative to describe the ozone auto-decomposition kinetics (Oke *et al.*, 1998). In that expression, the reaction rate constant was replaced by a variable referred to as the specific ozone utilization rate constant (k_w) that is a function of the utilized ozone dose (ΔO_3):

$$\frac{dC_L}{dt} = -k_w C_L = -\left(k_1 + k_2 e^{-k_3 \Delta O_3}\right) C_L \qquad [7.2]$$

where: C_L = instantaneous dissolved ozone concentration (mgL^{-1}), k_w = specific ozone utilization rate constant (s^{-1}), k_1 = empirical non-linear regression constant (s^{-1}), k_2 = empirical non-linear regression constant (s^{-1}), k_3 = empirical non-linear regression constant (Lmg^{-1}), t = reaction time (s), and ΔO_3 = amount of the utilized ozone (mgL^{-1}). k_1, k_2, and k_3 are empirical constants that can be obtained by applying non-linear regression analysis to the kinetics data and they are also characteristics of the water to be treated. As shown in Equation 7.2, as the utilized ozone dose increases along the course of ozonation k_w will decrease. At the beginning of the ozonation, i.e., when the amount of the utilized ozone is zero, k_w is equal to $k_1 + k_2$ as the ozone decay process is only attributed to the initial ozone demand. In the Oke *et al.* (1998) study and for clean deionized water, the initial ozone demand was practically equal to zero and therefore, k_w could be assumed constant during the course of the ozonation.

The two-film model is usually used to describe the absorption of ozone gas from the gas phase into the liquid phase. In this model, the gas-absorption rate (ψ) is defined as:

$$\psi = k_L a\left(C_L^{*} - C_L\right) \qquad [7.3]$$

where: ψ = gas-absorption rate ($mgL^{-1}s^{-1}$), k_L = local liquid mass transfer coefficient (ms^{-1}), a = specific gas bubbles' interfacial area (m^{-1}), C_L^{*} = concentration of the dissolved ozone in equilibrium with the bulk ozone gas (mgL^{-1}), and C_L = concentration of the dissolved ozone in the bulk liquid (mgL^{-1}). Due to the fact that ozone gas diffuses much faster in the gas phase than in the liquid phase, the mass transfer in the liquid phase is assumed to be the rate-controlling step. Consequently, the overall mass transfer coefficient (k_La) is considered to entirely consist of the local mass transfer coefficient in the liquid phase.

7.2.2 Mass Transfer Process with Chemical Reactions

Chemical reactions occur during the ozonation of wastewater. In such applications, the dimensionless squared Hatta number ($H_a^2 = M$) is often applied to compare between the amount of dissolved gas that reacts at the gas-liquid interface or in the liquid film near the interface and the amount of dissolved gas that reaches the bulk liquid in an unreacted state:

$$H_a^2 = E^2 = M = \frac{Dk_w}{k_L^2} \qquad [7.4]$$

where: $H_a = E = \sqrt{M}$ = dimensionless Hatta number, k_L = local mass transfer coefficient (ms^{-1}), D_{O_3} = molecular diffusivity of ozone gas in water (m^2s^{-1}), and k_w = specific ozone utilization rate constant (s^{-1}). For pseudo-first-order irreversible reactions, the location of those reactions that take place during the gas absorption process could be classified into two categories (Kramers and Westertrep, 1963; Kaštánek *et al.*, 1993). Reactions would take place in the bulk of the liquid or at the gas-liquid interface and/or in the liquid film near the interface at $H_a < 0.03$ and $H_a > 5.00$, respectively (Kramers and Westertrep, 1963; Kaštánek *et al.*, 1993). Although, generally for bubble columns it can also be assumed that at that at $H_a > 3.00$, reactions would still be fast enough to occur predominantly at the gas-liquid interface and/or in the liquid film near the interface (Kaštánek *et al.*, 1993). Therefore, reactions would simultaneously take place in both regions at $0.03 < H_a < 3.00$. Equation 7.4 is only applicable in situations where two conditions have to be satisfied: (1) $\sqrt{M} >> 1$; and (2) fast or instantaneous irreversible first-order reactions with no bulk liquid concentration where the driving force for the mass transfer process will be maximized (Danckwerts, 1970). As a result, Equation 7.3 becomes:

$$\psi = Ek_L aC_L^{*} \qquad [7.5]$$

where: Ek_La = enhanced overall mass transfer coefficient (s^{-1}). Zhou and Smith (1999) proposed that for wastewater ozonation, both the ozone auto-decomposition and its reactions with the organic and inorganic constituents in wastewater could be lumped together in a first-order rate constant (k_w). Danckwerts (1970) proposed the following equation for the conditions when $M > 0$ and $C_L > 0$:

$$\psi = k_L a\sqrt{1+M}\left(C_L^* - \frac{C_L}{1+M}\right) \qquad [7.6]$$

When $M >> 1$ and C_L approaches zero (i.e., $C_L \cong 0$), Equation 7.6 reduces to Equation 7.5. The effects of chemical reactions on the local mass transfer coefficient for an irreversible first-order reaction could be neglected and the gas absorption could be dealt with as pure physical absorption when M approaches zero (Danckwerts, 1970). Therefore, this assumption is valid when:

$$H_a^2 = M = \frac{Dk_w}{k_L^2} << 1 \qquad [7.7]$$

k_w was reported to be equal to $4.7 \times 10^{-4}\ s^{-1}$ for the deionized water tested by Zhou (1995). Yurteri and Gurol (1988) reported that k_w was in the order of $2.8 \times 10^{-3}\ s^{-1}$ for the tested raw surface water. The diffusivity of ozone in water was determined by the Wilke-Chang formula to be $1.74 \times 10^{-9}\ m^2s^{-1}$ (at 20 °C) which is comparable to the value of $1.71 \times 10^{-9}\ m^2s^{-1}$ obtained using the equation recommended by Johnson and Davis (1996). k_L was reported to be in the order of $3.1 \times 10^{-4}\ ms^{-1}$ for clean water and in the order of $1.9 \times 10^{-4}\ ms^{-1}$ for water containing organic substances (Beltrán *et al.*, 1997). Substituting for these typical values of D, k_w, and k_L into Equation 7.4 yields squared-Hatta numbers of 8.5×10^{-6} and 1.4×10^{-4} for the deionized and the surface water, respectively. Based on these small Hatta numbers, it can be concluded that the chemical reactions that occur during the course of clean or surface water ozonation has negligible effect on the local mass transfer coefficient and hence, Equation 7.3 will be applied for ozone absorption without any modification.

7.2.3 Two-Phase Axial Dispersion Model (2P-ADM)

Zhou *et al.* (1994) applied the complete two-phase axial dispersion model (2P-ADM) to study the performance of ozone bubble columns under various operating conditions for water treatment applications. When modeling gas-liquid flows, several assumptions govern the development of the 2P-ADM as reported by Zhou *et al.* (1994). The enhancement factor of the mass transfer process due to the occurrence of chemical reactions was assumed to be negligible (i.e., $M = 0$) as the absorption of ozone gas in water could be considered to take place in the slow-reaction kinetics regime. For wastewater, the fast-reaction kinetics regime was assumed to prevail and the enhancement factor (M) was assumed to be higher than 0.

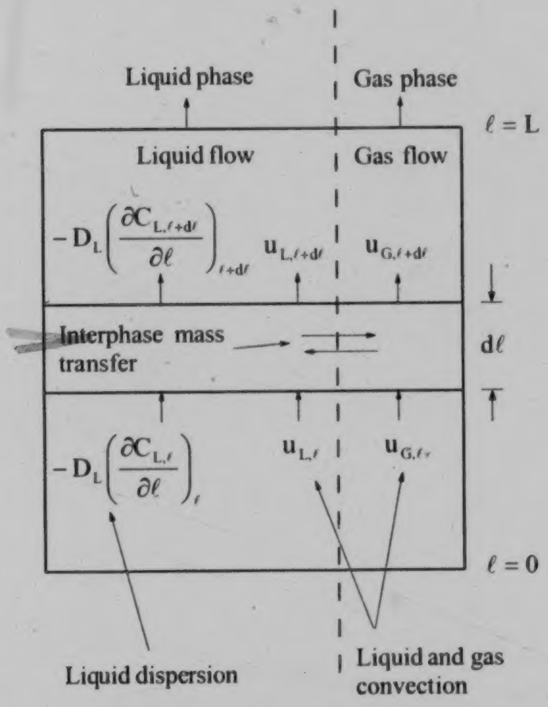
Liquid phase
Gas phase
$\ell = L$
Liquid flow
Gas flow
$-D_L\left(\frac{\partial C_{L,\ell+d\ell}}{\partial \ell}\right)_{\ell+d\ell}$
$u_{L,\ell+d\ell}$
$u_{G,\ell+d\ell}$
Interphase mass transfer
$d\ell$
$-D_L\left(\frac{\partial C_{L,\ell}}{\partial \ell}\right)_{\ell}$
$u_{L,\ell}$
$u_{G,\ell}$
$\ell = 0$
Liquid dispersion
Liquid and gas convection

Figure 7.2 Schematic representation of the co-current ADM.

Considering the control volume shown in Figure 7.2, and conducting mass balance for the liquid and gas phases with respect to the dissolved and the gaseous ozone concentrations and applying mathematical manipulations, one can obtain the generalized model equations for water and wastewater treatment applications as presented in Table 7.2.

Table 7.1 Dimensionless parameters that are used to describe the 1P-ADM and the 2P-ADM.

Dimensionless parameter	**1P-ADM/2P-ADM**
Z	ℓ/L
$\alpha^{\blacklozenge}$	$\rho g \varepsilon_L L/P_T$
$\beta^{\blacklozenge}$	$1+\alpha$
Pe_L	$u_L L/D_L \varepsilon_L$
St_L	$k_L aL/u_L$
St_G	$(k_L aL/u_{G,0})(RT/H)$
D_a	$k_w \varepsilon_L L/u_L$
M	Dk_w/k_L^2
X	$C_{L,\ell}/C^*_{L,0}$
Y	y_ℓ/y_0

Note: ◆ denotes the parameters that are only used in the 2P-ADM.

The boundary conditions pertaining to those equations are the same as those described by Zhou *et al.* (1994). The dimensionless parameters pertaining to those equations are presented in Table 7.1. As shown in Table 7.2, the 2P-ADM is described mathematically by a system of two non-linear partial differential equations that need to be solved simultaneously. A numerical technique must be used to solve those equations by transforming them into non-linear algebraic equations. Therefore, for the design and the process control purposes, solving that system of non-linear algebraic equations becomes complicated and time-consuming. A simple and accurate model needed to be developed to simplify the design process of ozone contactors and for the operators of such contactors to use when modifications to the operating conditions need to be done in order to optimize the performance of ozone contactors.

Table 7.2 Mathematical representation of the 2P-ADM for water and wastewater treatment applications.

Model equations	Aqueous ozone	$\frac{1}{Pe_L}\frac{\partial^2 X}{\partial Z^2} + I\frac{\partial X}{\partial Z} + \frac{\sqrt{1+M}St_L}{\beta}(\beta - \alpha Z)Y - \left(\frac{St_L}{\sqrt{1+M}} + D_a\right)X = 0$
	Gaseous ozone	$\frac{\partial Y}{\partial Z} + \frac{St_G}{\beta(1-y_0)}(1-y_0 Y)^2\left[\sqrt{1+M}(\beta - \alpha Z)Y - \frac{\beta}{\sqrt{1+M}}X\right] = 0$

Note:

$I = -1$ for co-current flow mode and $I = +1$ for counter-current flow mode.

$M = 0$ for water treatment applications.

7.2.4 Development of the One-Phase Axial Dispersion Model (1P-ADM)

The assumptions pertaining to the modified non-isobaric steady-state one-phase axial dispersion model (1P-ADM) are the same as those used to develop the steady-state 2P-ADM with the exception that the 1P-ADM describes only the liquid phase. In order to account for changes in the superficial gas velocity due to the effects of gas shrinkage and expansion caused by the gas absorption and depletion and the reduced hydrostatic head, respectively, an exponential function was assumed to describe the variation of the gaseous mole fraction along the column height:

$$y_Z = y_\ell = y_0 \exp(-a_1 Z) \qquad [7.8]$$

where: y_0 = gaseous ozone mole fraction in the gas phase at the column entrance, Z = dimensionless axial coordinate of the column, and a_1 = dimensionless coefficient of gaseous ozone mole fraction decrease along the column height. It was assumed that a_1 is a function of Pe_L, St_L, St_G, and D_a for water treatment conditions and a function of Pe_L, St_L, St_G, D_a, and M for wastewater treatment conditions. The proposed exponential model represented by Equation 7.8 was obtained by fitting an exponential function to the theoretical gaseous ozone profiles predicted by the complete axial dispersion model (2P-ADM) in the study conducted by Zhou *et al.* (1994) for water treatment applications under a wide range of operating conditions. For wastewater treatment applications, the 2P-ADMwas executed under a wide range of operating conditions. Then, the model predictions of the gaseous ozone profiles were fitted to an exponential function. The correlation coefficient (r) ranged from 0.90 to 0.99. The proposed exponential model can be considered semi-empirical in its nature since it is based on fitting the exponential function to the ozone gas-phase concentration profiles predicted by the 2P-ADM. There was an attempt to verify the applicability of the exponential model to predict the ozone gas-phase concentration profiles. Figure 7.3 depicts examples of the gaseous ozone profiles for the counter-current and the co-current flow modes for water and wastewater treatment applications.

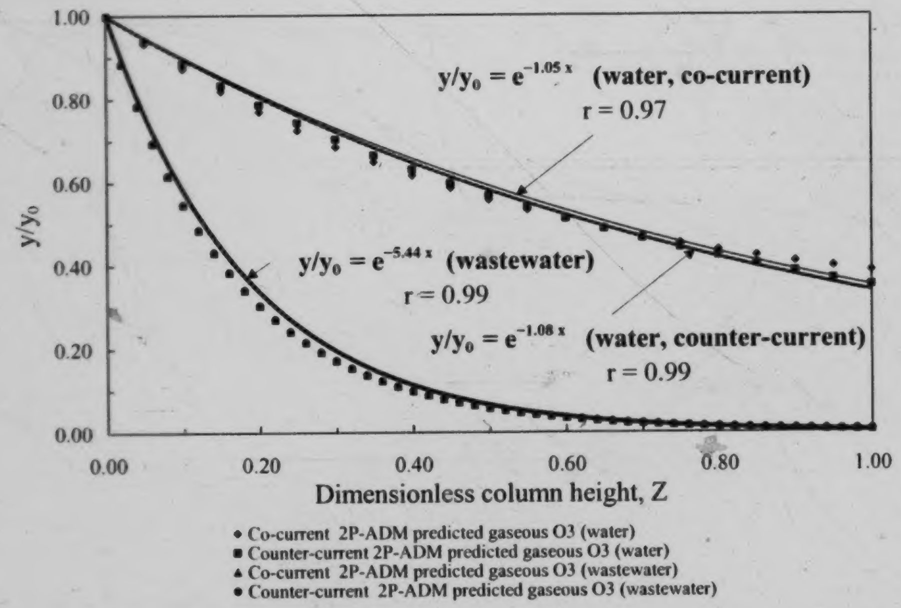

Figure 7.3 Typical gaseous ozone profiles in bubble columns for water and wastewater treatment conditions.

For wastewater treatment applications, the 2P-ADM predicted identical gaseous ozone profiles for the two flow modes, while the profiles were almost identical for water treatment applications. Linear regression technique was applied to correlate between the independent parameter (a_1) and the dependent parameters (Pe_L, St_L, St_G, D_a, and M). The models obtained for water and wastewater treatment applications in the counter-current and the co-current flow modes are presented in Table 7.3. For water treatment applications, the models have some similarities in terms of the number and types of the dependent parameters that were included and they are different in terms of the values of the regression coefficients. The dependent parameter (St_L) was excluded by the linear regression process from the predicted models for the water treatment applications. Interestingly, as shown in Table 7.3, the models for the counter-current and the co-current flow modes are almost identical for wastewater treatment conditions. For water treatment conditions, the correlation coefficient (r) for the linear regression models was 0.99 and 0.97 for the counter-current and the co-current flow modes, respectively. For wastewater treatment conditions, r was equal to 0.99 for both the counter-current and the co-current flow modes.

Table 7.3 Coefficients of the exponential model used for the prediction of the gaseous ozone profiles.

Treatment type	Flow mode	Equations
Water	Co-current	$a_1 = 0.413 + 0.35\,St_G + 1.646\times10^{-3}\,Pe_L + 0.121\,D_a$
	Counter-current	$a_1 = 0.221 + 0.515\,St_G - 8.93\times10^{-3}\,Pe_L + 0.1\,D_a$
Wastewater	Co-current	$a_1 = 0.13 + 0.816\,St_G - 2.71\times10^{-2}\,St_L - 1.04\times10^{-3}\,Pe_L - 3.3\times10^{-7}\,D_a + 0.613\,M$
	Counter-current	$a_1 = 0.129 + 0.817\,St_G - 2.69\times10^{-2}\,St_L - 1.05\times10^{-3}\,Pe_L - 3.29\times10^{-7}\,D_a + 0.612\,M$

Conducting mass balance for the liquid phase in the co-current flow mode and for water treatment conditions yields:

$$\frac{d^2C_{L,\ell}}{d\ell^2}D_L\varepsilon_L - u_L\frac{dC_{L,\ell}}{dl} + k_La(C^*_{L,\ell} - C_{L,\ell}) - k_wC_{L,\ell}\varepsilon_L = 0 \qquad [7.9]$$

Using the relationships of P_ℓ, P_0, and $C^*_{L,\ell}$:

$$P_\ell = P_T + \rho g\varepsilon_L(L - \ell) \qquad [7.10]$$

$$P_0 = P_T + \rho g\varepsilon_L L \qquad [7.11]$$

$$C^*_{L,\ell} = \frac{P_T + \rho g\varepsilon_L(L - \ell)}{H}y_\ell \qquad [7.12]$$

Since:

$$y_Z = y_\ell = y_0\exp(-a_1Z) \qquad [7.13]$$

and

$$Z = \frac{\ell}{L} \qquad [7.14]$$

Therefore, substituting for Equations 7.13 and 7.14 into Equation 7.12 yields:

$$\begin{aligned} C^*_{L,\ell} &= \frac{[P_T + \rho g\varepsilon_L L(1 - Z)]}{H}y_0\exp(-a_1Z) = (P_T + \rho g\varepsilon_L L)\frac{y_0}{H}\exp(-a_1Z) \\ &\quad - \frac{\rho g\varepsilon_L L}{H}y_0Z\exp(-a_1Z) \end{aligned} \qquad [7.15]$$

Equation 7.15 can be re-written as:

$$C^{*}_{L,\ell} = a' y_0 \exp(-a_1 Z) + b' y_0 Z \exp(-a_1 Z) \qquad [7.16]$$

where:

$$a' = \frac{(P_T + \rho g \varepsilon_L L)}{H} \qquad [7.17]$$

and

$$b' = \frac{-\rho g \varepsilon_L L}{H} \qquad [7.18]$$

Re-writing Equation 7.16 as:

$$C^{*}_{L,\ell} = \alpha_1 \exp(-a_1 Z) + \beta_1 Z \exp(-a_1 Z) \qquad [7.19]$$

where:

$$\alpha_1 = a' y_0 \qquad [7.20]$$

and

$$\beta_1 = b' y_0 \qquad [7.21]$$

As a result:

$$C^{*}_{L,0} = \alpha_1 \qquad [7.22]$$

Multiplying Equation 7.9 by $\frac{L}{u_L C^{*}_{L,\ell}}$, substituting for the dimensionless parameters defined in Table 7.1 and Equation 7.22 into the resulting equation, and rearranging, one can obtain:

$$\frac{1}{Pe_L}\frac{dX^2}{dZ^2}-\frac{dX}{dZ}-(St_L+D_a)X+St_L\left[\exp(-a_1Z)+\frac{\beta_1}{\alpha_1}Z\exp(-a_1Z)\right]=0 \qquad [7.23]$$

The general 1P-ADM for the co-current and counter-current flow modes is as follows:

$$\frac{1}{Pe_L}\frac{dX^2}{dZ^2}+I\frac{dX}{dZ}-(St_L+D_a)X+St_L\left[\exp(-a_1Z)+\frac{\beta_1}{\alpha_1}Z\exp(-a_1Z)\right]=0 \qquad [7.24]$$

where: I = −1 for the co-current flow mode and I = +1 for the counter-current flow mode. The boundary conditions pertaining to Equation 7.24 are the same as those for the 2P-ADM. Equation 7.24 is a non-homogeneous linear second-order ordinary differential equation that represents the 1P-ADM. This equation was solved analytically by applying the method of variation of parameters (Kreyszig, 1988). The analytical solution of Equation 7.24 for the co-current flow conditions is as follows:

$$X=\frac{\left[D_1\lambda_2e^{\lambda_2}+E_1\left(1-\frac{\lambda_2}{Pe_L}\right)\right]}{N}\exp(\lambda_1Z)-\frac{\left[D_1\lambda_1e^{\lambda_1}+E_1\left(1-\frac{\lambda_1}{Pe_L}\right)\right]}{N}\exp(\lambda_2Z) \qquad [7.25]$$
$$+K_0\exp(-a_1Z)+K_1Z\exp(-a_1Z)$$

where:

$$\lambda_{\substack{1\\2}}=Pe_L\pm\sqrt{Pe_L^2+4Pe_L(St_L+D_a)} \qquad [7.26]$$

$$K_0 = \frac{Pe_L St_L}{(\lambda_2 - \lambda_1)}\left[\frac{1}{(a_1 + \lambda_2)} + \frac{\beta_1}{\alpha_1 (a_1 + \lambda_2)^2} - \frac{1}{(a_1 + \lambda_1)} - \frac{\beta_1}{\alpha_1 (a_1 + \lambda_1)^2}\right] \quad [7.27]$$

$$K_1 = \frac{-\beta_1 Pe_L St_L}{\alpha_1 (a_1 + \lambda_1)(a_1 + \lambda_2)} \quad [7.28]$$

$$D_1 = X_{inf} - K_0\left(\frac{a_1}{Pe_L} + 1\right) + \frac{K_1}{Pe_L} \quad [7.29]$$

$$E_1 = \left[-(K_0 + K_1)a_1 + K_1\right]\exp(-a_1) \quad [7.30]$$

and

$$N = \left(1 - \frac{\lambda_1}{Pe_L}\right)\lambda_2 \exp(\lambda_2) - \left(1 - \frac{\lambda_2}{Pe_L}\right)\lambda_1 \exp(\lambda_1) \quad [7.31]$$

The same procedure can be followed to obtain the 1P-ADM for the counter-current flow conditions. The general 1P-ADM for the counter-current and the co-current flow modes and for wastewater treatment applications is as follows:

$$\begin{aligned} &\frac{1}{Pe_L}\frac{dX^2}{dZ^2} + I\frac{dX}{dZ} - \left(\frac{St_L}{\sqrt{1+M}} + D_a\right)X + \\ &St_L\sqrt{1+M}\left[\exp(-a_1 Z) + \frac{\beta_1}{\alpha_1} Z \exp(-a_1 Z)\right] = 0 \end{aligned} \quad [7.32]$$

The analytical solution of Equation 7.32 for the co-current flow conditions is as follows:

$$\begin{aligned} X = {} & \frac{\left[D_1\lambda_2 e^{\lambda_2} + E_1\left(1 - \frac{\lambda_2}{Pe_L}\right)\right]}{N}\exp(\lambda_1 Z) - \frac{\left[D_1\lambda_1 e^{\lambda_1} + E_1\left(1 - \frac{\lambda_1}{Pe_L}\right)\right]}{N}\exp(\lambda_2 Z) \\ & + K_0\sqrt{1+M}\exp(-a_1 Z) + K_1\sqrt{1+M}\, Z\exp(-a_1 Z) \end{aligned} \quad [7.33]$$

where: D_1, E_1, and N are defined by Equations 7.29 to 7.31 and:

$$\lambda_{\substack{1\\2}} = Pe_L \pm \sqrt{Pe_L^2 + 4Pe_L\left(\frac{St_L}{\sqrt{1+M}} + D_a\right)} \qquad [7.34]$$

7.3 OPERATING CONDITIONS FOR THE MODEL SIMULATIONS AND TESTING

7.3.1 Water Treatment Conditions

Similar operating conditions to those used in the study of Zhou *et al.* (1994) were considered for examining the applicability of the 1P-ADM compared to the 2P-ADM to describe the performance of ozone bubble columns. In order to examine the effects of Pe_L, k_La, and D_a on the dissolved and the gaseous ozone profiles for ozone applications in water treatment, the following typical conditions for the operation of ozone bubble columns were assigned as the base values for the 1P-ADM simulations: column height (L) = 5000 mm; ozone concentration in the feed gas (C_0) = 1 % (w/w %); applied ozone dose = 1.35 mgL^{-1}; mean theoretical hydraulic retention time (τ) = 180 s; $Pe_L = 5$; $k_w = 4.7 \times 10^{-4}\ s^{-1}$; $k_La = 5.0 \times 10^{-3}\ s^{-1}$; bubble column aspect ratio = L/D = 12.5; gas-to-liquid flowrate (G/L) ratio = 0.1; and gas hold-up (ε_G) = 0.008. Henry's law constant (H) of 0.22 $kPaLmg^{-1}$ was obtained from Sotelo *et al.* (1989). Water temperature was assumed to be 20 °C and the pressure at the top of the column was assumed to equal 1.0 atm. The basic model input parameters were then calculated and they were as follows: $Pe_L = 5.0$; $St_L = 0.9$; $St_G = 2.07$; $D_a = 0.0831$; and $y_0 = 0.00675$. The sensitivity analyses of the 1P-ADM to changes in each one of the parameters (Pe_L, k_La, and D_a) were performed by varying each one of the parameters while maintaining the others constant.

7.3.2 Wastewater Treatment Conditions

It was reported by Zhou and Smith (1999) that for pulp mill effluents, k_w ranged from 1,000 to 5,000 s^{-1} and the enhancement factor (E) ranged from 2 to 10. For the sake of practicality, the bulk liquid ozone concentration was assumed to equal zero since it was below the detection limit. They suggested that a typical value of k_L in the range from 6.6×10^{-4} to 9.3×10^{-4} ms^{-1} and k_La in the range from 8.3×10^{-3} to 2.5×10^{-2} s^{-1}. The effects of Pe_L, k_La, D_a, and M on the dissolved and the gaseous ozone profiles for wastewater treatment conditions were examined by assigning the same typical operating conditions used for the water treatment conditions except for: $k_w = 500\ s^{-1}$; and $k_L = 8.0 \times 10^{-4}$ ms^{-1}. The basic model input parameters were then calculated and they were as follows: $Pe_L = 5.0$; $St_L = 0.9$; $St_G = 2.07$; $D_a = 89{,}000$; $M = 1.166$ (to investigate the effect of the chemical reactions when they occur simultaneously near and/or at the gas-liquid interface and in the bulk liquid); and $y_0 = 0.00675$. The sensitivity analyses of the 1P-ADM were performed by varying each one of the parameters (Pe_L, k_La, D_a, and M) while maintaining the others constant except for M and D_a as they were varied together since they are interrelated through the pseudo-first-order specific ozone utilization rate constant (k_w) and the local mass transfer coefficient (k_L) as shown in Table 7.1.

7.3.3 Experimental Conditions for the Initial Testing of the 1P-ADM

The 1P-ADM was tested for the ozone application in water treatment using the pilot-scale experimental data of Zhou (1995). The pilot-scale bubble column used in the experiments was a cylindrical glass column with an inside diameter of 100 mm and a total height of 2,000 mm. The water depth was maintained constant at 1,750 mm by using an overflow weir. A 25 mm-spherical fused crystalline aluminum stone was used as the gas sparger. For the tested deionized water, k_w was determined experimentally by Zhou (1995) to be equal to 4.7×10^{-4} s^{-1}. The operating conditions for the counter-current and the co-current flow modes are presented in Tables 7.4 and 7.5, respectively.

Table 7.4 Operating conditions for the counter-current flow mode (water treatment).

Case #	Pe_L	P_T (atm)	St_L	St_G	D_a	y_0	$C_{L,0}^*$ (mgL^{-1})
DW17	10.53	1.0	0.560	1.119	0.139	0.010	5.56
DW23	9.71	1.0	1.365	1.098	0.139	0.007	3.63

Table 7.5 Operating conditions for the co-current flow mode (water treatment).

Case #	Pe_L	P_T (atm)	St_L	St_G	D_a	y_0	$C_{L,0}^*$ (mgL^{-1})
DW4	34.48	1.0	0.235	1.247	0.056	0.013	7.20
DW5	9.84	1.0	1.755	1.258	0.056	0.002	0.92
DW9	4.63	1.0	0.235	0.081	0.139	0.002	0.88

7.4 RESULTS AND DISCUSSION

7.4.1 Theoretical Analyses of the 1P-ADM Predictions

7.4.1.1 Water Treatment Applications: Counter-Current Flow Mode

Figures 7.4 to 7.6 depict the dissolved and the gaseous ozone profiles as functions of the dimensionless axial coordinate (Z). The superficial liquid and gas velocities effects that are represented by St_L and St_G, respectively, were investigated together by studying the effects of the overall mass transfer coefficient (k_La) as both St_L and St_G are directly proportional to k_La. The predicted dissolved ozone concentrations increased monotonically along the column height as the contact time between the gas phase and the liquid phase increases as the liquid flow passes through from the top to the bottom of the column. As shown in Figure 7.4 and as Pe_L increased, i.e., the magnitude of the backmixing decreased, the dissolved ozone profiles became steeper. The highest dissolved ozone concentrations occurred at the bottom of the column and as Pe_L increased from 1.0 to 20.0, the highest bottom concentration (i.e., the predicted dissolved ozone concentration in the effluent leaving the column) increased from 1.14 to 1.50 mgL^{-1}, respectively. As Pe_L increased, the effects of Pe_L on the dissolved ozone profiles and the rate of increase of ($C_L/C_{L,0}^*$) per increase of Pe_L, at Z = 0.00, decreased. The dissolved ozone profiles exhibited an increasing axial gradient (slope) up to a turning point after which the slope of the profiles started to decrease. This could be explained by the boundary conditions applied at the bottom (zero-axial gradient of the profile) and at the top of the column (a concentration jump). As the liquid phase reaches plug flow conditions, the backmixing and the concentration jump will diminish (Lev and Regli, 1992; Zhou *et al.*, 1994). As Pe_L increased, the gaseous ozone concentrations increased and their profiles became flatter which was the only contradiction between the predictions of the 1P-ADM and the 2P-ADM, but interestingly, both models were insensitive to changes in Pe_L in terms of their predicted gaseous ozone profiles. The rate of increase of (y/y_0) per increase of Pe_L, at $Z = 1.00$, increased and the predicted ozone off-gas concentration increased from 3.72 to 4.41 mgL^{-1} as Pe_L increased from 1.0 to 20.0, respectively.

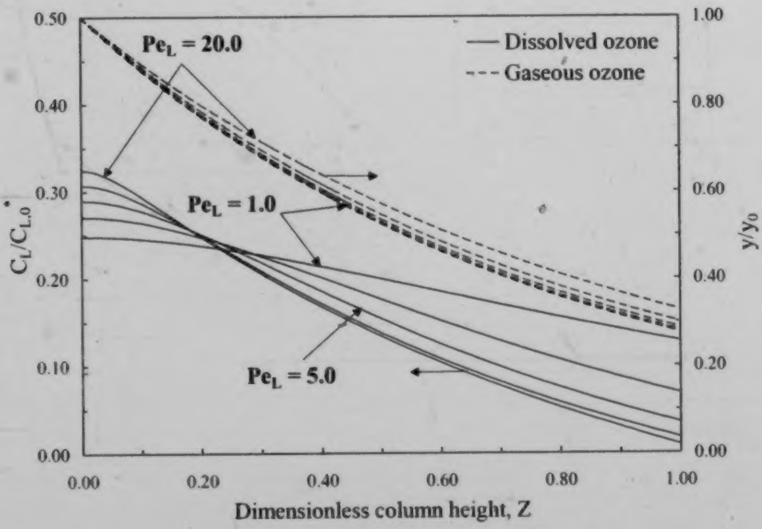

Figure 7.4 Pe_L effects on the concentration profiles in the counter-current flow mode and water treatment applications.

As shown in Figure 7.5, the k_La effects on the concentration profiles decreased as k_La increased and those effects were more significant in the range of k_La from 1.0×10^{-3} to 7.0×10^{-3} s^{-1}. In that range, the mass transfer increased along the entire column height and the profiles became steeper, while the mass transfer increased only near the bottom of the column (up to $Z = 0.10$) and beyond that point the dissolved ozone concentrations decreased and the profiles became much more steeper as k_La increased from 7.0×10^{-3} to 1.5×10^{-2} s^{-1}. As k_La increased, the rate of increase of $(C_L/C_{L,0}^*)$ per increase of k_La, at $Z = 0.00$, decreased. Zhou *et al.* (1994) observed the same phenomenon when they applied the 2P- ADM to predict the performance of ozone bubble columns under water treatment conditions.

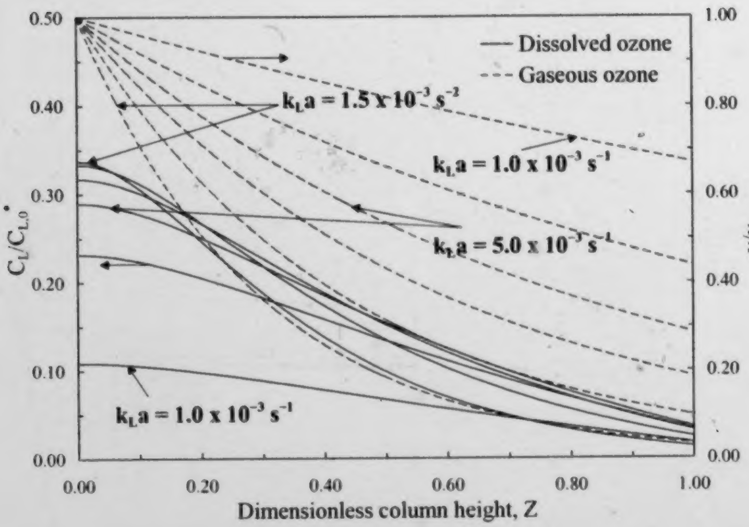

Figure 7.5 k_La effects on the concentration profiles in the counter-current flow mode and water treatment applications.

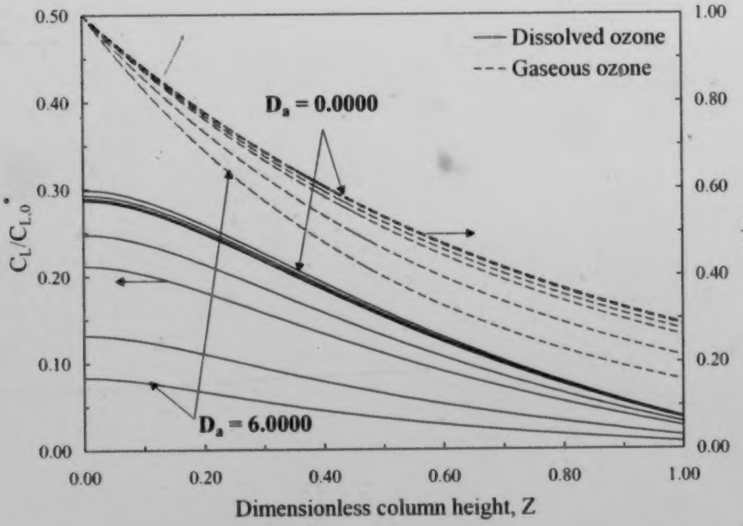

Figure 7.6 D_a effects on the concentration profiles in the counter-current flow mode and water treatment applications.

As a result, improving the design of bubble columns to enhance the mass transfer process is essential and is only crucial near the column entrance. The same phenomenon was observed before by Zhou *et al.* (1994). As k_La increased, the dissolved ozone profiles became steeper and the predicted residual ozone concentration, in the effluent, increased from 0.50 to 1.55 mgL^{-1}. The slope of the dissolved ozone profiles exhibited a similar trend to that observed over the studied range of Pe_L. As k_La increased, the gaseous ozone profiles became steeper and the gaseous ozone concentrations decreased considerably along the entire column height. The rate of decrease of (y/y_0) per increase of k_La, at $Z = 1.00$, decreased and the predicted ozone off-gas concentration decreased from 9.05 to 0.46 mgL^{-1} as k_La increased from 1.0×10^{-3} to 1.5×10^{-2} s^{-1}, respectively.

Figure 7.6 depicts the effects of the overall pseudo-first order specific ozone utilization rate constant (k_w) as one of the parameters that describe the quality of the water. k_w is represented by the dimensionless parameter (D_a). A zero specific ozone utilization rate constant was included in the analysis as a base line and for the sake of comparison. As k_w increased from 0.00 to 0.05 s^{-1} (i.e., D_a increased from 0.0000 to 6.0000), the dissolved ozone profiles became flatter, the predicted effluent dissolved ozone concentration decreased, the gaseous ozone profiles became steeper, the predicted ozone off-gas concentration decreased, and the mass transfer process was suppressed over the entire column height. The effects of the D_a on the dissolved ozone profiles were more significant in the range of D_a from 0.0000 to 0.5050. The effluent dissolved ozone concentration decreased from 1.38 to 1.14 mgL^{-1} and from 1.14 to 0.38 mgL^{-1} as D_a increased from 0.0000 to 0.5050 and from 0.5050 to 6.0000, respectively. The rate of decrease of $(C_L/C_{L,0}^*)$ per increase of D_a, at $Z = 0.00$, decreased as D_a increased. This is in agreement with the concept of slow and fast-reaction-kinetics regimes, and the slow-reaction kinetics regime exists when k_w is equal to or less than 2.8×10^{-3} s^{-1}. The slope of the dissolved ozone profiles exhibited a similar trend to that observed over the studied range of Pe_L. The rate of decrease of (y/y_0) per increase of D_a, at $Z = 1.00$, decreased and the predicted ozone off-gas concentration decreased from 3.89 to 2.13 mgL^{-1} as D_a increased from 0.0000 to 6.0000, respectively.

The effects of k_La on the gaseous ozone profiles were more significant than the effects of Pe_L and D_a. This is in agreement with the gas-liquid mass transfer process being the main process that dictates the overall performance of ozone bubble columns operating in the slow-reaction kinetics regime. Regarding the dissolved ozone profiles, k_La and D_a were superior to Pe_L in their effects on the effluent residual dissolved ozone concentration.

7.4.1.1 Water Treatment Applications: Co-Current Flow Mode

Figures 7.7 to 7.9 show the effects of Pe_L, k_La, and D_a, respectively, on the dissolved and the gaseous ozone profiles in the co-current flow mode in which the liquid and gas phases flow together in the same direction from the bottom to the top of the column.

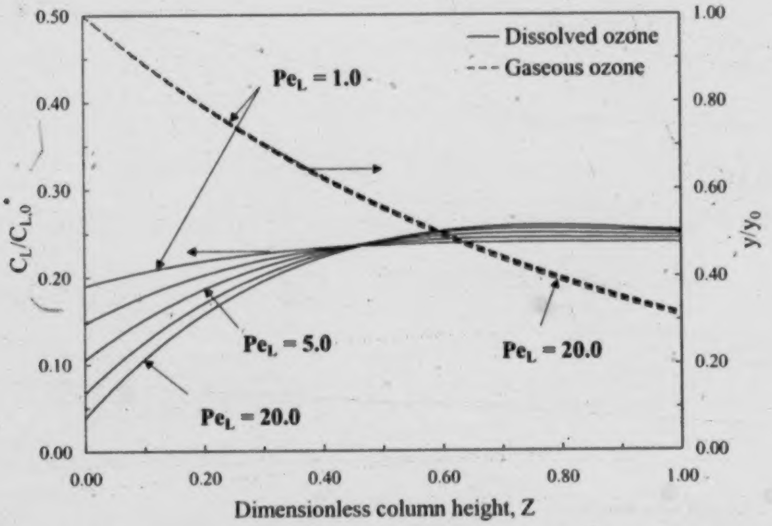

Figure 7.7 Pe_L effects on the concentration profiles in the co-current flow mode and water treatment applications.

Based on that, the boundary conditions that are applied for the liquid phase are different from those applied in the counter-current flow mode and the dissolved ozone profiles exhibited a different trend from the one observed in the counter-current flow mode. The 1P-ADM predicted a concentration jump at the column inlet and the profiles reached their peaks at different locations along the column height depending on the operating conditions that were considered for the model simulations. This phenomenon was observed before in the study of Zhou *et al.* (1994). Therefore, the effluent did not have the highest dissolved ozone concentration and the dissolved ozone profiles were flatter than those in the counter-current flow mode. Under some of the operating conditions assumed for the model simulations, the dissolved ozone profiles were closer to being uniformly distributed along the column height. The slope of the dissolved ozone profiles exhibited a decreasing trend up to a turning point after which it started to increase. The only exception for that observed trend was in the lower range of k_La from 1.0×10^{-3} to 3.0×10^{-3} s^{-1} where the axial gradient of the dissolved ozone profiles exhibited a decreasing trend along the entire column height. As Pe_L and k_La increased and D_a decreased, the dissolved ozone profiles became steeper and they were generally more sensitive to changes in k_La and D_a. As Pe_L increased, the maximum predicted dissolved ozone concentration and the effluent dissolved ozone concentration increased from 1.10 to 1.20 mgL^{-1} and from 1.10 to 1.16 mgL^{-1}, respectively. Interestingly, the location at which the maximum dissolved ozone concentration occurred ($Z = 0.76$) remained the same for the entire Pe_L range. The effects of Pe_L on the dissolved ozone profiles are similar to those observed in the counter-current flow mode. As Pe_L increased, the changes in the gaseous ozone profiles were insignificant and the predicted ozone off-gas concentration remained practically constant at 4.22 mgL^{-1}.

The k_La effects on the dissolved ozone profiles were similar to those observed in the counter-current flow mode. As k_La increased from 1.0×10^{-3} to 7.0×10^{-3} s^{-1}, the effluent and the maximum dissolved ozone concentrations increased from 0.45 to 1.17 mgL^{-1} and from 0.45 to 1.25 mgL^{-1}, respectively, and the location of the maximum concentration shifted from $Z = 1.00$ to $Z = 0.56$, respectively. Meanwhile, as k_La increased from 7.0×10^{-3} to 1.5×10^{-2} s^{-1}, the maximum dissolved ozone concentration increased from 1.25 to 1.40 mgL^{-1}, the effluent dissolved ozone concentration decreased from 1.17 to 0.81 mgL^{-1}, and the location of the maximum concentration shifted from $Z = 0.56$ to $Z = 0.22$, respectively.

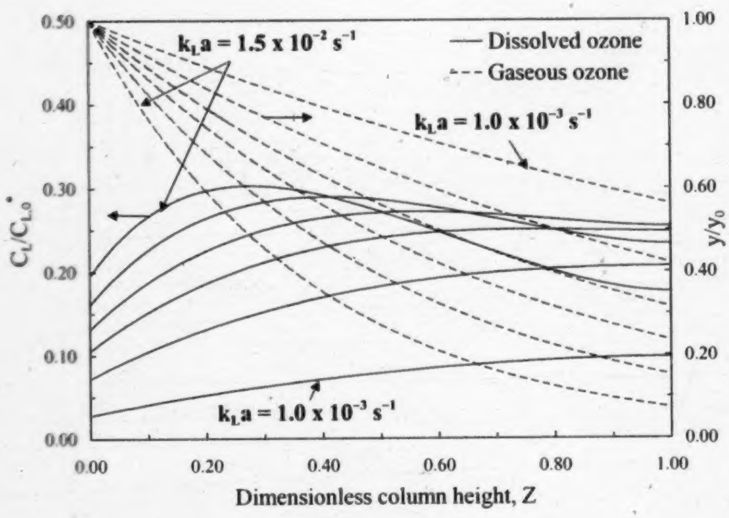

Figure 7.8 k_La effects on the concentration profiles in the co-current flow mode and water treatment applications.

Therefore, we can define two distinctive regions of the mass transfer process as the behavior of the co-current ozone bubble column changed in terms of the predicted dissolved ozone concentration in the effluent leaving the column. As k_La increased above $7.0 \times 10^{-3}\ s^{-1}$, most of the gaseous ozone would have been absorbed near the bottom of the column, thus, causing the peak of the dissolved ozone profiles to increase and consequently, the concentrations at $Z > 0.40$ and $Z > 0.63$, at $k_La = 1.0 \times 10^{-2}$ and $1.5 \times 10^{-2}\ s^{-1}$, respectively, to decrease. The k_La effects on the gaseous ozone profiles were similar to those observed in the counter-current flow mode. The predicted ozone off-gas concentration decreased from 7.57 to 1.00 mgL^{-1} as k_La increased from 1.0×10^{-3} to $1.5 \times 10^{-2}\ s^{-1}$, respectively.

As k_w increased from 0.00 to 0.05 s^{-1} (i.e., D_a increased from 0.0000 to 6.0000), the effects on the dissolved and the gaseous ozone profiles were similar to those observed in the counter-current flow mode. As shown in Figure 7.9 and as D_a increased from 0.0000 to 0.5050, respectively, the effluent and the maximum dissolved ozone concentrations decreased from 1.19 to 0.90 mgL^{-1} and from 1.20 to 0.94 mgL^{-1}, respectively, and the location of the maximum concentration shifted from Z = 0.80 to Z = 0.60, respectively. Then, as D_a increased from 0.5050 to 6.0000, respectively, the effluent and the maximum dissolved ozone concentrations decreased from 0.90 to 0.12 mgL^{-1} and from 0.94 to 0.30 mgL^{-1}, respectively, and the location of the maximum concentration shifted from Z = 0.60 to Z = 0.22, respectively. As D_a increased, the ozone off-gas concentration decreased from 4.28 to 2.07 mgL^{-1}.

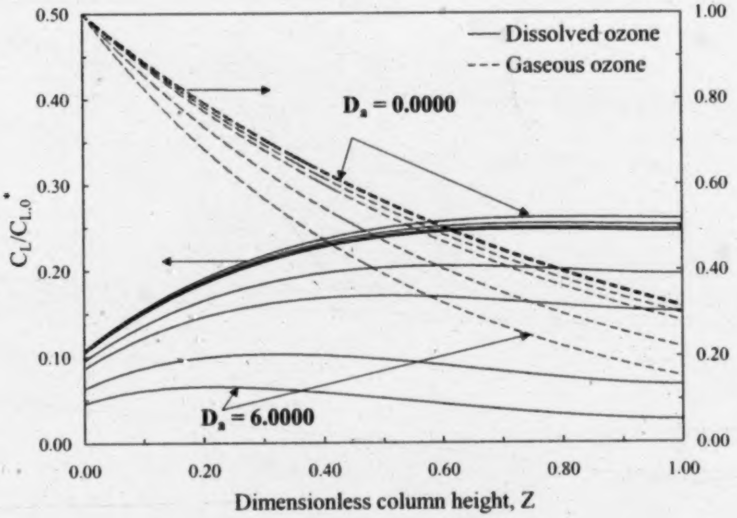

Figure 7.9 D_a effects on the concentration profiles in the co-current flow mode and water treatment applications.

Under the same operating conditions, the counter-current flow mode was superior compared to the co-current flow mode in terms of the predicted dissolved ozone concentrations in the effluent leaving the column. In the counter-current and the co-current flow modes, the effects of k_La on the gaseous ozone profiles were more significant than the effects of Pe_L and D_a as the gas-liquid mass transfer process being the main process that dictates the overall performance of ozone bubble columns operating in the slow-reaction kinetics regime. Regarding the predicted ozone off-gas concentrations, both models predicted comparable concentrations with a relative difference that ranged from 13 to 6%, 16 to 54%, and 9 to 3% over the studied ranges of Pe_L, k_La, and D_a, respectively, going from the low end to the high end of those ranges. Interestingly, the high relative difference (54%) at the high end of the k_La range should not mislead us as the predicted ozone off-gas concentration ranged from 0.16 to 0.50 mgL^{-1}.

7.4.1.2 Wastewater Treatment Applications: Counter-Current and Co-Current Flow Modes

Figures 7.10 to 7.12 depict the effects of Pe_L, k_La, and D_a and M, respectively, on the dissolved and the gaseous ozone profiles in the counter-current flow mode. Interestingly, both flow modes produced similar dissolved and gaseous ozone profiles except for the lower range of D_a and M ($D_a = 89$, $M = 0.037$; and $D_a = 534$, $M = 0.090$) as shown in Figure 7.12. Under these operating conditions, the co-current 1P-ADM predicted dissolved ozone profiles with concentration jumps near the bottom of the column.

Generally, the dissolved ozone profiles exhibited a decreasing slope along the entire column height except at the high end of the D_a and M range as shown in Figure 7.12. The effects of k_La on the gaseous ozone profiles were more significant than the effects of Pe_L, and D_a and M. Since the D_a-M range used in the model simulations represents an intermediate range between the slow and the fast-reaction kinetics regimes, their effects on the gaseous ozone profiles are still inferior to the effects of k_La. It should be noted that at Pe_L higher than 5.0, the 1P-ADM predicted very small dissolved ozone concentrations that were virtually equal to zero. As Pe_L increased from 1.0 to 5.0 and from 1.0 to 20.0, respectively, the dissolved and the gaseous ozone profiles were virtually identical. As shown in Figure 7.11 and as k_La increased, the dissolved and the gaseous ozone profiles became steeper. The rate of increase of $(C_L/C_{L,0}^*)$ per increase of k_La, at $Z = 0.00$, was relatively high and it decreased as k_La increased. Interestingly, the effluent dissolved ozone concentration exhibited a very small rate of change of $(C_L/C_{L,0}^*)$ per increase of k_La at $Z = 1.00$. As k_La increased, this rate decreased. The dissolved ozone concentration, at $Z = 1.00$, started to increase as k_La increased from 1.0×10^{-3} to 3.0×10^{-3} s^{-1}, then as k_La increased above 3.0×10^{-3} s^{-1}, it started to decrease. As k_La increased, its effect on the gaseous ozone profiles decreased and the rate of decrease of (y/y_0) per increase of k_La, at $Z = 1.00$, was relatively high and it decreased as k_La increased.

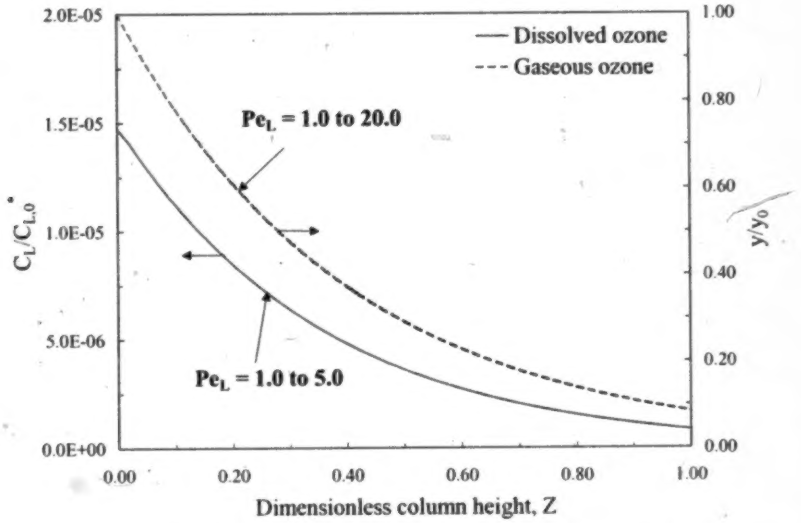

Figure 7.10 Pe_L effects on the concentration profiles in the wastewater treatment applications.

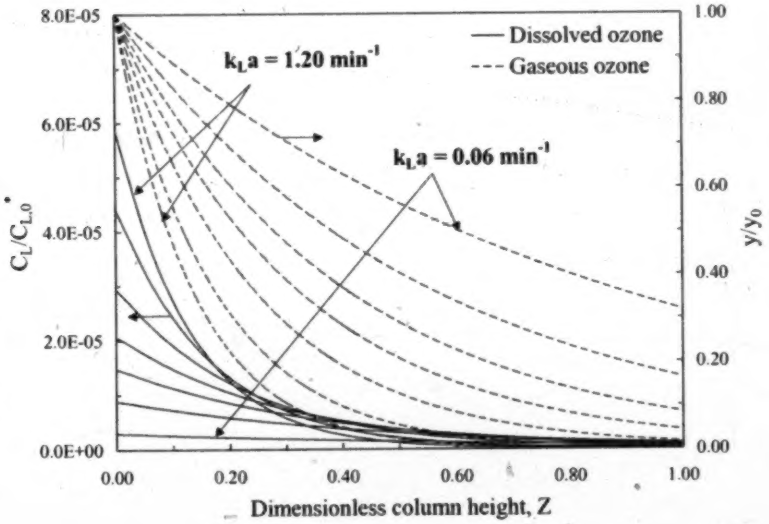

Figure 7.11 k_La effects on the concentration profiles in the wastewater treatment applications.

As shown in figure 7.12 and as D_a and M increased, the dissolved ozone profiles became flatter and the gaseous ozone profiles became steeper. The effects of D_a and M on the dissolved and the gaseous ozone profiles were more significant at the lower end of the D_a and M range. As D_a and M reached 35600 and 0.737, respectively, the dissolved ozone concentrations were practically equal to zero. The rates of decrease of $(C_L/C_{L,0}^*)$ and (y/y_0) per increase of D_a and M, at Z = 0.00 and Z = 1.00, respectively, increased as D_a and M increased. Those rates were virtually identical in the counter-current and the co-current flow modes.

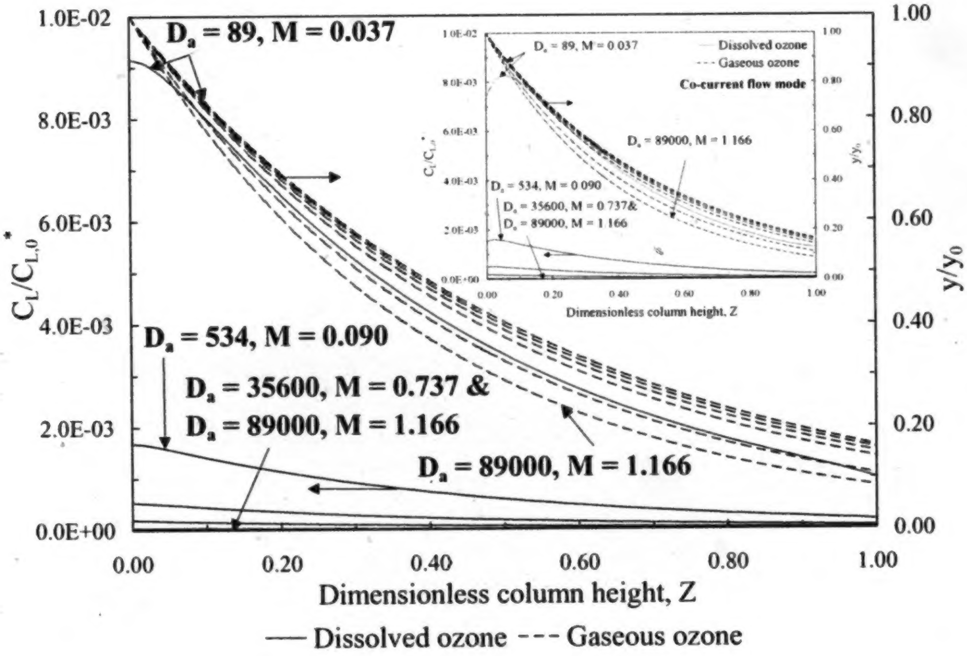

Figure 7.12 D_a and M effects on the concentration profiles in the wastewater treatment applications.

The predicted ozone off-gas concentration ranged from 1.13 to 1.15 mgL^{-1}, from 4.30 to 0.01 mgL^{-1}, and from 2.20 to 1.13 mgL^{-1} over the tested ranges of Pe_L, k_La, and D_a and M, respectively (going from the low end to the high end of those ranges). Under the typical operating conditions (Pe_L = 5.0; St_L = 0.9; St_G = 2.07; D_a = 89000 (i.e., k_w =

500 s^{-1}); and M = 1.166), the predicted ozone off-gas concentration was 1.13 mgL^{-1}. With all the operating parameters being the same except for k_La which was set equal to 1.5 x 10^{-2} s^{-1}, the ozone off-gas concentration was predicted to be 0.04 mgL^{-1} which is less than the detection limit of the iodometric titration (KI) method. Therefore, the model predictions of the ozone off-gas are in agreement with the previous experimental observations reported by Zhou and Smith (1997) and Zhou and Smith (2000).

Regarding the dissolved ozone profiles, k_La, and D_a and M were superior to Pe_L in their effects on those profiles and D_a and M had the highest effects on the dissolved ozone concentrations. The predicted dissolved and gaseous ozone profiles were virtually identical in both the counter-current and the co-current flow modes. As a result, both flow modes are identical in terms of their efficiency towards the ozone absorption in bubble columns operating under wastewater treatment conditions. The maximum predicted dissolved ozone concentration of 4.2 x 10^{-2} mgL^{-1} (at the lower end of D_a and M range) is less than the detection limit of the Indigo method which is in agreement with the experimental observations of undetectable dissolved ozone concentrations in the studies conducted by Zhou and Smith (1997) and Zhou and Smith (2000).

7.4.2 Initial Model Testing for Water Treatment Conditions

Figures 7.13 and 7.14, respectively, demonstrate the applicability of the IP-ADM to predict the performance of counter-current and co-current bubble columns that use conventional fine-bubble diffusers as the gas spargers. Generally, there was an excellent agreement between the predicted and the experimental dissolved ozone profiles except for few data points where the model slightly predicted higher concentrations.

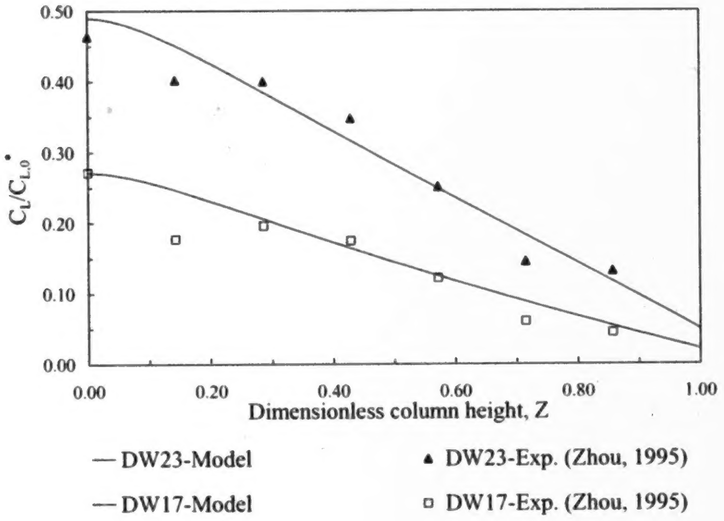

Figure 7.13 Comparison between the predicted and the experimental dissolved ozone concentrations in an ozone bubble column under water treatment conditions for the counter-current flow mode.

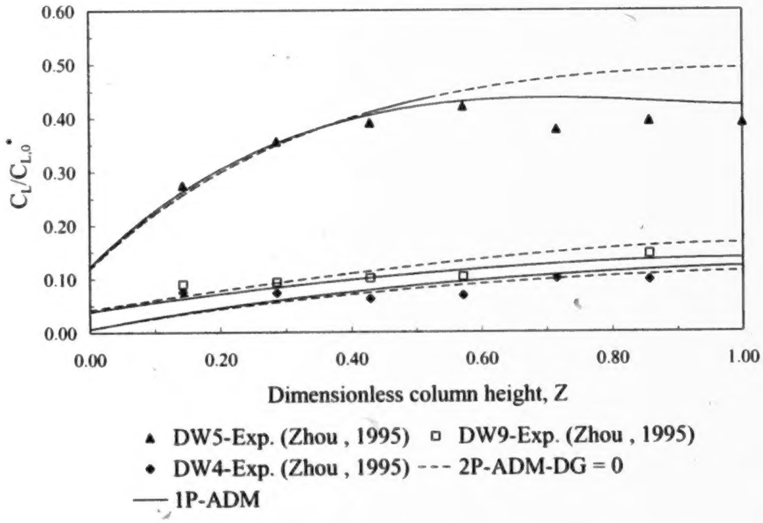

Figure 7.14 Comparison between the predicted and the experimental dissolved ozone concentrations in an ozone bubble column under water treatment conditions for the co-current flow mode.

Figure 7.14 depicts a comparison between the predictions of the 2P-ADM and the 1P-ADM in a co-current flow mode. There was a good agreement between the predicted and the experimental dissolved ozone profiles except for few data points where there was slight deviation between the predicted and the measured dissolved ozone concentrations. At 5 % significance level, t-tests have shown that there was no significant difference between the predictions of the 2P-ADM ($D_G = 0$) and the 1P-ADM with the exception of run # 9, where there was no significant difference at a 1 % significance level. Therefore, when compared to the complete versions of the ADM, the 1P-ADM has proven to be an easy, reliable, and accurate tool for describing the performance of fine-diffuser ozone bubble columns.

7

7.5 CONCLUSIONS

The 1P-ADM can be solved analytically while the complete axial dispersion model (2P-ADM) requires an elaborate numerical technique to solve the model's equations. Therefore, describing the analytical solution of the 1P-ADM in terms of a simple spreadsheet program facilitates obtaining the model predictions for any operating conditions represented by the model input parameters entered into the spreadsheet program. Compared to the 2P-ADM predictions of the ozone bubble column performance that was presented in the study of Zhou *et al.* (1994), the 1P-ADM has proven to provide excellent predictions of the performance of ozone bubble columns operating under either water treatment conditions and in both the counter-current and the co-current flow modes. The 1P-ADM also provided good predictions of the performance of ozone bubble columns for the wastewater treatment applications. The 1P-ADM is easy and reliable tool to be used for the design and the process-control of bubble columns' operations.

7.6 REFERENCES

1. Alvarez-Cuenca, M. and M.A. Nerenberg, "Oxygen Mass Transfer in Bubble Columns Working at Large Gas and Liquid Flow Rates", AIChE J. 27(1): 66-73 (1981).
2. Alvarez-Cuenca, M., C.G.J. Baker, and M.A. Bergougnou, "Oxygen Mass Transfer in Bubble Columns", Chem. Eng. Sci. 35: 1121-1127 (1980).
3. Beltrán, F.J., J.F. García-Araya, and J.M. Encinar, "Henry and Mass Transfer Coefficients in the Ozonation of Wastewaters", Ozone Sci. & Eng. 19: 281-296 (1997).
4. Beltrán, F.J., J.M. Encinar, J.F. García-Araya, and M.G. Muñoz, "Modelling Industrial Wastewater Ozonation in Bubble Contactors-Part I: Rate Coefficient Determination", Ozone Sci. & Eng. 17: 355-378 (1995).
5. Chang, B.-J. and E.S.K. Chian, "A model Study of Ozone-Sparged Vessels for the Removal of Organics from Water", Wat. Res. 15(7): 929-936 (1981).
6. Danckwerts, P.V., *Gas-Liquid Reactions* (NY, USA: McGraw-Hill, Inc., 1970), pp. 105-114.
7. Deckwer, W.-D., K. Nguyen-Tien, B.G. Kelkar, and Y.T. Shah, "Applicability of Axial Dispersion Model to Analyze Mass Transfer Measurements in Bubble Columns", AIChE J. 29(6): 915-922 (1983).
8. Deckwer, W.-D. and J. Hallensleben, "Exclusion of Gas Sparger Influence on Mass Transfer in Bubble Columns", Canadian J. Chem. Eng. 58: 190-196 (1980).
9. Heinzle, E., F. Geiger, M. Fahmy, and O.M. Kut, "Integrated Ozonation-Biotreatment of Pulp Bleaching Wastewaters Containing Chlorinated Phenolic Compounds", Biotechnol. Prog. 8(1): 67-77 (1992).
10. Hoigné, J., "Mechanisms, Rates and Selectivities of Oxidants of Organic Compounds Initiated by Ozonation in Water", *Handbook of Ozone Technology and Applications* (MI, USA: Ann Arbor Science Publishers, 1982).
11. Hull, C.S., P.C. Singer, K. Saravanaan, and C.T. Miller, "Ozone Mass Transfer and Reaction: Completely Mixed Systems", *Proc. of the Annual AWWA Conf.: Water Quality*, Vancouver, BC, Canada, 1992.

12. Jokela, J.K., M. Lalne, M. Ek, and M. Salkinoja-Salnoen, "Effect of Biological Treatment on Halogenated Organics in Bleached Kraft Pulp Mill Wastewaters Studied by Molecular Weight Distribution Analysis", Environ. Sci. & Technol. 27(3): 547-557 (1993).

13. Johnson, P.N. and R.A. Davis, "Diffusivity of Ozone in Water", J. Chem. Eng. Data 41: 1485-1487 (1996).

14. Kaštánek, J., J. Zahradník, J. Kratochvíl, and J. Čermák, *Chemical Reactors for Gas-Liquid Systems* (Chichester, England: Ellis Horwood, 1993), pp. 22-23.

15. Kramers, H. and K.R. Westerterp, *Elements of Chemical Reactor Design and Operation* (NY, USA: Academic Press, Inc., 1963), pp. 146-150.

16. Kreyszig, E., *Advanced Engineering Mathematics, 6th ed.* (NY, USA: John Wiley and Sons, Inc., 1988), pp. 145-146.

17. Kuo, C.H., "Mass Transfer in Ozone Absorption", Environ. Prog. 1(3): 189-195 (1982).

18. Langlais, B., D.A. Reckhow, and D.R. Brink, *Ozone in Water Treatment: Application and Engineering* (MI, USA: Lewis Publishers, Inc., 1991).

19. Laplanche, A., N. Le Sauze, G. Martin, and B. Langlais, "Simulation of Ozone Transfer in Water: Comparison with a Pilot Unit", Ozone Sci. & Eng. 13(5): 13, 535-558 (1991).

20. Lev, O. and S. Regli, "Evaluation of Ozone Disinfection Systems: Characteristic Contact Time T", J. Environ. Eng., ASCE 118(2): 268-285 (1992).

21. Levenspiel, O., *Chemical Reaction Engineering, 2nd ed.* (NY, USA: John Wiley and Sons, Inc., 1972).

22. Mecklenburgh, J.C. and S. Hartland, *The Theory of Backmixing* (NY, USA: John Wiley and Sons, Inc., 1975), pp. 15-23.

23. Oke, N.J., D.W. Smith, and H. Zhou, "An Empirical Analysis of Ozone Decay Kinetics in Natural Waters", Ozone Sci. & Eng. 20: 361-379 (1998).

24. Sotelo, J.L., F.J. Beltrán, F.J. Benitez, and J. Beltrán-Heredia, "Henry's Law Constant for the Ozone-Water System", Wat. Res. 23(10): 1239-1246 (1989).

25. Yurteri, C. and M.D. Gurol, "Ozone Consumption in Natural Waters: Effects of Background Organic Matter, pH and Carbonate Species", Ozone Sci. & Eng. 10: 277-290 (1988).

26. Zhou, H. and D.W. Smith, "Ozone Mass Transfer in Water and Wastewater Treatment: Experimental Observations Using a 2D-Laser Particle Dynamics Analyzer", Wat. Res. 34: 909-921 (2000).

27. Zhou, H. and D.W. Smith, "Applying Mass Transfer Theory to Study the Kinetics of Fast Ozone Reactions in Pulp Mill Effluents", *Proc. of the 14th Ozone World Congress*, Detroit, MI, USA, 1999.

28. Zhou, H. and D.W. Smith, "Process Parameter Development for Ozonation of Kraft Pulp Mill Effluents", Wat. Sci. & Technol. 35(2-3): 251-259 (1997).

29. Zhou, H., *Investigation of Ozone Disinfection Kinetics and Contactor Performance Modeling: Ph.D. Thesis* (Edmonton, AB, Canada: University of Alberta, 1995), pp. 307-312.

30. Zhou, H., D.W. Smith, and S.J. Stanley, "Modeling of Dissolved Ozone Concentration Profiles in Bubble Columns", J. Environ. Eng., ASCE 120(4): 821-840 (1994).

CHAPTER 8. DEVELOPMENT OF DESIGN PARAMETERS OF AN IMPINGING-JET BUBBLE COLUMN*

8.1 INTRODUCTION

Ozonation is one of the treatment processes used in treating water and wastewater and it is one of many chemical processes that take place in gas-liquid reactors. In water treatment applications, ozonation is limited by the mass transfer process as it is considered the controlling process that dictates the overall performance of ozone contactors (Gamal El-Din and Smith, 2000; Zhou *et al.*, 1994). Bubble-diffuser contactors are the most common method used for treating water using the on-site generated ozone gas. In order to maximize the treatment level achieved in ozone contactors, the contactor and the gas absorber geometry need to be modified to achieve higher turbulence and mixing in the liquid phase. According to Danckwerts' theory of surface renewal, as the mixing increases, the liquid film at the gas-liquid interface will be renewed at a higher rate causing the local mass transfer coefficient (k_L) to increase (Danckwerts, 1970). Increasing the turbulence in the liquid phase will lead to higher turbulent shear stresses. As a result, the gas bubbles will become smaller. Consequently, the gas bubbles' specific interfacial area will increase leading to higher overall mass transfer coefficient (k_La). The ozone gas-absorption in water treatment is assumed to follow the slow-reaction kinetics regime (Zhou *et al.*, 1994; Gamal El-Din and Smith, 2000). Since the ozone gas diffusivity in the liquid phase is much smaller than that in the gas phase, the gas diffusion through the liquid film becomes the rate-limiting step of the mass transfer process (Valentin, 1967). The higher turbulent shear stresses will also cause the liquid film to become thinner, and as a result, the ozone gas will diffuse through the liquid film at a higher rate causing k_L to increase.

In the study of Witze (1974), when two axisymmetrical circular turbulent air jets (i.e., having the same nozzle diameter and momentum) intersected at an angle of 180°, the resultant jet behaved like a radial jet that grew at about three times the rate of a single radial jet.

A version of this chapter has been submitted for publication. Gamal El-Din, M. and D.W. Smith, Wat. Res. (March 2001).

As a result of the impingement, higher turbulent shear stresses were developed in the ambient fluid and a region of backflow was observed. The same phenomenon was observed in the study of Khan (1989) who studied the impingement of circular turbulent water and air jets. Guo and Sharp (1996) studied the characteristics of radial jets and mixing under buoyant conditions. They observed that the turbulence intensity increased with the width of the orifice. Unger and Muzzio (1999) investigated the effect of a jet impingement at an intersecting angle of 90^o on the mixing characteristics. It was observed that efficient and homogeneous mixing occurred at jets' Reynolds numbers (Re_j's) greater than 300. Fitzgerald and Holley (1979) used two turbulent jets intersecting at an angle of 90^o to investigate the resultant effects on the mixing behaviour. They observed more uniform and improved mixing across the annular tube.

Many researchers have attempted to improve the performance of bubble columns by maximizing the rate of physical gas absorption process. These attempts included: adding internal baffles (Catros, 1986), utilizing perforated plates (Chen *et al.*, 1986), inducing internal liquid circulation in air-lift reactors (Lewis and Davidson, 1985), and utilizing motionless mixers (Wang and Fan, 1978).

Gas injectors were utilized by many researchers in order to improve the mass transfer process. Wachsmann *et al.* (1984) studied the mass transfer process using an injection-type nozzle. Gas was introduced under positive and negative pressures. They observed remarkable increase in the overall mass transfer coefficient (k_La) due to the generation of bubbles that had a large specific interfacial area. They also observed that the values of k_La in the gas-injection mode varied from those in the gas-ejection mode. Thalasso *et al.* (1995) used a venturi-type injector to increase the gas transfer rates, and that led to an improvement in the performance of a bioreactor. Under gas injection mode, they observed an increase in k_La as the liquid superficial velocity (u_L) and the gas superficial velocity (u_G) increased. In a gas-liquid spouted vessel, gas was absorbed under positive pressure into the liquid-phase flow (Nishikawa *et al.*, 1977). It was observed that as u_G and u_L increased, k_La increased and k_La was more dependent on u_G than on u_L. Wang and Fan (1978) studied the mass transfer process in bubble columns packed with motionless mixers. They observed that k_La was dependent on u_G and u_L and as u_G and u_L increased, k_La increased. Huynh *et al.* (1991) studied the mass transfer process in an upward venturi-bubble column combination. They correlated k_La with u_G and u_L for the bubble/venturi combination. As u_G and u_L increased, k_La increased. The increase in u_G could have caused an increase in the gas bubbles' specific interfacial area while the increase in u_L could have resulted in an increase in the liquid-phase shear stresses (Huynh *et al.*, 1991). Higher turbulent shear stresses would cause the formation of smaller bubbles resulting in higher specific interfacial area. Also, higher shear stresses would cause the mixing to increase and the liquid film at the gas-liquid interface to be renewed at a higher rate leading to an increase in k_L. Zhou and Smith (2000) investigated the effects of gas flowrates on the gas bubbles' specific interfacial area using a 2D-Laser particle dynamics analyzer. They observed a proportional increase in the bubbles' specific interfacial area with the increase in u_G as a result of the linear increase in the gas hold-up. The same phenomenon was also reported by Roustan *et al.* (1996).

In the current study, two venturi injectors (Mazzei® injectors) were utilized to create turbulent gas-liquid jets in the ambient fluid. The intersecting of the gas-liquid jets caused an increase in the turbulence intensity produced in the ambient fluid and therefore, increased the rate of the gas mass transfer. The ozone auto-decomposition process in the deionized water was investigated in a headspace-free reactor under a wide range of initial ozone concentrations and liquid-phase temperatures. The ozonation experiments were conducted in a pilot-scale impinging-jet bubble column that was operated in a co-current flow mode under a wide range of operating conditions. The mass transfer and the backmixing processes were characterized by fitting the measured dissolved and gaseous ozone concentration profiles with the concentration profiles obtained using the modified non-isobaric one-phase axial dispersion model (1P-ADM) through a three-parameter optimization technique.

8.2 OUTLINE OF THE MODIFIED NON-ISOBARIC ONE-PHASE AXIAL DISPERSION MODEL (1P-ADM)

A number of processes occur simultaneously during the ozonation treatment. These processes are: convection and backmixing processes of the liquid and gas phases flowing through the contacting chamber, ozone gas mass transfer process, ozone auto-decomposition process, and competitive reactive processes of dissolved ozone with the constituents that are present in the water. In addition to these processes, the contactor configuration, the operating conditions, and the water quality will influence the overall performance of the ozonation treatment (Zhou, 1995). The overall ozone auto-decomposition rate is influenced by the concentration and the history of the ozonation process. Ozone auto-decomposition process could be represented by a modified pseudo-first-order rate expression when ozonation is used to treat waters that do not exhibit significant initial ozone demand (Yurteri and Gurol, 1988; Oke et al., 1998):

$$\frac{dC_L}{dt} = -k_w C_L \tag{8.1}$$

where: C_L = instantaneous dissolved ozone concentration (mgL^{-1}), k_w = specific ozone utilization rate constant (s^{-1}), and t = reaction time (s).

Axial dispersion model visualizes the flow of fluids in tubular bubble columns as plug flow on top of which a diffusion-like process is superimposed. When applying this model, it should be noted that the dispersion process is a macroscopic phenomenon. Thus, dispersed flow might not be fully developed close to the boundaries of the reactor (Deckwer *et al.*, 1983). The assumptions pertaining to the development of the modified non-isobaric steady-sate one-phase axial dispersion model (1P-ADM) along with the detailed model development can be found in Gamal El-Din and Smith (2000). Schematic representation of a gas-liquid flow in a co-current bubble column is shown in Figure 8.1. The 1P-ADM is different from the complete axial dispersion model, or referred to as the two-phase axial dispersion model (2P-ADM), in its simple use for practical design and process control of ozone contacting chambers. The 2P-ADM is represented by a system of two non-linear partial differential equations (Zhou *et al.*, 1994; Gamal El-Din and Smith, 2000). In order to solve that system of equations, an elaborate numerical solving technique is needed. On the other hand, the 1P-ADM is composed of a single non-homogeneous second-order linear ordinary differential equation representing the liquid phase. Yet, this liquid-phase differential equation accounts for the countering effects of the gas shrinkage and expansion caused by gas depletion and absorption and reduced liquid hydrostatic head.

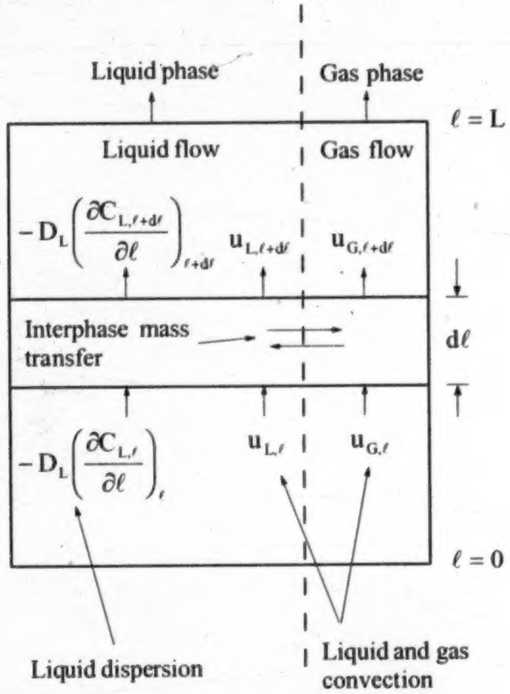
Liquid phase
Gas phase
$\ell = L$
Liquid flow
Gas flow
$-D_L\left(\frac{\partial C_{L,\ell+d\ell}}{\partial \ell}\right)_{\ell+d\ell}$
$u_{L,\ell+d\ell}$
$u_{G,\ell+d\ell}$
Interphase mass transfer
$d\ell$
$-D_L\left(\frac{\partial C_{L,\ell}}{\partial \ell}\right)_{\ell}$
$u_{L,\ell}$
$u_{G,\ell}$
$\ell = 0$
Liquid dispersion
Liquid and gas convection

Figure 8.1 Schematic representation of the 1P-ADM.

The differential equation was solved analytically by the method of variation of parameters. The 1P-ADM was expressed in terms of dimensionless operating parameters and the available analytical solution of the differential equation representing the model was applied to determine the column-average overall mass transfer coefficient (k_La), the liquid-phase axial dispersion coefficient (D_L), and the coefficient of the gas-phase ozone molar fraction decrease along the column height (a_1). This was achieved through a three-parameter optimization technique by fitting the measured dissolved and gaseous ozone concentration profiles to the concentration profiles obtained using the 1P-ADM. In order to account for variable superficial gas velocity along the height of the bubble column, an exponential function was assumed to describe the variation of the gaseous ozone molar fraction along the column height (Gamal El-Din and Smith, 2000):

$$y_Z = y_\ell = y_0\, e^{-a_1 Z} \qquad [8.2]$$

where: $Z = \frac{\ell}{L}$ = dimensionless axial co-ordinate of the column, L = total height of the bubble column, y_0 = gas-phase ozone molar fraction at the column entrance (i.e., at Z = 0), y_Z = gas-phase ozone mole fraction at the dimensionless axial co-ordinate (Z), and a_1 = coefficient of the gas-phase ozone molar fraction decrease along the column height. It is practically impossible to measure experimentally the rate of any ozone auto-decomposition that would take place inside the gas bubbles flowing through the bubble column. In the development of the 1P-ADM, the ozone auto-decomposition was assumed to be negligible in the gas phase as done by several researchers when they modeled the ozonation treatment process in ozone bubble columns (Roustan, 1987; Zhou *et al.*, 1994). The gas phase was assumed to flow in a plug flow regime as a result of the relatively high buoyancy of the gas bubbles. Based on the above, a_1 represents the overall decrease in the gas-phase ozone mole fraction due to the effects of the gas-liquid mass transfer and the gas-phase convection processes. Based on the theoretical data of Zhou *et al.* (1994) and Gamal El-Din and Smith (2000) regarding the gaseous ozone concentration profiles, it was assumed that a_1 is a function of the ozonation process operating parameters. Those parameters include: Peclet number (Pe_L), liquid-phase and gas-phase Stanton numbers (St_L and St_G, respectively), and Damköhler number (D_a). The exponent (a_1) can be determined experimentally by continuously monitoring the ozone concentrations in the feed and off-gas lines. The mathematical representations of the 1P-ADM input parameters are shown in Table 8.1. The non-homogeneous second-order linear ordinary differential equation representing the 1P-ADM and the pertaining boundary conditions are presented in Table 8.2.

Table 8.1 Dimensionless parameters pertaining to the 1P-ADM.

Dimensionless parameters	**1P-ADM**
Z	ℓ/L
Pe_L	$u_L L/D_L \varepsilon_L$
St_L	$k_L aL/u_L$
St_G	$(k_L aL/u_{G,0})(RT/H)$
D_a	$k_w \varepsilon_L L/u_L$
X	$C_{L,\ell}/C^*_{L,0}$
Y	y_ℓ/y_0

Table 8.2 Mathematical representation of the 1P-ADM differential equation and boundary conditions.

Equations	
Model differential equation	$\frac{1}{Pe_L}\frac{dX^2}{dZ^2}-\frac{dX}{dZ}-(St_L+Da)X+St_L(e^{-a_1 Z}+\frac{\beta_1}{\alpha_1}Ze^{-a_1 Z})=0$
Closed-closed boundary conditions	at $Z=0$: $X_{inf}=X\vert_{Z=0}-\frac{1}{Pe_L}\frac{\partial X}{\partial Z}\vert_{Z=0}$ $Y=1$ at $Z=1$: $\frac{\partial X}{\partial Z}\vert_{Z=1}=0$

Gamal El-Din and Smith (2000) developed the closed-form solution of the differential equation that describes the 1P-ADM to be as follows:

$$X = \frac{\left[D_1\lambda_2 e^{\lambda_2} + E_1\left(1 - \frac{\lambda_2}{Pe_L}\right)\right]}{N} e^{\lambda_1 Z} - \frac{\left[D_1\lambda_1 e^{\lambda_1} + E_1\left(1 - \frac{\lambda_1}{Pe_L}\right)\right]}{N} e^{\lambda_2 Z}$$

$$+ K_0 e^{-a_1 Z} + K_1 Z e^{-a_1 Z} \qquad [8.3]$$

where:

$$\lambda_1 = Pe_L + \sqrt{Pe_L^2 + 4Pe_L(St_L + D_a)} \qquad [8.4]$$

$$\lambda_2 = Pe_L - \sqrt{Pe_L^2 + 4Pe_L(St_L + D_a)} \qquad [8.5]$$

$$K_0 = \frac{Pe_L St_L}{(\lambda_2 - \lambda_1)}\left[\frac{1}{(a_1 + \lambda_2)} + \frac{\beta_1}{\alpha_1(a_1 + \lambda_2)^2} - \frac{1}{(a_1 + \lambda_1)} - \frac{\beta_1}{\alpha_1(a_1 + \lambda_1)^2}\right] \qquad [8.6]$$

$$K_1 = \frac{-\beta_1 Pe_L St_L}{\alpha_1(a_1 + \lambda_1)(a_1 + \lambda_2)} \qquad [8.7]$$

$$D_1 = X_{inf} - K_0\left(\frac{a_1}{Pe_L} + 1\right) + \frac{K_1}{Pe_L} \qquad [8.8]$$

$$E_1 = e^{-a_1}[-(K_0 + K_1)a_1 + K_1] \qquad [8.9]$$

$$N = \left(1 - \frac{\lambda_1}{Pe_L}\right)\lambda_2 e^{\lambda_2} - \left(1 - \frac{\lambda_2}{Pe_L}\right)\lambda_1 e^{\lambda_1} \qquad [8.10]$$

$$\alpha_1 = a'y_0 = \frac{\left(P_T + \rho g \varepsilon_L L\right)}{H} y_0 \qquad [8.11]$$

and

$$\beta_1 = b'y_0 = \frac{-\rho g \varepsilon_L L}{H} y_0 \qquad [8.12]$$

8.3 EXPERIMENTAL AND DATA ANALYSES METHODS

8.3.1 Bench Tests: Ozone Auto-Decomposition kinetics Study

The ozone auto-decomposition kinetics batch experiments were conducted in a 1200 mL floating-lid headspace-free reactor made from glass (see Figure 8.2). Clean deionized water was used in these experiments as the test water. The main average characteristics of the test water are summarized in Table 8.3. As shown in Table 8.3, the quality of the deionized water was not high as indicated by its relatively high TOC (total organic carbon) concentration that was about 0.51 mgL^{-1}.

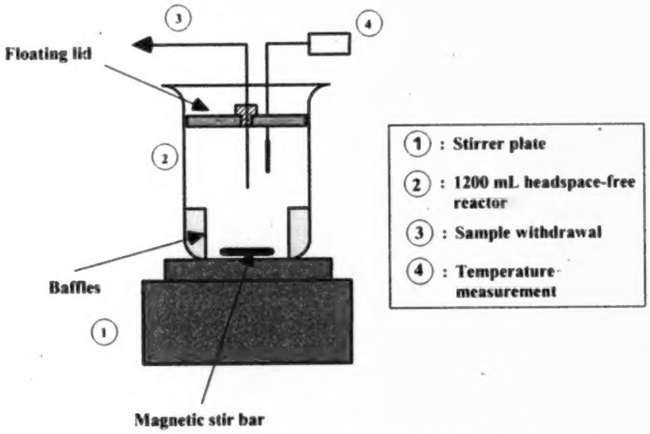
③
④
Floating lid
②
Baffles
①
Magnetic stir bar
① : Stirrer plate
② : 1200 mL headspace-free reactor
③ : Sample withdrawal
④ : Temperature measurement

Figure 8.2 Schematic of the headspace-free reactor.

Table 8.3 Main Average characteristics of the deionized water.

Parameters	**TOC (mgL^{-1})**	**pH**	**$A_{245\ nm}^{10\ mm}$ (mm^{-1})**
Mean	0.51	5.99	0.004
Standard deviation	0.29	0.26	0.000

A volume of 800 mL of the deionized water was added to a 400 mL of an ozone stock solution to obtain a total of 1200 mL of an ozonated solution. The ozone gas was generated from an extra-dry oxygen gas using a corona-discharge ozone generator (model C2P-9C-4 PCI®). The ozone stock solution was prepared by continuously bubbling the generated ozone gas into 400 mL of clean deionized water in a 500 mL gas wash bottle for about 1,800 s to ensure that enough dissolved ozone concentration was present in the solution. In every test and after the ozone stock solution was transferred into the reactor, mixing started immediately. In all the tests, care was taken to ensure minimum ozone loss during the transfer of the ozone stock solution into the reactor.

Quality control tests were conducted in each test to assess the ozone loss during the transfer of the ozone stock solution, two samples were withdrawn from the ozone stock solution before transfer and after it was transferred and initially mixed with the deionized water. The two samples were analyzed to correct for the ozone loss during the transfer of the ozone stock solution into the reactor. The 1200 mL volume of the headspace-free reactor was chosen to allow for an adequate number of the samples to be withdrawn during the experiments while leaving enough water volume in the reactor to keep the floating-lid above the baffles and therefore, to prevent any headspace to develop. Immediately after the ozone stock solution was added to the test water inside the reactor, mixing was started and timing was initiated using a stopwatch. The contents of the reactor were mixed continuously using a slow magnetic stirrer bar. At pre-set sampling times, 15 mL samples of the reactor test water were withdrawn from the reactor and transferred immediately into 100 mL volumetric flasks to minimize any ozone loss during the sampling process. Each 100 mL volumetric flask contained 10 mL of indigo reagent and 75 mL of ozone demand-free (ODF) water. In all the tests, all the glassware that came in contact with ozone was made ozone demand-free. An ozone-saturated solution was prepared by bubbling ozone gas into clean deionized water (ELGA® water) for at least 2,700 s. The ozonated water was then poured into the glassware that was sealed with aluminum foil and left overnight to satisfy any ozone demand. After that, the glassware was emptied and oven-dried before being used. All the experimental set-up components that came in contact with ozone during the experiments were made of glass, teflon, stainless steel, or PVC to reduce any possible interference that would result from the reactions between ozone and the experimental set-up components.

In order to measure the initial ozone demand of the test water, the first sample was withdrawn immediately, at t = 0 s, as the ozone stock solution was initially mixed with the test water inside the reactor and after 30 s, the second sample was withdrawn. The difference in the dissolved ozone concentrations between the two samples represented the initial ozone demand of the test water. The samples absorbances were measured using a spectrophotometer (model ULTROSPEC 3000®) at a wave length of 600 nm and a path length of 10 mm. Each sample absorbance was then compared to the absorbance of a blank solution that was prepared by adding 10 mL of indigo reagent and 75 mL of ODF water into 15 mL of the test water. The dissolved ozone concentration was then calculated based on an absorbance coefficient of 0.042 $mm^{-1}Lmg^{-1}$ according to the indigo method developed by Bader and Hoigné (1982). The tests were conducted over a wide range of initial dissolved ozone concentrations and water temperatures to investigate their effects on the ozone auto-decomposition kinetics. The initial dissolved ozone concentration and temperature of the test water ranged from 2.0 to 3.1 mgL^{-1} and from 2.6 to 38.5 °C, respectively.

8.3.2 Pilot-Scale Tests: Ozone Mass Transfer Study

The ozone mass transfer experiments were conducted in a pilot-scale impinging-jet bubble column (see Figure 8.3). The bubble column was made from PVC and had an inside diameter of 100 mm and a total height of 1,520 mm.

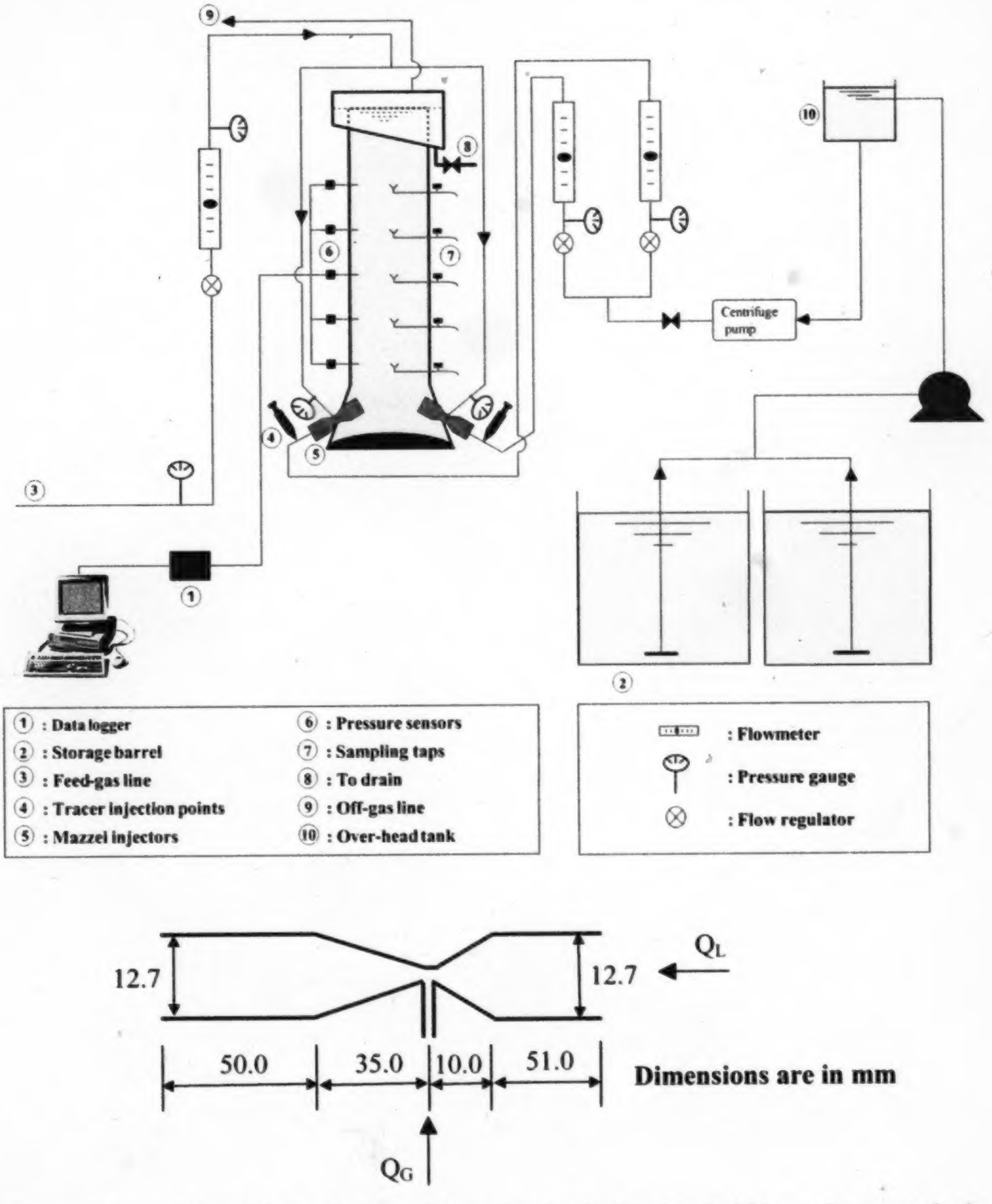
Centrifuge pump
① : Data logger
② : Storage barrel
③ : Feed-gas line
④ : Tracer injection points
⑤ : Mazzei injectors
⑥ : Pressure sensors
⑦ : Sampling taps
⑧ : To drain
⑨ : Off-gas line
⑩ : Over-head tank
: Flowmeter
: Pressure gauge
: Flow regulator
12.7
12.7
Q_L
50.0
35.0
10.0
51.0
Dimensions are in mm
Q_G

Figure 8.3 Schematics of the pilot-scale impinging-jet bubble column and the configuration of the Mazzei® injector (model 384).

The water depth was kept constant at 1,315 mm using an overflow weir that was placed at the top of the column. A ring tube was also installed at the top of the column with a 20 mm-diameter hole facing downward. A schematic of the configuration of the kynar Mazzei® venturi injectors (model 384) is shown in Figure 8.3. The injectors were placed 25 mm above the bottom of the column at an intersecting angle of 125° and the distance between the centers of the nozzles was set equal to 60 mm. The bottom part of the bubble column consisted of an elliptical base to reduce the effect of the backward jet that was created in the ambient fluid as a result of the jet impingement and the sidewalls of that part of the column had a conical shape. With this geometry at the bottom of the column, the effects of short-circuiting were minimized. Based on the above reactor configuration, it was reasonable to assume that the backmixing along the column height was uniform. This assumption was also validated by the results of tracer experiments that were conducted in the bubble column.

During ozonation tests, water samples were withdrawn from the column from five bell-shaped sampling taps that were inserted inside the reactor at a distance equal to 1/3 of the column diameter and at equal intervals along the column height. The bell shape of the sampling taps helped minimizing the entrainment of gas bubbles into the withdrawn water samples for measuring the dissolved ozone concentrations. During each ozonation test, five water samples were withdrawn directly from the sampling taps into volumetric flasks at an adequate flowrate to minimize any ozone loss during the sampling procedure. The dissolved ozone concentrations were measured and calculated following the same procedure described in the kinetics study section. Five pressure sensors (Model 26PC Honeywell®) were inserted inside the reactor, at a distance equal to 1/3 of the column diameter and at intervals equal to those of the bell-shaped sampling taps, to monitor the pressure along the column height. The test water used in the experiments was clean deionized water of similar characteristics to those of the water used in the kinetics study. The ozone gas was generated from extra-dry pure oxygen using a corona discharge ozone generator (model GLS-7, PCI-WEDECO®). The ozone generator was allowed to stabilize for at least 1,800 s in order to obtain a stable ozone concentration in the feed gas. During the ozonation tests, the ozone concentrations in the feed and off-gas lines were continuously monitored using PCI-WEDECO® ozone monitors (models HC400 and LC, respectively). The ozone monitors were allowed at least 900 s to stabilize before recording their readings. Periodic calibration of the ozone monitors was conducted using the KI method as described by the standard methods for examination of water and wastewater (APHA-AWWA-WEF, 1995). All the materials that came in contact with ozone during the experiments were made of glass, teflon, stainless steel, or PVC to reduce the possible interference that would result from the reactions between the dissolved and/or gaseous ozone and the experimental set-up components.

The ozone contactor was operated in a co-current flow mode and the gas was sparged into the liquid flow under two modes of pressure: positive pressure (i.e., injection) mode and negative or suction pressure (i.e., ejection) mode. In order to minimize the fluctuations in the liquid flowrates during experiments, the test water was pumped from two storage barrels into an overhead tank using peristaltic pumps then the water was pumped from the overhead tank into two lines leading into the injectors using a centrifugal pump. As the liquid motive flow passed though the injectors, the gas flow was introduced into the flow through the injectors' throats. The liquid flow, after being divided into two lines, was passed through two flowmeters to measure the liquid flowrates. The gas flow was passed through a gas rotameter to measure the gas flowrate. Pressure gauges were installed on the liquid-flow lines to measure the liquid pressure in the lines. Pressure gauges were also installed at the gas rotameter exit and at the injectors' throats to measure the gas pressures in the gas lines. All the pressure gauges were calibrated prior to their use. The bubble column was operated for a period of time that was at least eight theoretical reactor retention times to allow for the ozonation process to reach isothermal steady-state conditions and that was verified by reaching a constant off-gas ozone concentration in the exhaust-gas line. The gas hold-up data along the column height was obtained by continuous monitoring of the pressure readings along the column height. The pressure data were collected instantaneously and downloaded to a PC using a Lakewood® data logger. A wide range of superficial liquid velocities, and feed-gas velocities, and feed-gas ozone concentrations was investigated in order to study their effects on the performance of the impinging-jet ozone bubble column. The operating conditions of the pilot-scale ozonation experiments are presented in Table 8.4.

Table 8.1 Operating conditions of the pilot-scale ozone mass transfer experiments.

TR#	Flow pattern	Gas sparging mode	u_G (ms^{-1})	u_L (ms^{-1})	T_L °C	T_G °C	$C_{G,in}$ (mgL^{-1})	$C_{G,off}$ (mgL^{-1})	1P-ADM fitted D_L (m^2s^{-1})	1P-ADM fitted k_La (s^{-1})	1P-ADM fitted a_l	SSR	St_L	St_G	Pe_L	D_a
1	⇈	Injection	2.5E-03	7.7E-03	23.4	22.3	75.0	35.1	8.3E-03	1.3E-02	0.76	1.0E-03	2.20	1.55	1.17	6.1E-02
2			2.5E-03	1.4E-02	22.0	23.0	74.3	27.0	1.0E-02	1.8E-02	1.01	2.0E-03	1.59	2.05	1.70	2.9E-02
3			3.8E-03	7.7E-03	23.0	22.0	73.7	40.9	4.1E-03	2.5E-02	0.50	8.3E-03	4.05	1.93	2.35	5.9E-02
4			2.4E-03	1.4E-02	21.1	21.8	37.8	14.3	1.1E-02	2.1E-02	0.97	1.8E-03	1.93	2.60	1.61	2.6E-02
5			3.8E-03	7.5E-03	24.5	22.0	37.2	21.5	3.0E-03	2.2E-02	0.55	5.8E-04	3.67	1.70	3.21	7.0E-02
6			3.6E-03	1.4E-02	23.0	22.0	37.9	17.1	6.1E-03	2.4E-02	0.80	1.7E-04	2.13	1.93	2.91	3.2E-02
7			7.5E-03	7.7E-03	24.2	22.1	37.5	26.4	1.5E-03	3.9E-02	0.30	2.7E-03	6.51	1.56	6.58	6.8E-02
8			7.3E-03	1.4E-02	23.1	22.1	37.4	21.8	5.3E-03	5.2E-02	0.54	8.8E-04	4.75	2.15	3.44	3.3E-02
9			1.1E-02	2.4E-02	22.7	22.5	37.3	21.2	3.2E-03	8.0E-02	0.30	6.9E-03	4.40	2.17	9.51	1.9E-02
10			2.6E-03	7.7E-03	22.7	22.3	11.6	5.7	5.7E-03	1.7E-02	0.50	2.2E-03	2.86	2.00	1.71	5.7E-02
11			3.8E-03	7.9E-03	24.0	22.5	11.2	6.5	3.3E-03	2.1E-02	0.50	2.2E-05	3.32	1.61	2.99	6.4E-02
12			2.6E-03	7.9E-03	21.1	22.0	37.5	18.5	6.3E-03	1.6E-02	0.33	1.4E-03	2.56	1.83	1.57	4.7E-02
13	⇈	Ejection	1.8E-03	2.4E-02	21.3	22.8	74.6	15.8	2.4E-02	1.2E-02	1.55	4.1E-04	0.67	2.06	1.24	1.6E-02
14			2.8E-03	2.4E-02	21.3	22.3	75.4	21.2	2.3E-02	1.8E-02	1.27	2.6E-04	0.94	1.84	1.29	1.6E-02
15			1.4E-02	2.8E-02	21.0	22.5	22.5	13.3	1.2E-02	1.2E-01	0.53	1.9E-03	5.56	2.66	3.08	1.3E-02
16			1.8E-03	2.3E-02	19.5	22.1	38.0	8.2	2.3E-02	1.3E-02	1.53	3.8E-04	0.72	2.18	1.28	1.3E-02
17			2.9E-03	2.3E-02	22.6	22.2	37.8	11.1	2.3E-02	1.8E-02	1.23	4.9E-04	0.95	1.81	1.27	1.9E-02
18			6.4E-03	2.3E-02	22.2	21.7	37.9	17.2	2.2E-02	5.2E-02	0.79	8.6E-04	2.89	2.46	1.40	1.8E-02
19			1.0E-02	2.8E-02	22.4	22.4	38.8	20.2	1.2E-02	7.6E-02	0.40	1.1E-03	3.46	2.19	3.00	1.5E-02
20			1.8E-03	2.3E-02	22.0	21.8	14.5	3.9	2.6E-02	1.1E-02	1.30	3.5E-04	0.58	1.75	1.13	1.7E-02
21			2.9E-03	2.3E-02	22.4	21.9	11.8	3.9	2.3E-02	1.6E-02	1.11	1.1E-03	0.90	1.70	1.31	1.9E-02
22			8.8E-03	2.3E-02	19.9	22.0	22.1	12.0	2.1E-02	8.7E-02	0.53	1.3E-03	4.75	2.95	1.41	1.4E-02
23			8.0E-03	2.8E-02	19.9	22.7	22.3	10.7	1.3E-02	5.7E-02	0.58	7.2E-03	2.61	2.13	2.74	1.2E-02

8.3.3 Data Analysis Method for the Kinetics Study

The ozone auto-decomposition process was assumed to follow first-order kinetics as described by Equation 8.1 and this assumption was considered valid if the plotted data of ln $[O_3]_t$ versus t could be represented by a straight line. The slope of that line would represent specific ozone utilization rate constant (k_w) while the intercept would represent $\ln[O_3]_{t=0\,s}$. In all the ozonation tests, $\ln[O_3]_{t=30\,s}$ was compared to $\ln[O_3]_{t=0\,s}$ to calculate the initial ozone demand of the test water. A linear regression technique was employed to obtain the slope and the intercept of the proposed straight line. The predicted values of k_w were pooled together to investigate the effect of the water temperature (T_L) on the ozone auto-decomposition kinetics. It was assumed that this effect could be described by the well-known van't Hoff-Arrhenius relationship:

$$\ln\left(k_w\big|_{T_L{}^\circ C}\right) = \ln\left(k_w\big|_{20^\circ C}\right) + (T_L - 20)\ln\theta \qquad [8.13]$$

where: θ = dimensionless temperature correction factor, k_w = specific ozone utilization rate constant (s^{-1}), and T_L = water temperature (^oC).

8.3.4 Data Analysis Method for the Mass Transfer Study

The solution of the steady-state 1P-ADM represented by Equation 8.3 was used to create a simple spreadsheet program in which the product cells were assigned to the column-average overall mass transfer coefficient (k_La), liquid-phase axial dispersion coefficient (D_L), and coefficient of the gas-phase ozone molar fraction decrease along the column height (a_1). The specific ozone utilization rate constant ($k_w\big|_{T_L{}^\circ C}$) had to be provided through the dimensionless Damköhler number (D_a). For each ozonation test, since the water temperature (T_L) was measured, a temperature correction factor (θ) that was obtained from the kinetics study was used to calculate $k_w\big|_{T_L{}^\circ C}$. In the spreadsheet program, the target cell was assigned to the following error norm:

$$\mathrm{SSR}\left(k_L a, D_L, a_l\right) = \sum_{i=1}^{i=6}\left(X_{\mathrm{measured},i} - X_{\mathrm{calculated},i}\right)^2 \qquad [8.14]$$

Equation 8.14 represents the summation of squared residuals (SSR) of the difference between the measured and predicted dimensionless dissolved ozone concentrations. The spreadsheet program executed and the values of $k_L a$, D_L, and a_l were varied until the SSR was minimized.

8.4 EXPERIMENTAL RESULTS

8.4.1 Bench Tests: Ozone Auto-Decomposition Kinetics Study

Comparisons of the $\ln[O_3]_{t=30\ s}$ with the $\ln[O_3]_{t=0\ s}$ values produced a relative error of ≤ 0.6 %. This result supported the assumption that the clean deionized water had negligible or essentially no initial ozone demand. The plots of $\ln[O_3]_t$ versus the reaction time (t) were described by straight lines through the linear regression analyses with the coefficients of correlation (r's) ≥ 0.87.

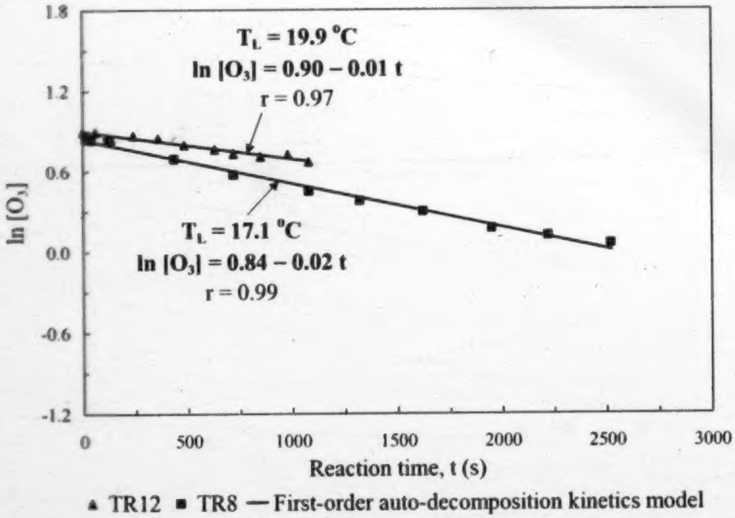

Figure 8.4 Typical ozone auto-decomposition kinetics in deionized water.

Figure 8.4 depicts typical plots of $\ln[O_3]_t$ values versus as functions of the reaction time during two of the ozone auto-decomposition kinetics experiments under two different temperatures.As shown in Figure 8.4, the first-order kinetics can adequately describe the ozone auto-decomposition process in clean waters that have negligible initial ozone demand. The regression analysis produced similar specific ozone utilization rate constants (k_w's) for the tests that were conducted at the same initial water temperature and different initial dissolved ozone concentrations. Therefore, it can be concluded that there was no effect of the initial ozone concentration on the specific ozone utilization rate constant.

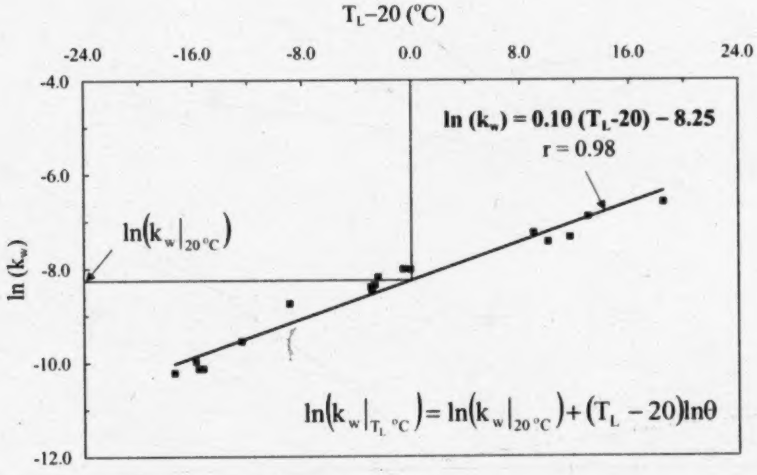

Figure 8.5 The effect of water temperature on the ozone auto-decomposition rate constant.

Figure 8.5 shows the effect of temperature on the ozone auto-decomposition rate constant. The temperature correction factor (θ) and $k_w\big|_{20°C}$ were found to be 1.11 and $2.61 \times 10^{-4}\ s^{-1}$, respectively, and the coefficient of correlation (r) was equal to 0.96. Yurteri and Gurol (1988) investigated the ozone auto-decomposition process in natural waters that are characterized by their high initial ozone demands. $k_w\big|_{20°C}$ was determined to be 2.78 x 10^{-3} s^{-1}. A comparison of the $k_w|_{20°C}$ value obtained in the current study with value obtained in the study of Yurteri and Gurol (1988) indicates that the ozone auto-decomposition process in clean waters, that exhibit negligible initial ozone demands, is a very slow process.

8.4.2 Pilot-Scale Tests: Ozone Mass Transfer Study

In order to solve Equation 8.3 that represents the 1P-ADM, the spreadsheet program was allowed a maximum number of 200 iterations. Despite that, the convergence criterion was satisfied in less than 200 iterations and the SSR was minimized with a relative error in the SSR $\leq 10^{-3}$. Sensitivity analysis was conducted to test the sensitivity of the predicted dissolved ozone concentration profiles towards changes in k_La, D_L, and a_1. The results indicated that these profiles were more sensitive to changes in k_La than changes in D_L and a_1. The same phenomenon was observed before by Deckwer *et al.* (1983) when they solved the axial dispersion model (ADM) in the liquid phase only to estimate k_La and D_L for a co-current 1mm-perforated-plate bubble column using a similar two-parameter minimization technique by varying k_La and D_L. At low liquid superficial velocity (u_L) of 5.4 x 10^{-2}, there was reasonable agreement between the D_L values obtained using the minimization technique and the values using the correlation of Deckwer *et al.* (1974). The operating conditions and the results of the minimization solution technique for the pilot-scale ozone mass transfer experiments are shown in Table 8.4. Figures 8.6 and 8.7 depict typical dimensionless dissolved ozone concentration profiles in the injection and ejection modes, respectively. The dimensionless dissolved ozone concentrations are plotted as functions of the dimensionless axial co-ordinate of the column. Henry's law constant (H) of 0.22 kPaLmg^{-1} was obtained from Sotelo *et al.* (1989).

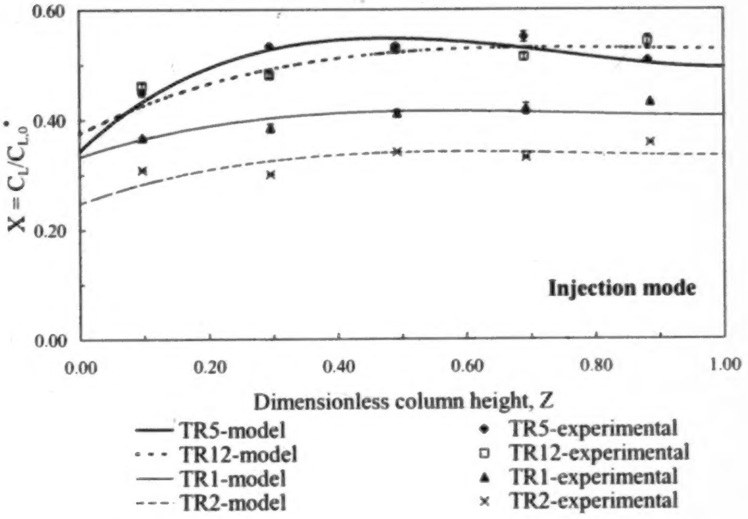

Figure 8.6 Typical dimensionless dissolved ozone concentration profiles in the impinging-jet bubble column operated in a gas-injection mode.

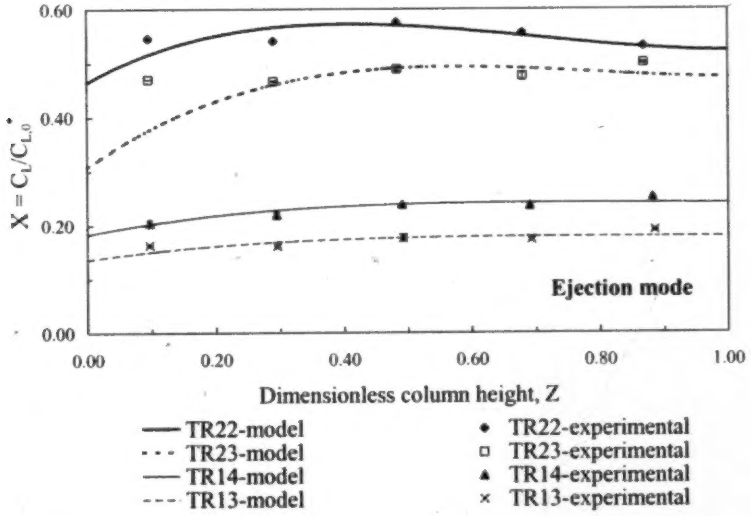

Figure 8.7 Typical dimensionless dissolved ozone concentration profiles in the impinging-jet bubble column operated in a gas-ejection mode.

Each ozone concentration was based on a number of two replicates. The absolute error between each pair of dissolved ozone concentrations was ≤ 5.5 % with a mean value of 1.3 %. The normalized standard deviation ($SD/C^{*}_{L,0}$) of each pair of replicates was ≤ 1.9×10^{-2} with a mean value of 3.7×10^{-3}. As shown in Figures 8.6 and 8.7 and despite some deviations of the measured concentrations from the ones estimated by the 1P-ADM, the 1P-ADM has provided excellent predictions of the dissolved ozone concentration profiles. This is evident from the conformity between the measured and the predicted dissolved ozone concentrations. At the first sampling tap near the bottom of the column, the measured concentrations were sometimes higher than the estimated concentrations. This could be a result of the location of the first sampling tap being very close to the injectors' exit points and sometimes that led to entrainment of some gas bubbles into the liquid withdrawn from the sampling tap especially in the experiments that were conducted at high u_G's. Due to the operating nature of the venturi injectors, the impinging-jet bubble column had to be operated in a co-current flow mode. Generally, the dissolved ozone concentrations, estimated by the 1P-ADM, increased along the column height up to a point where they started decreasing. The location of this point varied depending on the operating conditions.

Regarding the effect of u_G on the dissolved ozone concentration profiles, the profiles of TR's 5 and 12 were compared. Those tests were conducted in the injection mode at almost the same u_L. As u_G increased from 2.6×10^{-3} ms^{-1} in TR 12 to 3.8×10^{-3} ms^{-1} in TR 5, the maximum estimated dissolved ozone concentrations increased and their locations shifted from $Z = 0.72$ to $Z = 0.47$. The same phenomenon was reported by Gamal El-Din and Smith (2000) when they investigated the effect of k_La on the dissolved ozone concentration profiles in conventional diffuser bubble columns. The estimated k_La increased from 1.6×10^{-2} in TR 12 to 2.2×10^{-2} s^{-1} in TR 5 and the estimated D_L decreased by almost 50 %. The estimated a_l increased from 0.33 in TR 12 to 0.55 in TR 5. A similar trend was observed in the ejection mode when comparing the profiles of TR's 13 and 22 except that the effect of increasing u_G on the estimated value of k_La was higher than that in the injection mode. Meanwhile, the effect of increasing u_G on the estimated value of D_L was lower than that in the injection mode.

Regarding the effect of u_L on the dissolved ozone concentration profiles, the profiles of TR's 1 and 2 were compared. Those tests were conducted in the injection mode at the same u_G. As u_L increased from 7.7×10^{-3} ms^{-1} in TR 1 to 1.4×10^{-2} ms^{-1} in TR 2, the maximum estimated dissolved ozone concentrations decreased. Also, the locations, of those maximum concentrations, were near the near the middle point of the column height (at $Z = 0.54$ and $Z = 0.58$ in TR 1 and 2,respectively). The same phenomenon was reported by Gamal El-Din and Smith (2000) when they investigated the effect of Pe_L on the dissolved ozone concentration profiles in conventional diffuser bubble columns. The estimated k_La increased from 1.3×10^{-2} in TR 1 to 1.8×10^{-2} s^{-1} in TR 2 and the estimated D_L increased by almost 20 %. The estimated a_l decreased from 1.55 in TR 13 to 0.53 in TR 22.

In the current bubble column design, the mass transfer process was maximized considerably and that led to higher mass transfer driving force ($C^*_{L,\ell} - C_{L,\ell}$) throughout the entire column height. The ozone auto-decomposition process had minimal impact on the dissolved ozone profiles as a result of the low specific ozone utilization rate constant exhibited by the deionized water used in the current study. As a result, the mass transfer process was superior to the ozone auto-decomposition process in determining the shape of the dissolved ozone concentration profiles as well as the residual ozone concentration levels achieved in the column effluent.

The design of the impinging-jet bubble column is different from the conventional bubble column designs in terms of the interrelated effects of the superficial gas and liquid velocities (u_G and u_L) on the performance of the gas-liquid injectors and ultimately, on the performance of he impinging-jet bubble column. Operating the venturi injectors in the injection or ejection mode and increasing u_L, an increase in u_G and a decrease in the injector throat pressure will occur, while operating at the same u_L and increasing u_G will cause the injector throat pressure to increase. The difference in pressure between the gas introduction point and the exit point of the injector, inside the column, will affect the size of the gas bubbles leaving the injectors and consequently, the bubbles' specific interfacial area will change. At almost similar u_G, this differential pressure was generally higher and occurred at higher u_G's in the ejection mode compared to those in the injection mode. As a result, the same combination of u_G and u_L cannot coexist in the injection and ejection modes. Therefore, the two modes of gas absorption had to be analyzed separately. Part of the overall system-mass-transfer efficiency is attributed to the contact time between the gas phase and the liquid phase inside the intense mixing zone inside the venturi injector, i.e., from the gas introduction point to the exit point of the injector inside the column (Mazzei and Bollyky, 1991). As a result, an increase in this contact time will lead to an increase in the efficiency of the overall mass transfer process.

8.5 DEVELOPMENT OF PROCESS-PARAMETER CORRELATIONS

In order to study the effects of the gas and liquid flowrates on the 1P-ADM estimations of the column-average k_La and D_L, relationships that correlate these two parameters with the superficial gas and liquid velocities (u_G and u_L) were developed through non-linear regression analyses. Comparisons of the performance of the impinging-jet bubble column with the conventional bubble columns, in terms of k_La, were also conducted in order to assess the improvement in the mass transfer process by utilizing the impinging-jet technique for the ozone gas absorption process. The effects of the process variables on a_l were also studied by correlating a_l to the process variables Pe_L, St_L, St_G, and D_a by applying a linear regression technique.

As discussed earlier regarding the dynamic nature of the venturi injectors as gas absorbers, it was observed that they exhibited variable behaviour in the injection mode from that in the ejection mode. Therefore, the regression analyses were conducted for the gas-injection mode separately from the gas-ejection mode to obtain process parameter correlations that can be used for estimating the process variables (k_La, D_L, and a_l) using the operating conditions encountered during the ozonation process. The mass transfer process is a liquid-phase-temperature dependent while the backmixing process dependency on the liquid-phase temperature is minimal (Deckwer, 1992). As a result, and due to the variable water temperature during the tests, the predicted k_La's were corrected for the temperature effect using a temperature correction factor (θ) equal to 1.024 as suggested by Roustan *et al.* (1996).

8.5.1 Correlations of the Mass Transfer Coefficient

In the impinging-jet bubble column, k_La was affected by u_G and u_L in contrast to the case in most conventional bubble columns where it is usually affected only by u_G except for few studies involving other designs of bubble columns where k_La was affected by u_G and u_L. Among these few studies, the combined venturi-bubble columns studied by Huynh *et al.* (1991) and Briens *et al.* (1992) emerged as promising new bubble column designs. For conventional diffuser bubble column, Deckwer *et al.* (1974) proposed an empirical correlation to be as follows:

$$k_La = \alpha\, u_G^{\beta} \qquad [8.15]$$

where: k_La = overall mass transfer coefficient (s^{-1}), u_G = superficial gas velocity (ms^{-1}), and α and β = empirical coefficients that are obtained through a non-linear regression analysis. In order to correct for the difference in diffusivity between oxygen and ozone, Danckwerts' surface renewal theory is applied as follows:

$$\frac{(k_La)_{O_3}}{(k_La)_{O_2}} = \sqrt{\frac{D_{O_3}}{D_{O_2}}} \qquad [8.16]$$

The use of Equation 8.17, to correct k_La from being an oxygen-based to ozone-based, has been previously validated (Sherwood *et al.*, 1975). D_{O_3} and D_{O_2} are the molecular diffusivities of ozone and oxygen gases, respectively, in water. D_{O_3} and D_{O_2} were taken as 1.74 x 10^{-9} and 2.50 x 10^{-9} m^2s^{-1}, respectively. Based on "state of science" review of the literature, and after correcting for the temperature effect and converting k_La to be ozone-based instead of oxygen-based parameter, it was found that α and β varied from 0.06 to 1.16 and from 0.54 to 0.88. β was found to be independent on the sparger type, however, α was strongly affected by the sparger type and the liquid medium (Shah *et al.*, 1982). This variability in α and β values could be attributed to the variable bubble column physical properties and scales, the type of gas sparging technique, neglecting the effect of test water properties on the ozone decay process, and more importantly the method of k_La determination. In most of these studies, k_La was calculated based on one of two assumptions regarding the backmixing in the liquid phase. The liquid phase was considered to flow in an ideal completely mixed or plug flow regimes. As a matter of fact, neither one of these flow regimes exists in bubble columns, since the liquid flow is usually closer to be in the completely mixed regime as a result of the backmixing process (Zhou *et al.*, 1994).

In the study conducted by Roustan *et al.* (1987), the conventional ozone contactor had a water height of 4,300 mm and two compartments in series, 117 m^3 and 128 m^3 in volume, respectively. In that study, two assumptions were made that seemed to have a significant impact on the determined values of k_La's and that might have led to some discrepancy with the reported values of k_La in the literature. First, a complete mixing regime was assumed to dominate the liquid flow through the contactor and second, the ozone decay process was neglected in the potable test water since the water temperature was about 5 ^oC. Another source of discrepancy may have resulted from k_La being calculated based on conducting mass balance analyses of the ozone in the gas and liquid phases using only the influent and effluent dissolved and gaseous ozone concentrations. This method was not appropriate since the dissolved ozone concentration in the effluent might not have been sensitive to k_La, especially in situations where high-absorption efficiency existed. Also, any experimental errors that might be encountered in measuring the effluent concentration can lead to a large bias in estimating k_La (Zhou, 1995).

Laplanche *et al.* (1991) studied the ozone mass transfer process in a bubble column that had a height and a diameter equal to 4300 mm and 190 mm, respectively. They neglected the ozone decay process in the potable test water that was used in the experiments and also the backmixing in the liquid phase was neglected leading to the assumption that the liquid flow through the reactor was in perfect plug flow regime.

Deckwer *et al.* (1974) studied the oxygen mass transfer process in two bubble columns that had diameters of 200 mm 150 mm, and heights of 7230 mm and 4400 mm. They used the axial dispersion model to describe the bubble column performance. A one-parameter minimization technique was applied to determine k_La by fitting the measured dissolved oxygen profiles to the predicted profiles. This approach seems to be the most appropriate method to characterize the mass transfer in bubble columns operated in a continuous-flow mode since it takes into account the backmixing effect on k_La and the resultant concentration jump occurring at the column inlet due to the column inlet boundary conditions. Also, it uses the concentration profiles along the entire column height to determine the column-average k_La.

Deckwer *et al.* (1983) examined the applicability of the 2P-ADM to analyze the mass transfer measurements in bubble columns. They used the same approach applied by Deckwer *et al.* (1974) except for using a two-parameter (k_La and D_L) instead of a 1-parameter (k_La) minimization technique. In order to examine the sensitivity of the predicted k_La to changes in the backmixing coefficient (D_L), they calculated D_L using the relationship suggested by Deckwer *et al.* (1974) that correlated D_L with the superficial gas velocity and the bubble column diameter. Then, they used the one-parameter minimization technique to determine k_La. They observed that k_La varied only slightly (< 10 %) between the two minimization techniques.

In the studies conducted by Huynh *et al.* (1991) and Briens *et al.* (1992), k_La was correlated to u_G and u_L according to the following relationship:

$$k_L a = \alpha\, u_G^{\beta}\, u_L^{\gamma} \qquad [8.17]$$

where: k_La = overall mass transfer coefficient (s^{-1}), u_G = superficial gas velocity (ms^{-1}), u_L = superficial liquid velocity (ms^{-1}), and α, β, and γ = empirical coefficients that are obtained through a non-linear regression analysis. Huynh *et al.* (1991) correlated u_G and u_L to the venturi-bubble column average k_La. In that system, the liquid flowed upward and the injection mode was used for the gas absorption process. They assumed that ideal plug flow conditions existed in the venturi injector and the bubble column based on visual observations of the Methylene blue mixing patterns. The venturi injector had a 95.3 mm exit-diameter and a 380 mm height. The bubble column had a diameter and a height of 95 mm and 790 mm, respectively. α, β, and γ were estimated to be 2.56, 0.53, and 0.96, respectively.

Briens *et al.* (1992) correlated u_G and u_L to the venturi injector k_La separately from the bubble column k_La. In that system, the liquid flowed downward and the ejection mode was used for the gas absorption process. α, β, and γ were estimated to be 0.81, 1.91, and −1.91, respectively, for the venturi injector. For the bubble column, α, β, and γ were estimated to be 7.64, 0.99, and 0.00, respectively. Based on their tracer experiments, they assumed that ideal complete mixing conditions existed in the bubble column that had a height of 790 mm and a diameter of 95 mm. They observed that the superficial liquid velocity (u_L) had no effect on k_La. As a result the relationship represented by Equation 8.16 was used to correlate k_La to u_G in the bubble column.

In the current study and under the injection mode for the gas absorption process, k_La was found to be dependent on u_G and u_L. The non-linear regression parameters (α, β, and γ) were estimated to be 12.50, 0.83, and 0.37, respectively. The non-linear regression analysis produced a correlation coefficient (r) of 0.99. As u_G increased, k_La increased considerably as observed before by several researchers (Deckwer *et al.*, 1974; Roustan *et al.*, 1987; Laplanche *et al.*, 1991; Huynh *et al.*, 1991; Zhou, 1995; Zhou and Smith, 2000). This could be explained by the following phenomenon: as u_G increases, the gas bubbles' mean specific interfacial area increases due to the increase in the volume-to-surface area mean bubble diameter (i.e., Sauter diameter, d_S). Also as u_L increased, k_La increased. Similar observations were reported by Wang and Fan (1978) and Huynh *et al.* (1991).

In the impinging-jet bubble column, it is expected that as u_L increases, the intensity of turbulence will increase causing the turbulent shear stresses to increase considerably in the venturi injector as well as in the bubble column. Consequently, this will result in smaller bubbles and higher gas bubbles' mean specific interfacial area and as a result, k_La will increase. By contrast, and since a considerable amount of the overall mass transfer efficiency that can be obtained in the impinging-jet bubble will be attributed to the mass transfer process that takes place inside the venturi injector. Increasing u_L will cause the residence time inside the injectors to decrease, thus, leading to a decrease in the overall bubble column mass transfer efficiency, i.e., the column-average k_La will decrease. An experimental study was conducted in the impinging-jet bubble column to investigate the effects of the operating conditions on the characteristics of the gas bubbles. A 2-D laser particle dynamics analyzer that utilizes the laser Doppler anemometry (LDA) technique to measure the turbulence intensity and the phase Doppler anemometry (PDA) technique to measure the bubble size and concentration was used to perform such measurements in the impinging-jet bubble column. The same experimental procedure for the laser system set up as described by Zhou and Smith (2000) was used in the current study.

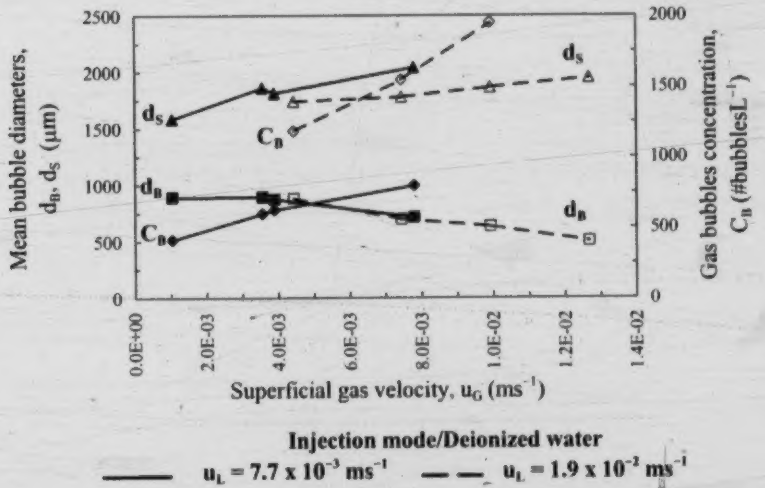

Figure 8.8 Effects of the u_G and u_L on the gas bubble diameters and concentrations in the injection mode.

Figure 8.8 depicts the effects of u_G and u_L on the Sauter mean bubble diameter (d_S, μm), the count mean bubble diameter (d_B, μm), and the concentration of gas bubbles (C_B, #bubblesL^{-1}). As u_G increased, d_B decreased almost linearly while d_S and C_B increased almost linearly. As u_L increased, there was virtually no effect on d_B while it caused a significant decrease in d_S and also a significant increase in C_B. The Mixing intensities were found to be significantly high in the vertical and radial directions. Under the operating conditions represented in Figure 8.8, the turbulence % in the gas phase (= root mean square velocity/mean velocity) reached a maximum of 95 % and 5550 % in the vertical and radial directions, respectively. Although the turbulence intensity in the liquid phase was not measured, it was expected that since the turbulence levels in the gas phase were high, the liquid phase would as well exhibit high levels of turbulence.

During the gas-injection mode, the effect of the residence time inside the injectors on reducing k_La as u_L increases perhaps was smaller than that of increasing u_L leading to an increase in the shearing of the large gas bubbles into smaller bubbles and consequently, causing the mean gas bubbles' specific interfacial area to increase as well as k_La.

Figure 8.9 depicts a comparison between the k_La correlation developed in the current study, in the gas injection mode, with those developed in previous studies. As shown in Figure 8.9, the impinging-jet bubble column has proven to cause a significant increase in the overall ozone mass transfer coefficient (k_La) compared to the conventional and upward-venturi-injector bubble columns. By operating the gas absorption process in the ejection mode, k_La was found to be dependent on u_G and u_L. The non-linear regression parameters (α, β, and γ) were estimated to be 0.09, 1.43, and –1.78, respectively. These coefficients are comparable with those of Briens *et al.* (1992). The non-linear regression analysis produced a correlation coefficient of 1.00. The effect of u_G on k_La was higher than that in the injection mode. When operating in the ejection mode and contrary to its overall effect on k_La in the injection mode, as u_L increased, k_La decreased. As discussed earlier and since the injection mode was associated with higher u_L's, the effect of the residence time inside the injectors might have been higher than the effect of increasing the turbulent shear stresses on the shearing of the large gas bubbles into smaller bubbles.

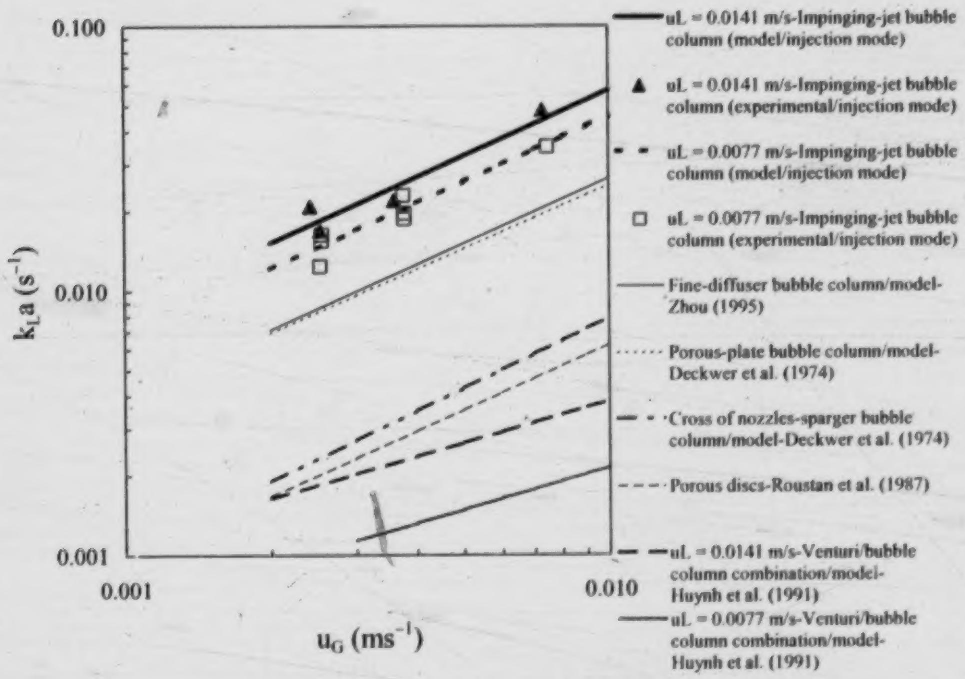

Figure 8.9 Comparison of the k_La correlations for gas sparging under positive pressure in various types of bubble columns.

Figure 8.10 depicts a comparison between the k_La predicted in the current study, in the gas ejection mode, with that predicted in the study conducted by Briens *et al.* (1992). Due to the downward-flow arrangement in the study of Briens *et al.* (1992), the gas-phase residence time inside the system increased leading to higher k_La. As shown in Figure 8.10, and despite the above operational advantage of the system investigated by Briens *et al.* (1992), the impinging-jet bubble column has proven to k_La that was comparable to that in the downward-venturi-injector bubble column. Comparisons between the impinging-jet-bubble-column average k_La's that were obtained in the ejection mode with the k_La's obtained in conventional bubble column designs have shown that the impinging-jet design was also superior in terms of its higher mass transfer efficiency.

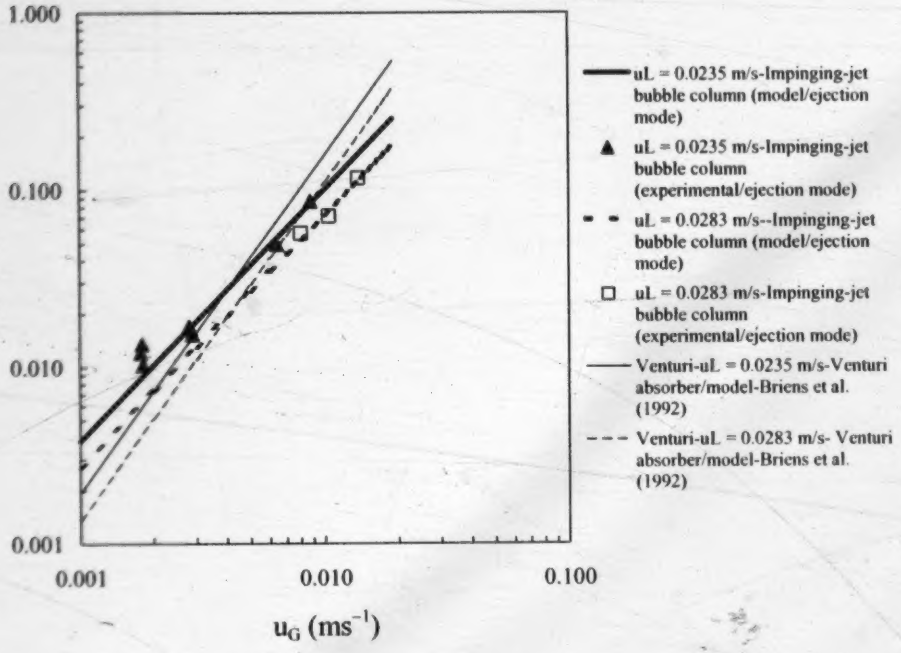

Figure 8.10 Comparison of the k_La correlations for gas sparging under negative pressure in various types of bubble columns.

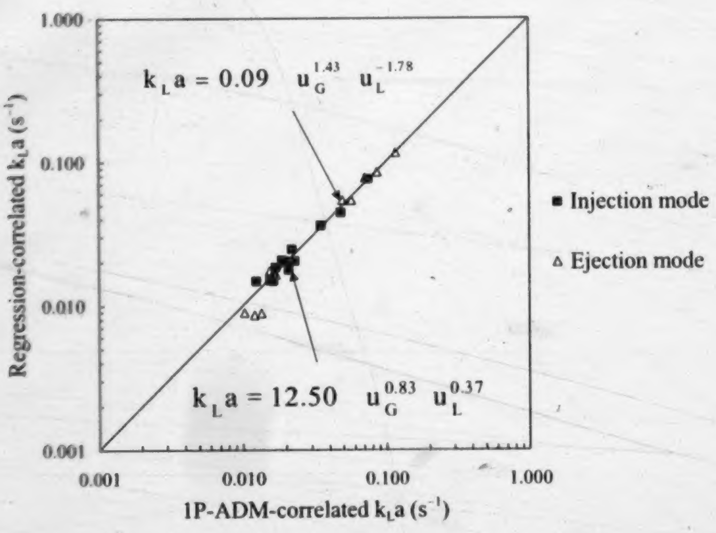

Figure 8.11 Comparison between the 1P-ADM and the non-linear regression correlations of k_La.

Figure 8.11 presents a comparison between the k_La values that were estimated using the 1P-ADM and the k_La values estimated using the non-linear regression technique. The excellent conformity between the two methods strongly suggests the consistency of the 1P-ADM in estimating k_La under a wide range of gas and liquid flowrates.

8.5.2 Correlations of the Backmixing Coefficient

The liquid phase dispersion results from the entrainment of the surrounding liquid by the rising gas bubbles that carry the entrained liquid upwards (Deckwer, 1992). Using two-phase jets to create jet impingement in the ambient fluid will produce a jet that grows at a higher rate than a single jet. As the resultant jet travels forward and grows, it will entrain some of the surrounding ambient fluid, thus causing the mean jet flow to be higher than that at the jet nozzle as observed by several researchers (Rajaratnam, 1976). Based on the above, a circular flow will be developed above the convective flow and as a result, the liquid near the central axis of the flow will move upwards with most of the gas bubbles and the liquid near the walls will move downwards. Measurements of the radial velocity profiles can confirm the existence of the circular flow pattern (Deckwer, 1992).

In bubble columns characterized by their small bubble Sauter diameter range, all the liquid almost envelops the gas bubble and is entrained and dragged upwards. As a result, a sink will be developed near the gas distributor and pressure oscillations will occur. This will cause the gas-liquid dispersion to flow downwards again (Deckwer, 1992). The experimental data of König *et al.* (1978) have shown that, in an air-water bubble column equipped with perforated plates and as u_G increased up to 2.0×10^{-2} ms^{-1}, D_L decreased from about 1.4×10^{-2} m^2s^{-1} to 1.0×10^{-2} m^2s^{-1}. This could have been a result of the gas-liquid flow being in a homogeneous bubbly regime where it would be characterized by its high gas bubble concentration and, uniform gas bubble size, and gas bubble size distribution and therefore, constant rise velocity. This would have led to rising of the gas bubbles without mutual interference leading to uniform degrees of axial and radial distribution of gas hold-up and a low degree of macro-turbulence (Kaštánek *et al.*, 1993). Tracer tests were conducted and the estimated backmixing coefficients (D_L's) were in good agreement with the 1P-ADM estimated D_L's under the tested conditions of $u_G \leq 1.4 \times 10^{-2}$ ms^{-1} and $u_L \leq 2.8 \times 10^{-2}$ ms^{-1}. The same phenomenon was observed in the study of Deckwer *et al.* (1983) when u_L was $\leq 3.0 \times 10^{-2}$ ms^{-1}. The estimated D_L's, using the 1P-ADM, were converted to the dimensionless Peclet numbers (Pe_L's). Pe_L ranged from 1.2 to 9.5 in the injection mode and from 1.1 to 3.1 in the ejection mode. The corresponding number of continuously flow stirred tank reactors (CFSTR's) in-series ranged from 1.4 to 5.3 in the injection mode and from 1.4 to 2.2 in the ejection mode. These results suggests that the backmixing in the impinging-jet bubble column can be described adequately using the axial dispersion model (ADM) rather than an ideal plug flow (PF) model or an ideal CFSTR model.

Non-linear regression analyses produced power-law relationships of the backmixing coefficient (D_L) with respect to the gas and liquid superficial velocities (u_G and u_L). For the injection mode, the relationship was as follows:

$$D_L = 5.4 \times 10^{-4}\, u_G^{-1.07}\, u_L^{0.81} \qquad [8.18]$$

and for the ejection mode:

$$D_L = 3.9 \times 10^{-7}\, u_G^{-0.09}\, u_L^{-2.79} \qquad [8.19]$$

where: D_L = liquid-phase dispersion coefficient (m^{2}s^{-1}), u_G = superficial gas velocity (ms^{-1}), and u_L = superficial liquid velocity (ms^{-1}). The coefficient of correlation was equal to 0.94 and 0.99 for the injection and ejection modes, respectively. The injection mode was characterized by a higher Sauter mean bubble diameter (d_S) and a gas bubble concentration (C_B) than the ejection mode and as a result the gas-liquid flow was closer to the ideal homogeneous bubbly flow regime. Consequently, D_L was higher in the injection mode than in the ejection mode. In the injection mode and considering the above discussion, an increase in u_G will be expected to cause a decrease in D_L as a result of the increase in d_S. This phenomenon was verified by the results as shown in Equation

8.18. The same phenomenon occurred in the ejection mode (as shown by Equation 8.19) but to a lesser extent due to the fact that gas flowrates associated used in the ejection mode were slightly lower than those in the injection mode. Another reason is that during the ejection mode runs, the flow inside the column was closer to the ideal bubbly regime but still not in the homogeneous regime due to low gas bubble concentration (C_B) as observed during the tests. The same phenomenon was reported before in the literature (Kaštánek *et al.*, 1993).

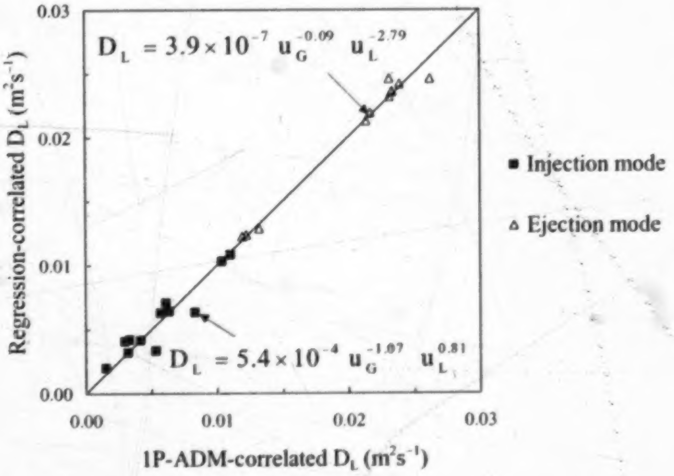

Figure 8.12 Comparison between the 1P-ADM and the non-linear regression correlations of D_L.

In the injection mode and as u_L increases, the entrainment of the surrounding ambient fluid will increase as the resultant (due to jet impingement) jet grows upward and the entrainment of the liquid by the gas bubbles will increase as a result of the decrease in d_S and thus, D_L will increase. The same phenomenon was also observed in three other types of bubble columns, the first type was an upward-flow bubble column equipped with a gas-liquid ejector (Ogawa *et al.*, 1982), the second type was equipped with gauze cylinders suspended in the liquid phase (Deckwer, 1992), and the third type was equipped with porous plates (Kaštánek *et al.*, 1993). In the ejection mode and by contrast, u_L

exhibited an opposite effect on D_L. In the ejection mode, the flow was closer to the ideal bubbly flow regime and as u_L increased, D_L decreased. The same phenomenon was observed before by Zhou (1995) who investigated the effect of u_L on D_L in a fine-bubble diffuser ozone bubble column in which the gas-liquid flow was in the bubbly flow regime. As shown in Figure 8.12, there was an excellent correlation between the estimated D_L's using the 1P-ADM and the estimated D_L's using the non-linear regression analyses.

8.5.3 Correlations of the Gas-phase-Concentration-Decrease Exponent

Linear regression analyses were performed in order to study the effects of the process variables on the exponent (a_l) of the gas-phase ozone concentration decrease following the exponential decrease function represented by Equation 8.2. It was assumed that the ozone decay in the gas phase was negligible as well as the gas phase was flowing in a plug flow regime.

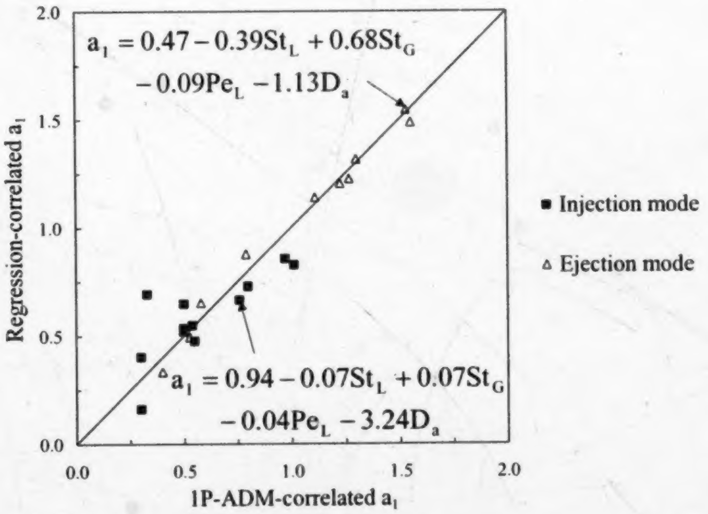

Figure 8.13 Comparison between the 1P-ADM and the linear regression correlations of a_l.

As a result, a_l represents the overall decrease in the gas-phase ozone molar fraction due to the effects of the gas-liquid mass transfer and the gas-phase convection processes (Gamal El-Din and Smith, 2000). a_l was correlated to the process dimensionless variables: Peclet number (Pe_L), liquid-phase Stanton number (St_L), gas-phase Stanton number (St_G), and Damköhler number (D_a) through a relationship similar to the one suggested by Gamal El-Din and Smith (2000):

$$a_l = A' + B' \cdot St_L + C' \cdot St_G + D' \cdot Pe_L + E' \cdot D_a \qquad [8.20]$$

where: A', B', C', D', and E' = empirical coefficients that were estimated through linear regression analyses. As a result of the linear regression analyses, and for the injection mode, the coefficients (A', B', C', D', E') were found to be 0.94, –0.07, 0.07, –0.04, and –3.24, respectively, and the coefficient of correlation was equal to 0.79. For the ejection mode, A', B', C', D', E' were 0.47, –0.39, 0.68, –0.09, and –1.13, respectively with the correlation coefficient equal to 0.99. Figure 8.13 shows an excellent conformity comparison between 1P-ADM and the linear regression estimations of a_l.

8.6 CONCLUSIONS

With respect to the measured dissolved and gaseous ozone concentration profiles in the impinging-jet bubble column, it can be concluded that:

(1) the dissolved ozone concentration profiles along the bubble column height, can be well estimated using the one-phase axial dispersion model (1P-ADM) through the use of bubble column average parameters with respect to the overall mass transfer coefficient (k_La), liquid-phase backmixing coefficient (D_L), and coefficient of the gas-phase ozone molar fraction decrease along the column height (a_1).

(2) for the tested deionized water, it was found that k_La and D_L were dependent on the liquid and gas superficial velocities. The nature of this dependency varied from the gas injection mode to the gas ejection mode, and

(3) the gas-phase dimensionless ozone concentration profiles can be well described using an exponential relationship representing the gas-phase ozone molar decrease along the column height. The exponent (a_1) was found to be dependent on the process dimensionless variables (Pe_L, St_L, St_G, and D_a) and the nature of this dependency was different in the injection mode from that in the ejection mode.

The use of the venturi injectors for the ozone gas absorption caused an increase in the mass transfer rates due to the contact between the gas and the liquid phases inside the injectors. Placing the injectors at an intersecting angle of 125° at the bottom of the bubble column caused an intersecting of the gas-liquid jets. This arrangement has led to a significant increase in the turbulence intensities in the ambient fluid and consequently, a significant increase in the mass transfer rates was achieved. The impinging-jet bubble column has proven to be a very promising gas-liquid contacting unit, when compared to the traditional bubble column designs due to its compact size that can handle higher liquid and gas flowrates without causing any decrease in the mass transfer efficiency of the bubble column.

8.7 REFERENCES

1. APHA-AWWA-WEF *Standard Methods for the Examination of Water and Wastewater. 19th Ed. American Public Health Association, American Water Works Association, and Water Environment Federation*, (Washington, DC, USA: American Public Health Association, 1995).
2. Bader, H., and Hoigné, J. "Determination of Ozone in Water by the Indigo Method: A Submitted Standard Method", Ozone Sci & Eng. 4: 169-176 (1982).
3. Briens, C.L., , L.X. Huynh, J.F. Large, A. Catros, J.R. Bernard, and M.A. Bergougnou, "Hydrodynamics and Gas-Liquid Mass Transfer in a Downward Venturi-Bubble Column Combination", Chem. Eng. Sci. 47: 3549-3556 (1992).
4. Catros, A. *Hydrodynamics and Mass Transfer in Three-Phase Fluidized Beds with Baffles, Ph.D. Thesis*, (London, Ontario, Canada: University of Western Ontario, 1986).
5. Chen, B.H., N.S. Yang, and A.F. McMillan, "Gas Holdup and Pressure Drop for Air-Water Flow through Plate Bubble Columns", Can. J. Chem. Eng. 64: 387-399 (1986).
6. Danckwerts, P.V., *Gas-Liquid Reactions* (NY, USA: McGraw-Hill, Inc., 1970).
7. Deckwer, W.-D., *Bubble Column Reactors*, Cottrell V. (Trans.), Field R.W. (Ed.), (Chichester, England: John Wiley & Sons Ltd., 1992).
8. Deckwer, W.-D., R.Burckhart, and G. Zoll, "Mixing and Mass Transfer in Tall Bubble Columns", Chem. Eng. Sci. 29: 2177-2188 (1974).
9. Deckwer, W.-D., K. Nguyen-Tien, , B.G. Kelkar, and Y.T. Shah, "Applicability of Axial Dispersion Model to Analyze Mass Transfer Measurements in Bubble Columns", AIChE J. 29: 915-922 (1983).
10. Fitzgerald, S.D. and E.R. Holley, *Research Report No. 144* (Urbana, IL, USA: Water Resources Centre, University of Illinois, 1979).
11. Gamal El-Din, M. and D.W. Smith, "Designing Ozone Bubble Columns: A Spreadsheet Approach to Axial Dispersion Model", *Proc. of IOA/PAG Conf.: Advances in Ozone Technology*, Orlando, FL, USA, 2000.

12. Guo, Z.-R. and J.J. Sharp, "Characteristics of Radial Jets and Mixing Under Buoyant Conditions", J. Hydr. Eng., ASCE 122: 495-502 (1996).

13. Huynh, L.X., C.L. Briens, J.F. Large, A. Catros, J.R. Bernard, and M.A. Bergougnou, "Hydrodynamics and Mass Transfer in an Upward Venturi/Bubble Column Combination", Can. J. Chem. Eng. 69: 711-722 (1991).

14. Kaštánek, J., J. Zahradník, J. Kratochvíl, and J. Čermák, *Chemical Reactors for Gas-Liquid Systems* (Chichester, England: Ellis Horwood, 1993).

15. Khan, A.A. *A Study of Intersecting Circular Turbulent Jets, Ms.C. Thesis*, (Edmonton, AB, Canada: University of Alberta, 1989).

16. König, B., R. Buchholz, J. Lücke, and K. Schügger, "Longitudinal Mixing of the Liquid Phase in Bubble Columns", Ger. Chem. Eng. 1: 199-205 (1978).

17. Laplanche, A., N. Le Sauze, G. Martin, and B. Langlais, "Simulation of Ozone Transfer in Water: Comparison with a Pilot Unit", Ozone Sci. & Eng. 13(5): 13, 535-558 (1991).

18. Lewis, D.A. and J.F. Davidson, "Mass Transfer in a Recirculation Bubble Column", Chem. Eng. Sci. 40: 2013-2017 (1985).

19. Mazzei, A.L. and L.J. Bollyky, "Optimizing Mass Transfer Efficiency and Ozone Utilization with High Efficiency Venturi Injectors", *Proc. of the IOA/PAG Conf.*, Toronto, ON, Canada, 1991.

20. Nishikawa, M., K. Kosaka, and K. Hashimoto, "Gas Absorption in Gas-Liquid or Solid-Gas-Liquid Spouted Vessel", *Proc. 2nd Pacific Chem. Eng. Congress*, Denver, CO, USA, 1977.

21. Ogawa, S., M. Kobayashi, S. Tone, and T. Otake, "Liquid Phase Mixing in the Gas-Liquid Jet Reactor with Liquid Jet Ejector", J. Chem. Eng. Japan 15: 469-474 (1982).

22. Oke, N.J., D.W. Smith, and H. Zhou, "An Empirical Analysis of Ozone Decay Kinetics in Natural Waters", Ozone Sci & Eng. 20: 361-379 (1998).

23. Rajaratnam, N., *Developments in Water Science: Turbulent* Jets (New York, NY, USA: Elsevier, Inc., 1976).

24. Roustan, M., J.P. Duguet, B. Brette, E. Brodard, and J. Mallevialle, "Mass Balance Analysis of Ozone in Conventional Bubble Contactors", Ozone Sci. & Eng. 9: 289-297 (1987).

25. Roustan, M., R.Y. Wang, and D. Wolbert, "Modeling Hydrodynamics and Mass Transfer Parameters in a Continuous Ozone Bubble Column", Ozone Sci. & Eng. 18: 99-115 (1996).

26. Shah, Y.T., B.G. Kelkar, S.P. Godbole, and W.-D. Deckwer, "Design Parameters Estimations for Bubble Columns", AIChE J. 28: 353-379 (1982).

27. Sherwood, T.K., L.P. Robert, and R.W. Charles, *Mass* Transfer (New York, NY, USA: McGraw-Hill, Inc., 1975).

28. Sotelo, J.L., F.J. Beltrán, F.J. Benitez, and J. Beltrán-Heredia, "Henry's Law Constant for the Ozone-Water System", Wat. Res. 23: 1239-1246 (1989).

29. Thalasso, F., H. Naveau, and E.-J. Nyns, "Design and Performance of a Bioreactor Equipped with a Venturi Injector for High Gas Transfer Rates", Chem. Eng. J. 57: B1-B5 (1995).

30. Unger, D.R. and F. Muzzio, "Laser-Induced Fluorescence Technique for the Quantification of Mixing in Impinging Jets", AIChE J. 45: 2477-2486 (1999).

31. Valentin, F.H.H., *Absorption in Gas-Liquid Dispersions: Some Aspects of Bubble Technology*, Donald M.B. (Ed.). (London, England: E. & F.N. Spon Ltd., 1967).

32. Wachsmann, U., N. Räbiger, and A. Vogelpohl, "The Compact Reactor-A Newly Developed Loop Reactor with a High Mass Transfer Performance", Ger. Chem. Eng. 7: 39-44 (1984).

33. Wang, K.B. and L.T. Fan, "Mass Transfer in Bubble Columns Packed with Motionless Mixers", Chem. Eng. Sci. 33: 945-952 (1978).

34. Witze, P.O., *A Study of Impinging Axisymmetric Turbulent Flows: The Wall Jet, The Radial and Opposing Free Jets: Ph.D. Thesis* (Davis, CA, USA.: University of California, Davis, 1974).

35. Yurteri, C. and M.D. Gurol, "Ozone Consumption in Natural Waters: Effects of Background Organic Matter, pH and Carbonate Species", Ozone Sci. & Eng. 10: 277-290 (1988).

36. Zhou, H. and D.W. Smith, "Ozone Mass Transfer in Water and Wastewater Treatment: Experimental Observations Using a 2D-Laser Particle Dynamics Analyzer", Wat. Res. 34: 909-921 (2000).

37. Zhou, H., *Investigation of Ozone Disinfection Kinetics and Contactor Performance Modeling: Ph.D. Thesis* (Edmonton, AB, Canada: University of Alberta, 1995).

38. Zhou, H., D.W. Smith, and S.J. Stanley, "Modeling of Dissolved Ozone Concentration Profiles in Bubble Columns", J. Environ. Eng., ASCE 120(4): 821-840 (1994).

CHAPTER 9. MAXIMIZING THE ENHANCED OZONE OXIDATION OF KRAFT PULP MILL EFFLUENTS IN AN IMPINGING-JET BUBBLE COLUMN*

9.1 INTRODUCTION

Ozone contactors that utilize bubble diffusers are the most common practice used for treating water and wastewater. In order to achieve higher treatment levels in ozone contactors, the configuration and the design of the contacting unit and the type of the gas absorber need to be modified in an attempt to achieve higher turbulent mixing in the liquid phase. According to the theory of surface renewal proposed by Danckwerts (1970), an increase in the mixing intensity will cause the liquid film at the gas-liquid interface to be renewed at a higher rate leading to a higher local mass transfer coefficient (k_L). Increasing the turbulence in the liquid phase will lead to higher turbulent shear stresses that will cause the thickness of the liquid film to decrease, and consequently, the ozone gas will diffuse through the liquid film at a higher rate causing k_L to increase. Higher turbulent shear stresses will also cause the gas bubbles to become smaller. As a result, the gas bubbles' specific interfacial area (bubbles' surface area/liquid volume) will increase leading to higher overall mass transfer coefficient (k_La).

When two axisymmetrical circular turbulent air jets intersected at an angle of 180°, the resultant jet behaved like a radial jet that grew at about three times the rate of a single radial jet (Witze, 1974). The impingement produced higher turbulent shear stresses in the ambient fluid. The resultant radial jet consisted of two flow regions: a forward jet flow and a backward jet flow. The same phenomena were observed in the study of Khan (1989) who studied the impingement of circular turbulent water and air jets. Efficient and homogeneous mixing occurred at jets' Reynolds numbers (Re_j's) greater than 300 when two liquid jets impinged at an intersecting angle of 90° (Unger and Muzzio, 1999). In an annular tube, when two turbulent liquid jets intersected at an angle of 90°, uniform and improved mixing across the tube was observed (Fitzgerald and Holley, 1979).

A version of this chapter has been accepted for publication. Gamal El-Din, M. and D.W. Smith, Ozone Sci. & Eng. (July, 2001)

There have been many attempts by several researchers to improve the performance of bubble columns. These attempts were aimed at maximizing the rate of the gas absorption process. These attempts included: (1) utilizing motionless mixers (Wang and Fan, 1978); (2) inducing internal liquid circulation in an air-lift reactor (Lewis and Davidson, 1985); (3) adding internal baffles (Catros, 1986); and (4) utilizing perforated plates (Chen *et al.*, 1986). Gas injectors were investigated by a number of researchers for dissolving gas into the liquid phase in order to improve the mass transfer rates. In the study of Wachsmann *et al.* (1984), the mass transfer process was examined using an injection-type nozzle. The gas was introduced into the liquid flow under positive and negative pressures. Significant increase in the overall mass transfer coefficient was observed. This was due to the generation of gas bubbles that had a large specific interfacial area. They also observed that the values of k_La, in the gas-injection mode, varied from those in the gas-ejection mode. A venturi-type injector was used for achieving higher gas transfer rates in a bioreactor (Thalasso *et al.*, 1995). Under gas injection mode, it was observed that an increase in k_La occurred as the liquid superficial velocity (u_L) and the gas superficial velocity (u_G) increased. Huynh *et al.* (1991) investigated the mass transfer process in an upward venturi-bubble column combination. k_La was correlated with u_G and u_L for the bubble column as well as for the venturi-bubble column combination. In that contacting system, it was observed that there was essentially no backmixing and consequently, k_La in the bubble column was only dependent on the u_G as observed before in most conventional bubble columns. In the venturi-bubble column combination, k_La was dependent on u_G and u_L and as they increased, k_La increased. In an attempt to study the effects of gas flowrates on the bubbles' specific interfacial area in a conventional diffuser bubble column, Zhou and Smith (2000) used a 2D-laser particle dynamics analyzer. They observed that as u_G increased, the bubbles' specific interfacial area increased almost proportionally. This phenomenon was attributed to the linear increase in the gas hold-up (ε_G) as a result of the increase in u_G.

Pulp mill effluents are characterized by their high concentrations of color, AOX, COD, and TOC-causing compounds. Recently, the color and AOX-causing contaminants have become the center of attention as a result of their high resistance towards conventional biological treatment processes. In order to comply with the more stringent effluent discharge regulations, the focus of the pulp mill effluent treatment industry has shifted from the conventional biological treatment processes to other treatment alternatives (Haberl *et al.*, 1991; Zhou and Smith, 1997). Ozonation has emerged as a very promising technology for treating pulp mill effluents due to its high reduction efficiencies of color and AOX-causing compounds (Bauman and Lutz, 1974; Zhou and Smith, 1997). Ozone can selectively react with the chromophoric (color-causing) and halogenated (AOX-causing) functional groups through fast oxidation reactions as a result of these compounds' electrophilic nature (Bauman and Lutz, 1974). They observed that the color reduction efficiency was dependent mainly on the amount of the utilized ozone (ΔO_3), but to some extent it was also dependent on the wastewater initial characteristics in terms of color, COD, pH, and dissolved and suspended solids' concentrations.

For any ozonation system, it is important to quantify the dissolved ozone to achieve reliable designs and optimum operations of ozone contactors. Also, quantifying the ozone off-gas exiting the contactor is essential for optimum and reliable designs of the off-gas destruction facilities.

In the current study, two venturi injectors (Mazzei® injectors) were used to create turbulent gas-liquid jets in the ambient fluid. The intersecting of the gas-liquid jets caused an increase in the turbulence intensity produced in the liquid phase and therefore, increased the gas-liquid mass transfer. For modeling the ozonation process in deionized water, the ozone auto-decomposition kinetics had to be characterized. This was achieved through an ozone decay kinetics study that was conducted in a headspace-free reactor under a wide range of initial ozone concentrations and liquid-phase temperatures. Then, the mass transfer and the backmixing processes were characterized by fitting the measured dissolved and gaseous ozone concentration profiles with the modified non-isobaric one-phase axial dispersion model (1P-ADM) predictions through a three-parameter optimization technique. The ozone gas absorption process, in deionized water and pulp mill effluents, was investigated under two modes of gas sparging: the injection and ejection modes. The injection mode refers to the gas introduction, into the motive liquid flow, under positive pressure and the ejection mode refers to the gas introduction under vacuum or negative pressure. The ozonation experiments, in deionized water and Kraft pulp mill effluent, were conducted in the pilot-scale impinging-jet bubble column that was operated in a co-current continuous-flow mode under a wide range of operating conditions. Meanwhile, in some of the pulp mill effluent ozonation experiments, the liquid phase was recirculated to simulate the conditions of the semibatch-flow mode.

This chapter presents: (1) a simple and reliable method for predicting the impinging-jet bubble-column average overall mass transfer coefficient (k_La); and (2) an examination of the effects of various ozonation process variables on the treatment efficiencies and gas absorption dynamics during the ozonation of a Kraft pulp mill effluent.

9.2 FUNDAMENTALS OF THE OZONATION PROCESS

A number of processes occur simultaneously during the ozonation treatment. These processes are: convection and backmixing processes of the liquid and gas phases flowing through the contacting chamber; ozone gas mass transfer process; ozone auto-decomposition process; and competitive reactive processes of the dissolved ozone with the various constituents in the liquid phase (Zhou, 1995). A detailed discussion of the fundamentals of these processes can be found in Gamal El-Din and Smith (2000).

9.3 THE MODIFIED NON-ISOBARIC ONE-PHASE AXIAL DISPERSION MODEL (1P-ADM)

The assumptions pertaining to the development of the modified non-isobaric steady-state one-phase axial dispersion model (1P-ADM) and the detailed model development can be found in Gamal El-Din and Smith (2000). The 1P-ADM is composed of a single non-homogeneous second-order linear ordinary differential equation. Although this differential equation represents the liquid phase, it still accounts for the countering effects of the gas shrinkage and expansion caused by gas depletion and absorption and reduced liquid hydrostatic head. The differential equation was solved analytically by the method of variation of parameters. The 1P-ADM was expressed in terms of a simple spreadsheet program. This program produced the model predictions of the dissolved and gaseous ozone concentration profiles along the bubble column under a wide range of the ozonation process operating conditions that were represented by the model-input parameters.

9.4 EXPERIMENTAL METHODS

9.4.1 Bench Tests: Ozone Auto-Decomposition Kinetics Study

The ozone auto-decomposition kinetics batch experiments were conducted in a 1200 mL floating-lid headspace-free reactor (see Figure 9.1).

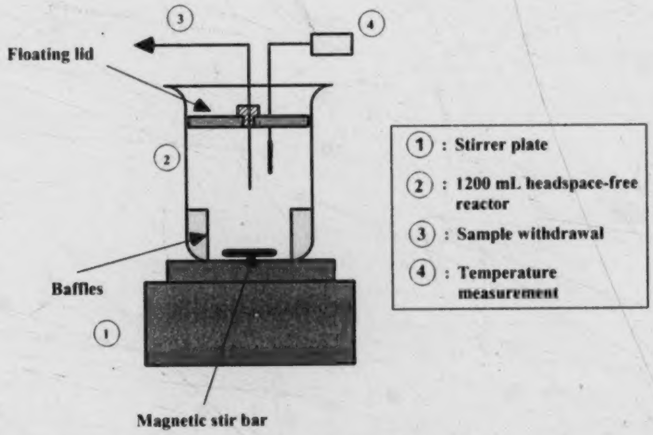

Figure 9.1 Schematic of the floating-lid headspace-free reactor.

The design of the experimental set-up and the experimental procedure were adapted from the study of Oke *et al.* (1998). Detailed description of the experimental methods can be found in Oke *et al.* (1998). In the current study, clean deionized water was used as the test water. The main average characteristics of the test water are summarized in Table 9.1. As shown in Table 9.1, the quality of the deionized water, that was used a the test water, was not high as indicated by its relatively high TOC (total organic carbon) concentration that was about 0.51 mgL^{-1}. The kinetics study was conducted over a range of water temperatures and initial dissolved ozone concentrations in order to investigate their effects on the ozone auto-decomposition kinetics. The initial dissolved ozone concentration ranged from 2.0 to 3.1 mgL^{-1} and the water temperature ranged from 2.6 to 38.5 °C.

Table 9.1 Average characteristics of the test water.

Parameters	**TOC (mgL^{-1})**	**pH**	**$A_{245\ nm}^{10\ mm}$ (mm^{-1})**
Mean	0.51	5.99	0.004
Standard deviation	0.29	0.26	0.000

The ozone mass transfer experiments were conducted in a pilot-scale impinging-jet bubble column (see Figure 9.2). The bubble column was made from PVC and had an inside diameter of 100 mm and a total height of 1,520 mm. The water depth was kept constant at 1,315 mm by placing an overflow weir at the top of the column. A ring tube was also installed at the top of the column with a 20 mm-diameter hole facing downward. The Kynar Mazzei® venturi injectors had an inside diameter of 12.7 mm and were placed 25 mm above the bottom of the column. The injectors were placed at an intersecting angle of 125° and the distance between the centers of the nozzles was 60 mm. The bubble column had an elliptical base to reduce the effect of the backward jet that was created in the ambient fluid as a result of the jet impingement. The sidewalls of the bottom part of the column had a conical shape. With this configuration at the bottom of the column, dead pocketing effects were minimized. Based on the above reactor configuration, it was reasonably assumed that the backmixing along the column height was relatively uniform.

9.4.2 Pilot-Scale Tests: Continuous-Flow Mode/Ozonation of Water and Pulp Mill Effluent

Five bell-shaped sampling taps were inserted inside the reactor at a distance equal to 1/3 of the column diameter and at equal intervals along the column height. The shape of the sampling taps minimized the possible gas bubbles' entrainment into the withdrawn liquid samples. During each ozonation test, five liquid samples were withdrawn directly from the sampling taps into volumetric flasks and the dissolved ozone concentrations were measured and calculated following the procedure described by Bader and Hoigné (1982). Five pressure sensors (Model 26PC Honeywell®) were inserted inside the reactor, at a distance equal to 1/3 of the column diameter and at intervals equal to those of the bell-shaped sampling taps, to monitor the pressure along the column height. The liquid used in the water ozonation experiments was clean deionized water that had similar characteristics to those of the water used in the kinetics study. The ozone gas was generated from extra-dry pure oxygen using a corona discharge ozone generator (model GLS-7, PCI-WEDECO®). The ozone generator was allowed to stabilize for at least 1,800 s in order to obtain a stable ozone concentration in the feed gas. During the ozonation tests, the ozone concentrations in the feed and off-gas lines were continuously monitored using PCI-WEDECO® ozone monitors (models HC400 and LC, respectively). The ozone monitors were allowed at least 900 s to stabilize before recording their readings. Periodic calibration of the ozone monitors was conducted using the KI method as described by the Standard Methods for Examination of Water and Wastewater (APHA-AWWA-WEF, 1995). All the materials that came in contact with ozone during the experiments were made of glass, teflon, stainless steel, or PVC to reduce the possible interference that would result from the reactions between the dissolved and/or gaseous ozone and the experimental set-up components.

The ozone contactor was operated in a co-current flow mode. The test liquid was pumped from two storage barrels into an overhead tank using peristaltic pumps. Then, the test liquid was pumped from the overhead tank into the bottom of the bubble column using a centrifugal pump to reduce any fluctuations in the liquid flowrates during experiments. The liquid flow was divided equally into two lines leading into the injectors. As the liquid motive flow passed though the injectors, the gas flow was introduced into the liquid flow through the injectors' throats. The experiments were conducted under two modes of the gas sparging: positive pressure (i.e., injection) mode and vacuum or negative pressure (i.e., ejection) mode. The liquid flow, after being divided into two lines, was passed through two flowmeters to measure the liquid flowrates. The gas flow was passed through a gas rotameter to measure the gas flowrate before the gas flow was divided into two lines leading to the injectors' throats. Pressure gauges were installed on the liquid-flow lines to measure the liquid pressure in the lines. Pressure gauges were also installed at the gas rotameter exit as well as at the injectors' throats to measure the gas pressures in the gas lines. All the pressure gauges were calibrated prior to their use.

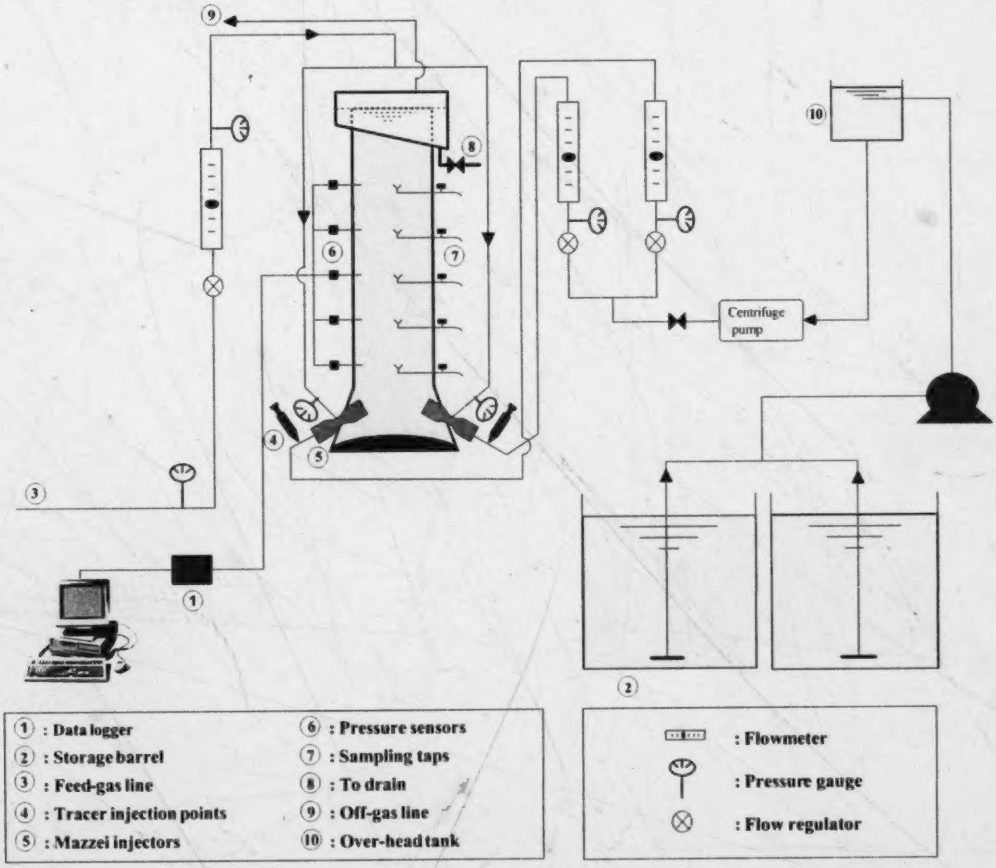
⑨
⑩
⑧
⑥
⑦
Centrifuge pump
④
⑤
③
①
②
① : Data logger
② : Storage barrel
③ : Feed-gas line
④ : Tracer injection points
⑤ : Mazzei injectors
⑥ : Pressure sensors
⑦ : Sampling taps
⑧ : To drain
⑨ : Off-gas line
⑩ : Over-head tank
: Flowmeter
: Pressure gauge
: Flow regulator

Figure 9.2 Schematic of the experimental set-up of the pilot-scale impinging-jet bubble column.

The bubble column was operated for a period of time that was at least eight turnovers of the reactor working volume to allow for the ozonation process to reach isothermal steady-state conditions in terms of the liquid flowrate, gas flowrate, dissolved ozone concentrations along the column height, and off-gas ozone concentration. During the experiments, the point of time at which the steady-state conditions were reached was verified by reaching a constant off-gas ozone concentration in the exhaust-gas line. The gas hold-up data along the column height was obtained by continuous monitoring of the pressure readings. These readings were collected instantaneously and downloaded to a PC using a Lakewood® data logger. Wide ranges of the liquid flowrates, the feed-gas flowrates, and the feed-gas ozone concentrations were investigated. The liquid flowrate ranged from 6.2 x 10^{-5} to 2.2 x 10^{-4} m^3s^{-1} leading to an average theoretical hydraulic retention time in the range of 48 to 174 s. During the water ozonation experiments, the feed-gas flowrate ranged from 1.4 x 10^{-5} to 1.1 x 10^{-4} m^3s^{-1}, the feed-gas ozone concentration ranged from 0.9 to 6.0 % w/w, and the water temperature ranged from 19.5 to 24.5 °C. During the pulp mill effluent ozonation experiments, the feed-gas flowrate ranged from 1.4 x 10^{-5} to 1.1 x 10^{-4} m^3s^{-1}, the feed-gas ozone concentration ranged from 9.0 to 11.0 % w/w, and the pulp mill effluent temperature ranged from 16.0 to 25.0 °C.

9.4.3 Pilot-Scale Tests: Semibatch-Flow Mode/Ozonation of Pulp mill Effluent

Under similar operating conditions to those used in the pulp mill effluent ozonation tests that were operated in the continuous-flow mode, the liquid-phase was recirculated while the gas-phase was continuously introduced through the injectors' throats. This part of the experimental study was particularly designed for investigating the effects of the ozone contact time (t) and the corresponding amount of the utilized ozone (ΔO_3) on the ozone gas absorption dynamics in terms of the enhanced overall mass transfer coefficient (Ek_La), the enhancement factor (E), and the ozone off-gas concentration. For that purpose, the ozone contact time was varied from 240 to 2,880 s. The measured feed-gas flowrates and ozone concentrations were corrected based on the actual air temperatures and barometric pressures during the experiments.

9.4.4 Pulp Mill Effluent Characterization

During the continuous-flow mode ozonation tests, samples of the wastewater before and after ozonation were analyzed to determine the ozonation process treatment efficiencies. These analyses were performed to determine the color, AOX, COD, TOC, and BOD_5. The true color was analyzed according to the H5.P method suggested by the Canadian Pulp and Paper Association (1974). AOX was analyzed using Euroglas AOX analyzer according to the adsorption-pyrolysis- titrimetric method (APHA-AWWA-WEF, 1995). COD was analyzed according to the closed reflux-colorimetric method (APHA-AWWA-WEF, 1995) by employing silver-catalyzed oxidation with potassium dichromate in sulfuric acid. TOC was analyzed according to the combustion-infrared method (APHA-AWWA-WEF, 1995) using a Dohrmann carbon analyzer (model DC-80®). It should be noted that the raw pulp mill effluent characteristics varied over time and the average characteristics of the pulp mill effluent used in the current study are shown in Table 9.2.

Table 9.2 Average characteristics of the pulp mill effluent.

Raw pulp mill effluent parameters	**Continuous-flow mode**	**Semibatch-flow mode**
Color (TCU)	1199	1106
AOX (mgL^{-1})	10.1	11.2
COD (mgL^{-1})	750	681
TOC (mgL^{-1})	250	240
BOD_5 (mgL^{-1})	21.5	18.8
pH	7.7	7.6

9.5 RESULTS AND DISCUSSION

9.5.1 Bench Tests: Ozone Auto-Decomposition Kinetics

The ozone auto-decomposition process was assumed to follow first order decay kinetics as follows:

$$\frac{dC_L}{dt} = -k_w C_L \qquad [9.1]$$

where: C_L = instantaneous dissolved ozone concentration (mgL^{-1}), k_w = specific ozone utilization rate constant (s^{-1}), and t = reaction time (s). Therefore, the kinetics data were analyzed by plotting the $\ln[O_3]_t$ versus the reaction time (t). The assumption was considered applicable if the plotted data could be represented by a straight line that would be predicted through a linear regression technique. For further investigation of the effect of water temperature (T_L) on the ozone specific utilization rate constant (k_w), the predicted k_w's, for all the tests, were pooled together and analyzed using a linear regression technique. This kinetics' temperature-dependency was assumed to follow the well-known van't Hoff-Arrhenius relationship as follows:

$$\ln\left(k_w\big|_{T_L{}^\circ C}\right)=\ln\left(k_w\big|_{20^\circ C}\right)+(T_L-20)\ln\theta \qquad [9.2]$$

where: θ = temperature correction factor, and T_L = water temperature (^oC). The linear regression technique was applied to obtain θ and $k_w\big|_{20^\circ C}$.

In all the tests, comparisons of the $\ln[O_3]_{t\,=\,30\text{ sec}}$ with the $\ln[O_3]_{t\,=\,0}$ yielded a very small relative error (≤ 0.6 %). This was in agreement with the assumption that the clean deionized water had a negligible initial ozone demand. The plots of the $\ln[O_3]_t$ versus the reaction time (t) were well described by straight lines and the linear regression analyses produced correlation coefficients (r's) ≥ 0.87. For the tests that had the same initial water temperature and different initial dissolved ozone concentrations, similar decay rate constants (k_w's) were obtained suggesting that there was no effect of the initial ozone concentration on the decay rate constant of the ozone decay kinetics. The linear regression of the pooled k_w's and T_L's produced a correlation coefficient of 0.98. Figure 9.3 depicts the effect of water-temperature on the ozone specific utilization rate constant. The water-temperature correction factor (θ) and $k_w\big|_{20^\circ C}$ were predicted to be 1.11, and $2.61 \times 10^{-4}\ s^{-1}$, respectively. The $k_w\big|_{20^\circ C}$ value implies that the ozone decay process in clean waters, with negligible initial ozone demands, is a very slow process compared to the fast ozone decay process that takes place in natural waters that are characterized by their high initial ozone demands.

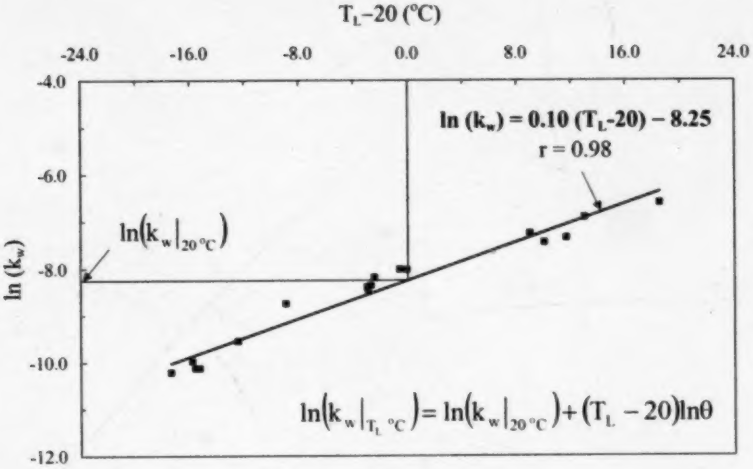

Figure 9.3 The effect of water temperature on the ozone auto-decomposition kinetics in deionized water.

9.5.2 Pilot-Scale Tests: Ozone Mass Transfer in Water

The design of the impinging-jet bubble column is different from the conventional bubble column designs in terms of the unique dynamic and interrelated effects of the liquid and gas flowrates on the performance of the venturi injectors. When the venturi injectors were operated in the injection or ejection mode and as the liquid flowrate was increased, an increase in the gas flowrate and a decrease in the injector throat pressure occurred. Operating at the same liquid flowrate and increasing the gas flowrate caused the injector throat pressure to increase. The differential pressure between the gas injection or ejection point and the backpressure inside the bubble column would affect the size of the gas bubbles leaving the injectors and as a result, the bubbles' specific interfacial area will change. At almost similar gas flowrates, this differential pressure was generally higher and coexisted with higher liquid flowrates in the ejection mode compared to those in the injection mode. Therefore, the same gas and liquid flowrates cannot coexist for the injection and ejection modes and as a result, the two modes of gas absorption had to be analyzed separately. Part of the overall system-mass-transfer efficiency is attributed to the contact time between the gas phase and the liquid phase inside the intense mixing zone within the venturi injectors (Mazzei and Bollyky, 1991). As a result, an increase in this contact time will lead to an increase in the overall mass transfer efficiency in the impinging-jet bubble column.

Although the spreadsheet program that represented the 1P-ADM was allowed a maximum number of 200 iterations, the convergence criterion was met in less than 200 iterations and the minimum summation of the squared residuals ($SSR = \sum\left(C_{O_3,\text{measured}} - C_{O_3,\text{calculated}}\right)^2$) was reached.

In the impinging-jet bubble column, k_La was affected by u_G and u_L. In an attempt to investigate the effects of the gas and liquid flowrates on the 1P-ADM predictions of the column-average k_La, relationships that correlate k_La with the superficial gas and liquid velocities (u_G and u_L, respectively) were developed, for the gas injection and ejection modes, through non-linear regression analyses. k_La was correlated to u_G and u_L according to the following relationship:

$$k_La = \alpha\, u_G^{\beta}\, u_L^{\gamma} \qquad [9.3]$$

where: k_La = overall mass transfer coefficient (s^{-1}), u_G = superficial gas velocity (ms^{-1}), u_L = superficial liquid velocity (ms^{-1}), and α, β, and γ = empirical coefficients that were obtained through non-linear regression analyses. The mass transfer process is dependent on the liquid-phase temperature. Meanwhile, the backmixing process dependency on the liquid-phase temperature is minimal (Deckwer, 1992). Due to the variability of the water temperature from one experiment to another, the predicted k_La's were corrected for the temperature effect, to obtain the corresponding k_La's at 20 °C, using a temperature correction factor (θ) of 1.024. Operating in the gas injection mode, the non-linear regression analysis predicted the parameters (α, β, and γ) to be 12.50, 0.83, and 0.37, respectively with a correlation coefficient (r) of 0.99. When the gas absorption process was conducted in the ejection mode, the non-linear regression parameters (α, β, and γ)

were estimated to be 0.09, 1.43, and –1.78, respectively with a correlation coefficient of 1.00.

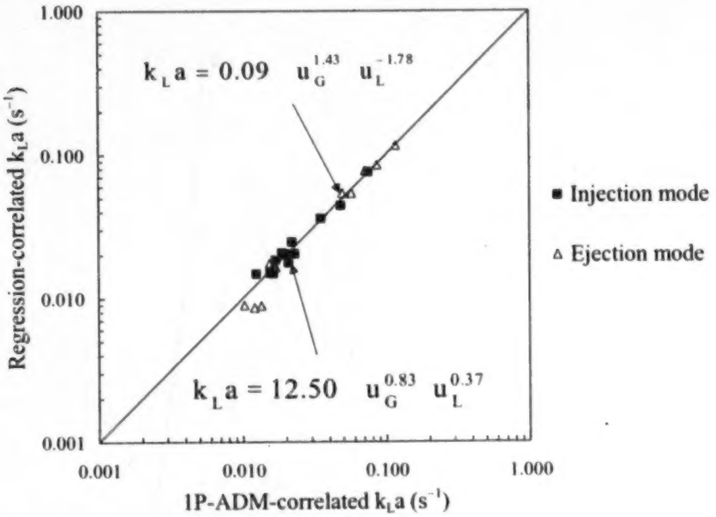

Figure 9.4 A comparison between the k_La's predicted using the 1P-ADM and the non-linear regression analyses.

A comparison between the predictions of k_La using the 1P-ADM and the non-linear regression analyses is depicted in Figure 9.4. Excellent conformity between the two techniques of predictions has proven the consistency of the 1P-ADM in predicting k_La under a wide range of gas and liquid flowrates in the gas-injection and ejection modes.

9.5.3 Ozone Mass Transfer in Pulp Mill Effluent: Gas Absorption Dynamics

In order to account for the different characteristics between the clean water and the pulp mill effluent and their effects on the overall mass transfer coefficient, a correction factor of 0.9 was used, as suggested by Metcalf and Eddy (1991), to correct k_La that was obtained during the clean water ozonation tests. For ozone gas absorption in highly reactive environments, such as pulp mill effluents, the overall mass transfer coefficient (k_La) was enhanced by a factor (E). The enhanced overall mass transfer coefficient (Ek_La)

was measured in order to determine the enhancement factor of the ozone gas absorption process ($E = Ek_La/k_La$).

In the ozonation experiments, the residual ozone in the liquid phase was insignificant compared to the amount of the utilized ozone (< 1 %). As a result, at the beginning of the ozonation process, the ozone gas absorption in pulp mill effluent was assumed to occur in the fast or instantaneous-reaction-kinetics regime. In order to analyze the gas absorption data to determine Ek_La as a function of the amount of the utilized ozone (ΔO_3) and the ozone contact time (t), the bubble column was operated in a semibatch mode. This was achieved by continuously feeding the gas-phase into the bubble column through the injectors' throats while the liquid-phase was recirculated. In the semibatch mode, further assumptions needed to be considered. These assumptions included:

(1) the gas phase flowed from the bottom to the top of the bubble column in a plug flow regime due to the relatively large buoyancy of the gas bubbles;
(2) the ozone mass balance was conducted only for the gas phase as a result of the residual dissolved ozone concentrations being practically undetectable;
(3) negligible accumulation of the ozone concentration in the gas phase, i.e., pseudo-steady state condition was assumed for the gas phase for the relatively small time intervals (30 s) over which the gas absorption data were collected;
(4) due to the relatively small height of the bubble column, the off-gas flowrate decrease due to ozone gas auto-decomposition, ozone reactions with the contaminants in the liquid phase and the off-gas flowrate increase due to the hydrostatic head decrease along the reactor height were negligible, i.e., $Q_{G,out} = Q_{G,in} = Q_G$; and
(5) Henry's law was applicable.

For the impinging-jet bubble column that was operated in the semibatch mode, conducting an ozone mass balance in the gas phase, and for pseudo-steady state conditions at any given contact time, the bubble-column-average Ek_La was determined as reported before by Zhou and Smith (1997) to be as follows:

$$Ek_La = \left(\frac{Q_G H}{V_L}\right) \ln\left[\frac{C_{G,in}}{C_{G,out}}\right] \qquad [9.4]$$

where: Ek_La = enhanced overall mass transfer coefficient (s^{-1}), Q_G = gas flowrate (m^3s^{-1}), $C_{G,in}$ = feed-gas ozone concentration (mgL^{-1}), $C_{G,out}$ = off-gas ozone concentration (mgL^{-1}), V_L = effective reactor volume (m^3), and H = Henry's constant. Henry's constant was calculated and found to be 4.0 mg gaseous ozone/mg dissolved ozone for the reactor used in the current study. Ek_La was calculated for each ozonation test using Equation 9.4 and by using the previously determined k_La, E was then calculated.

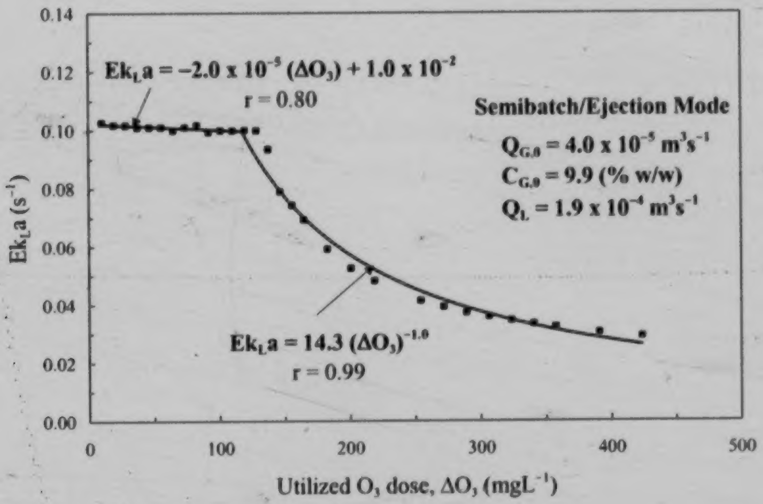

Figure 9.5 The effect of ozonation on Ek_La values.

Figures 9.5 and 9.6 represent typical Ek_La and E as functions of the amount of the utilized ozone in a semibatch-ejection mode. It is evident that the enhancement was higher at the beginning of the ozonation due to the very rapid ozone reactions with the contaminants in the liquid phase. As the ozonation proceeded, the enhancement factor gradually decreased as observed before by Zhou and Smith (1997), except that in the impinging-jet bubble column, two distinctive regions of this gradual decrease in E and Ek_La were observed as shown in Figures 9.5 and 9.6. This observation supports the phenomenon of the shift of the ozone gas absorption process from the fast or instantaneous to the intermediate-reaction kinetics regime as the ozonation proceeds. The rates of this gradual decrease in Ek_La and E with the increase in the amount of the utilized ozone were much lower, especially at the beginning of ozonation process, than those observed in the conventional diffuser bubble column used in the study of Zhou and Smith (1997). This phenomenon could be attributed to the maximization of the enhanced ozone mass transfer process as a result of the use of the venturi injectors for the ozone gas absorption.

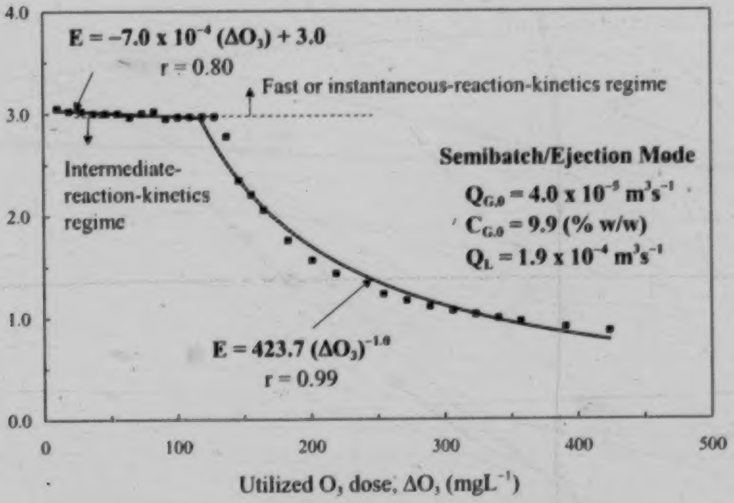

Figure 9.6 The effect of ozonation on E values.

Figure 9.7 depicts a comparison between the cumulative amounts of the applied, utilized, and exhausted ozone in a semibatch-ejection mode. The amount of the utilized ozone was practically equal to the amount of the applied ozone for most of the ozone contact time. As the ozonation proceeded, the amount of the exhausted ozone started to slightly increase due to the decrease in the available easily oxidizable sites for further ozone oxidation. Consequently, the competing reactions between the remaining complex organic structures and ozone became more dominant and that led to a decrease in the amount of the utilized ozone.

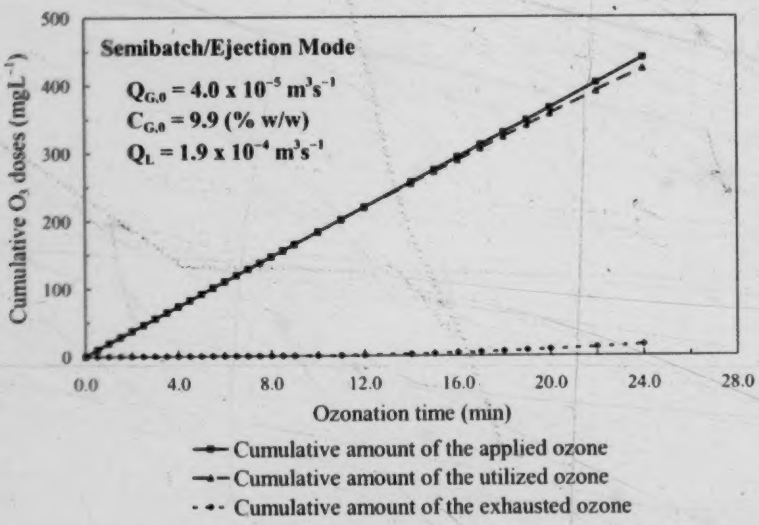

Figure 9.7 The effects of the ozone contact time on the amounts of the applied, utilized, and exhausted ozone.

Figure 9.8 shows a comparison between the measured and the predicted off-gas ozone concentrations in a semibatch-ejection mode. Equation 9.4 was used for predicting the off-gas ozone concentrations by applying the predicted Ek_La's that were obtained using the best-fit linear and power expressions as shown in Figure 9.5. As shown in Figure 9.8, good correlation between the two sets of the off-gas ozone concentrations is evident.

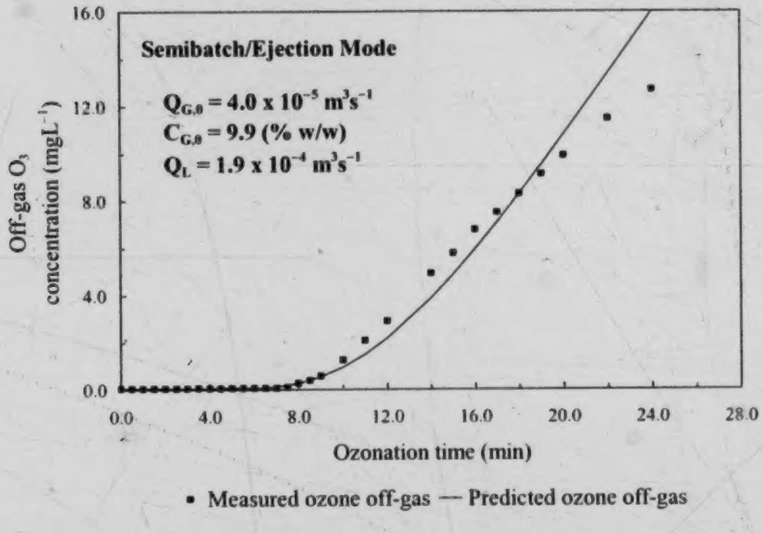

Figure 9.8 A comparison between the measured and the predicted off-gas ozone concentrations.

9.5.4 Ozone Oxidation Efficiencies

The ozonation treatment efficiencies were defined as the reduction percentages of color, AOX, COD, and TOC and the increase percentage of the BOD_5 of the pulp mill effluent. The amount of the utilized ozone is defined as the amount of the applied ozone minus the amount of the unused ozone. The amount of the unused ozone is composed of the amount of the ozone off-gas that leaves the system in the exhaust-gas line and the amount of the residual ozone in the liquid phase. The average amount of the utilized ozone (ΔO_3) for an ozonation system operating in a continuous-flow mode is defined as:

$$\Delta O_3 = \left(\frac{Q_{G,in}C_{G,in}}{Q_L}\right) - \left(\frac{Q_{G,out}C_{G,out}}{Q_L}\right) - C_L \qquad [9.5]$$

where: ΔO_3 = average amount of the utilized ozone (mgL^{-1}), $C_{G,in}$ = feed-gas ozone concentration (mgL^{-1}), $C_{G,out}$ = off-gas ozone concentration (mgL^{-1}), Q_L = liquid flowrate (m^3s^{-1}), $Q_{G,in}$ = feed-gas flowrate (m^3s^{-1}), $Q_{G,out}$ = off-gas flowrate (m^3s^{-1}), and C_L =

residual ozone concentration in the liquid phase (mgL^{-1}). When the bubble column is operated in a continuous-flow mode, the amount of the utilized ozone increases along the column height due to the increase in the ozone contact time with the fluid elements passing through the column. In the current study, and as a result of the relatively short liquid depth (1,315 mm), it was reasonable to assume that the increase in the amount of the utilized ozone along the column height was minimal. Therefore, the bubble-column average amount of the utilized ozone was considered for the assessment of the ozone treatment efficiencies. The residual ozone concentration in the liquid phase was measured and found to be insignificant (< 1 %) when compared to the amount of the utilized ozone. As a result, for estimating ΔO_3, C_L was assumed to equal zero.

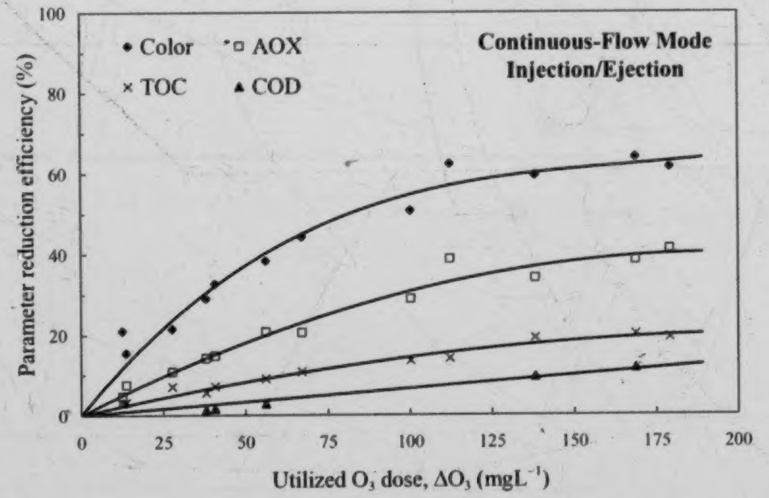

Figure 9.9 The ozonation treatment reduction efficiencies of color, AOX, TOC, and COD.

For the continuous-flow mode, typical reduction efficiencies of color, AOX, TOC, and COD, as functions of ΔO_3, are shown in Figure 9.9. On any parameter reduction performance curve, each data point represents a separate ozonation test that was conducted under certain set of operating conditions that included the feed-gas flowrate, the feed-gas ozone concentration, the liquid flowrate, the gas sparging mode (injection or ejection), the pH, and the liquid-phase temperature. The solid lines in Figure 9.9 represent the average trends in terms of the induced reduction efficiencies of the parameters under investigation (color, AOX, TOC, and COD) as a result of the ozonation treatment. Interestingly, the ozonation treatment efficiencies were only dependent on the amount of the utilized ozone regardless of the other process variables. The ozonation treatment process was more effective in reducing color and AOX compared to TOC and COD. The maximum reduction efficiencies of color, AOX, TOC, and COD were 64, 41, 20, and 12 %, respectively, at ΔO_3 of 180 mgL^{-1}. These maximum reduction efficiencies are comparable to those observed by Zhou and Smith (1997) under the same ΔO_3 and in a larger conventional diffuser bubble column (150 mm in diameter and 3960 mm in depth). The higher color and AOX reduction efficiencies, compared to TOC and COD, could be explained by the higher selectivity of ozone towards oxidizing the easily degradable chromophoric (color-causing) and halogenated (AOX-causing) functional groups compared to the ozone selectivity towards reacting with the remaining organic structures. The same phenomenon was observed by Zhou and Smith (1997). As shown in Figure 9.9, as the ozonation treatment proceeded, the ozone induced reduction of color and AOX exhibited two distinct regions.

The two oxidation regions could be defined as follows: (1) during the initial stage of ozonation, higher and rapidly increasing reduction efficiencies occurred, then followed by, (2) gradual reduction in the treatment efficiency. This phenomenon was observed in several studies (Prat and Esplugas, 1989; Heinzle *et al.*, 1992; Zhou and Smith, 1997). Following the initial oxidation stage, the easily oxidizable sites became less available for further ozone oxidation and consequently, the competing reactions between the remaining complex organic structures and ozone became more dominant. As the ozonation proceeded and as the amount of the utilized ozone increased, the rate of increase of color and AOX reduction efficiencies, per increase of the amount of the utilized ozone, decreased.

Figure 9.10 shows the effects of ozonation on the biochemical oxygen demand (BOD_5) of the Kraft pulp mill effluent. The solid line in Figure 9.10 represents the average trend in terms of the induced increase in the BOD_5 of the Kraft pulp mill effluent as a result of the ozonation treatment. As the amount of the utilized ozone increased, the BOD_5 of the pulp mill effluent increased substantially by about 615 % at ΔO_3 of 180 mgL^{-1}. This phenomenon could be related to the simultaneous ozone reactions with the relatively recalcitrant long-chain-high-molecular-weight organic compounds that are not easily aerobically biodegradable and the simple biodegradable organic compounds that are present in the wastewater. The relative proportions of these organic compounds determine the tendency of the wastewater towards changes in its biodegradability (Zhou and Smith, 1997). The final pulp mill effluent, that is biologically treated in an aerated lagoon, is expected to contain larger percentages of the high-molecular-weight organic compounds since the easily biodegradable organic compounds have been oxidized in the biological treatment process. Consequently, the effect of ozonation, on increasing the BOD_5 of the final pulp mill effluent, is expected to be higher as the reactions between ozone and the recalcitrant organic compounds will be dominant. The rate of increase of pulp mill effluent BOD_5 was a function of the initial wastewater BOD_5 and the amount of the utilized ozone.

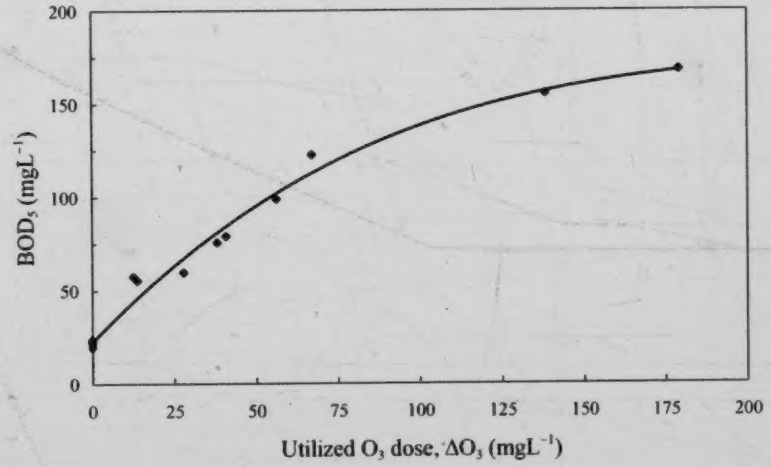

Figure 9.10 The ozonation effects on the biodegradability of pulp mill effluents.

9.6 CONCLUSIONS

Using the impinging-jet bubble column as an ozone-contacting unit has led to a significant increase in the mass transfer rates. As a result, the ozone mass transfer in pulp mill effluents was maximized. Excellent predictions of the overall mass transfer coefficients (k_La's), in the impinging-jet bubble column, have been achieved through the use of the modified non-isobaric one-phase axial dispersion model (1P-ADM). The 1P-ADM is characterized by its simplicity, reliability, and most importantly, its great potential for practical applications in the design of ozone contactors and the on-line process control.

The ozone treatment was more effective in reducing color and AOX than TOC and COD from the biologically treated Kraft pulp mill effluents. The reduction efficiencies were only dependent on the amount of the utilized ozone regardless of the other process variables. The ozonation process caused a significant increase in the BOD_5 of the pulp mill effluent. Therefore, an additional biological treatment process is required after ozonation to remove the increased amount of the easily biodegradable organic content of the ozonated Kraft pulp mill effluents. As a result, using a combined ozonation-biological treatment system can lead to higher treatment levels of the Kraft pulp mill effluents before being discharged into the receiving environment. The use of the impinging-jet bubble column in treating pulp mill effluents has led to comparable contaminant reduction efficiencies compared to those achieved in larger-scale conventional diffuser bubble columns. As a result, the impinging-jet bubble column has proved to be an efficient and compact contacting unit that can lead to significant decrease in the capital and operating costs of the ozonation treatment facilities.

Ozone gas absorption in highly reactive environments is a dynamic process in which the enhanced overall mass transfer coefficient (Ek_La), the enhancement factor (E), and the off-gas ozone concentration are affected by the amount of the utilized ozone, the feed-gas flowrate, the liquid flowrate, and the wastewater characteristics. During the course of ozonation, and operating under the same ozonation process variables, Ek_La and

E will decrease, and the off-gas ozone concentration will increase as a result of the changes in the wastewater characteristics. Good predictions of the off-gas ozone concentrations were achieved by applying the model represented by Equation 9.4. Therefore, the off-gas ozone destruction facilities can be adequately and reliably designed and consequently, optimized operations of the off-gas destruction facilities can be achieved leading to a hazard-free working environment in ozone treatment plants.

9.7 REFERENCES

1. APHA-AWWA-WEF, *Standard Methods for the Examination of Water and Wastewater, 19th Ed. American Public Health Association, American Water Works Association, and Water Environment Federation* (Washington, DC, USA: American Public Health Association, 1995).
2. Bader, H. and J. Hoigné, "Determination of Ozone in Water by the Indigo Method: A Submitted Standard Method", Ozone Sci. & Eng. 4: 169-176 (1982).
3. Bauman, H.D. and L.R. Lutz, "Ozonation of a Kraft Mill Effluent", Tappi J. 57(5): 116-119 (1974).
4. Canadian Pulp and Paper Association, *CPPA technical section, H5P Standard Method* (CPPA, 1974).
5. Catros, A., *Hydrodynamics and Mass Transfer in Three-Phase Fluidized Beds with Baffles: Ph.D. Thesis* (London, ON, Canada: University of Western Ontario, 1986).
6. Chen, B.H., N.S. Yang, and A.F. McMillan, "Gas Holdup and Pressure Drop for Air-Water Flow Through Plate Bubble Columns", Can. J. Chem. Eng. 64: 387-399 (1986).
7. Danckwerts, P.V., *Gas-Liquid Reactions* (NY, USA: McGraw-Hill, Inc., 1970).
8. Deckwer, W.-D., *Bubble Column Reactors*, Cottrell V. (Trans.), Field R.W. (Ed.) (Chichester, England: John Wiley & Sons Ltd, Inc., 1992).
9. Fitzgerald, S.D. and E.R. Holley, *Research Report No. 144* (Urbana, IL, USA: Water Resources Center, University of Illinois, 1979).
10. Gamal El-Din, M. and D.W. Smith, "Designing Ozone Bubble Columns: A Spreadsheet Approach to Axial Dispersion Model", *Proc. of the IOA/PAG Conf.: Advances in Ozone Technology*, Orlando, FL, USA, 2000.
11. Haberl, R., R. Urban, R. Gehringer, and R. Szinovata, "Treatment of Pulp-Bleaching Wastewaters by Activated Sludge, Precipitation, Ozonation, and Irradiation", Wat. Sci. & Technol. 24: 229-239 (1991).
12. Heinzle, E., F. Geiger, M. Fahmy, and O.M. Kut, "Integrated Ozonation-Biotreatment of Pulp Bleaching Wastewaters Containing Chlorinated Phenolic Compounds", Biotechnol. Prog. 8(1): 67-77 (1992).

13. Huynh, L.X., C.L. Briens, J.F. Large, A. Catros, J.R. Bernard, and M.A. Bergougnou, "Hydrodynamics and Mass Transfer in an Upward Venturi/Bubble Column Combination", Can. J. Chem. Eng. 69: 711-722 (1991).
14. Khan, A.A. *A Study of Intersecting Circular Turbulent Jets, Ms.C. Thesis*, (Edmonton, AB, Canada: University of Alberta, 1989).
15. Lewis, D.A. and J.F. Davidson, "Mass Transfer in a Recirculation Bubble Column", Chem. Eng. Sci. 40: 2013-2017 (1985).
16. Mazzei, A.L. and L.J. Bollyky, "Optimizing Mass Transfer Efficiency and Ozone Utilization with High Efficiency Venturi Injectors", *Proc. of the IOA/PAG Conf.*, Toronto, ON, Canada, 1991.
17. Metcalf and Eddy, Inc., *Wastewater Engineering: Treatment, Disposal and Reuse* (NY, USA: McGraw-Hill, Inc., 1991).
18. Oke, N.J., D.W. Smith, and H. Zhou, "An Empirical Analysis of Ozone Decay Kinetics in Natural Waters", Ozone Sci & Eng. 20: 361-379 (1998).
19. Prat, V.M. and S. Esplugas, "Ozonation of Bleaching Water of the Paper Industry", Wat. Res. 23: 51-55 (1989).
20. Thalasso, F., H. Naveau, and E.-J. Nyns, "Design and Performance of a Bioreactor Equipped with a Venturi Injector for High Gas Transfer Rates", Chem. Eng. J. 57: B1-B5 (1995).
21. Unger, D.R. and F. Muzzio, "Laser-Induced Fluorescence Technique for the Quantification of Mixing in Impinging Jets", AIChE J. 45: 2477-2486 (1999).
22. Wachsmann, U., N. Räbiger, and A. Vogelpohl, "The Compact Reactor-A Newly Developed Loop Reactor with a High Mass Transfer Performance", Ger. Chem. Eng. 7: 39-44 (1984).
23. Wang, K.B. and L.T. Fan, "Mass Transfer in Bubble Columns Packed with Motionless Mixers", Chem. Eng. Sci. 33: 945-952 (1978).
24. Witze, P.O., *A Study of Impinging Axisymmetric Turbulent Flows: The Wall Jet, The Radial and Opposing Free Jets: Ph.D. Thesis* (Davis, CA, USA: University of California, Davis, 1974).

25. Zhou, H. and D.W. Smith, "Ozone Mass Transfer in Water and Wastewater Treatment: Experimental Observations Using a 2D-Laser Particle Dynamics Analyzer", Wat. Res. 34: 909-921 (2000).
26. Zhou, H. and D.W. Smith, "Process Parameter Development for Ozonation of Kraft Pulp Mill Effluents", Wat. Sci. & Technol. 35(2-3): 251-259 (1997).
27. Zhou, H., *Investigation of Ozone Disinfection Kinetics and Contactor Performance Modeling: Ph.D. Thesis* (Edmonton, AB, Canada: University of Alberta, 1995).

CHAPTER 10. COMPARING DIFFERENT DESIGNS AND SCALES OF BUBBLE COLUMNS FOR THEIR EFFECTIVENESS IN TREATING KRAFT PULP MILL EFFLUENTS*

10.1 INTRODUCTION

Kraft pulp mill effluents contain high concentrations of color, AOX, COD, and TOC. Recently, the color and AOX-causing compounds have attracted a large attention due to their high resistance to the conventional biological treatment processes. As a result, the pulp mill final effluent that is discharged into the receiving environment will contain high concentrations of those compounds. Therefore, the interest has shifted to other treatment alternatives in order to comply with the more stringent effluent discharge regulations (Haberl *et al.*, 1991; Zhou and Smith, 1997). Among those treatment alternatives, ozonation has been recognized as one of the highly promising technologies for treating pulp mill effluents due to its high induced reduction efficiencies of color and AOX-causing compounds (Bauman and Lutz, 1974; Nebel *et al.*, 1974; Zhou and Smith, 2000).

Through fast oxidation reactions, ozone can selectively react with the color-causing (chromophoric) and AOX-causing (halogenated) functional groups as a result of the their electrophilic nature (Bauman and Lutz, 1974; Nebel *et al.*, 1974). The color reduction efficiency was found to be dependent mainly on the amount of the utilized ozone (ΔO_3) and to some extent on the wastewater initial characteristics in terms of color, COD, pH and dissolved and suspended solids. Zhou and Smith (1997 and 2000) investigated the ozonation effects on reducing color and AOX-causing compounds from a biologically treated Kraft pulp mill wastewater. In the semibatch experiments, maximum reduction efficiencies up to 75 % and 50 % of the color and AOX-causing compounds, respectively, were achieved at a utilized ozone dose of 125 mgL^{-1}.

A part of this chapter has been accepted for publication. Gamal El-Din, M. and D.W. Smith, J. Environ. Eng. & Sci. (August 2001).
Another part of this chapter has been submitted for publication. Gamal El-Din, M. and D.W. Smith, Ozone Sci. & Eng. (August 2001).

In the pilot-scale experiments of Zhou and Smith (1997 and 2000), the maximum reduction efficiencies were up to 60 % and 30 % of the color and AOX-causing compounds, respectively, at a utilized ozone dose up to 125 mgL^{-1}. As the utilized ozone dose increased to 240 mgL^{-1}, the reduction efficiencies of color and AOX-causing compounds increased up to 80 % and 45 %, respectively. The pulp mill wastewater biodegradability can be improved as a result of the conversion of the high-molecular-weight organic compounds to low-molecular-weight organic compounds through the ozone oxidation reactions (Zhou and Smith, 1997). They reported that the pulp mill effluent BOD_5 increased by about 165 % at a utilized ozone dose of 175 mgL^{-1} (Zhou and Smith, 1997). Applying a combined ozonation-biological treatment process can help achieving higher treatment levels (Heinzel *et al.*, 1992; Zhou and Smith, 1997). In general, the ozonation treatment induced low reduction efficiencies of the COD and TOC-causing compounds as observed in several studies (Mohammed and Smith, 1992; Zhou and Smith, 1997). The modeling of the induced reduction of color, AOX, TOC, and COD and induced increase of the pulp mill effluent biodegradability, caused by the ozonation process, can lead to more understanding of the effects of the various operating parameters on the performance of the ozonation process. Quantifying the ozonation process parameters and the process treatment efficiencies in various designs of ozonation systems and over a wide range of operating conditions will lead to a reliable and accurate scale-up of the ozonation process.

The experimental results obtained in three different types of ozone contactors were analyzed to study the effects of the ozone contactor design, configuration, operating conditions, and scale-up on the ozonation process reduction efficiencies of the impurities found in Kraft pulp mill effluents. The increase of the biodegradability of this type of wastewater and the dynamics of the ozone gas absorption process were also investigated in two types of ozone contactors. These ozone contactors included: (1) an extra-coarse-bubble diffuser ozone contactor; (2) an impinging-jet ozone contactor; and (3) a fine-bubble diffuser ozone contactor.

10.2 EXPERIMENTAL METHODS

10.2.1 Extra-Coarse-Bubble Diffuser Ozone Contactor

The ozonation tests were conducted in a semibatch-flow mode in an extra-coarse-bubble diffuser contactor. A detailed schematic of the experimental set-up is shown in Figure 10.1.

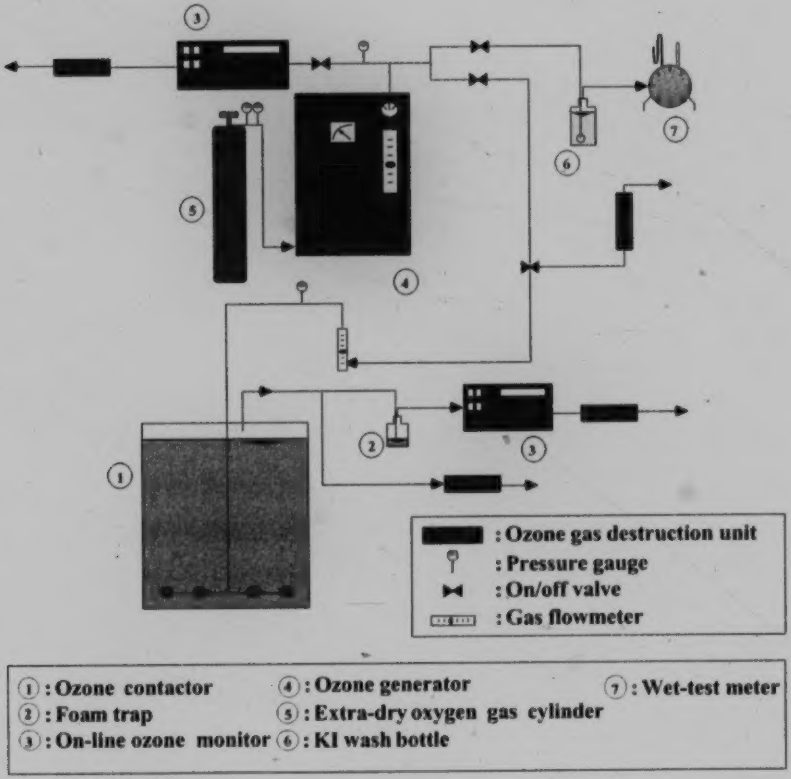
③
⑦
⑥
⑤
④
①
②
③
: Ozone gas destruction unit
: Pressure gauge
: On/off valve
: Gas flowmeter
① : Ozone contactor
② : Foam trap
③ : On-line ozone monitor
④ : Ozone generator
⑤ : Extra-dry oxygen gas cylinder
⑥ : KI wash bottle
⑦ : Wet-test meter

Figure 10.1 Schematic of the experimental set-up of the extra-coarse-bubble diffuser ozone contactor.

The ozone contactor was made from PVC with an inside diameter of 570 mm and a total height of 900 mm. The headspace was restricted to only 6 % of the total reactor volume to shorten the lag-time for the ozone off-gas to travel through the exhaust-gas line to the off-gas ozone monitor. An average volume of 2.1×10^{-1} m^3 of a Kraft pulp mill effluent was pumped into the reactor. Ozone gas was generated from extra-dry pure oxygen using a corona discharge ozone generator (model GLS-7, PCI-WEDECO®). The ozone generator was allowed to stabilize for about 1,800 s in order to obtain a stable ozone concentration in the feed gas. The feed gas that contained 4.0 to 8.1 % w/w ozone was sparged into the liquid phase through a set of eight extra-coarse diffusers (95 mm x 15 mm) that were equally spaced over the cross-sectional area of the contactor and elevated about 10 mm from the bottom of the contactor to provide better contact between the gas bubbles and the liquid phase. The feed-gas flowrate ranged from 2.7×10^{-4} to 3.2×10^{-4} m^3s^{-1}. Those flowrates corresponded to superficial gas velocities ranging from 1.0×10^{-3} to 1.2×10^{-3} ms^{-1}. In order to achieve different utilized ozone doses of up to 230 mgL^{-1}, the ozonation time was varied up to 2,820 s. During the ozonation tests, the ozone concentrations in the feed-gas and off-gas were continuously monitored using PCI-WEDECO® ozone monitors (models HC400 and LC, respectively). Those monitors were allowed at least 900 s to stabilize before registering their readings. Periodic calibration of the ozone monitors was conducted using the KI method as described by the Standard Methods for Examination of Water and Wastewater (APHA-AWWA-WEF, 1995). All the materials that came in contact with the dissolved and gaseous ozone during the experiments were made of glass, teflon, stainless steel, or PVC to reduce the possible interference that would result from the reactions between ozone and the experimental set-up components.

10.2.2 Impinging-Jet Ozone Contactor

10.2.2.1 Continuous-Flow Mode

The ozonation experiments were conducted in a pilot-scale impinging-jet bubble column (see Figure 10.2) in a continuous-flow mode. The bubble column was made from PVC and had an inside diameter of 100 mm and a total height of 1520 mm. The water depth was kept constant at 1315 mm by placing an overflow weir at the top of the column. A ring tube was also installed at the top of the column with a 20 mm-diameter hole facing downward.

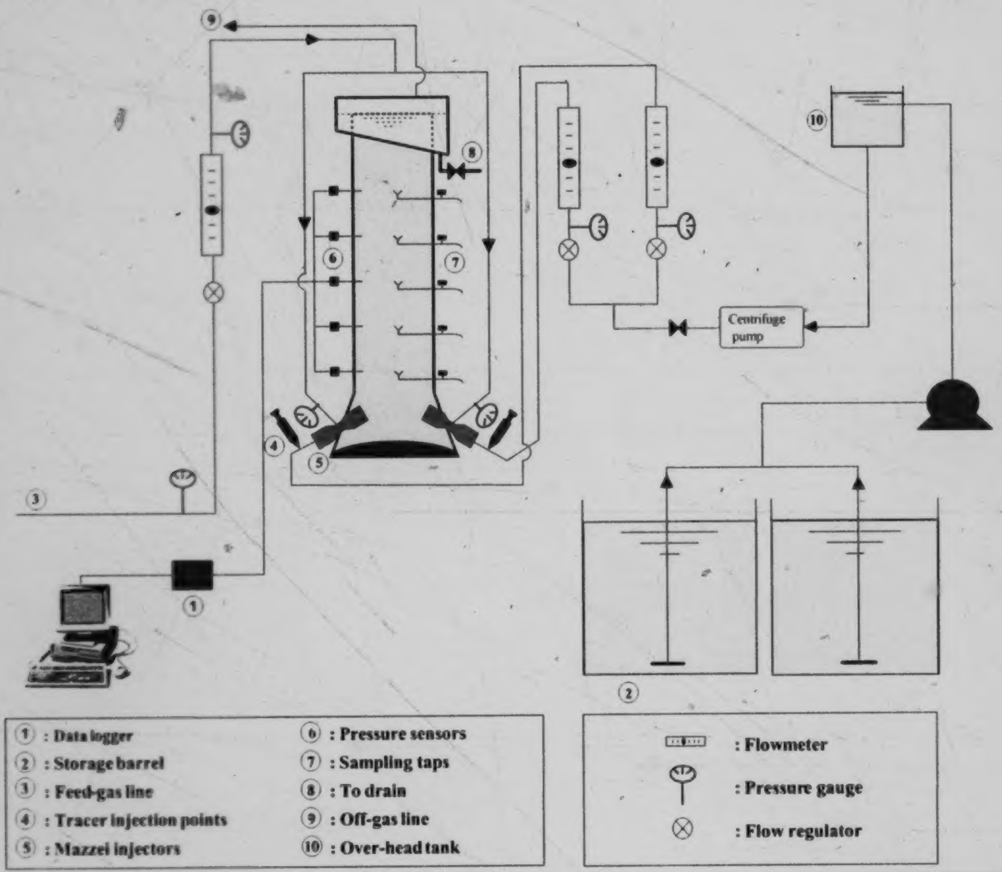
⑨
⑩
⑧
⑥
⑦
Centrifuge pump
④
⑤
③
①
②
① : Data logger
② : Storage barrel
③ : Feed-gas line
④ : Tracer injection points
⑤ : Mazzei injectors
⑥ : Pressure sensors
⑦ : Sampling taps
⑧ : To drain
⑨ : Off-gas line
⑩ : Over-head tank
: Flowmeter
: Pressure gauge
: Flow regulator

Figure 10.2 Schematic of the experimental set-up of the pilot-scale impinging-jet ozone contactor.

The Kynar Mazzei® venturi injectors had an inside diameter of 12.7 mm and were placed 25 mm above the bottom of the column. The injectors were placed at an intersecting angel of 125° and the distance between the centers of the nozzles was 60 mm. The bubble column had an elliptical base to reduce the effect of the backward jet that was created in the ambient fluid as a result of the jet impingement. The sidewalls of the bottom part of the column had a conical shape. With this configuration at the bottom of the column, dead pocketing effects were minimized. Based on the above reactor configuration, it was reasonably assumed that the backmixing along the column height was relatively uniform. The same protocols as described in the previous section, concerning the generation of the ozone gas and the monitoring of the ozone concentrations in the feed and exhaust-gas lines, were applied during the ozonation experiments conducted in the impinging-jet bubble column. Again, all the materials that came in contact with the dissolved and gaseous ozone during the experiments were made of glass, teflon, stainless steel, or PVC. The ozone contactor was operated in a co-current flow mode under two modes of the gas sparging: (1) positive pressure (i.e., injection) mode; and (2) vacuum or negative pressure (i.e., ejection) mode. At least eight turnovers of the reactor working volume were allowed for the ozonation process to reach isothermal steady-state conditions that was verified by reaching a constant off-gas ozone concentration in the exhaust-gas line. The liquid flowrate ranged from 6.2×10^{-5} to 2.2×10^{-4} m^3s^{-1} leading to an average theoretical hydraulic retention time in the range of 48 to 174 s. During the ozonation experiments, the feed-gas flowrate ranged from 1.4×10^{-5} to 1.1×10^{-4} m^3s^{-1}, the feed-gas ozone concentration ranged from 9.0 to 11.0 % w/w, and the pulp mill effluent temperature ranged from 16.0 to 25.0 °C. The raw pulp mill effluent characteristics were variable over time and the average characteristics of the pulp mill effluent used in the current study are shown in Table 10.1.

Table 10.1 Average characteristics of the raw pulp mill effluent.

Wastewater parameters	**Average concentrations**				
	Extra-coarse-bubble diffuser ozone contactor	**Impinging-jet ozone contactor**		**Fine-bubble diffuser ozone contactor**	
	Semibatch-flow mode	**Continuous-flow mode**	**Semibatch-flow mode**	**Continuous-flow mode**	**Semibatch-flow mode**
Color (TCU)	1129	1199	1106	1213	1223
AOX (mgL^{-1})	9.6	10.1	11.2	9.1	7.8
COD (mgL^{-1})	671	750	681	607	485
TOC (mgL^{-1})	268	250	240	239	192
BOD_5 (mgL^{-1})	16.5	21.5	18.8	9.1	11.0
pH	7.7	7.7	7.6	7.6	7.6

10.2.2.2 Semibatch-Flow Mode

The same operating conditions used in the pulp mill effluent ozonation tests that were operated in the continuous-flow mode, were used in the experiments conducted under semibatch-flow conditions as the liquid-phase was recirculated while the gas-phase was continuously introduced through the injectors' throats. Those experiments were conducted for the purpose of investigating the effects of the ozone contact time (t) and the corresponding amount of the utilized ozone (ΔO_3) on the: (1) ozone gas absorption dynamics in terms of the enhanced overall mass transfer coefficient (Ek_La) and the enhancement factor (E); and (2) the off-gas ozone concentration. Therefore, the ozone contact time was varied from 240 to 2,880 s.

10.2.3 Fine-Bubble Diffuser Ozone Contactor

Zhou and Smith (1997) conducted bench-scale and pilot-scale ozonation experiments in a fine-bubble diffuser ozone contactor. They investigated the ozonation treatment efficiencies and the ozone gas absorption dynamics in two different scales of the fine-bubble diffuser ozone contactor and under two different modes of operation: (1) the semibatch-flow mode; and (2) the continuous-flow mode. The liquid phase used in their experiments was Kraft pulp mill effluent that was discharged from an aerated lagoon basin of a Kraft pulp mill. Detailed description of the experimental protocols and the experimental set-up can be found in Zhou and Smith (1997). The raw pulp mill effluent characteristics were variable over time and the average characteristics of the pulp mill effluent used in the study of Zhou and Smith (1997) are shown in Table 10.1.

10.2.4 Characterization of the Pulp Mill Wastewater

Before and after ozonation, samples of the pulp mill wastewater were analyzed to determine the ozonation process-induced treatment efficiencies. These analyses were performed to determine the color, AOX, COD, TOC, and BOD_5. The true color was analyzed according to the H5.P method suggested by the Canadian Pulp and Paper

Association (1974). AOX was analyzed using Euroglas AOX analyzer according to the adsorption-pyrolysis-titrimetric method (APHA-AWWA-WEF, 1995). COD was analyzed according to the closed reflux-colorimetric method (APHA-AWWA-WEF, 1995) by employing silver-catalyzed oxidation with potassium dichromate in sulfuric acid. TOC was analyzed according to the combustion-infrared method (APHA-AWWA-WEF, 1995) using a Dohrmann carbon analyzer (model DC-80®).

10.3 RESULTS AND DISCUSSION

10.3.1 Ozonation Treatment Efficiencies

10.3.1.1 Extra-Coarse-Bubble Diffuser Ozone Contactor

The amount of the utilized ozone (ΔO_3) for a semibatch system is defined as;

$$\Delta O_3 = \int_0^t \frac{\left(Q_{G,in} C_{G,in} - Q_{G,out} C_{G,out}\right)}{V_L} dt - C_L \qquad [10.1]$$

where: ΔO_3 = amount of the utilized ozone (mgL^{-1}), $C_{G,in}$ = ozone concentration in the feed gas (mgL^{-1}), $C_{G,out}$ = ozone concentration in the exhaust gas (mgL^{-1}), C_L = residual ozone concentration in the liquid phase (mgL^{-1}), V_L = effective reactor volume (m^3), $Q_{G,in}$ = feed-gas flowrate (m^3s^{-1}), $Q_{G,out}$ = exhaust-gas flowrate (m^3s^{-1}), and t = ozone contact time (s). In all the ozonation tests, the residual ozone concentration in the liquid phase was measured and found to be insignificant (< 1 %) compared to the amount of the utilized ozone. As a result, for estimating the utilized ozone doses, C_L was assumed to equal zero. Typical induced reduction efficiencies of color, AOX, COD, and TOC as functions of the amount of the utilized ozone are shown in Figure 10.3. On any parameter-reduction-efficiency curve, each data point represents a separate ozonation test that was conducted under certain set of operating conditions that included the feed-gas flowrate, the feed-gas ozone concentration, the pH, and the liquid and the gas-phase temperatures. The solid lines in Figure 10.3 represent the average trends in terms of the induced reduction efficiencies of the parameters under investigation (color, AOX, COD, and TOC) as a result of the ozonation treatment. As shown in Figure 10.3, the ozonation process was more effective in reducing color and AOX compared to COD and TOC. The maximum reduction efficiencies of color, AOX, COD, and TOC were 86, 44, 22, and 15 %, respectively, at ΔO_3 of 230 mgL^{-1}. These observations are consistent with those of Zhou and Smith (1997). An explanation of this phenomenon is that the ozone has a higher selectivity towards oxidizing the easily degradable chromophoric (color-causing) and halogenated (AOX-causing) functional groups compared to the remaining organic structures.

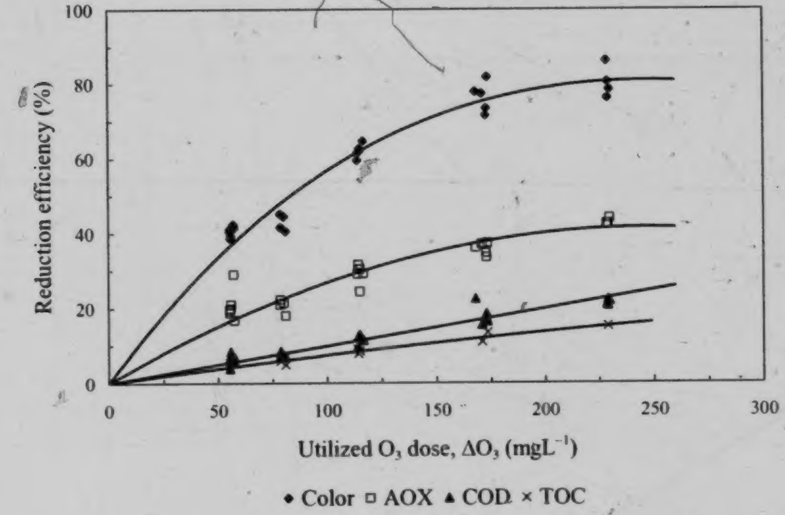

Figure 10.3 Reduction efficiencies of color, AOX, COD, and TOC in the extra-coarse-bubble diffuser ozone contactor.

Figure 10.4 shows the effect of ozonation on the BOD_5 of the Kraft pulp mill wastewater treated in the extra-coarse-bubble diffuser ozone contactor. The solid line in Figure 10.4 represents the average trend in terms of the induced increase in the BOD_5 of the Kraft pulp mill effluent as a result of the ozonation treatment. As the amount of the utilized ozone increased, the BOD_5 of the Kraft pulp mill wastewater increased considerably by about 320 % at ΔO_3 of 230 mgL^{-1}. This phenomenon can be attributed to the reactions of ozone with the relatively recalcitrant long-chain-high-molecular-weight organic compounds that are not easily aerobically biodegradable and with the simple biodegradable organic compounds that are simultaneously present in the wastewater. The relative proportions of those organic compounds and their reaction rates with ozone determine the level of increase in the biodegradability of the wastewater (Zhou and Smith, 1997). The Kraft pulp mill wastewater that is treated biologically in aerated lagoons is expected to contain larger proportions of the high-molecular-weight organic compounds since most of the easily biodegradable organic compounds have been oxidized in the biological treatment process.

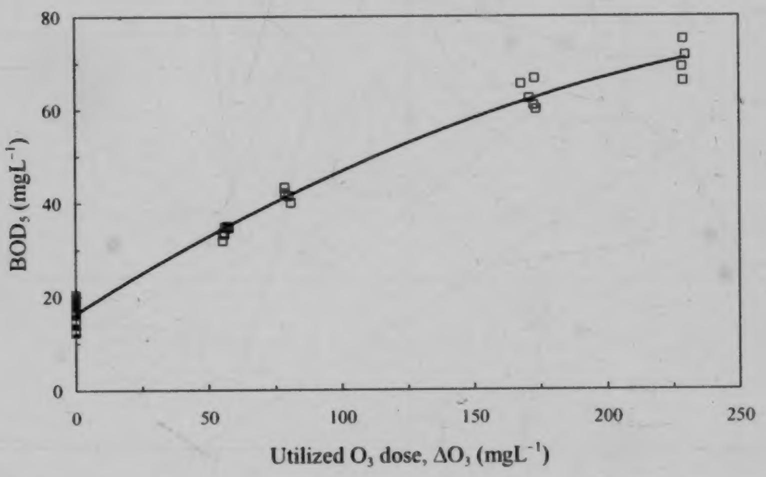

Figure 10.4 The effect of ozonation on the BOD$_5$ of the pulp mill wastewater treated in the extra-coarse-bubble diffuser ozone contactor.

10.3.1.2 Impinging-Jet Ozone Contactor

For a semibatch-flow mode, the amount of the utilized ozone can be determined using Equation 10.1. Meanwhile, the average amount of the utilized ozone (ΔO$_3$) for a continuous-flow mode is defined as:

$$\Delta O_3 = \left(\frac{Q_{G,in} C_{G,in}}{Q_L}\right) - \left(\frac{Q_{G,out} C_{G,out}}{Q_L}\right) - C_L \qquad [10.2]$$

where: ΔO_3 = average amount of the utilized ozone (mgL^{-1}), $C_{G,in}$ = ozone concentration in the feed gas (mgL^{-1}), $C_{G,out}$ = ozone concentration in the exhaust gas (mgL^{-1}), Q_L = liquid flowrate (m^3s^{-1}), $Q_{G,in}$ = feed-gas flowrate (m^3s^{-1}), $Q_{G,out}$ = exhaust-gas flowrate (m^3s^{-1}), and C_L = residual ozone concentration in the liquid phase (mgL^{-1}). For a bubble column operating in a continuous-flow mode, the amount of the utilized ozone will increase along the column height as a result of the increase in the contact time between the ozone and the fluid elements flowing through the column. Due to the relatively short liquid depth (1315 mm) inside the impinging-jet ozone contactor, it was assumed that the increase in the amount of the utilized ozone along the column height was negligible.

The reduction efficiencies of each parameter under investigation were pooled together and plotted as function of the amount of the utilized ozone. The data points, representing a wide range of the operating conditions in the injection and the ejection modes, were overlapping suggesting that there was no effect of the gas sparging mode (injection or ejection mode) on the performance of the ozonation process in terms of reducing the concentrations of color, AOX, COD, and TOC. Consequently, the oxidation efficiencies were only dependent on the amount of the utilized ozone regardless of the other process variables. As observed before, the ozonation process was more effective in reducing color and AOX compared to TOC and COD. The maximum reduction efficiencies of color, AOX, COD, and TOC were 82, 72, 34, and 25 %, respectively, at ΔO_3 of 473 mgL^{-1}. At ΔO_3 of 180 mgL^{-1}, the reduction efficiencies of color, AOX, COD, and TOC were 67, 40, 8, and 11 %, respectively. When the ozone contactor was operated in a continuous-flow mode, the maximum reduction efficiencies of color, AOX, COD, and TOC were 64, 41, 12, and 20 %, respectively, at ΔO_3 of 180 mgL^{-1}. For the semibatch and the continuous-flow modes, typical curves of the ozone oxidation performance are shown in Figures 10.5 and 10.6, respectively. The solid lines in Figures 10.5 and 10.6 represent the average trends in terms of the induced reduction efficiencies of the parameters under investigation (color, AOX, COD, and TOC) as a result of the ozonation treatment.

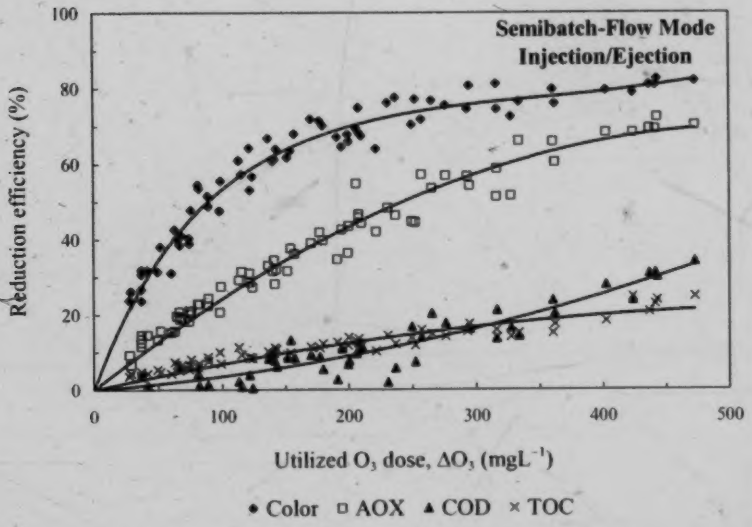

Figure 10.5 Reduction efficiencies of color, AOX, COD, and TOC in the impinging-jet ozone contactor operated in a semibatch-flow mode.

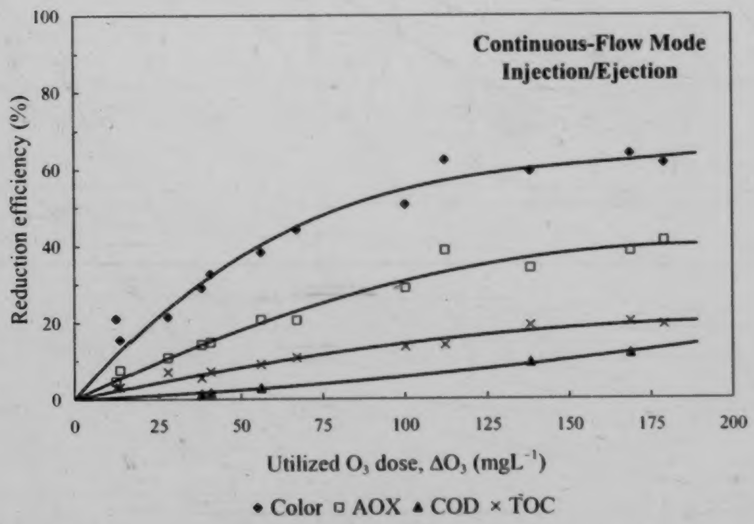

Figure 10.6 Reduction efficiencies of color, AOX, COD, and TOC in the impinging-jet ozone contactor operated in a continuous-flow mode.

As the ozonation process proceeded, the performance curves of the reduction of color and AOX exhibited two distinct regions that could be identified as follows:

(1) during the initial stage of ozonation, higher and rapidly increasing reduction efficiencies occurred; then followed by

(2) gradual reduction in the treatment efficiency.

The same phenomenon was reported by several researchers (Prat and Esplugas, 1989; Heinzle *et al.*, 1992; Zhou and Smith, 1997). After the initial oxidation stage, the sites that are easily oxidizable became less available for further oxidation by ozone and as a result, the competing reactions between the remaining complex organic structures and ozone became more dominant.

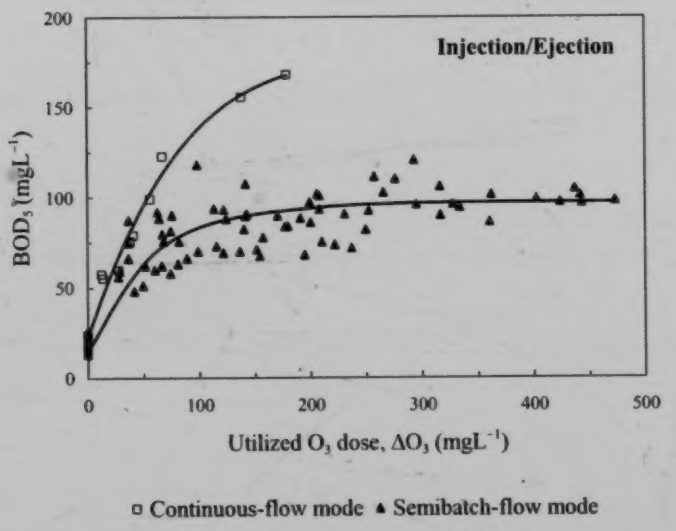

Figure 10.7 The effect of ozonation on the BOD$_5$ of the pulp mill wastewater treated in the impinging-jet ozone contactor.

Figure 10.7 depicts the effect of ozonation on the BOD$_5$ of the Kraft pulp mill wastewater treated in the impinging-jet ozone contactor. The solid lines in Figure 10.7 represent the average trends in terms of the induced increase in the BOD$_5$ of the Kraft pulp mill effluent as a result of the ozonation treatment. Operating the ozone contactor in a continuous-flow mode, and as the amount of the utilized ozone increased, the BOD$_5$ of the pulp mill wastewater increased considerably by about 615 % at ΔO$_3$ of 180 mgL^{-1}.

Meanwhile, in the semibatch-flow mode, the BOD_5 of the pulp mill wastewater increased by about 350 % at ΔO_3 of 180 mgL^{-1} and by about 430 % at ΔO_3 of 473 mgL^{-1}. As shown in Figure 10.7 for the continuous and the semibatch-flow modes and during the initial stage of the ozonation process, a fast rate of increase of the BOD_5 per increase of ΔO_3 occurred. As the ozonation process proceeded, this rate started to decrease and the BOD_5 profile almost reached asymptote at ΔO_3 of about 180 mgL^{-1}.

10.3.2 Ozone Gas Absorption Dynamics

A correction factor of 0.9 was used, as suggested by Metcalf and Eddy (1991), to correct k_La that was obtained for a clean-water ozonation system. As a result of the Kraft pulp mill effluents being highly reactive with ozone, the ozone gas absorption process was enhanced by an enhancement factor (E). Measuring the overall mass transfer coefficient (k_La) and the enhanced overall mass transfer coefficient (Ek_La) has allowed the determination of the enhancement factor of the ozone gas absorption process ($E = Ek_La/k_La$). During the ozonation experiments in all the ozone contactors, the residual ozone in the liquid phase was insignificant compared to the amount of the utilized ozone (< 1 %). Therefore, it can be reasonably assumed that at the beginning of the ozonation process, the ozone gas absorption followed the fast or instantaneous-reaction-kinetics regime.

In order to determine Ek_La as a function of the amount of the utilized ozone (ΔO_3), the ozone contactors were operated in a semibatch-flow mode. In the impinging-jet ozone contactor, the gas-phase was continuously fed into the contactor through the injectors' throats while the liquid-phase was recirculated. Several assumptions were considered for the operations of the ozone contactors under semibatch-flow conditions. These assumptions can be found in Gamal El-Din and Smith (2001). Considering an ozone contactor that is operated in a semibatch-flow mode, conducting an ozone mass balance in the gas phase, and assuming that pseudo-steady state conditions prevail at any contact time, the ozone-contactor-average Ek_La can be determined using the model developed by Zhou and Smith (1997) as follows:

$$Ek_L a = \left(\frac{Q_G H}{V_L}\right) \ln\left[\frac{C_{G,in}}{C_{G,out}}\right] \qquad [10.3]$$

where: Ek_La = enhanced overall mass transfer coefficient (s^{-1}), Q_G = gas flowrate (m^3s^{-1}), $C_{G,in}$ = ozone concentration in the feed gas (mgL^{-1}), $C_{G,out}$ = ozone concentration in the exhaust gas (mgL^{-1}), V_L = effective reactor volume (m^3), and H = Henry's constant. Ek_La was calculated for each ozonation test using Equation 10.3 and by using the previously determined k_La, E was then calculated. Negligible accumulation of the ozone concentration in the gas phase was assumed, i.e., pseudo-steady state conditions were assumed for the gas phase as a result of the relatively small time intervals (30 s) over which the gas absorption data were analyzed.

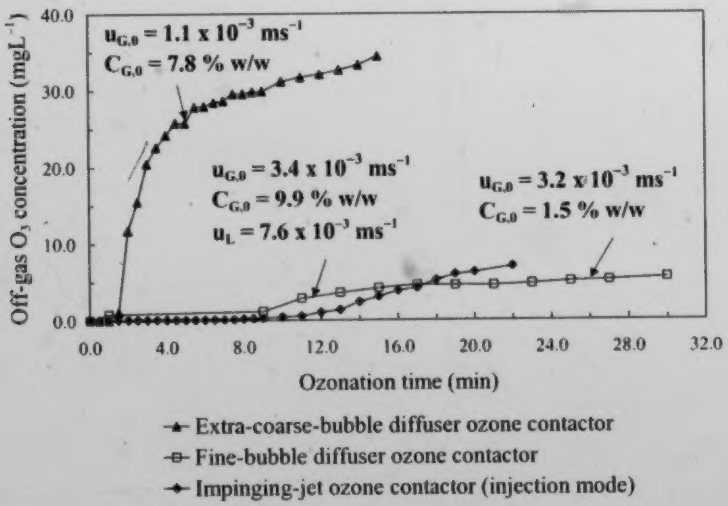

Figure 10.8 The effect of ozonation on the off-gas ozone concentration profiles in three different ozone contactors operated in a semibatch-flow mode.

Figure 10.8 represents a comparison between the fine-bubble diffuser, the extra-coarse-bubble diffuser, and the impinging-jet ozone contactors in terms of the off-gas ozone concentration profiles. The impinging-jet ozone contactor was superior to the other two contactors in terms of its higher mass transfer efficiency due to its lower off-gas ozone concentrations. Although, the impinging-jet contactor operated at higher feed-gas ozone concentrations and superficial gas velocities compared to the other two ozone contactors. When the impinging-jet ozone contactor was operated in a continuous-flow mode, the off-gas ozone concentrations were dependent on the operating conditions encountered during the ozonation tests.

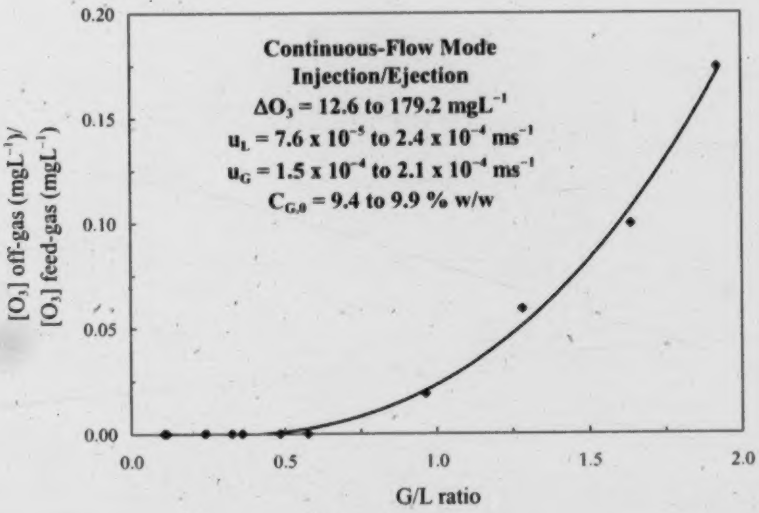

Figure 10.9 The effect of ozonation on the off-gas to the feed-gas ozone concentrations' ratio in the impinging-jet ozone contactor operated in a continuous-flow mode.

The off-gas ozone concentrations were generally low in most of the experimental runs except for those that were conducted at high gas-to-liquid (G/L) flowrate ratios. The ratios of the off-gas to the feed-gas ozone concentrations were pooled for all the ozonation tests that were conducted in the injection and ejection modes and plotted together versus the G/L ratios as shown in Figure 10.9. Interestingly, over the wide range of the operating conditions encountered in the ozonation tests, the ratio of the off-gas to the feed-gas ozone concentrations was only a function of the G/L ratio regardless of the other process variables. The ozonation system exhibited a mass transfer efficiency of 100 % up to G/L ratio of about 0.5 then the mass transfer efficiency started to decrease and the ratio of the off-gas to the feed-gas ozone concentrations started to increase above zero as G/L ratio increased above 0.5.

Figures 10.10 and 10.11 represent typical E and ESt_G values as functions of the amount of the utilized ozone in two types of ozone contactors operated in a semibatch-flow mode. The solid lines in Figures 10.10 and 10.11 represent the general trends in the decrease in E and ESt_G as ΔO_3 increases. In order to compare Ek_La's obtained in contactors that had different effective reactor volumes, Ek_La was presented in terms of the dimensionless enhanced gas-phase Stanton number ($ESt_G = Ek_LaLRT/u_GH$). Where L is the total column height, R is the universal gas constant, T is the gas-phase temperature, and H is the Henry's constant. The operating conditions pertaining to the data presented in Figures 10.10 and 10.11 are the same as those pertaining to the data presented in Figure 10.8 with respect to the extra-coarse-bubble diffuser and the impinging-jet contactors. The enhancement factor (E) was higher during the initial stage of the ozonation due to the very rapid ozone reactions with the contaminants that are present in the Kraft pulp mill effluent. As the ozonation progressed, E and ESt_G decreased gradually. E and ESt_G were significantly higher in the impinging-jet contactor than in E and ESt_G were significantly higher in the impinging-jet contactor than in the extra-coarse-bubble diffuser contactor. In the impinging-jet contactor, two distinctive regions of this gradual decrease in E and ESt_G were observed as shown in Figures 10.10 and 10.11: an initial stage of a very small gradual linear decrease (up to almost $\Delta O_3 = 100$ mgL^{-1}); then followed by a second stage of higher gradual decrease following a power-law function. The decrease in the E and ESt_G values along the course of ozonation supports the phenomenon of the shift of the ozone gas absorption process from the fast or instantaneous to the intermediate-reaction kinetics regime as the ozonation proceeds. In the impinging-jet ozone contactor, the rates of this gradual decrease in ESt_G and E with the increase in the amount of the utilized ozone were much lower, especially at the beginning of the ozonation process, than those observed in the conventional diffuser ozone contactors. This observation along with the low off-gas ozone concentrations produced in the impinging-jet ozone contactor have proved that this ozone contactor can provide a more efficient contacting technology for treating Kraft pulp mill effluents as compared to the conventional diffuser ozone contactors.

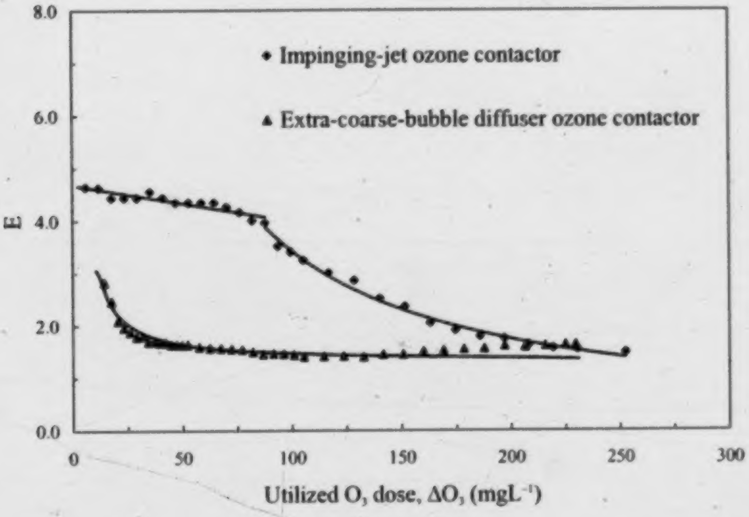

Figure 10.10 The effect of ozonation on the E values in three different ozone contactors operated in a semibatch-flow mode.

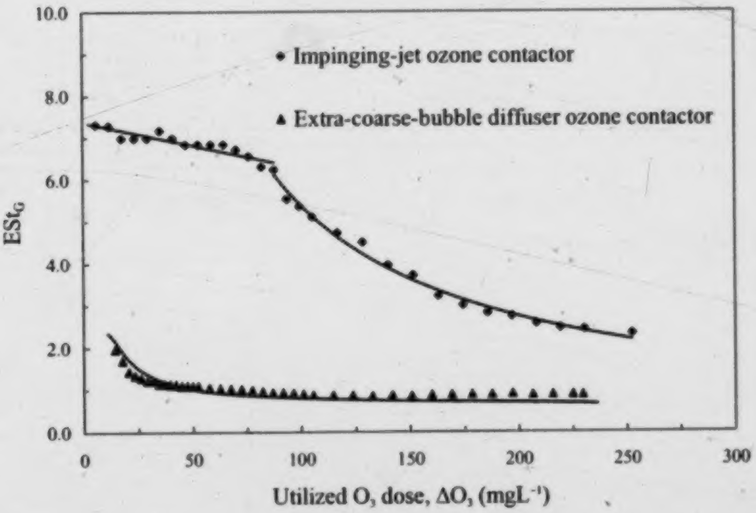

Figure 10.11 The effect of ozonation on the ESt$_G$ values in three different ozone contactors operated in a semibatch-flow mode.

10.3.3 Modeling of the Ozonation Treatment Efficiencies

Figures 10.12 to 10.15 depict typical plots of the BOD_5/COD, color/COD, AOX/COD, and TOC/COD concentrations' ratios as functions of ΔO_3. The solid lines in Figures 10.12 to 10.15 represent the general trends in the change in the BOD_5/COD, color/COD, AOX/COD, and TOC/COD concentrations' ratios as functions of ΔO_3. The relative ratio between the concentrations of the recalcitrant long-chain-high-molecular-weight organic compounds that are not easily aerobically biodegradable and the simple biodegradable organic compounds determines the effectiveness of the ozonation process in increasing the biodegradability of the Kraft pulp mill wastewater. It is more accurate to represent the biodegradability of the wastewater as a ratio of BOD_5 to COD.

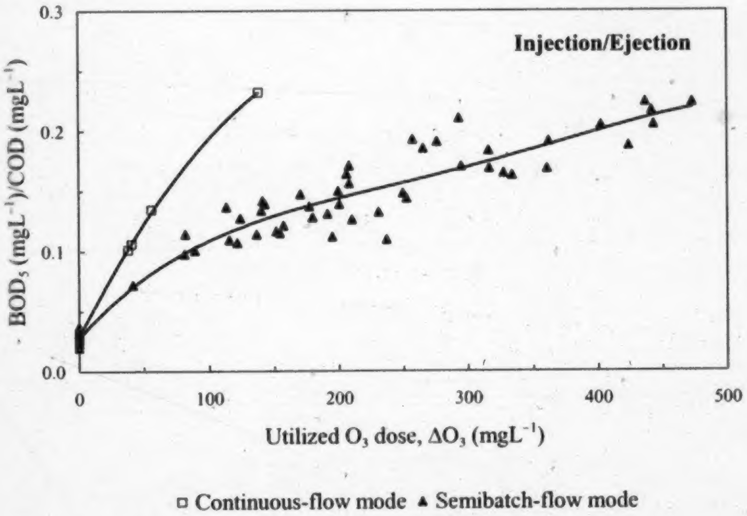

Figure 10.12 The effect of ozonation on the BOD_5/COD ratio of the treated Kraft pulp mill wastewater in the impinging-jet ozone contactor.

As shown in Figure 10.12, ozonation has caused the biodegradability (represented by BOD_5/COD) of the Kraft pulp mill wastewater treated in the impinging-jet ozone contactor to increase from 0.03 to 0.22 at ΔO_3 up to 473 mgL^{-1}. The small ratio of the final BOD_5/COD indicates the need for further treatment of the Kraft pulp mill wastewater to increase its biodegradability, and consequently, to remove the increase in the BOD_5 of the wastewater as a result of applying further treatment. One of the promising treatment options that can be investigated is the combination of hydrogen peroxide and ozone treatment followed by a biological treatment process.

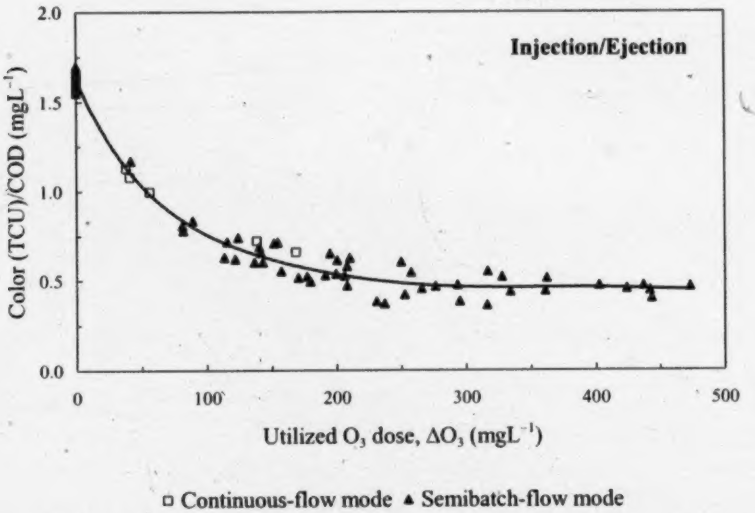

Figure 10.13 The effect of ozonation on the color/COD ratio of the treated Kraft pulp mill wastewater in the impinging-jet ozone contactor.

The color/COD ratios of the Kraft pulp mill wastewater that was treated in the continuous and the semibatch-flow modes under a wide range of operating conditions were pooled together and plotted versus ΔO_3 as shown in Figure 10.13. There was no effect of the operating mode on the ozonation treatment levels. For the AOX/COD and TOC/COD ratios, as shown in Figures 10.14 and 10.15, the same trend in the reduction of those ratios was observed in the continuous and the semibatch-flow modes except that the initial values (at $\Delta O_3 = 0$) of those ratios were lower in the experiments conducted in the continuous-flow mode. The COD decrease along the course of ozonation was well represented by a linear function that had the same slope for both the continuous and the semibatch-flow modes.

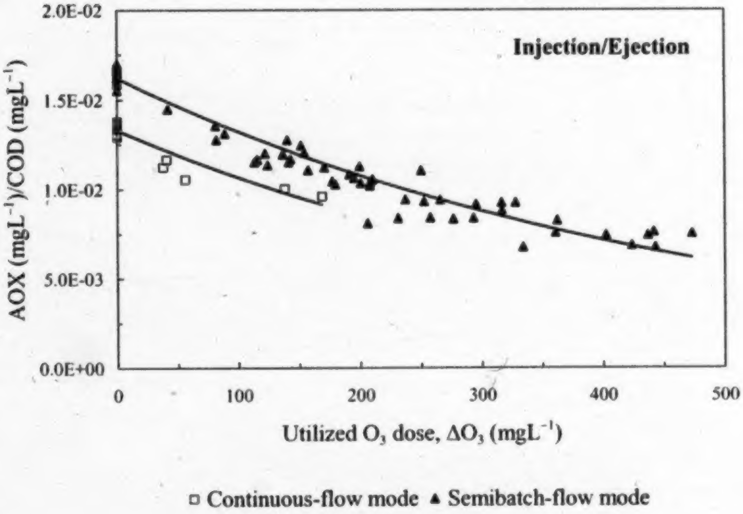

Figure 10.14 The effect of ozonation on the AOX/COD ratio of the treated Kraft pulp mill wastewater in the impinging-jet ozone contactor.

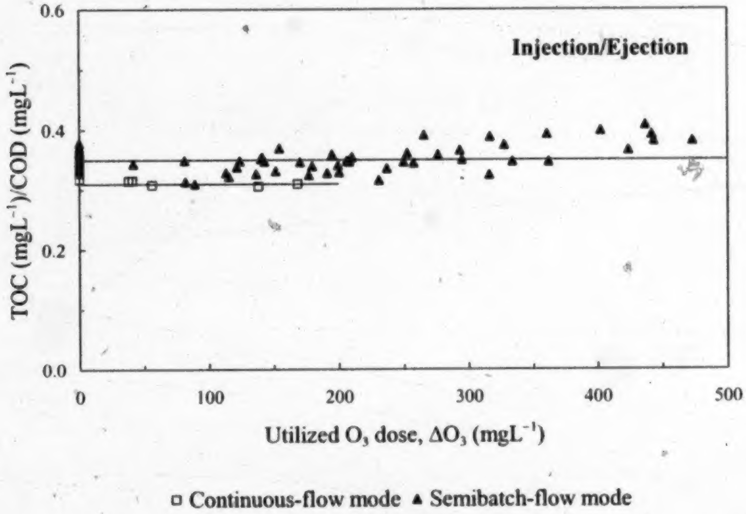

Figure 10.15 The effect of ozonation on the TOC/COD ratio of the treated Kraft pulp mill wastewater in the impinging-jet ozone contactor.

In order to achieve accurate modeling of the ozonation treatment efficiencies in terms of the color, AOX, COD, and TOC induced reduction efficiencies, the ratio of the initial concentration of the parameter, under investigation, to the initial COD concentration in the pulp mill wastewater can be introduced as another parameter that affects the ozonation treatment levels. This ratio represents the effects of the competing reactions between ozone and the various constituents that are present in the Kraft pulp mill wastewater during the course of ozonation. A general model that can describe the performance of the ozonation treatment can be represented as follows:

$$\log\left(\frac{Y}{Y_0}\right) = a \cdot \Delta O_3 + b \cdot \Delta O_3 \cdot \log\left(\frac{Y_0}{COD_0}\right) \qquad [10.4]$$

This model can be applied to describe the ozonation process reduction efficiencies of color, AOX, and TOC. For COD reduction, the term $\log\left(\frac{Y_0}{COD_0}\right)$ reduces to zero. As a result, Equation 10.4 becomes:

$$\log\left(\frac{Y}{Y_0}\right) = a \cdot \Delta O_3 \qquad [10.5]$$

where: Y = final wastewater characteristic parameter concentration (TCU for color, and mgL^{-1} for AOX, COD, and TOC), Y_0 = initial wastewater characteristic parameter concentration (TCU for color, and mgL^{-1} for AOX, COD, and TOC), ΔO_3 = amount of the utilized ozone (mgL^{-1}), COD_0 = initial wastewater COD concentration (mgL^{-1}), and a and b are empirical regression constants. Similar models to those represented by Equations 10.5 and 10.6 were developed before by Zhou and Smith (2000).

The experimental data representing the induced reduction efficiencies of color, AOX, COD, and TOC that were obtained in the continuous and the semibatch-flow modes were pooled together and linear regression analyses were performed to obtain the regression constants (a and b) for each parameter under investigation and finally to examine the applicability of the models represented by Equations 10.4 and 10.5 in predicting the ozone induced reductions of color, AOX, COD, and TOC. The same procedure was performed for the data obtained in the extra-coarse-bubble diffuser ozone contactor.

Table 10.2 Regression parameters for the modeling of the induced reduction efficiencies of color, AOX, COD, and TOC.

Wastewater parameters	**Estimated parameters** a	b	**Multiple r value**
Extra-coarse ozone contactor			
Color	-1.88E-03	-6.91E-03	0.95
AOX	-8.15E-03	-3.78E-03	0.89
TOC	-4.35E-04	-2.68E-04	0.97
COD	-4.74E-04	N/A	0.96
Impinging-jet ozone contactor			
Color	-4.06E-03	9.04E-03	0.81
AOX	2.92E-04	8.39E-04	0.98
TOC	8.64E-05	7.87E-04	0.79
COD	-2.79E-04	N/A	0.88

The regression analyses was performed at a 95 % confidence level and the constant parameter was set equal to zero in order to account for the no-treatment condition when the amount of utilized ozone is equal to zero. The regression analyses produced coefficients of correlation (r's) in the range of 0.89 to 0.97 for the data obtained in the extra-coarse-bubble diffuser ozone contactor and in the range of 0.79 to 0.98 for the data obtained in the impinging-jet ozone contactor. The regression parameters obtained for all the wastewater quality parameters representing the Kraft pulp mill wastewater that was treated in the impinging-jet and the extra-coarse-bubble diffuser ozone contactors are shown in Table 10.2.

A Comparison between the predicted and the measured induced ozone reduction efficiencies of the AOX of the Kraft pulp mill wastewater that was treated in the impinging-jet ozone contactor, under various amounts of the utilized ozone, is shown in Figure 10.16

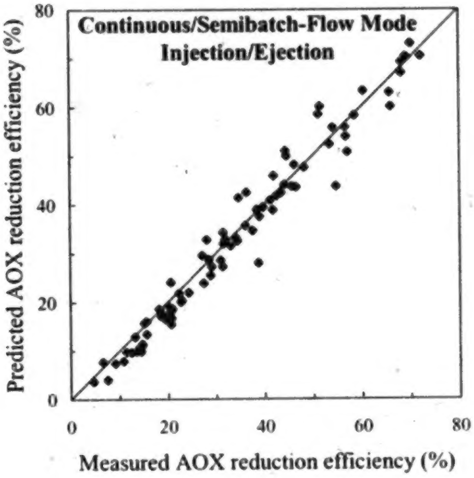

Figure 10.16 A comparison between the predicted and the measured reduction efficiencies of AOX.

10.3.4 Scale-Up of the Ozonation Process

Different ozone contactor designs and configurations should be tested over a wide range of operating conditions in order to achieve proper scale-up of the ozonation process for treating Kraft pulp mill wastewaters. Consequently, relationships can be developed to predict the ozonation treatment levels that can be achieved when scaling up ozone contactors. Zhou and Smith (1997 and 2000) investigated the factors that would influence the scale-up of conventional fine-bubble diffuser ozone contactors. They tested their unit in two operating modes: the semibatch and the continuous-flow modes. Also, two contactor sizes were tested: 6.0 x 10^{-2} m^3 and 4.0 x 10^{-3} m^3. Detailed description of their experimental protocols can be found in Zhou and Smith (1997 and 2000). They reported that there was a small scale-up factor associated with the ozonation treatment of Kraft pulp mill wastewaters, although, there was no effect of the mode of operations on the induced reductions of color, AOX, COD, and TOC. Furthermore, a comparison was conducted between the two scales of fine-bubble diffuser ozone contactors used by Zhou and Smith (1997 and 2000) and the ozone contactors used in the current study in terms of the ozonation treatment levels at a similar ΔO_3 of 125 mgL^{-1}.

Table 10.3 A comparison between three different scales and designs of ozone contactors in terms of the color, AOX, COD, and TOC reduction efficiencies.

Operating conditions	**Ozone contactor # (1)**	**Ozone contactor # (2)**	**Ozone contactor # (3)**	**Ozone contactor # (4)**
Mode of operations	semibatch	semibatch/ continuous	semibatch	semibatch/ continuous
Gas sparging technique	extra-coarse diffuser	impinging jets	fine diffuser	fine diffuser
Reactor volume (m^3)	2.1×10^{-1}	1.7×10^{-2}/ 1.0×10^{-2}	4.0×10^{-3}	6.0×10^{-2}/ 7.0×10^{-2}
Reactor aspect ratio	1.6	13.2	5.4	22.3/31.3
ΔO_3 (mgL^{-1})	125	125	125	125
Wastewater parameters	**% Reduction efficiencies**			
Color	65	60	75	63
AOX	31	35	52	32
COD	12	17	20	19
TOC	10	9	17	10

The ozonation induced reduction efficiencies in the four ozone contactors designs are shown in Table 10.3. The results indicated that the scale-up and reactor configuration have exhibited insignificant effects on the ozonation treatment efficiencies. Despite that the impinging-jet ozone contactor, as discussed earlier, has shown to produce lower off-gas ozone concentrations compared to the other ozone contactors that were operated in a semibatch-flow mode. The treatment levels achieved in the impinging-jet and fine-bubble diffuser ozone contactors that were operated in a continuous-flow mode were compared. The two designs of ozone contactors have produced almost identical treatment levels except that the volume of the impinging-jet contactor was one seventh of that of the fine-diffuser contactor. Consequently, the operating costs of the ozonation process and the ozone off-gas destruction facilities will be greatly reduced when the impinging-jet ozone contactor is used for treating Kraft pulp mill wastewaters.

10.4 CONCLUSIONS

Using the venturi injectors for sparging the ozone gas into the liquid phase in the impinging-jet contactor has led to a significant increase in the enhanced overall mass transfer coefficient (Ek_La) and the enhancement factor (E) compared to other designs of ozone contactors. As a result, the off-gas ozone concentrations that were produced from the impinging-jet contactor were substantially lower than those produced from the other contactors.

The ozonation process induced higher reductions in the color and AOX concentrations compared to COD and TOC of the treated Kraft pulp mill effluents. The small ratio of the BOD_5/COD of the treated wastewater indicates the need for further treatment of this type of wastewater to increase its biodegradability, and consequently, to remove the increase in the BOD_5 of the wastewater as a result of applying further treatment.

The reduction efficiencies of color, AOX, COD, and TOC indicated that the scale-up and reactor configuration have exhibited insignificant effects on the ozonation treatment levels achieved in the three types of ozone contactors examined in this study. This suggests that a small scale-up factor was associated with the ozonation treatment of Kraft pulp mill effluents, especially at large scales, where there was virtually no effect on the ozonation induced reduction efficiencies of color, AOX, COD, and TOC.

The treatment levels achieved in the impinging-jet and fine-bubble diffuser ozone contactors that were operated in a continuous-flow mode were compared and the two designs of ozone contactors were found to produce almost identical treatment levels except that the volume of the impinging-jet contactor was one seventh of that of the fine-diffuser contactor. Based on the above, it is evident that the operating costs of the ozonation process and the ozone off-gas destruction facilities will be greatly reduced when the impinging-jet ozone contactor is used for treating Kraft pulp mill wastewaters.

10.5 REFERENCES

1. APHA-AWWA-WEF, *Standard Methods for the Examination of Water and Wastewater, 19th Ed. American Public Health Association, American Water Works Association, and Water Environment Federation* (Washington, DC, USA: American Public Health Association, 1995).
2. Bauman, H.D. and L.R. Lutz, "Ozonation of a Kraft Mill Effluent", Tappi J. 57(5): 116-119 (1974).
3. Canadian Pulp and Paper Association, *CPPA technical section, H5P Standard Method* (CPPA, 1974).
4. Gamal El-Din, M.G. and D.W. Smith, "Maximizing the Enhanced Ozone Oxidation of Kraft Pulp Mill Effluents in an Impinging-Jet Bubble Column", *Proc. of the IOA/PAG Conf.: Advances in Ozone Technology*, Newport Beach, CA, USA, 2001.
5. Haberl, R., R. Urban, R. Gehringer, and R. Szinovata, "Treatment of Pulp-Bleaching Wastewaters by Activated Sludge, Precipitation, Ozonation, and Irradiation", Wat. Sci. & Technol. 24: 229-239 (1991).
6. Heinzle, E., F. Geiger, M. Fahmy, and O.M. Kut, "Integrated Ozonation-Biotreatment of Pulp Bleaching Wastewaters Containing Chlorinated Phenolic Compounds", Biotechnol. Prog. 8(1): 67-77 (1992).
7. Metcalf and Eddy, Inc., *Wastewater Engineering: Treatment, Disposal and Reuse* (New York, NY, USA: McGraw-Hill, Inc., 1991).
8. Mohammed, A. and D.W. Smith, "Effects of Ozone on Kraft Process Pulp Mill Wastewater", Ozone Sci. & Eng. 14: 461-485 (1992).
9. Nebel, C., R.D. Gottschling, and H.J. O'Neil, "Ozone Decolorization of Pulp and Paper Secondary Wastewaters", *Proc. of First Int. Symp. Ozone for Water and Wastewater Treatments*, 1974.
10. Prat, V.M. and S. Esplugas, "Ozonation of Bleaching Water of the Paper Industry", Wat. Res. 23: 51-55 (1989).
11. Zhou, H. and D.W. Smith, "Process Parameter Development for Ozonation of Kraft Pulp Mill Effluents", Wat. Sci. & Technol. 35(2-3): 251-259 (1997).

12. Zhou, H. and D.W. Smith, "Ozonation Dynamics and its Implication for Off-Gas Ozone Control in Treating Pulp Mill Wastewaters" Ozone Sci. & Eng. 22: 31-51 (2000).

CHAPTER 11. MEASUREMENTS OF THE SIZE, RISE VELOCITY, AND SPECIFIC INTERFACIAL AREA OF BUBBLES IN AN IMPINGING-JET BUBBLE COLUMN*

11.1 INTRODUCTION

Gas hold-up (ε_G) is one of the important variables that characterize the hydrodynamics of the gas-liquid flow, i.e., two-phase flow, in bubble columns. It is defined as the fraction of the dispersed volume occupied by the gas bubbles. ε_G can affect the performance of bubble columns in two ways: (1) it provides the fractional volume of the gas phase and therefore, its residence time inside the reactor; and (2) in conjunction with the knowledge of the Sauter mean (i.e., volume-to-surface area mean) bubble diameter, it allows the determination of the gas bubbles' specific interfacial area (Jamialahmadi and Müller-Steinhagen, 1992). Gas hold-up, Sauter mean diameter, and gas bubbles' specific interfacial area are interrelated through the following relationship:

$$a = \frac{A}{V} = \frac{6\varepsilon_G}{d_S} \qquad [11.1]$$

where: a = mean gas bubbles' specific interfacial area (m^{-1}), A = mean gas bubbles' surface area (m^2), V = volume of the dispersed phases (m^{-3}), ε_G = gas hold-up (m^3m^{-3}), and d_S = Sauter mean bubble diameter (m). Since the overall mass transfer coefficient (k_La) can be measured experimentally and with the knowledge of a, the local mass transfer coefficient (k_L) could be determined for the gas-liquid flow in bubble columns.

The use of computational fluid dynamics (CFD) has grown over the past decade since it can offer detailed predictions of the behaviour and the characteristics of multiphase flows such as gas-liquid flow in bubble columns. CFD can lead to significant improvements in the area of scale-up of bubble columns. In order to achieve successful application of CFD in the scale-up process, a better understanding of the fundamentals of the gas-liquid flow phenomena has to be provided.

A version of this chapter has been submitted for publication. Gamal El-Din, M. and D.W. Smith, J. Environ. Eng. & Sci. (August, 2001).

Gas-liquid flows are complex in their nature and their behaviour can vary substantially depending on the design, configuration, and operating conditions of the bubble columns. It is very hard to conduct experimental measurements inside gas-liquid flows because of their sensitive nature to any disturbances caused by intrusive measuring devices such as electric probes (Mudde *et al.*, 1998). As a result, the use of non-intrusive measurement techniques such as laser Doppler anemometry (LDA) and phase Doppler anemometry (PDA) can provide great tools for characterizing and better understanding of the local rather than the global flow phenomena in gas-liquid flows (Mudde *et al.*, 1998).

Several studies have been conducted for measuring the size of gas bubbles in air-water systems by using a photographic technique (Akita and Yoshida, 1974; Yamashita *et al.*, 1978; Roustan *et al.*, 1996). They observed that, especially at higher gas throughputs, the bubbles were not spherical but could be approximated by oblate ellipsoids. Yamashita *et al.* (1978) measured the d_S of the ellipsoidal bubbles using a photographic study. Alternatively, and assuming that the bubbles are perfect spheres, they measured the d_S of the bubbles using an electric probe. Interestingly, and at low gas throughputs, they observed that the two measures of the mean d_S were almost identical. Also, from their photographic measurements, they observed that d_B was almost equal to d_S.

In the current study, a 2-D laser particle dynamics analyzer, that utilizes phase Doppler anemometry (PDA) and laser Doppler anemometry (LDA), was used to obtain simultaneous measurements of: (1) the gas bubble size; (2) the gas bubble size distributions; (3) the gas-phase axial and radial velocity distributions; and (4) the gas-phase turbulence intensities in the axial and radial directions in an impinging-jet bubble column. Two types of liquids were tested: clean deionized water and Kraft pulp mill effluent. The Kraft pulp mill effluent was ozonated using a wide range of utilized ozone doses to investigate its effects on pulp mill effluent characteristics. Of primary interest was its surface active agents (SAA) content and the resulting effect on the surface tension and consequently, on the bubble size (d_B and d_S), the gas hold-up (ε_G), and the gas bubbles' specific interfacial area (a). The gas and liquid flowrates were varied in order to determine their effects on the bubble size, the gas bubbles' specific interfacial area, and the gas hold-up.

11.2 MEASUREMENT METHODS

11.2.1 Particle Dynamics Analyzer

11.2.1.1 Operating Principle

The operating principle of the particle dynamics analyzer can be explained through the use of a simple fringe model. An optical system is used to split a continuous laser beam into two parallel beams. As the two beams pass through a spherical lens, they get reflected and consequently they intersect at the focal point of the lens. Two sets of plane parallel interference fringes are produced, at the intersection point of the laser beams, in the Y-Z and X-Z planes. The spacing between the fringes depends on the intersecting angle and the laser wavelength.

11.2.1.2 Principle of the Bubble Rise Velocity Measurement

The laser Doppler anemometry (LDA) is utilized for measuring the velocity of the bubbles in a gas-liquid flow. As the bubbles rise inside the column and pass through the interference fringes, that are formed in an ellipsoidal volume or referred to as the probe or measurement volume, they will cause a scattering of light in different directions. The scattered light, received by the receiving optics, will have another frequency as a result of the Doppler effect. The Doppler burst is detected by a high-speed photo-multiplier and converted into an electronic signal that will have a frequency proportional to the bubble rise velocity. Therefore, the measurement of those frequencies will allow the determination of the bubble rise velocity. The frequency of the scattered light will carry no information of the sign of the velocity of the bubble. To overcome this velocity sign ambiguity, a small frequency shift is introduced in the transmitting optics to one of the crossing laser beams. As a result, the fringe pattern is no longer stationary but moves perpendicularly to the fringe plane and the light intensity at any point will be modulated at the shift frequency. A bubble moving in the probe volume will scatter light such that the difference between the modulation frequency and the shift frequency is proportional to the velocity. Therefore, for a bubble moving in the opposite direction to the fringe movement, the modulation frequency will increase. Meanwhile, for a bubble moving in the same direction of the fringe movement, the modulation frequency will decrease. In order to achieve that, a 40 MHz frequency shift was applied via the use of a Bragg cell.

11.2.1.3 Principle of the Bubble Size and Concentration Measurements

The laser Doppler anemometry (LDA) and phase Doppler anemometry (PDA) are utilized for measuring the size and concentration of the bubbles in a gas-liquid flow. As the bubbles pass through the probe volume, they scatter light. The scattered light will contain information about the bubble size. The PDA operating principle can be explained using a fringe model of the phase shift. Considering the interference fringes in the probe volume to be light rays, they are reflected and refracted by the transparent gas bubbles as they pass through the probe volume. A set of two detectors are located at separate locations and will observe alternately light and dark fringes at the same frequency with a relative phase proportional to the spacing between the detectors divided by the spacing between the projected fringes. The spacing between the projected fringes at the location of the detectors is inversely proportional to the effective focal length of the bubble that is proportional to the bubble diameter (d_B). Therefore, the measured phase shift is proportional to d_B of the bubble passing through the probe volume. In order to obtain an exact and accurate linear relationship between d_B and the phase shift, a specific scattering pattern has to be dominant. The refractive index of water is larger than that of air. Therefore, a 70° scattering angle in a forward scattering mode provides the highest signal levels and an excellent linear relationship between the phase shift and the bubble diameter for measuring the size of an air bubble moving in water (DANTEC, 1989).

The concentration of the bubbles (C_B) can be determined based on the knowledge of the arrival rate and the velocity of the rising bubble as well as the cross-sectional area of the probe volume. The cross-sectional area of the probe volume is a function of the laser power, the electronic sensitivity, and the size of the bubble passing through the laser beam. For a bubble to be detected, the light level must be above a fixed detection threshold. Large bubbles can pass near the edge of the probe volume and still be detected as a result of their ability to scatter more light than small bubbles. Consequently, the concentrations obtained by the PDA will be biased towards large bubbles. This ambiguity in concentration determination is resolved by using the residence time of the bubble as a weighting factor for the bubble size distribution.

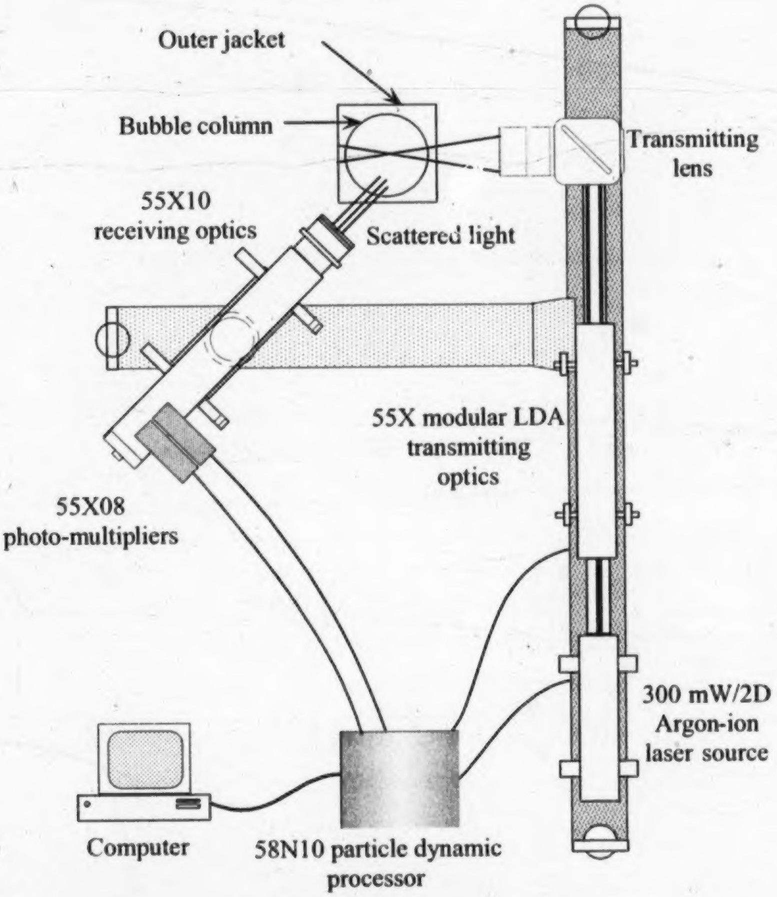
Outer jacket
Bubble column
Transmitting lens
55X10 receiving optics
Scattered light
55X modular LDA transmitting optics
55X08 photo-multipliers
300 mW/2D Argon-ion laser source
Computer
58N10 particle dynamic processor

Figure 11.1 Components of the particle dynamics analyzer set-up (adapted from Shawwa, 1998).

11.2.1.4 PDA System Configuration and Operational Settings Adjustment

A 2-D DANTEC® laser particle dynamics analyzer was used in the current study. It consisted of (1) 55X modular LDA transmitting optics; (2) 57X10 receiving optics; (3) 55X08 photo-multipliers; and (4) 58N10 processor. The set-up of the PDA system is shown in Figure 11.1. The configuration and operational settings used in the current study are presented in Table 11.1. Those settings were chosen after investigating a wide range of PDA operational configurations and settings to match the velocity and bubble size measurements with those obtained in a photographic study. Therefore, the information obtained from the photographic study helped in adjusting the transmitting and receiving optics configuration and the electronics' operational settings to obtain accurate and reliable results.

11.2.2 Digital Photographic Measurements of the Bubble Size and the Bubble Rise Velocity

Measurements of the bubble size and the bubble rise velocity were conducted using a Canon Powershot G1® digital camera. The same operating conditions and the location of measurements that were to be used during the PDA measurements were applied in the photographic study. The camera was leveled and mounted on a stable tripod. An adequate source of light was used and the lens of the camera was focused on a fixed vertical line at the center of the column before the photographic images were recorded. The video photographic study provided rough estimates of the bubble rise velocity by selecting a swarm of bubbles and recording the time it took them to rise over a certain distance along the column height. The rate of video capture was 15 frames per second and the resolution was adjusted to 320/240 pixels. The video images were downloaded and viewed using digital video software. The shutter speed was adjusted to 1/1000 s during the capture of still digital images and the resolution was adjusted to 2048/1536 pixels. Measurements of the bubble size were conducted by selecting a number of individual bubbles that were sharply focused allowing for the shapes and sizes of the bubbles to be obtained.

Table 11.1 PDA system configuration and operational settings.

Laser specifications	
Argon-Ion Laser Power (mW)	300
Bragg Cell Frequency Shift (MHz)	40
U-velocity Laser beam wavelength, λ (nm)	514.5
V-velocity Laser beam wavelength, λ (nm)	488.0
Electronics set-up	
Signal bandwidth (MHz)	0.12
Validation level during DI water experiments (dB)	0
Validation level during Kraft pulp mill effluent experiments (dB)	-3
Spherical validation	no
Gain	high
Transmitting optics set-up	
Front lens focal length (mm)	600
Laser beam spacing (mm)	12
Fringe spacing, $\delta_{f,x}$ (μm)	25.726
Fringe spacing, $\delta_{f,y}$ (μm)	24.401
Number of fringes	8
Measurement volume dimensions, δ_x x δ_y x δ_z (mm x mm x mm)	0.2159 x 0.2159 x 28.804
Frequency shift sign	positive
Polarization angle (degree)	0
Polarization orientation w.r.t. scattering plane	parallel
Gaussian beam diameter (mm)	0.82
Beam expansion ratio	1.85
Beam collimation ratio	1.20
Receiving optics set-up	
Front lens focal length (mm)	600
Polarization angle (degree)	0
Polarization orientation w.r.t. scattering plane	parallel
Scattering angle (degree)	70
Scattering mode	Forward reflection
Direction of fringe motion	positive
Fringe direction angle (degree)	0
Angle adjustment (mm)	0

The size measurements were corrected using the proper scale factor that was obtained by mounting a measuring tape of a known scale in the area where the photographic images were recorded. The photographic study was conducted only for the clean deionized water due to the difficulties encountered in obtaining high-quality images when Kraft pulp mill was used as the test liquid. This was a result of the high color content of the effluent.

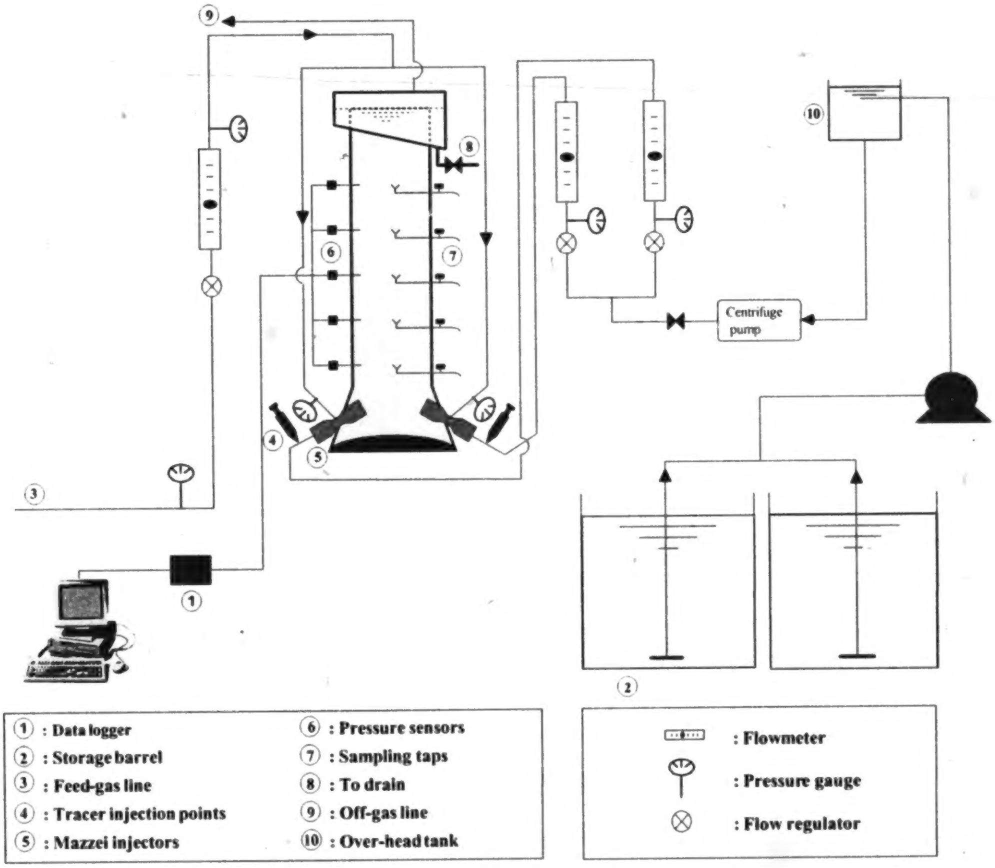
⑨
⑩
⑧
⑥
⑦
Centrifuge pump
④
⑤
③
①
②
① : Data logger
② : Storage barrel
③ : Feed-gas line
④ : Tracer injection points
⑤ : Mazzei injectors
⑥ : Pressure sensors
⑦ : Sampling taps
⑧ : To drain
⑨ : Off-gas line
⑩ : Over-head tank
: Flowmeter
: Pressure gauge
: Flow regulator

Figure 11.2 Schematic of the experimental set-up of the pilot-scale impinging-jet bubble column.

11.2.3 Experimental Set-Up for the Photographic and the PDA Studies

During the photographic and the PDA studies, the measurements were conducted in a pilot-scale impinging-jet bubble column (see Figure 11.2). A detailed description of the different components of the pilot-scale set-up can be found in Gamal El-Din and Smith (2001). The bubble column was made from clear acrylic and had an inside diameter of 100 mm and a total height of 1,520 mm. The column was surrounded by a 150 mm x 150 mm clear acrylic jacket that had flat surfaces and the gap between the column and the jacket was filled with clean deionized water. The outer jacket was used to minimize the distortions caused by the curved surface of the column (Mudde *et al.*, 1997).

Extra dry air was used as the gas phase and the bubble column was operated for a period of time that was at least eight theoretical reactor hydraulic retention times before measurements were taken to allow the system to reach an isothermal steady-state condition. The pilot-scale bubble column was operated under a wide range of liquid and feed-gas flowrates. During the experiments, the liquid flowrate ranged from 6.0×10^{-5} to 2.2×10^{-4} m^3s^{-1} and the feed-gas flowrate ranged from 8.2×10^{-6} to 1.0×10^{-4} m^3s^{-1}. During the PDA and the photographic studies, measurements were conducted at a point located at the middle of the column height and at a distance equal to 1/3 of the column diameter from the column wall.

11.2.4 Experimental Set-Up for the Ozonation of Kraft Pulp Mill Effluent

The Kraft pulp mill effluent was withdrawn from a stilling basin that followed a two-stage aerated lagoon treatment. The average characteristics of the raw pulp mill effluent are shown in Table 11.2.

Table 11.2 Kraft pulp mill effluent average characteristics.

Raw pulp mill effluent parameters	**Average concentrations**
Colour (TCU)	1129
AOX (mgL^{-1})	9.6
COD (mgL^{-1})	671
TOC (mgL^{-1})	268
BOD_5 (mgL^{-1})	16.5
pH	7.7

The ozonation tests were conducted in a semibatch-flow mode. A detailed schematic of the experimental set-up is shown in Figure 11.3. The ozone contactor was made from PVC with an inside diameter of 570 mm and a total height of 900 mm. The headspace was restricted to only 6 % of the total reactor volume to shorten the lag-time for the ozone off-gas to travel in the exhaust line to the ozone off-gas monitor. An average volume of 2.1×10^{-1} m^3 of Kraft pulp mill effluent was pumped into the reactor. Ozone gas was generated from extra-dry pure oxygen using a corona discharge ozone generator (model GLS-7, PCI-WEDECO®). The ozone generator was allowed to stabilize for about 1,800 s in order to obtain a stable ozone concentration.

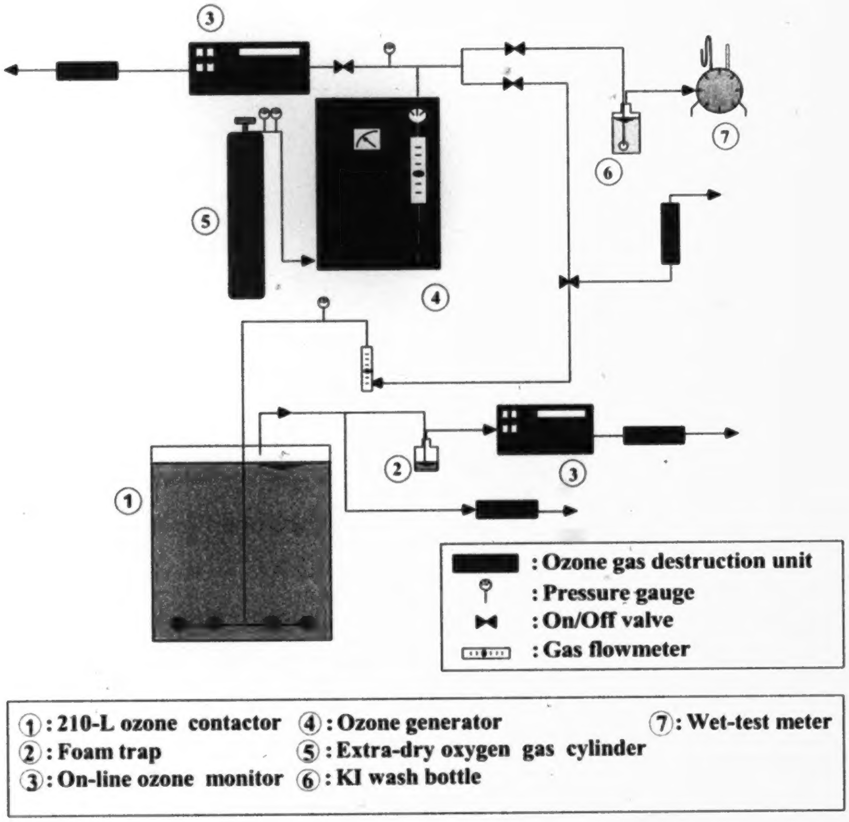
③
⑦
⑥
⑤
④
②
③
①
▬ : Ozone gas destruction unit
: Pressure gauge
⋈ : On/Off valve
: Gas flowmeter
①: 210-L ozone contactor
②: Foam trap
③: On-line ozone monitor
④: Ozone generator
⑤: Extra-dry oxygen gas cylinder
⑥: KI wash bottle
⑦: Wet-test meter

Figure 11.3 Schematic of the ozonation system set-up.

The feed gas that contained 4.4 to 8.3 % w/w ozone was sparged into the liquid phase through a set of eight extra-coarse diffusers (95 mm x 15 mm) equally spaced over the cross-sectional area of the contactor and elevated about 10 mm from the bottom of the contactor to provide better contact between the gas bubbles and the liquid phase. During the ozonation tests, the feed-gas flowrate ranged from 2.7 x 10^{-4} to 3.3 x 10^{-4} m^3s^{-1} and the ozone concentrations in the feed gas and off gas were continuously monitored using PCI-WEDECO® ozone monitors (models HC400 and LC, respectively). The monitors were allowed at least 900 s to stabilize before registering their readings. Periodic calibration of the ozone monitors was conducted using the KI method (APHA-AWWA-WEF, 1995). The amount of the utilized ozone ranged from 0 to 300 mgL^{-1}.

11.3 RESULTS AND DISCUSSION

11.3.1 Digital Photographic Measurements

The rise velocity of bubble swarms was measured to be in the range of 2.4 x 10^{-1} to 3.0 x 10^{-1} ms^{-1}. Similar ranges of bubble rise velocity were obtained by several researchers who investigated the hydrodynamics of gas bubbles in air-water systems (Kaštánek *et al.*, 1993). The photographic images revealed that the majority of the bubbles had an oblate ellipsoidal shape as shown in Figures 11.4 to 11.6. Therefore, the bubble diameter (d_B) was calculated as the arithmetic mean of the maximum and minimum diameters of the bubbles. The angle between the major axis of the bubble and the horizontal direction was defined as ϕ and it was generally $\leq 90^o$ (see Figure 11.7). The maximum diameter was measured along the major axis of the bubble while the minimum diameter was measured along the minor axis of the bubble as shown in Figure 11.7.

For all operating conditions, the mean d_B ranged from about 1,400 μm to 2,200 μm and an increase in u_G caused d_B to increase while an increase in u_L caused d_B to decrease. Yamashita *et al.* (1978) observed in their photographic study of the gas bubbles in an air-water system that although most of the bubbles were oblate ellipsoids rather than spheroids, d_S and d_B were almost identical. Therefore, it can be reasonably assumed that d_B obtained in the current photographic study is an indicator of, if not equal to, d_S.

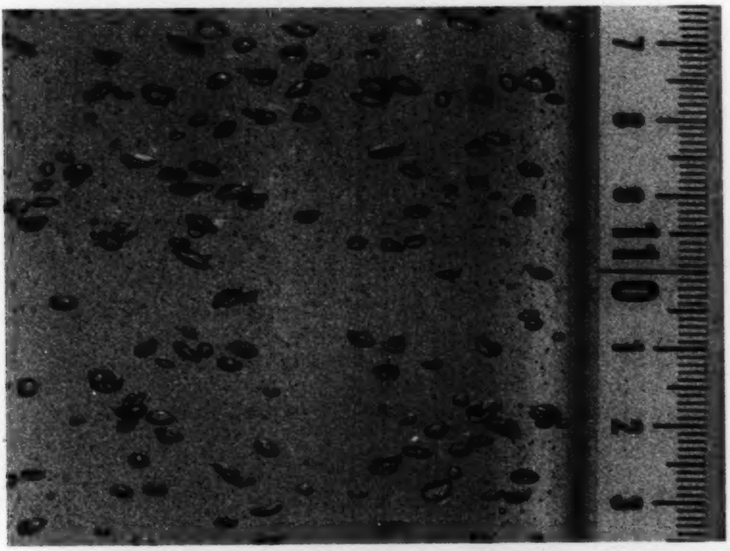

Figure 11.4 A digital image of the air bubbles at $u_L = 7.7 \times 10^{-3}$ ms^{-1} and $u_G = 1.0 \times 10^{-3}$ ms^{-1}.

Figure 11.5 A digital image of the air bubbles at $u_L = 7.7 \times 10^{-3}$ ms^{-1} and $u_G = 7.8 \times 10^{-3}$ ms^{-1}.

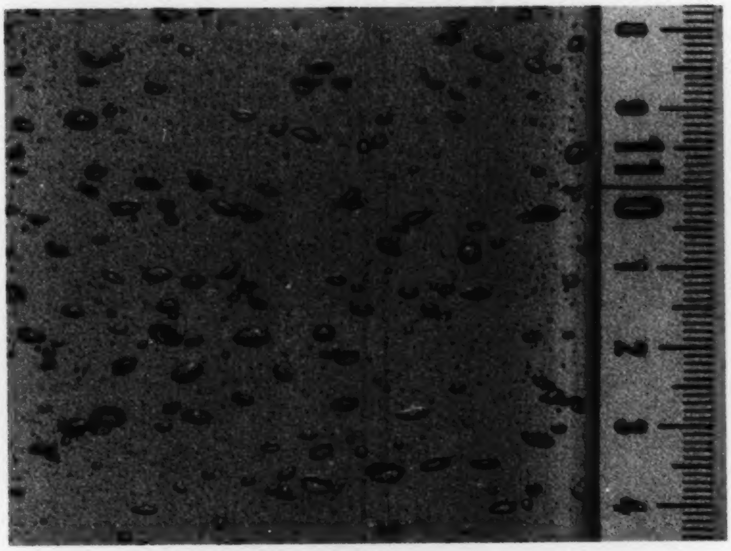

Figure 11.6 A digital image of the air bubbles at $u_L = 1.9 \times 10^{-2}$ ms^{-1} and $u_G = 8.7 \times 10^{-4}$ ms^{-1}.

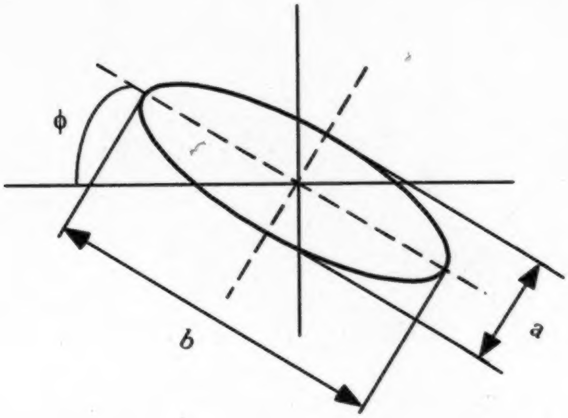

Figure 11.7 Definition of angle ϕ.

11.3.2 Particle Dynamics Analyzer Measurements

11.3.2.1 Deionized Water

Figure 11.8 depicts the effects of the superficial gas and liquid velocities (u_G and u_L, respectively) on the count mean and Sauter mean bubble diameters (d_B and d_S, respectively). The gas phase was sparged under positive pressure, i.e., in the injection mode. The values of u_L and u_G reported in this study were calculated as follows:

u_L = liquid flowrate/cross-sectional area of the straight section of the impinging-jet bubble column; and

u_G = feed-gas flowrate/ cross-sectional area of the straight section of the impinging-jet bubble column.

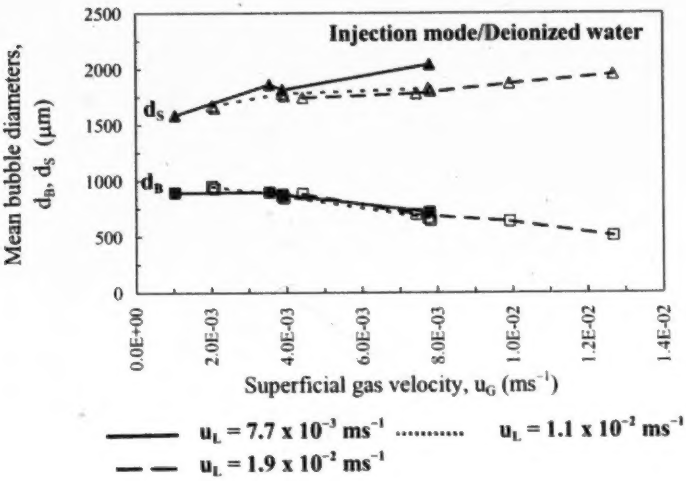

Figure 11.8 Effects of u_G and u_L on d_B and d_S in deionized water.

As shown in Figure 11.8, at $u_G \leq 4.0 \times 10^{-3}$ ms^{-1} and as u_L increased, the rate of decrease in d_B per increase in u_G was lower than that at $u_G \geq 4.0 \times 10^{-3}$ ms^{-1}. At $u_G \geq 4.0 \times 10^{-3}$ ms^{-1}, the rate of decrease in d_B per increase in u_G was almost the same for different u_L's. A similar phenomenon was observed by Zhou and Smith (2000). Meanwhile, as u_L increased, d_S decreased. Alternatively, as u_G increased, d_S increased almost proportionally as observed before in the study of Unno and Inoue (1980) that involved measurements of the sizes of bubbles produced from an orifice mixer that was placed at the bottom of a bubble column. In the impinging-jet bubble column, it was observed that as u_L increased, the turbulence intensity and turbulent shear stresses increased. Consequently, this resulted in higher shearing of the large gas bubbles into smaller bubbles. Therefore, the mean d_B

and d_S decreased and they were smaller than those observed before in the studies of Zhou and Smith (2000) and Roustan *et al.* (1996) that were conducted in conventional bubble columns. As indicated earlier by the photographic study, most of the bubbles were ellipsoids rather than spheroids. Therefore, the value of d_B, obtained in the PDA study, was dependent on the local curvature of the scattering surface of the bubble and the orientation of the bubble with respect to the optical measurement volume. The same observation was reported before by Stanley and Nikitopoulos (1996) when they investigated the effects of the hydrodynamics of an upward gas-liquid jet on the bubble size. Therefore, the value of d_B, obtained in the PDA study, is not a true measure of the actual count mean bubble diameter of an oblate ellipsoidal bubble. The value of d_B, obtained in the PDA study, ranged from 500 to 950 μm. Under similar operating conditions to those used in the photographic study, the value of d_S, obtained in the PDA study, ranged from 1,585 to 2,040 μm. These values were in good agreement with those obtained in the photographic study. Similar trends were observed when the gas phase was sparged under vacuum or negative pressure, i.e., in the ejection mode.

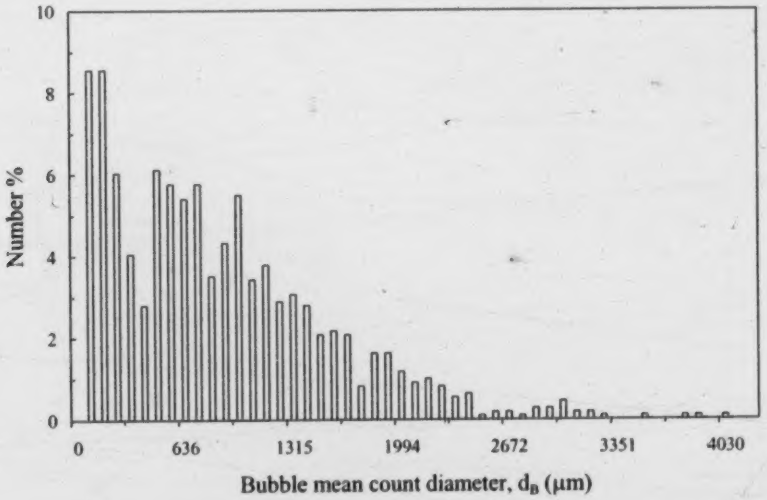

Figure 11.9 A typical plot of the count-based bubble size distribution in deionized water at high u_G and low u_L.

Figures 11.9 to 11.11 present typical plots of the count bubble size distributions in terms of the number %, volume %, and surface area %, respectively, in one of the tests (TR8) conducted in the injection mode. TR8 was conducted at u_L of 7.7×10^{-3} and u_G of 3.9×10^{-3} ms^{-1}. Under the above operating conditions, d_B was equal to 874 µm. The count-based size distribution was skewed to the side of small bubbles as compared to a normal distribution and it could be represented by a gamma or log-normal density function. The same phenomenon was reported by Varley (1995) who studied the bubble size characteristics in an aeration tank using a submerged gas-liquid jet.

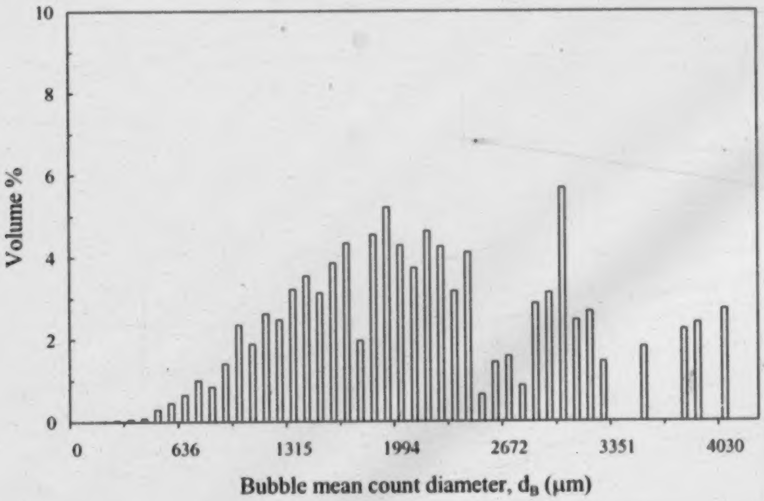

Figure 11.10 A typical plot of the volume-based bubble size distribution in deionized water at high u_G and low u_L.

The volume-based size distribution was skewed to the side of large bubbles as compared to a normal distribution and it could be represented by a gamma or log-normal density function. The same phenomenon was reported before in the study of Zhou and Smith (2000) that involved PDA measurements of bubble sizes in a conventional fine-diffuser bubble column. The difference in skews between the count and volume-based size distributions could be explained by the larger contribution of large bubbles to the overall fractional gas volume in the dispersed flow compared to small bubbles. The surface area-based size distribution was slightly skewed to the side of small bubbles suggesting that small bubbles contributed larger surface area compared to large bubbles. Similar observations were obtained in the experiments conducted in the ejection mode.

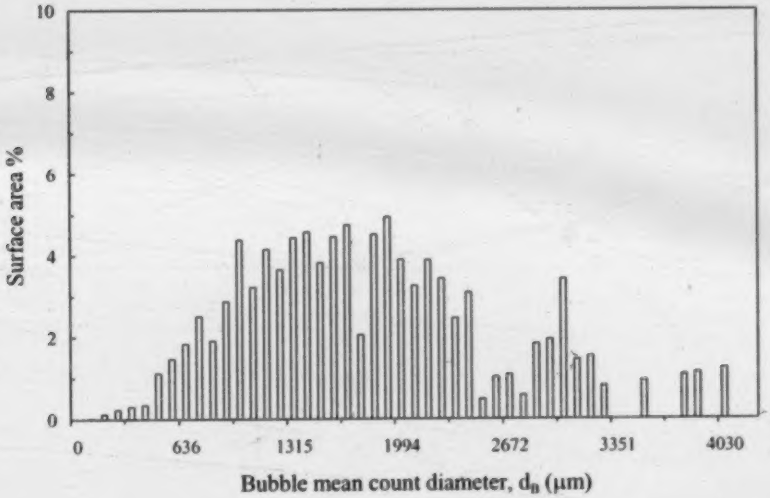

Figure 11.11 A typical plot of the surface area-based bubble size distribution in deionized water at high u_G and low u_L.

Figure 11.12 presents a typical plot of the count bubble size distributions in terms of the number % in one of the tests (TR56) conducted in the injection mode. TR56 was conducted at u_L of 7.7 x 10^{-3} and u_G of 1.0 x 10^{-3} ms^{-1}. In TR56, the mean d_B was equal to 892 μm. u_G was higher in TR56 than in TR8. As a result and compared to TR8, the count-based size distribution was skewed to the side of small bubbles but to a lesser extent, the distribution had a shape close to that of a skewed normal distribution, the peak of the distribution was higher, and d_B was higher.

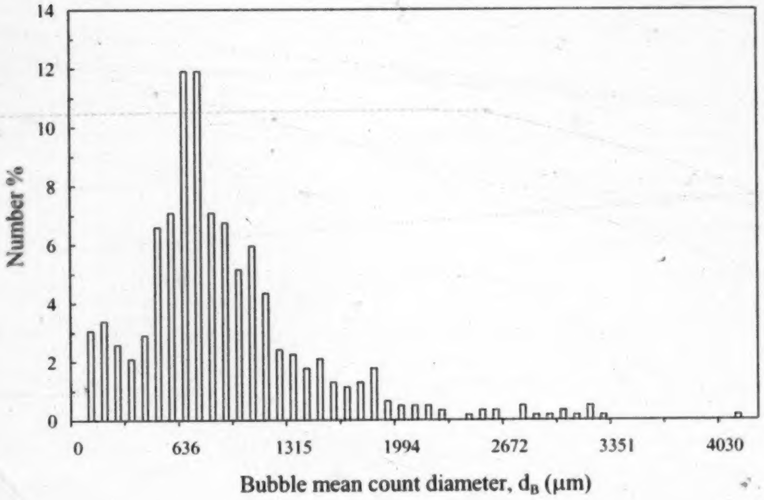

Figure 11.12 A typical plot of the count-based bubble size distribution in deionized water at low u_G and low u_L.

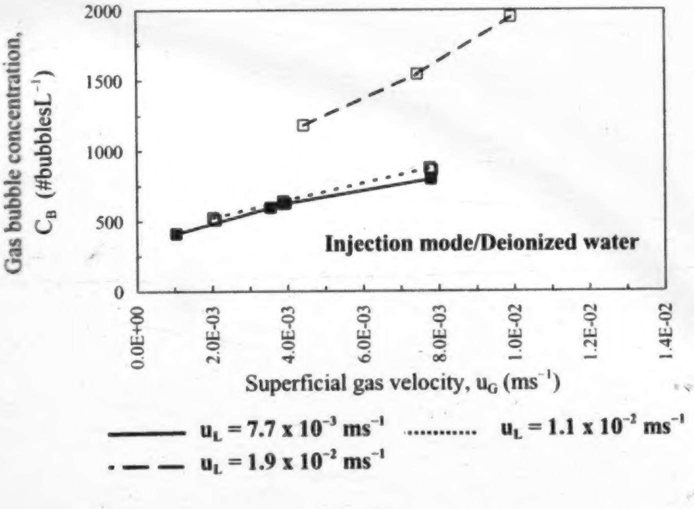

Figure 11.13 Effects of u_G and u_L on C_B in deionized water.

The effects of u_G and u_L on the concentration of the bubbles (C_B) are shown in Figure 11.13. C_B increased almost proportionally with the increase in u_G and u_L. The rate of increase in C_B per increase in u_L was higher than the rate of increase in C_B per increase in u_G. This could have been a result of a high shearing of the large gas bubbles caused by the increase in u_L. Similar trends were observed during the experiments conducted in the ejection mode.

During the experiments conducted in the injection mode and as shown in Figure 11.14, it was observed that the gas-phase turbulence % in the axial direction (i.e., the root mean square (RMS) velocity divided by the mean axial velocity) increased almost linearly as u_G increased. Meanwhile as u_L increased from 7.7 x 10^{-3} to 1.9 x 10^{-2} ms^{-1} and at $u_G \leq 4.5$ x 10^{-3} ms^{-1}, the turbulence % in the axial direction generally increased. Although the turbulence intensity in the liquid phase was not measured, it was expected that since the turbulence levels in the gas phase were high, the liquid phase would as well exhibit high levels of turbulence. The increase in turbulence % could be a result of the gas-liquid flow being in the bubbly flow regime due to the low u_G encountered in this range of operating conditions.

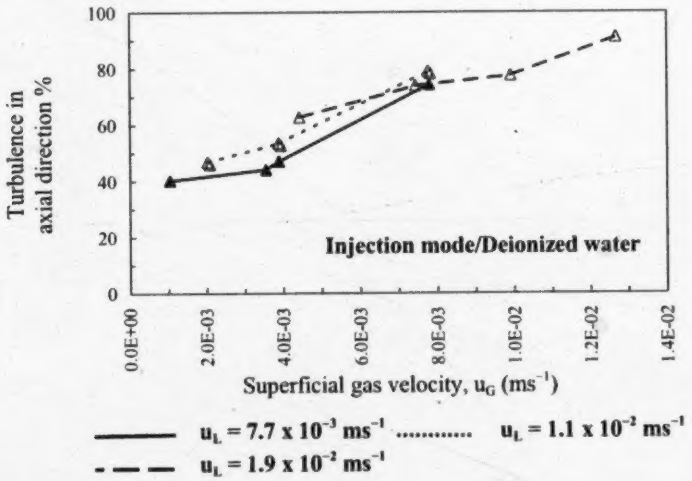

Figure 11.14 Effects of u_G and u_L on the gas-phase axial turbulence % in deionized water.

The latter phenomenon could be a result of the decrease in the Sauter mean diameter of the bubbles, and consequently, that could have caused an increase in the entrainment of the surrounding liquid by the rising gas bubbles that carried the entrained liquid upwards. Therefore, the circulation flow pattern could have increased and caused more turbulence in the dispersed flow. At $u_G \geq 4.5 \times 10^{-3}$ ms^{-1}, the turbulence % in the axial direction decreased gradually as u_L increased. This could be a result of the gas-liquid flow approaching a homogeneous bubbly flow regime that is usually characterized by its high bubble concentration. Also, a somewhat uniform bubble rise velocity distribution was observed. This could have led to the rising of the bubbles without much of mutual bubble interferences, thus, leading to somewhat uniform degrees of axial and radial distributions of gas hold-up and a low degree of turbulence in the axial direction. Similar phenomenon was reported by (Kaštánek *et al.*, 1993). The gas sparging mode had no effect on the dependency of turbulence % on u_G and u_L.

Figure 11.15 depicts typical plots of the probability density distributions of the axial bubble rise velocity (u) as well as the radial velocity (v) for two different tests (TR8 and TR10) that were conducted in the injection mode (i.e., the gas phase was sparged under positive pressure). TR8 was conducted at u_L of 7.7×10^{-3} and u_G of 3.9×10^{-3} ms^{-1} while, TR10 was conducted at u_L of 1.9×10^{-2} and u_G of 4.4×10^{-3} ms^{-1}. The velocity profiles were normally distributed as shown in Figure 11.15. The mean radial velocity (v) was 1.2×10^{-3} and 1.1×10^{-3} ms^{-1} in TR8 and TR10, respectively. The radial velocity profiles confirmed the existence of a circular flow pattern in the bubble column as suggested before by Deckwer (1992). The circular flow pattern is a result of the liquid phase dispersion caused by the entrainment of the surrounding liquid by the rising gas bubbles that carry the entrained liquid upwards (Deckwer, 1992). The mean axial bubble rise velocity (u) was 3.1×10^{-1} and 2.9×10^{-1} ms^{-1} in TR8 and TR10, respectively. Since u_G was almost constant between the two runs and as u_L increased, u decreased and the spread of the profile was narrowed. In the impinging-jet bubble column, it was observed that as u_L increased, the gas-phase axial turbulence % increased (at $u_G \leq 4.5 \times 10^{-3}$ ms^{-1}) causing the turbulent shear stresses to increase considerably. Consequently, this resulted in higher shearing of the large gas bubbles into smaller bubbles, i.e., smaller d_B and as a result, u decreased. Similar trends were observed during the experiments conducted in the ejection mode.

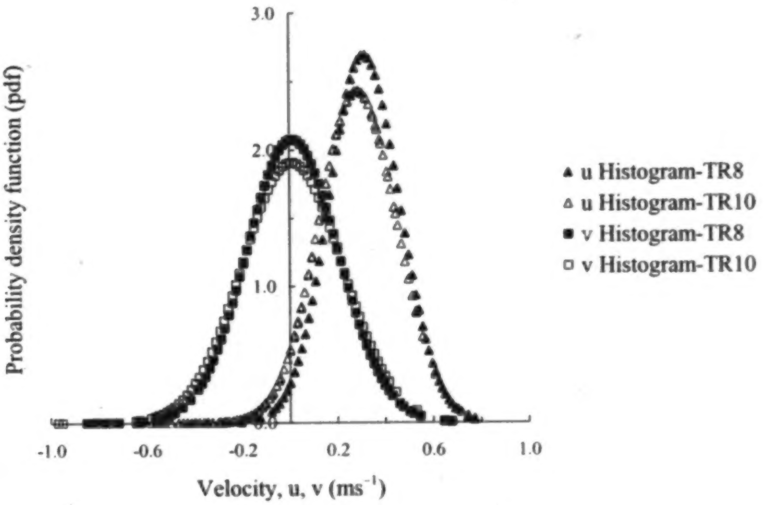

Figure 11.15 Typical probability density distributions of the gas-phase u and v in deionized water.

Figure 11.16 depicts the effects of u_G and u_L on the bubble rise velocity (u) during the experiments conducted in the injection mode. As u_G increased up to about 4.0 x 10^{-3} ms^{-1}, changes in u_L had no effect on u. This could be explained by the gas-liquid flow being in the bubbly flow regime as discussed earlier. Then, as u_L increased and at $u_G >$ 4.0 x 10^{-3} ms^{-1}, u started to decrease gradually until it reached asymptote at u_G of about 1.0 x 10^{-2} ms^{-1} as a result of the gas-liquid flow approaching a homogeneous bubbly flow regime. Similar observations were reported by Deckwer (1992). When the experiments were conducted in the ejection mode, similar trends of the dependency of u on u_G and u_L were observed.

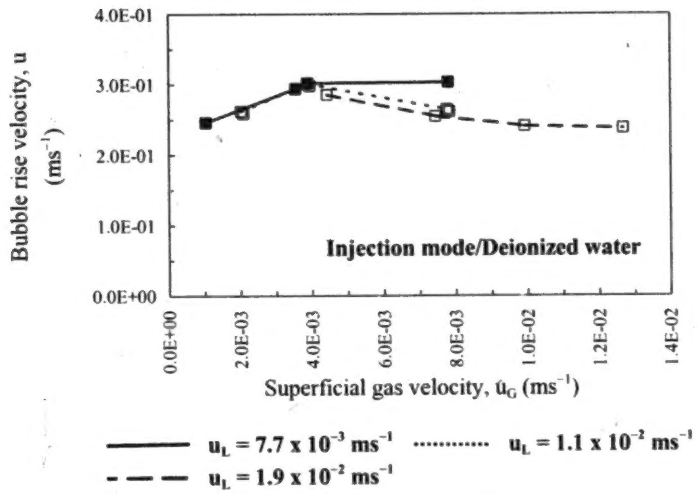

Figure 11.16 Effects of u_G and u_L on u in deionized water.

Figure 11.17 presents the effects of u_G and u_L on the gas hold-up (ε_G). The gas hold-up was estimated based on the bubble concentration (C_B) and the count mean bubble diameter (d_B) measurements. As shown in Figure 11.17, ε_G increased proportionally with the increase in u_G as reported before by several researchers (Deckwer, 1992; Kaštánek *et al.*, 1993; Roustan *et al.*, 1996; Zhou and Smith, 2000). This phenomenon was a result of the decreased bubble size as u_G and u_L increased, and thus, leading to a longer bubble residence time in the bubble column. Also, as u_L increased, an increase in ε_G occurred due to the smaller bubble size that resulted from the increase in the shearing of the large gas bubbles into smaller bubbles.

As shown in Figure 11.18, an increase in u_G and u_L led to a proportional increase in the gas bubbles' specific interfacial area (a). This could be a result of the increase in ε_G as u_G and u_L increased. The same phenomenon was reported by (Zhou and Smith, 2000). Once more, there was no observed effect of the gas sparging mode on the dependency of ε_G and a on u_G and u_L.

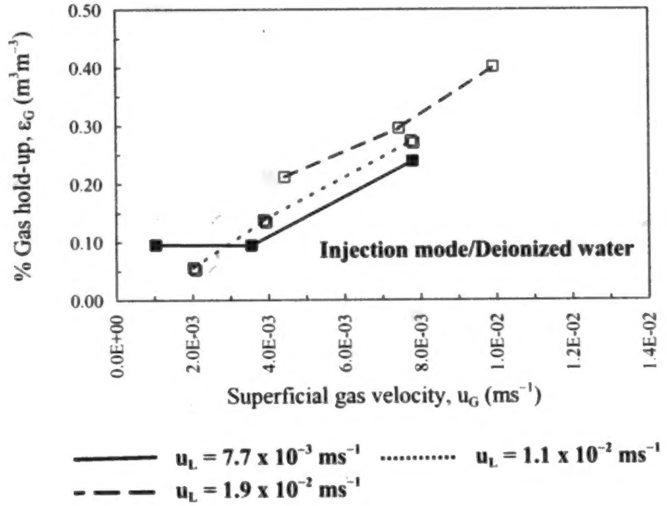

Figure 11.17 Effects of u_G and u_L on ε_G in deionized water.

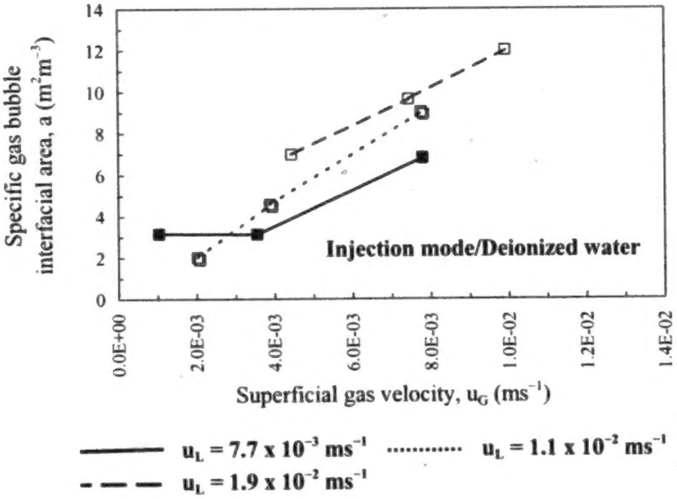

Figure 11.18 Effects of u_G and u_L on a in deionized water.

11.3.2.2 Kraft pulp mill effluent

Kraft pulp mill effluents contains surfactants, or referred to as surface active agents (SAA's), and other organic and inorganic compounds that can affect the liquid viscosity and the bubble surface tension. These effects depend on the type, concentration, and chemical structure of such compounds. The organic compounds can be divided into two main groups (Voigt and Schügerl, 1979): polar organic compounds with low molecular weight; and polar organic compounds with high molecular weight. The SSA's tend to accumulate at the gas-liquid interface with their hydrophobic groups positioned towards the gas phase (Zhou and Smith, 2000). As a result, the surface tension at the interface will be lower than the surface tension in the bulk liquid. Therefore, the surface tension gradient across the liquid film, surrounding the gas bubble, will be higher than that in the bulk liquid leading to a decrease in the size of the gas bubbles. Also, the SAA's can cause damping of the turbulence intensity at the gas-liquid interface and that will lead to a suppression of the coalescence of the mutually contacting gas bubbles (Kaštánek *et al.*, 1993). The coalescence suppressing effect is smallest during the bubble formation and increases as the contact time between the gas phase and the liquid phase increases (Voigt and Schügerl, 1979). The higher the molecular weight of the polar organic compounds, the stronger the suppression of the coalescence but the longer it takes the coalescence suppressing effect to increase as the age of the bubble increases inside the bubble column.

In contrast to the SAA's, the inorganic (i.e., salt) compounds exhibit a different effect on the coalescence suppression (Voigt and Schügerl, 1979). In inorganic solutions, the concentration of the salt compounds in the bulk liquid is the same as that at the gas-liquid interface. This is a result of the liquid phase immediately forming a liquid film around the gas bubble following the bubble formation, therefore, the gradient in the salt concentration between the bulk liquid and at the gas-liquid interface begins to decrease over time. As a result, the salt compounds have their maximum coalescence suppressing effect at the initial stage of the bubble formation and this effect starts to decrease as the age of the gas bubble inside the bubble column increases (Voigt and Schügerl, 1979).

Regarding the effects of the superficial gas and liquid velocities (u_G and u_L, respectively) on the count mean bubble diameter (d_B), the Sauter mean bubble diameter (d_S), the gas bubble concentration (C_B), the gas-phase axial turbulence intensity, the gas bubble rise velocity (u), the gas hold-up (ε_G), and the gas bubbles' specific interfacial area (a), similar trends of those effects were observed when the PDA measurements were conducted during the aeration of the raw Kraft pulp mill effluent as well as the ozonated effluent.

The effects of u_G and u_L on d_B and d_S during the aeration of raw Kraft pulp mill effluents (i.e., $\Delta O_3 = 0.0$ mgL^{-1}) are shown in Figure 11.19. As u_G increased, the Sauter mean diameter increased at a rate similar to that observed during the aeration experiments conducted in the deionized water. Also, as u_L increased, d_S decreased at a rate similar to that observed in the deionized water. Interestingly, during the aeration of the raw Kraft pulp mill effluent, and as u_G increased, d_B increased slightly then it started decreasing. This phenomenon could be a result of the low coalescence suppressing effect of the SAA's due to the short gas bubble residence time in the column that resulted from the increase in the bubble rise velocity (u) as u_G increased up to 4.0×10^{-3} ms^{-1}.

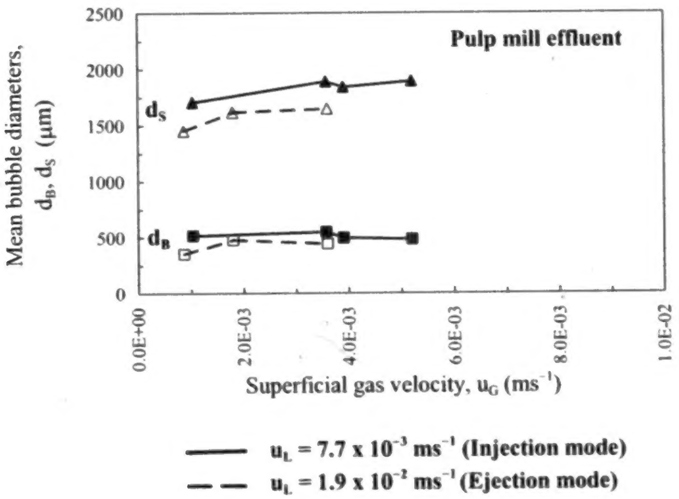

Figure 11.19 Effects of u_G and u_L on d_B and d_S in raw Kraft pulp mill effluent.

As observed during the aeration of the deionized water and at $u_G > 4.0 \times 10^{-3}$ ms^{-1}, u started to decrease and that led to an increase in the gas bubble residence time.

Consequently that might have caused an increase in the coalescence suppressing effect of the SAA's, and as a result, d_B started decreasing. Alternatively, during the aeration of the ozonated Kraft pulp mill effluents, the effect of u_G on d_B was similar to that observed in the deionized water. Generally, the effect of increasing u_L on decreasing d_B, during the aeration of the raw and the ozonated Kraft pulp mill effluents, was higher than that observed during the aeration of deionized water. This effect gradually decreased as the amount of the utilized ozone (ΔO_3) increased, possibly due to the increase in the partial or complete oxidation and/or destruction of the surfactants and the inorganic compounds that were present in the raw Kraft pulp mill effluent. The measured d_B and d_S in the raw and ozonated Kraft pulp mill effluents were smaller than those obtained in conventional diffuser bubble columns that were tested in the study of Zhou and Smith (2000).

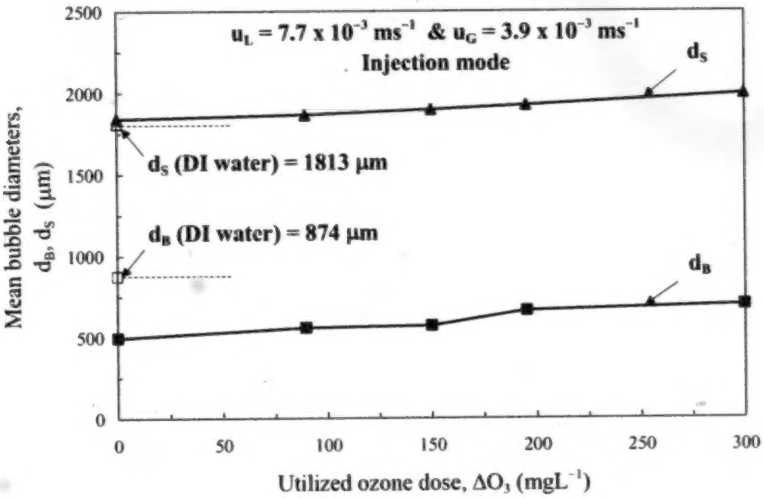

Figure 11.20 Effects of ΔO_3 on d_B and d_S in Kraft pulp mill effluent.

The effects of ΔO_3 on d_B and d_S, for one set of u_G and u_L in the injection mode, are presented in Figure 11.20. As ΔO_3 increased from 0 to 300 mgL^{-1}, d_S increased by almost 8 % (from 1,840 to 1,990 μm) and d_B increased by almost 41 % (from 495 to 700 μm). As shown in Figure 11.20, d_S was virtually identical in both the deionized water and the raw Kraft pulp mill effluent. Meanwhile, d_B in the deionized water was almost two times larger than that in the raw Kraft pulp mill effluent.

The rate of increase in C_B per increase in u_G was doubled and the rate of increase in C_B per increase in u_L was almost identical in the raw Kraft pulp mill effluent compared to the deionized water. The effects of u_G and u_L on C_B are shown in Figure 11.21. Generally, based on the PDA measurement and visual observations, the gas-liquid flow during the aeration of Kraft pulp mill effluent could be characterized as a homogeneous bubbly flow and the degree of homogeneity decreased as ΔO_3 increased. Under similar operating conditions, the higher homogeneity of the bubbly flow in the raw Kraft pulp mill effluent compared to the deionized water could be a result of the lower d_B and d_S, and the higher C_B observed in the raw Kraft pulp mill effluent. As a result of the lower d_B in the raw Kraft pulp mill effluent and under the same operating conditions, the bubble rise velocity (u) decreased by about 50 % compared to that in the deionized water. Therefore, lower d_B and d_S, higher C_B, and lower u caused the gas hold-up (ε_G) and the gas bubbles' specific interfacial area (a) to increase and they were about four times higher than those in the deionized water.

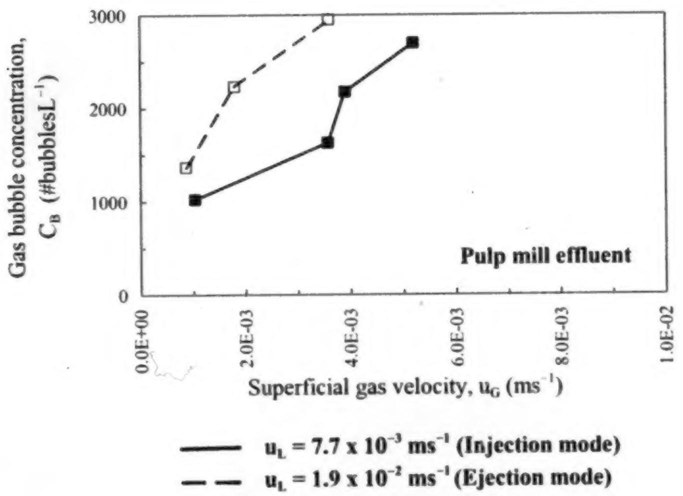

Figure 11.21 Effects of u_G and u_L on C_B in raw Kraft pulp mill effluent.

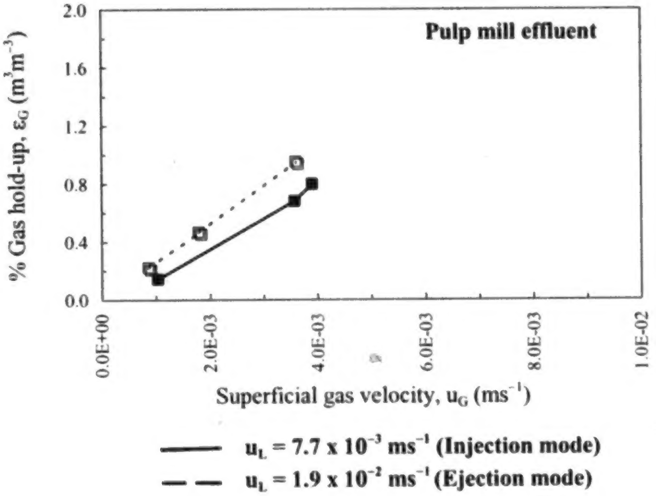

Figure 11.22 Effects of u_G and u_L on ε_G in raw Kraft pulp mill effluent.

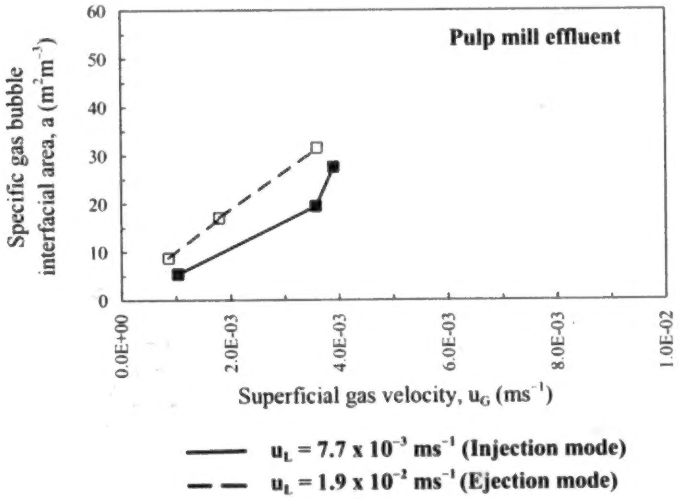

Figure 11.23 Effects of u_G and u_L on a in raw Kraft pulp mill effluent.

The effects of u_G and u_L on ε_G and a are shown in Figures 11.22 and 11.23, respectively. Under the same operating conditions, the rates of increase in ε_G and a per increase in u_G were almost four times higher in the raw Kraft pulp mill effluent compared to the deionized water. In the raw Kraft pulp mill effluent, at low superficial liquid velocity (u_L) and at either low or high superficial gas velocity (u_G), the count-based bubble size distributions exhibited different trends from those observed in the deionized water. Figure 11.24 depicts the count-based bubble size distribution in a test (TR28) that was conducted at low u_G (1.0×10^{-3} ms^{-1}) and low u_L (7.7×10^{-3} ms^{-1}). Figure 11.25 depicts the count-based bubble size distribution in a test (TR52) that was conducted at high u_G (3.6×10^{-3} ms^{-1}) and low u_L (7.7×10^{-3} ms^{-1}). The measured d_B was equal to 516 and 549 μm, in TR28 and TR52, respectively. The distributions were somewhat bimodal and skewed to the side of small bubbles as compared to a normal distribution. Under the same u_L, an increase in u_G caused a shift of the low peak towards the side of large bubbles and a decrease in the magnitude of the high peak. Interestingly, at low u_G and as u_L increased, the low peak observed before at low u_L, diminished possibly due to the shearing of the large gas bubbles into smaller bubbles, and consequently, the mean d_B decreased. This phenomenon is presented in Figure 11.26. As u_L increased from 7.7×10^{-3} (in TR28) to 1.9×10^{-2} ms^{-1} (in TR37) and at almost similar u_G (1.0×10^{-3} ms^{-1} in TR28 and 8.6×10^{-4} ms^{-1} in TR37), the mean d_B decreased from 516 to 351 μm.

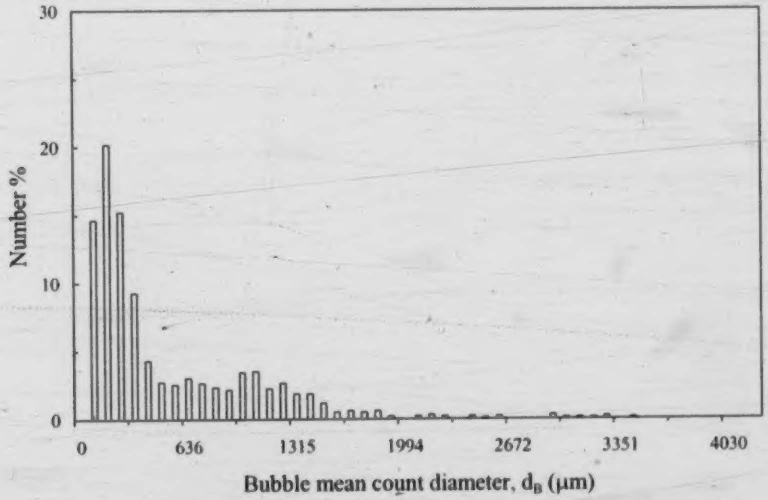

Figure 11.24 A typical plot of the count-based bubble size distribution in raw Kraft pulp mill effluent at low u_G and low u_L.

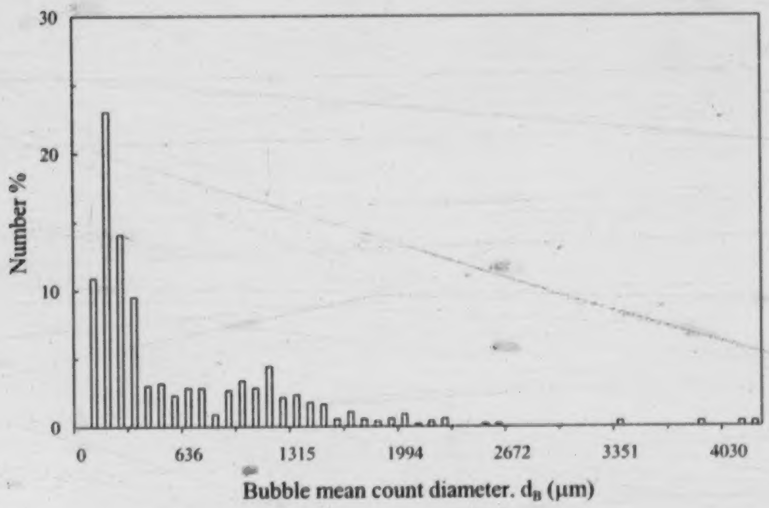

Figure 11.25 A typical plot of the count-based bubble size distribution in raw Kraft pulp mill effluent at high u_G and low u_L.

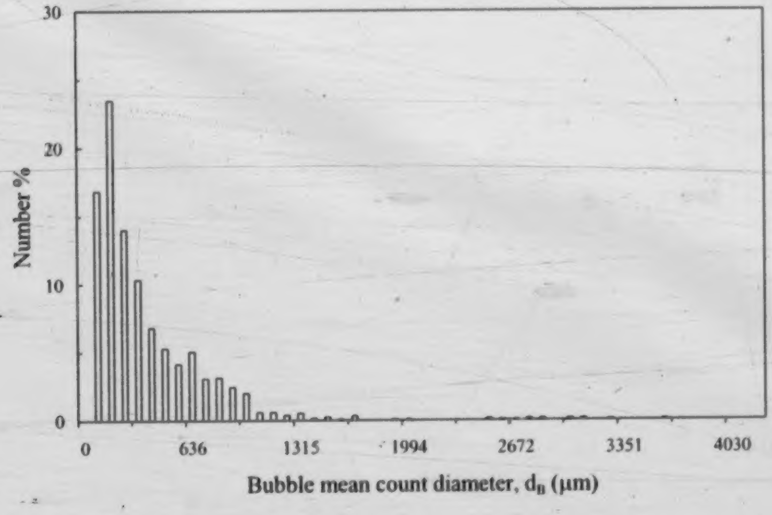

Figure 11.26 A typical plot of the count-based bubble size distribution in raw Kraft pulp mill effluent at low u_G and high u_L.

11.4 CONCLUSIONS

The two-phase (i.e., gas-liquid) flows are sensitive to any disturbances caused by intrusive measuring devices such as electric probes. Therefore, the 2-D laser and phase Doppler anemometry and the digital photographic measurement techniques provided great non-intrusive tools for characterization and better understanding of the gas bubbles in the impinging-jet bubble column. The digital photographic study provided valuable information on the shape and size of the gas bubbles as well as rough estimates of the bubble rise velocity that aided in optimizing the particle dynamics analyzer configuration and operational settings during the PDA study.

The PDA provided rapid and accurate simultaneous measurements of the bubble size, bubble rise velocity, bubble size distribution, and turbulence intensities in an impinging-jet bubble column that utilized two venturi injectors to create turbulent gas-liquid jets in the ambient fluid.

The intersecting of the gas-liquid jets caused an increase in the turbulence produced in the ambient fluid and as a result the count mean bubble diameter and the Sauter mean bubble diameter decreased and they were smaller than those obtained in conventional bubble columns. This has led to a significant increase in the gas bubbles' specific interfacial area compared to that in conventional bubble columns.

The count mean bubble and Sauter mean bubble diameters were found to be dependent on the superficial gas and liquid velocities. As u_L increased, d_S decreased slightly. During the aeration of the deionized water and increasing u_G caused a slight decrease in d_B. Meanwhile, d_B increased slightly then it started decreasing as u_G increased during the aeration of the raw Kraft pulp mill effluent. During the aeration of ozonated Kraft pulp mill effluent and as u_G increased, d_B decreased. The count and the Sauter mean bubble diameters were smaller in the raw Kraft pulp mill effluent compared to those in the deionized water. This has led to a significant increase in the gas bubbles' specific interfacial area and the gas hold-up compared to those in the deionized water. As the raw

Kraft pulp mill effluent was ozonated and the amount of utilized ozone increased, the count mean and Sauter mean bubble diameters increased.

The bubble size distributions exhibited different trends depending on the type of the test liquid and on the operating conditions in terms of the superficial gas and liquid velocities. Generally, those distributions could be well described using normal, gamma, or log-normal density functions.

The measurements of the gas hold-up and the gas bubbles' specific interfacial area obtained in the current study provided valuable information that will lead to a better understanding of the mass transfer process in clean environments such as deionized water as well as in highly reactive environments such as Kraft pulp mill effluents.

11.5 REFERENCES

1. APHA-AWWA-WEF, *Standard Methods for the Examination of Water and Wastewater, 19th Ed. American Public Health Association, American Water Works Association, and Water Environment Federation* (Washington, DC, USA: American Public Health Association, 1995).
2. Akita, K. and F. Yoshida, "Bubble Size, Interfacial Area, and Liquid-Phase Coefficient in Bubble Columns", Ind. Eng. Chem., Proc. Des. Develop. 3: 84-91 (1974).
3. DANTEC, *Particle dynamics analyzer: Users manual*, DANTEC (1989).
4. Deckwer, W.-D., *Bubble Column Reactors*, Cottrell V. (Trans.), Field R.W. (Ed.) (Chichester, England: John Wiley & Sons Ltd, Inc., 1992).
5. Gamal El-Din, M. and D.W. Smith, "Modeling the Ozonation Process in an Impinging-Jet Bubble Column", *Proc. 7th Environ. Eng. Specialty Conf., 29th Annual CSCE Conf.*, Victoria, BC, Canada, 2001.
6. Jamialahmadi, M. and H. Müller-Steinhagen, "Effect of Superficial Gas Velocity on Bubble Size, Terminal Bubble Rise Velocity and Gas Hold-Up in Bubble Columns", Develop. Chem. Eng. 1: 16-31 (1992).
7. Kaštánek, J., J. Zahradník, J. Kratochvíl, and J. Čermák, *Chemical Reactors for Gas-Liquid Systems* (Chichester, England: Ellis Horwood, 1993).
8. Mudde, R.F., J.S. Groen, and H.E.A. Van Den Akker, "Application of LDA to Bubbly Flows", Nuc. Eng. & Des. 184: 329-338 (1998).
9. Mudde, R.F., J.S. Groen, and H.E.A. Van Den Akker, "Liquid Velocity Field in a Bubble Column: LDA Experiments", Chem. Eng. Sci. 52: 4217-4224 (1997).
10. Roustan, M., R.Y. Wang, and D. Wolbert, "Modeling Hydrodynamics and Mass Transfer Parameters in a Continuous Ozone Bubble Column", Ozone Sci. & Eng. 18: 99-115 (1996).
11. Shawwa, A.R., *Rational Approach for Dissolved Air Floatation Contact Zone Modeling: Ph.D. Thesis* (Edmonton, AB, Canada: University of Alberta, 1998).
12. Stanley, K.N. and D.E. Nikitopoulos, "Bubble Measurements in a Gas-Liquid Jet", Chem. Eng. Comm. 143: 1-22 (1996).

13. Unno, H. and I. Inoue, "Size Reduction of Bubbles by Orifice Mixer", Chem. Eng. Sci. 35: 1571-1579 (1980).

14. Varley, J., "Submerged Gas-Liquid Jets: Bubble Size Prediction", Chem. Eng. Sci. 50: 901-905 (1995).

15. Voigt, J. and K. Schügerl, "Absorption of Oxygen in Counter-Current Multistage Bubble Columns-I", Chem. Eng. Sci. 34: 1221-1229 (1979).

16. Yamashita, F., Y. Mori, and S. Fujita, "Sizes and Size Distributions of Bubbles in a Bubble Column-Comparison between the Two Point Electric Probe Method and the Photographic Method", J. Chem. Eng. Japan 12: 5-9 (1978).

17. Zhou, H. and D.W. Smith, "Ozone Mass Transfer in Water and Wastewater Treatment: Experimental Observations Using a 2D-Laser Particle Dynamics Analyzer", Wat. Res. 34: 909-921 (2000).

CHAPTER 12. GENERAL CONCLUSIONS AND RECOMMENDATIONS

12.1 GNERAL OVERVIEW

When designing ozone bubble columns, two major sources of uncertainties usually exist: (1) the measurement techniques and the estimation methods of the various operating parameters; and (2) the application of the pertinent design model. The performance of ozone contactors is controlled by the combined effects of the hydrodynamics, ozone mass transfer, and ozone reactions with the constituents present in the liquid phase. Although great advancements in the area of ozone treatment have been achieved, there is still a great demand for more efficient and compact designs of ozone contactors that can provide higher treatment levels in more compact contactors. If this goal can be achieved, the cost of the ozone treatment process will be significantly lowered. Further more, in order to obtain accurate and reliable modeling of the ozonation process, the development of reliable ozonation process parameters is needed. With the development and estimation of those parameters, a rational design approach that integrates those parameters can be designed for practical use in the design and on-line process control of ozone contactors.

The main scope of this research project was to design a new compact ozone contactor that can provide higher treatment levels than those achieved in the conventional ozone contactor designs. Therefore, an impinging-jet bubble column was designed for ozone treatment applications in the area of water and wastewater treatment. The venturi injectors were utilized to create turbulent gas-liquid jets in the ambient fluid by placing them at an intersecting angle of 125° and the distance between the centers of the nozzles was set equal to 60 mm. The main reason for this particular design was to increase the turbulence produced in the ambient fluid and therefore, increase the ozone mass transfer rates.

A number of models were developed for modeling the hydrodynamics and the overall ozonation process in ozone bubble columns. Transient Back flow cell model

(BFCM) was developed as an alternative approach to describe the hydrodynamics of ozone bubble columns. Transient BFCM, when compared to the traditionally used models such as transient ADM or CFSTR's in-series model, represents a flexible, reliable, accurate, and more importantly simple method to describe the backmixing in the liquid phase in bubble columns. The steady-state two-phase axial dispersion model (2P-ADM) and back flow cell model (BFCM) were developed and applied for modeling the ozonation process in ozone bubble columns. A simple and easy-to-use, yet accurate and reliable design model was developed. This model is a modified non-isobaric steady-sate one-phase axial dispersion model (1P-ADM). The 1P-ADM is different from the 2P-ADM in its simple use for practical design and process control of full-scale ozone contactors.

In order to model the ozonation process when applied for treating wastewaters such as Kraft pulp mill effluents, the experimental results obtained in three different types of ozone contactors were analyzed. The scope was to study the effects of the ozone contactor design, configuration, operating conditions, and scale-up on the: (1) ozonation process induced reduction efficiencies of the color, AOX, COD, and TOC from biologically treated Kraft pulp mill effluents; (2) the increase in the biodegradability of this type of wastewater; and (3) the dynamics of the ozone gas absorption process. Those ozone contactors had different designs, scales, and configurations. The types of the ozone contactors included: (1) an extra-coarse-bubble diffuser ozone contactor; (2) an impinging-jet ozone contactor; and (3) a fine-bubble diffuser ozone contactor.

Finally, a 2-D laser particle dynamics analyzer was used to simultaneously measure the bubble size, bubble rise velocity, bubble size distribution, and turbulence intensities in the impinging-jet bubble column. These measurements were conducted in clean deionized water and in a Kraft pulp mill effluent that was ozonated using a wide range of utilized ozone doses. The purpose of ozonation was to investigate the effects on surface tension by changing the pulp mill effluent characteristics, and consequently, on the bubble size, the gas hold-up (ε_G), and the gas bubbles' specific interfacial area (a).

12.2 CONCLUSIONS

Based on the theoretical and experimental studies conducted in this research program, the following main conclusions can be drawn:

1. As compared to the traditionally used transient ADM and transient CFSTR's in-series model, the transient BFCM can adequately describe the backmixing in the liquid phase in bubble columns over a wide range of operating conditions and under any given boundary conditions. Therefore, it has some advantages over the transient ADM and the transient CFSTR's in-series model. These advantages are as follows: (1) the transient BFCM can account for variable backmixing coefficient (i.e., variable Pe_L) along the column height or along the length of a contacting chamber while predicting simultaneously the RTD curves at various sampling ports; (2) the transient BFCM has the capability to account for variable cross-sectional area along the column height or along the length of a contacting chamber; (3) the analytical solution of the transient ADM for a tracer pulse-input is only available for small deviations from plug flow conditions (Equation 2.11). Therefore, in order to use the solution of transient ADM for a tracer pulse-input under small deviations from plug flow conditions (Equation 2.11) to describe the backmixing in the liquid phase in will lead to inadequate modeling of the hydrodynamics; and (4) the transient BFCM is easy to formulate and solve using a spreadsheet program even for the cases where the mixing parameters are variable along the column height.

2. The number of cells in-series, as one of the mixing parameters to be considered for the transient BFCM simulations, has to be chosen carefully so that the transient BFCM predictions, of the hydrodynamic behaviour in ozone contactors performance under different operating conditions, are closer to the actual backmixing conditions. The transient BFCM should be expanded to account for the backmixing in the gas phase to allow studying the effect of the gas-phase backmixing on the hydrodynamic performance of ozone bubble columns of small

aspect ratios and full-scale ozone contactors where the gas phase can no longer be considered in the plug flow regime.

3. The steady-state BFCM has proven to provide good predictions of the performance of pilot-scale ozone bubble columns. The model predictions should be further tested for different designs and scales of ozone contactors and under different operating conditions. Also, the model should be further expanded to account for variable mass transfer coefficient along the length of the contactor to account for situations where the mass transfer process is enhanced near the entrance of the contactor rather than along the entire contactor length.

4. The two-phase axial dispersion model (2P-ADM) has been developed for describing the performance of ozone bubble columns. Two cases of the model have been developed: (1) the axial dispersion was considered for the liquid and gas phases; and (2) the axial dispersion was considered only in the liquid phase. The main advantage of applying those comprehensive models is to be able to compare between their predictions when used to model the performance of ozone bubble columns. Those models' predictions may vary depending on the bubble column configuration and design as well as the operating conditions. As an example, regarding the effect of bubble column configuration, columns with small aspect ratios might exhibit large gas-phase backmixing that must be accounted for in the model equations. Therefore, most of the models that are currently applied to describe the performance of such ozone contactors are outdated because they are based on inaccurate assumptions with respect to the prevailing liquid and gas-phase flow regimes.

5. The two-phase axial dispersion model (2P-ADM) has proven to be a powerful, accurate and reliable tool for predicting the performance of ozone contactors for both water and wastewater treatment applications. By applying the 2P-ADM instead of the traditionally applied models such as the plug flow model (PFM) or the continuous-flow stirred-tank-reactors (CFSTR's) in-series model, accurate and

reliable designs of ozone contactors can be achieved. As a result, the operating and capital costs will be minimized and the desired treatment objectives can be met.

6. It should be noted that the current model testing is just an initial testing step. Therefore, further studies need to be conducted for both water and wastewater treatment applications and in different ozone contactors of different configurations, designs, and scales. This will help obtain a large and high-quality data set that can allow for further model testing in order to eliminate any uncertainties in the model predictions.

7. The simple version of the 2P-ADM that neglects the backmixing in the gas phase can be applied without affecting the accuracy of the model predictions in situations such as: (1) bubble columns that have large aspect ratios; and (2) when large bubbles are dominant in the gas-liquid flow as a result of using a gas sparging technique that creates large bubbles.

8. A comparison between the 2P-ADM and the BFCM was conducted to test the variability in their predictions of the performance of ozone contactors operating under water or wastewater treatment conditions. Both models have proven to be sufficient and reliable in their predictions of the performance of ozone bubble columns, however, the BFCM was easier to formulate and solve.

9. For wastewater treatment applications and with all the operating conditions being the same, the ADM and the BFCM predicted that the counter-current and the co-current flow modes would exhibit similar characteristics with respect to the dissolved ozone, gaseous ozone, and superficial gas velocity profiles. Changes in the backmixing coefficient, represented by changes in Pe_L, had relatively small effect on the dissolved ozone concentration profiles and virtually no effect on the gaseous ozone concentration and superficial gas velocity profiles. On the other hand, changes in the overall mass transfer coefficient (k_La) had large effects on the

dissolved ozone and gaseous ozone profiles and a very small effect on the superficial gas velocity profiles.

10. The 1P-ADM can be solved analytically while the complete axial dispersion model (2P-ADM) requires an elaborate numerical technique to solve the model's equations. Therefore, describing the analytical solution of the 1P-ADM in terms of a simple spreadsheet program facilitates obtaining the model predictions for any operating conditions represented by the model input parameters entered into the spreadsheet program. Compared to the 2P-ADM predictions of the ozone bubble column performance that was presented in the study of Zhou *et al.* (1994), the 1P-ADM has proven to provide excellent predictions of the performance of ozone bubble columns operating under either water treatment conditions and in both the counter-current and the co-current flow modes. The 1P-ADM also provided good predictions of the performance of ozone bubble columns for the wastewater treatment applications. The 1P-ADM is easy and reliable tool to be used for the design and the process-control of bubble columns' operations.

11. The 1P-ADM was applied to model the measured dissolved and gaseous ozone concentration profiles in the impinging-jet bubble column. The dissolved ozone concentration profiles along the bubble column height, can be well estimated using the one-phase axial dispersion model (1P-ADM) through the use of bubble column average parameters with respect to the overall mass transfer coefficient (k_La), liquid-phase backmixing coefficient (D_L), and coefficient of the gas-phase ozone molar fraction decrease along the column height (a_1). During the ozonation of deionized water, it was found that k_La and D_L were dependent on the liquid and gas superficial velocities and the nature of this dependency varied from the gas injection mode to the gas ejection mode. The gas-phase dimensionless ozone concentration profiles can be well described using an exponential relationship representing the gas-phase ozone molar decrease along the column height. The exponent (a_1) was found to be dependent on the process dimensionless variables

(Pe_L, St_L, St_G, and D_a) and the nature of this dependency was different in the injection mode from that in the ejection mode.

12. The use of the venturi injectors for the ozone gas absorption caused an increase in the mass transfer rates due to the contact between the gas and the liquid phases inside the injectors. Placing the injectors at an intersecting angle of 125^o at the bottom of the bubble column caused an intersecting of the gas-liquid jets. This arrangement has led to a significant increase in the turbulence intensities in the ambient fluid and consequently, a significant increase in the mass transfer rates was achieved. The impinging-jet bubble column has proven to be a very promising gas-liquid contacting unit, when compared to the traditional bubble column designs due to its compact size that can handle higher liquid and gas flowrates without causing any decrease in the mass transfer efficiency of the bubble column.

13. Using the venturi injectors for sparging the ozone gas into the liquid phase in the impinging-jet contactor has led to a significant increase in the enhanced overall mass transfer coefficient (Ek_La) and the enhancement factor (E) compared to other designs of ozone contactors. As a result, the off-gas ozone concentrations that were produced from the impinging-jet contactor were substantially lower than those produced from the other contactors.

14. The ozonation process induced higher reductions in the color and AOX concentrations compared to COD and TOC of the treated Kraft pulp mill effluents. The small ratio of the BOD_5/COD of the treated wastewater indicates the need for further treatment of this type of wastewater to increase its biodegradability, and consequently, to remove the increase in the BOD_5 of the wastewater as a result of applying further treatment.

15. The reduction efficiencies of color, AOX, COD, and TOC indicated that the scale-up and reactor configuration have exhibited insignificant effects on the ozonation treatment levels achieved in the three types of ozone contactors examined in this

study. This suggests that a small scale-up factor was associated with the ozonation treatment of Kraft pulp mill effluents, especially at large scales, where there was virtually no effect on the ozonation induced reduction efficiencies of color, AOX, COD, and TOC.

16. The treatment levels achieved in the impinging-jet and fine-bubble diffuser ozone contactors that were operated in a continuous-flow mode were compared and the two designs of ozone contactors were found to produce almost identical treatment levels except that the volume of the impinging-jet contactor was one seventh of that of the fine-diffuser contactor. Based on the above, it is evident that the operating costs of the ozonation process and the ozone off-gas destruction facilities will be greatly reduced when the impinging-jet ozone contactor is used for treating Kraft pulp mill wastewaters.

17. Therefore, the 2-D laser and phase Doppler anemometry and the digital photographic measurement techniques provided great non-intrusive tools for characterization and better understanding of the gas bubbles in the impinging-jet bubble column. The digital photographic study provided valuable information on the shape and size of the gas bubbles as well as rough estimates of the bubble rise velocity that aided in optimizing the particle dynamics analyzer configuration and operational settings during the PDA study.

18. The PDA provided rapid and accurate simultaneous measurements of the bubble size, bubble rise velocity, bubble size distribution, and turbulence intensities in an impinging-jet bubble column that utilized two venturi injectors to create turbulent gas-liquid jets in the ambient fluid.

19. The count mean bubble and Sauter mean bubble diameters were dependent on the superficial gas and liquid velocities.

20. The count and Sauter mean bubble diameters were smaller in the raw Kraft pulp mill effluent compared to those in the deionized water. This has led to a significant increase in the gas bubbles' specific interfacial area and the gas hold-up compared to those in the deionized water. As the raw Kraft pulp mill effluent was ozonated and the amount of the utilized ozone increased, the count mean and the Sauter mean bubble diameters increased.

21. The bubble size distributions exhibited different trends depending on the type of the test liquid and on the operating conditions in terms of the superficial gas and liquid velocities. Generally, those distributions could be well described using normal, gamma, or log-normal density functions.

22. The measurements of the gas hold-up and gas bubbles' specific interfacial area obtained in the current study provided valuable information that will lead to a better understanding of the mass transfer process in clean environments such as deionized water as well as in highly reactive environments such as Kraft pulp mill effluents.

12.3 RECOMMENDATIONS

In this study, different models have developed for describing the performance of ozone bubble columns and a new design of ozone bubble columns has been proposed. Based on the achieved goals and the drawn conclusions, several recommendations have to be addressed in further future research:

1. Additional testing of the models needs to be conducted in pilot-scale as well as full-scale ozone contactors to verify their applicability for describing the performance of the ozonation process in a wide range of scales and designs of ozone contactors over a wide range of operating conditions.

2. The models should be expanded to account for variable process parameters along the length of the contactor as it is usually the case in full-scale ozone contactors.

3. The models should be tested for their ability to describe the performance of ozonation systems when designed for disinfection purposes.

4. Additional studies need to be conducted to characterize the mass transfer efficiency of the impinging-jet ozone bubble column when used to treat various types of wastewaters such as different waste streams generated from the pulp and paper industry.

5. Additional PDA measurements should be carried out at different locations along the column height to examine the variability of the characteristics of the gas bubbles along the column height.

6. Different injector diameters and intersecting angles should be investigated to examine their effects on the performance of the bubble column. Also, the effect of the distance between the injector exit points should be investigated.

7. The impinging-jet bubble column should be tested for treating different types of wastewaters by utilizing ozone in conjunction with other advanced oxidants such as hydrogen peroxide, UV, fenton reagents, etc.

APPENDIX A. CURRICULUM VITAE

CURRICULUM VITAE

Full Name: Mohamed Gamal El-Din
Citizenship: Canadian
Postal Address: Department of Civil and Environmental Engineering
304 Environmental Engineering Building
University of Alberta
Edmonton, Alberta
Canada T6G 2M8
Telephone #: (780)492-5124
Fax #: (780)492-8289
E-mail: mgamalel-din@civil.ualberta.ca

UNIVERSITY EDUCATION

Ph.D. (Environmental Engineering) 1995-Current: Dissertation title "Theoretical Analysis and Experimental Verification of the Performance of Ozone Bubble Columns". Department of Civil and Environmental Engineering, University of Alberta, Edmonton, Alberta, Canada.

MS (Environmental Engineering) 1994-1995: Course based. Department of Civil and Environmental Engineering, Wayne State University, Detroit, MI, USA.

B.Sc. with Honours (Civil Engineering) 1986-1991: Faculty of Engineering, Cairo University, Cairo, Egypt.

RESEARCH INTEREST

My research interests include:

- Advanced oxidation processes (AOP's),
- Application of phase Doppler anemometry to multi-phase flows,
- Hydrodynamics modeling,
- Gas mass transfer in water and wastewater,
- Ozone treatment of industrial wastewater,
- Numerical modeling of treatment processes, and
- Water quality modeling.

WORK EXPERIENCE

Assistant Professor (July 2001-Current), Department of Civil and Environmental Engineering, University of Alberta, Edmonton, Alberta, Canada.

Research Assistant (September 1995-June 2001), Department of Civil and Environmental Engineering, University of Alberta, Edmonton, Alberta, Canada.

Research Assistant (January 1994-August 1995), Department of Civil and Environmental Engineering, Wayne State University, Detroit, Michigan, USA.

Structural Designer Engineer (August 1991-December 1993), ELOSEILY Consulting Office, Cairo, Egypt.

PUBLICATIONS

REFEREED JOURNAL PAPERS

Gamal El-Din, M. and D.W. Smith, "Development of Transient Backflow Cell Model (BFCM) for Bubble Columns", Ozone Sci. & Eng. 23(4): 313-326 (2001).

Gamal El-Din, M. and D.W. Smith, "Ozone Mass Transfer in Water Treatment: Hydrodynamics and Mass Transfer Modeling of Ozone Bubble Columns", Wat. Sci. & Technol.: Wat. Suppl. 1(2): 123-130 (2001).

Smith, D.W. and M. Gamal El-Din, "Theoretical Analysis and Experimental Verification of Ozone Mass Transfer in Bubble Columns", Environ. Technol. (Accepted, May 2001)

Gamal El-Din, M. and D.W. Smith, "Designing Ozone Bubble Columns: A Spreadsheet Approach to Axial Dispersion Model", Ozone Sci. & Eng. (Accepted, June 2001).

Gamal El-Din, M. and D.W. Smith, "Maximizing the Enhanced Ozone Oxidation of Kraft Pulp Mill Effluents in an Impinging-Jet Bubble Column", Ozone Sci. & Eng. (Accepted, July. 2001).

Gamal El-Din, M. and D.W. Smith, "Ozonation of Kraft Pulp Mill Effluent: Process Dynamics", J. Environ. Eng. & Sci. (Accepted, August 2001).

SUBMITTED JOURNAL PAPERS

Gamal El-Din, M. and D.W. Smith, "Measurements of the Size, Rise Velocity, and Specific Interfacial Area of Bubbles in an Impinging-Jet Bubble Column", J. Environ. Eng. & Sci. (submitted for publication, August 2001).

Gamal El-Din, M. and D.W. Smith, "Comparing Different Designs and Scales of Bubble Columns for Their Effectiveness in Treating Kraft Pulp Mill Effluents", Ozone Sci. & Eng. (submitted for publication, August 2001).

Gamal El-Din, M. and D.W. Smith, "Mass Transfer Analysis in Ozone Bubble Columns", J. Environ. Eng. & Sci. (submitted for publication, July 2001).

Gamal El-Din, M. and D.W. Smith, "Development of Design Parameters of an Impinging-Jet Bubble Column", Wat. Res. (submitted for publication, March 2001).

REFEREED PAPERS IN CONFERENCE PROCEEDINGS

Gamal El-Din, M. and D.W. Smith, "Comparing Different Designs and Scales of Bubble Columns for Their Effectiveness in Treating Kraft Pulp Mill Effluents". In: *Advances in Ozone Technology, Proc. of IOA/15th World Congress*, London, England (2001).

Smith, D.W. and M. Gamal El-Din, "Modeling the Hydrodynamics and Mass Transfer in an Impinging-Jet Bubble Column". In: *Advances in Ozone Technology, Proc. of IOA/15th World Congress*, London, England (2001).

Gamal El-Din, M. and D.W. Smith, "Ozonation of Kraft Pulp Mill Effluent: Process Dynamics and Scale-Up". In: *Proc. 7th Environmental Engineering Specialty Conf., 29th Annual CSCE Conf.*, Victoria, British Columbia, Canada (2001).

Gamal El-Din, M. and D.W. Smith, "Modeling the Ozonation Process in an Impinging-Jet Bubble Column". In: *Proc. 7th Environmental Engineering Specialty Conf., 29th Annual CSCE Conf.*, Victoria, British Columbia, Canada (2001).

Gamal El-Din, M. and D.W. Smith, "Maximizing the Enhanced Ozone Oxidation of Kraft Pulp Mill Effluents in an Impinging-Jet Bubble Column". In: *Advances in Ozone Technology, Proc. of IOA/PAG Conf.*, Newport Beach, California, USA (2001).

Gamal El-Din, M. and D.W. Smith, "Designing Ozone Bubble Columns: A Spreadsheet Approach to Axial Dispersion Model". In: *Advances in Ozone Technology, Proc. of IOA/PAG Conf.*, Orlando, Florida, USA (2000).

Gamal El-Din, M. and D.W. Smith, "Ozone Mass Transfer in Water Treatment: Hydrodynamics and Mass transfer Modeling of Ozone Bubble Columns". In: *Proc. of the Water Supply and Water Quality Conf.*, Kraków, Poland, pp. 623-635 (2000).

Gamal El-Din, M. and D.W. Smith, "Rational Approach to Hydrodynamic Modeling of an Ozone Jet-Bubble Column". In: *Proc. 6th Environmental Engineering Specialty Conf., 28th Annual CSCE Conf.*, London, Ontario, Canada, pp. 327-335 (2000).

CONFERENCE/WORKSHOP PAPER AND POSTER PRESENTATIONS

Gamal El-Din, M. and D.W. Smith, "Theoretical Analysis and Experimental Verification of the Ozonation Process in Bubble Columns". Oral presentation, In: *7th Int. Conf. on Advanced Oxidation Technologies for Water and Air Remediation*, Niagara Falls, Ontario, Canada, (2001).

Smith, D.W. and M. Gamal El-Din, "Testing the Applicability of One-Phase Axial Dispersion Model to Describe the Performance of Ozone Bubble Columns". Oral presentation, In: *Sustainable Forest Management Network Student Workshop*, Edmonton, Alberta, Canada, (2000).

Gamal El-Din, M. and D.W. Smith, "Comparing ADM and BFCM for Modeling Ozone Bubble Columns with Constant Dimensionless Operating Parameters". Oral presentation, In: *6th Int. Conf. on Advanced Oxidation Technologies for Water and Air Remediation*, London, Ontario, Canada, (2000).

Gamal El-Din, M. and D.W. Smith, "Hydrodynamics Modeling of Ozone Jet-Bubble Columns". Poster presentation, In: *Paper Week Int. Conf.*, Montreal, Quebec, Canada, (2000).

Gamal El-Din, M. and D.W. Smith, "Maximizing Enhanced Ozonation of Pulp Mill Effluents". Poster presentation, In: *Paper Week Int. Conf.*, Montreal, Quebec, Canada, (2000).

Gamal El-Din, M. and D.W. Smith, "Maximizing Enhanced Oxidation of Pulp Mill Effluents". Poster presentation, In: *Sustainable Forest Management Network Conf., Science and Practice: Sustaining the Boreal Forest*, Edmonton, Alberta, Canada, (1999).

TECHNICAL REPORTS

Gamal El-Din, M. and Smith, D.W. "Maximizing Enhanced Ozone Oxidation of Pulp Mill Effluents". Sustainable Forest Management Network, 2000-26, ISBN 1-55261-086-1.

AWARDS/RECOGNITIONS

July 1991: Awarded an Honours Degree as a result of maintaining a minimum grade of "Very Good" throughout the 5-year undergraduate program at Cairo University.

PROFESSIONAL MEMBERSHIP AND CONTRIBUTIONS

- Technical reviewer for the journal of Ozone Sci. & Eng.
- Current member of the Canadian Society for Civil Engineering (CSCE), International Association on Water Quality (IAWQ), American Water Works Association (AWWA), International Ozone Association (IOA), and Egyptian Syndicate of Civil Engineers.